INSTITUT DE FÍSICA D'ALTES ENERGIES

UNIVERSITAT AUTÒNOMA DE BARCELONA

Calibration of the MAGIC Telescope and Observation of Gamma Ray Bursts

Ph.D. Thesis

Markus Gaug
Universitat Autònoma de Barcelona
Departament de Física
08193 Bellaterra (Barcelona)
Spain
<markus@ifae.es>

March 2006

supervised by:

Prof. Manel Martínez Rodríguez
IFAE
Edifici Cn, UAB
08193 Bellaterra (Barcelona)

Contents

1 Introduction **1**
- 1.1 Cosmic Rays . . . 1
- 1.2 Gamma Ray Bursts . . . 2
- 1.3 Modern Cherenkov Telescopes . . . 2
- 1.4 This Work . . . 2

2 Creation of Gamma Rays **5**
- 2.1 Supernova Remnants . . . 7
- 2.2 Pulsars . . . 8
- 2.3 OB-Associations . . . 9
- 2.4 Unidentified EGRET Sources . . . 10
- 2.5 Active Galactic Nuclei . . . 10
- 2.6 Microquasars . . . 13
- 2.7 Starburst Galaxies . . . 13
- 2.8 Unidentified TeV Gamma Ray Sources . . . 14
- 2.9 Gamma Ray Bursts . . . 14
  - 2.9.1 Phenomenology . . . 14
  - 2.9.2 Progenitors . . . 19
  - 2.9.3 Fireball Model . . . 20
  - 2.9.4 Cannonball Model . . . 22
  - 2.9.5 Other Models . . . 22
  - 2.9.6 Emission of GeV and TeV Gamma Rays . . . 23
- 2.10 X-Ray Flashes . . . 28
- 2.11 Soft Gamma Repeaters . . . 28
- 2.12 Cosmology and Diffuse Background Radiation . . . 29
  - 2.12.1 Gamma Ray Horizon . . . 29
- 2.13 Fundamental Physics . . . 30
  - 2.13.1 Super-symmetric Particles and Dark Matter . . . 30
  - 2.13.2 Quantum Gravity Scale . . . 31

3 The Magic Telescope **33**
- 3.1 Air Showers . . . 33
  - Electromagnetic Air Showers . . . 33
  - Hadronic Air Showers . . . 35
- 3.2 The Imaging Air Cherenkov Technique . . . 37
- 3.3 Site . . . 43
- 3.4 Drive System . . . 43
- 3.5 Star-guider . . . 44
- 3.6 Reflector . . . 44
- 3.7 Camera . . . 46

3.8 Signal Transmission and Processing Chain . . . 52
3.9 Trigger . . . 55
Level-1 Trigger . . . 56
Level-2 Trigger . . . 56
3.10 Data Acquisition . . . 57
3.11 The GRB Alert System . . . 58
3.12 Software Packages . . . 58
Telescope Control Software: . . . 58
Monte Carlo (***MC***) Simulation Software: . . . 59
Analysis Software: . . . 59

4 The Calibration System **61**
4.1 Pulsed LEDs . . . 63
4.1.1 Spectra of the Pulsed LEDs . . . 65
4.1.2 Peripheries for the Pulsed LEDs . . . 71
4.1.3 Spatial Uniformity of the Pulsed Light . . . 72
4.2 The CT1-Pulser . . . 73
4.3 Continuous Light Source . . . 74
4.4 The Blinded Pixels . . . 75
4.4.1 Statistical Description of the Blinded Pixel . . . 78
The Ideal PMT . . . 78
Background Processes . . . 80
The Realistic PMT . . . 81
4.5 The PIN Diode . . . 85
4.5.1 Interaction of Gamma-Rays with Silicon . . . 88
Photo-Absorption . . . 89
Compton Scattering . . . 89
Coherent Scattering . . . 90
4.5.2 Interaction of Electrons with Silicon . . . 90
4.5.3 The HAMAMATSU PIN Diode S3590-08 . . . 90
4.5.4 The ^{241}Am Calibration Source . . . 91
The ^{133}Ba Calibration Source . . . 93
4.5.5 Noise Behaviour of the PIN Diode . . . 95
4.5.6 PIN Diode Readout . . . 97
4.6 The Camera . . . 101

5 Signal Extraction **107**
5.1 Review Signal Acquisition . . . 107
5.2 Statistical Properties of Signal Extractors . . . 108
5.3 Considerations Based on the MAGIC Readout System . . . 110
5.4 Signal Extraction Algorithms . . . 113
5.4.1 Fixed Window . . . 114
5.4.2 Sliding Window with Amplitude-weighted Time . . . 115
5.4.3 Cubic Spline with Sliding Window or Amplitude Extraction . . . 115

5.4.4 Digital Filter . . . 116
5.5 Statistical Parameters from MC Simulations . . . 122
5.5.1 Bias . . . 122
5.5.2 Root Mean Square Error . . . 123
5.5.3 Decomposition of Variance . . . 124
5.6 Statistical Parameters from Pedestal Runs . . . 125
5.7 Statistical Parameters from Calibration Runs . . . 129
5.7.1 Numbers of Photo-electrons . . . 131
5.8 Robustness Tests . . . 133
5.9 Time Resolutions . . . 137
5.10 CPU Requirements . . . 141
5.11 Results . . . 141
5.12 Outlook . . . 144

6 Characterization of the Telescope Using the Calibration System 145
6.1 High-gain vs. Low-gain Inter-calibration . . . 145
6.2 Linearity of the Amplification Chain . . . 151
6.3 Cross-Talk in the Camera and Short-term Temporal Uniformity of Light Pulses . . . 153
6.4 Medium-term Variations of Light Pulser Intensity and Camera Gains 156
6.5 Long-term Evolution of the Camera . . . 159
6.6 Absolute Light Calibration . . . 161
6.7 Arrival Time Offsets . . . 164
6.8 Summary . . . 165

7 Data Analysis 169
7.1 Signal Extraction from FADC Slices . . . 171
7.2 Calibration . . . 171
7.3 Image Cleaning . . . 173
The Absolute Cleaning . . . 174
The Time Cleaning . . . 174
7.4 Quality Parameters . . . 177
SIZE . . . 177
WIDTH, *LENGTH*, *DIST* and *ALPHA* . . . 178
CONC, *CONC4*, *LEAKAGE*, *NUMBER ISLANDS* . . . 181
7.5 Multivariate Classification . . . 181
Random Forest . . . 182
Energy Estimation . . . 183
7.6 Determination of Significances and Cuts on *HADRONNESS* and *ALPHA* . . . 183
7.7 Calculation of Effective Areas . . . 186
7.8 Calculation of Upper Limits . . . 186
7.8.1 Upper Limits for Number of Observable Events . . . 187
Construction of p.d.f. . . . 188

Inversion of p.d.f. . . . 188
7.8.2 Particle Flux Upper Limits . . . 190
7.8.3 Particle Fluence Upper Limits . . . 191
7.8.4 Spectral Energy Density Upper Limits . . . 191
7.9 Analysis of Muons . . . 192

8 Gamma Ray Bursts Observation 193
8.1 The Data Samples . . . 194
8.2 Pointing Precision in GRB Observation Mode . . . 196
8.3 Spherical Aberration of the Mirrors in GRB Mode . . . 199
8.4 Calibration and Excluded Pixels . . . 199
8.5 Image Cleaning . . . 200
8.6 Pre-selection . . . 201
SIZE . . . 203
DIST . . . 204
Spark Events . . . 204
8.6.1 *SIZE* after Pre-selection . . . 206
8.6.2 Camera Homogeneity after pre-selection . . . 206
8.6.3 Cut Efficiencies . . . 208
8.7 Calculation of *HADRONNESS* . . . 208
8.8 Test of Cut Parameters . . . 214
8.9 Rates with Increasing Cut Strength . . . 218
8.10 Energy Reconstruction . . . 218
8.11 Cut Optimization . . . 220
8.12 Results Mrk501 Test Data . . . 224
8.13 Results GRB050713a Data . . . 229
8.13.1 Prompt Emission Phase . . . 230
8.13.2 First 1000 Seconds . . . 234
8.13.3 Entire Data Sample . . . 236
8.14 Results Upper Limits . . . 238
8.15 Search in Time Slices of 100 Seconds . . . 238
8.16 Effect of Systematic Uncertainties on the Limits . . . 242
Point-spread Function . . . 242
Trigger Inefficiencies . . . 242
Absolute Energy Scale . . . 244
Further Systematic Uncertainties . . . 244
8.17 Fluence and Spectral Energy Density Limits . . . 245
8.18 Physical Interpretation . . . 246
8.19 Summary . . . 249

9 Conclusions 253

References 255

Glossary **I**

List of Tables

1 Characteristics Light Pulser System 66
2 Pulsed LEDs Spectral Parameters 69
3 Continuous Light Colours and Star Spectral Types 74
4 Averaged Efficiencies Blinded Pixels 77
5 Averaged Efficiencies PIN Diode 88
6 Important γ-ray Emission Lines of ^{241}Am 92
7 Important γ-ray Emission Lines of ^{133}Ba 92
8 Efficiencies Averaged Pixel 106
9 $\sqrt{\mathrm{Var}[\widehat{N}_{rec}]}$ for Pedestal Events and Fixed Extraction Window . . . 126
10 Bias and *RMSE* from Pedestal Events for Various Signal Extractors 128
11 Pulse Form Dependency of Integration Windows 135
12 Fit Results to Time Resolution vs. Intensity 141
13 Extraction Speed Different Signal Extractors 142
14 Results Signal Extractor Tests 143
15 Classification Signal Extractors High vs. Low-gain Corr. Properties 149
16 Absolute Calibration Results PIN Diode 162
17 Absolute Calibration Results Blind Pixels 163
18 Degradation Excess Noise Factor 167
19 Noise Island Probabilities for Absolute Image Cleaning 175
20 Noise Island Probabilities for Time Image Cleaning 176
21 Results Cleaning Levels 177
22 Observed GRBs MAGIC Cycle I Observation Phase 193
23 Data Samples Used for GRB Analysis 195
24 Cut Efficiencies GRB050713a 208
25 Cut Efficiencies Mrk501 209
26 Kolmogorov-Smirnov Test Probabilities 218
27 Results Mrk501 Data 228
28 Results GRB050713a Analysis - Prompt Emission 233
29 Results GRB050713a Analysis - First 1000 Seconds 235
30 Results GRB050713a Analysis - Entire Data 237
31 Differential Upper Limits for GRB050713a Prompt Emission Data . 239
32 Differential Upper Limits for First 1000 s of GRB050713a Data . . . 239
33 Differential Upper Limits for Total 2200 s of GRB050713a Data . . . 240
34 Results Analysis GRB050713a Data - 100 Seconds Time Slices . . . 241
35 Flux Density Upper Limits for GRB050713a Prompt Emission Data 246
36 Claims Optical Counterparts GRB050713a 247

List of Figures

1 Viktor Hess in Research Balloon 1
2 Energy Spectrum of Cosmic Rays 4
3 Energy Spectrum of Electrons and Positrons 4
4 The SNR RX J1713.7-3946 Seen in Gamma Rays and X-rays 7
5 The 7 Pulsars Detected by EGRET 9
7 NGC4261, Seen by the ***HST*** 10
6 The Gamma Ray Point Sources 11
8 Light Curve of Mrk 501, Seen in X-rays and Gamma Rays 12
9 Components of a Microquasar 13
10 The GRBs Detected by BATSE 15
11 Light Curves of GRBs 15
12 Example of Hard-to-soft Spectral Evolution 16
13 Burst Durations of BATSE GRBs 17
14 Distribution of Spectral Indices from Band Function 17
15 Example of an X-ray Flare 18
16 The Ghirlanda Relation 18
17 NS-NS Merger 19
18 Fireball Model Artist's View 20
19 Cannonball Model Artist's View 22
20 Averaged Spectra of Four Brightest EGRET Bursts 23
21 Light curve of GRB940217 24
22 Spectrum of GRB941017 Predicted from Different Fireball Models . 26
23 High-energy Light Curve and Spectra from Cannonball Model 27
24 Predicted Spectra from Compton Drag Model 27
25 Predicted Spectra from Stern and Poutanen Model 28
26 The Gamma Ray Horizon 30
27 Schematic View of Generation of an Electromagnetic Air Shower . . 33
28 Electromagnetic Shower Longitudinal Development 34
29 Schematic Ciew of Generation of a Hadronic Air Shower 35
30 Vertical Fluxes of Particles in Atmosphere 36
31 Schematic View of Cherenkov light Production 37
32 Spectrum of Cherenkov Light 38
33 Photon Spectrum Cherenkov Showers 39
34 Photon Density of Cherenkov Light 40
35 Lateral Distribution of Cherenkov Light 41
36 Simulated Gamma Showers on Ground 42
37 Simulated Proton Shower on GSiround 42
38 Example of Shower Types Recorded by MAGIC Camera 43
39 View of the MAGIC Telescope 44

40 Reflectivity of the Mirrors . . . 45
41 Schematic View of the MAGIC Camera . . . 46
42 After-pulse Probability ET9116A . . . 47
43 Quantum Efficiency Spectra and Spatial Uniformity MAGIC PMTs 48
44 Cornings Blue and Red in Camera . . . 49
45 Cornings Blue vs. Corning Red . . . 49
46 Normalized Photo-electron Spectrum in Coated PMT . . . 50
47 Relative Angular Response and Gain of Light Guides . . . 51
48 Transmission of Plexiglas . . . 52
49 Optical Transmitters in Camera . . . 53
50 Noise in Optical Transmitters . . . 54
51 Output Optical Transmitters . . . 54
52 Relative RMS Optical Transmitters vs. Input Pulse Amplitude . . . 55
53 Trigger Macro-cells . . . 56
54 Data Stream MAGIC . . . 57
55 Components of the Calibration System . . . 61
56 Schematic Circuit to Trigger the Avalanche Transistors . . . 62
57 Schematic Avalanche Transistor Circuit . . . 62
58 Probe LEDs Pulses . . . 63
59 The Pulser Board . . . 64
60 The Pulsed LEDs Set in Place . . . 64
61 Sketch of the Pulsed LEDs . . . 65
62 The Pulser Box . . . 66
63 Peak Wavelength vs. Temperature - Pulsed LEDs . . . 68
64 Peak Wavelength vs. Current - Pulsed LEDs (data sheet) . . . 68
65 Peak Wavelength vs. Current - Pulsed LEDs (measurement) . . . 68
66 Sketch of the Spectrum Measurement Setup . . . 69
67 Spectrum Pulsed LEDs Continuous Mode . . . 70
68 Spectrum Pulsed LEDs Pulsed Mode . . . 70
69 Time Dependency 600 V Supply . . . 71
70 Uniformity of Emitted Light from the Pulsed LEDs . . . 72
71 The CT1-pulser Box. . . . 73
72 Sketch of Continuous Light LEDs . . . 74
73 Current vs. DAC Value in Continuous Light Source . . . 74
74 Sketch of Functionning of a Blinded Pixel . . . 75
75 Photos of one Blinded Pixel . . . 76
76 Quantum Efficiency Blinded Pixel #1 . . . 79
77 Quantum Efficiency Blinded Pixel #3 . . . 79
78 Outgoing Pulse of Blinded Pixel . . . 80
79 Example of Single-photoelectron Fit . . . 84
80 The PIN Diode Box Set in Place . . . 85
81 Sketch of Functionning of the PIN Diode . . . 86
82 Transmission of the PIN Diode Box Glass Window . . . 87
83 Absorption Coefficients of Silicon and Germanium . . . 89

84 Quantum Efficiency and Photo-sensitivity PIN Diode 91
85 Spectrum Photon Emission ^{241}Am 94
86 Spectrum Photon Emission ^{133}Ba 94
87 Simplified Schematics PIN Diode Readout Circuit 95
88 Equiv. Noise Charge vs. Shaping Time 96
89 The PIN Diode Mounted on Pre-amplifier 97
90 PIN Diode Spectra Read out with LeCroy *QVT* at La Palma 98
91 Calibration Results from LeCroy *QVT* Readout 98
92 PIN Diode Spectra Read out with MAGIC FADCs at La Palma . . . 99
93 Positions 81 keV Peak of Barium Spectrum vs. Time 100
94 Width 81 keV Peak of Barium Spectrum vs. Time 100
95 Gauss Fit to Distribution of Charges 102
96 Charge Distribution of Ringing Pixel 103
97 Examples of the Razmick Plot 104
98 Offsets from Line Fit to Razmick Plot 104
99 Reconstructed Pulse Shapes 107
100 Average Normalized Reconstructed Pulse Shapes 108
101 Sketch Typical Signal Extractors 109
102 Evolution of Pedestal Parameters 112
103 Example Noise Auto-correlation Matrix 112
104 Pedestal RMS for Various Light Conditions and Summation Ranges 113
105 Pedestal Mean for Various Light Conditions and Summation Ranges 114
106 Example Sliding Window Reconstructor for Low Intensity Pulse . . 115
107 Example Spline Reconstructor for Low Intensity Pulse 115
108 Example Digital Filter Reconstructor for Low Intensity Pulse 116
109 Examples signal reconstructors for high intensity pulse 117
110 Noise Auto-correlation Various Levels of Night Sky Background . . . 119
111 Noise Auto-correlation Low-gain 120
112 Digital Filter Weights 121
113 Measured Biases from MC Simulation 123
114 Relative *RMSE* from MC simulation 124
115 Contributions to Relative *RMSE* 125
116 Example Calibration Pulses Lowest and Highest Intensity 129
117 Examples of the Razmick Plot - High Gain 130
118 Examples of the Razmick Plot Results - High Gain 131
119 Razmick Plot Results - Offsets High Gain 132
120 Reconstructed Number Photo-electrons Standard UV Calibration Pulse 133
121 Reconstructed Number Photo-electrons Green Calibration Pulse . . 134
122 Reconstructed Number Photo-electrons Blue Calibration Pulse . . . 134
124 Example Late Pulse Position 135
123 Reconstructed Number of Photo-electrons Different Pulse Forms . . 136
125 Mean Pulse Positions for Cosmics in 2005 137
126 Examples of Relative Arrival Time Distributions 138
127 Arrival Time Resolutions 139

128 High-gain vs. Low-gain Signal Ratios for Different Extractors 146
129 High-gain vs. Low-gain Signal Ratio Displayed in Camera 147
130 Correlation of High-gain Low-gain Ratios Between Extractors 148
131 High-gain vs. Low-gain Signals Linear Fits 150
132 Linearity Amplification Chain 151
133 Linearity Spline 152
134 Linearity Digital Filter 152
135 Distribution of Correlation Coefficients 155
136 Medium-term Test of Short-term Correlation 156
137 Long-term Test of Short-term Correlation 157
138 Medium-term Evolution of Light Pulser Intensity and Camera Gains 158
139 Evolution of Camera Gains during One Night 158
140 Evolution of Signal Dispersion during Two Years 160
141 Arrival Time Offsets 164
142 Evolution Excess Noise Factor 166
143 Example Simulated Gamma Shower 178
144 Sketch Image Parameters 179
145 Example *ALPHA* plot 184
146 Distributions of *ALPHA* for Simulated Gamma Signal 185
147 Typical Distribution of Effective Areas 187
148 Example Confidence Belt 189
149 SWIFT Light Curve GRB050713a 194
150 Raw Event Rates of GRB050713a 196
151 Raw Event Rates for Mrk501 ON Data 197
152 Pedestal RMS GRB050713a Data 197
153 Pointing Precision for GRB050713a Observation 198
154 Mean Calibrated Signals GRB050713a and Sparks 200
155 Mean Pulse Position GRB050713a 200
156 Signal after Image Cleaning 201
157 Center of Ellipse after Image Cleaning 202
158 Center of Ellipse after Image Cleaning - MC Simulation 202
159 Distributions log(*SIZE*): GRB050713a Data 203
160 Distributions log(*SIZE*): Mrk501 Flare Data 204
161 Distributions *DIST* 205
162 Distributions log(*CONC*) 205
163 Distributions log(*CONC*) for Spark Events 206
164 Distributions log(*SIZE*) after Pre-selection 207
165 Distributions Center-of-gravity after Pre-selection 207
166 Distributions *WIDTH* 211
167 Distributions *LENGTH* 211
168 Distributions *DIST* 211
169 Distributions *M3LONG* 212
170 Distributions *CONC* 212
171 Distributions *CONC4* 212

172 Mean Decrease of Gini Indices 213
173 Test Distributions *WIDTH* 215
174 Test Distributions *LENGTH* 215
175 Test Distributions *DIST* 216
176 Test Distributions *M3LONG* 216
177 Test Distributions *CONC* 217
178 Test Distributions *CONC4* 217
179 Event Rates with Increasing Cuts Strength 219
180 Reconstructed vs. True Energy 221
181 Distributions Relative Energy Reconstruction Error 221
182 Distributions *DIST* vs. *ALPHA* 222
183 Distributions *HADRONNESS* 223
184 Test Significance vs. *HADRONNESS* Cut Simulated Gamma Signals 224
185 Distributions $|ALPHA|$ Mrk501 Data and Absolute Image Cleaning . 225
186 Distribution $|ALPHA|$ Mrk501 Data and Time Image Cleaning . . . 226
187 Distributions Simulated Gamma Energies Mrk501 Data 227
188 Spectrum of Mrk501 229
189 Distributions Simulated Gamma Energies GRB050713a Data 231
190 Distributions $|ALPHA|$ for Prompt GRB Emission 232
191 Distributions $|ALPHA|$ for First 1000 Seconds 234
192 Distributions $|ALPHA|$ for Entire GRB050713a Data 236
193 Excess Events vs. Time 241
194 Significances Peak Emission Search 242
195 Center-of-gravity after All Cuts 243
196 Azimuthal Projection of COG after All Cuts 243
197 Distribution Redshifts Swift Bursts 247
198 Spectrum of SWIFT with MAGIC Upper Limits 248
199 Lightcurves GRB050713a All Observations 249

Summary

The thesis consists of a technical part, describing the MAGIC Telescope, its calibration and signal reconstruction, and an analysis part with the result of the first observation of the prompt emission of a gamma ray burst, made by a Cherenkov Telescope.

Technical Part

After a general introduction to the Imaging Atmospheric Cherenkov Technique, the MAGIC Telescope and its calibration system is presented: an assembly of ultra-fast and bright LEDs in three different colors are used to send calibration light pulses of various intensities to the camera, which in turn gets characterized by its response to the series of light pulses of a same intensity. Two additional devices measure the absolute amount of light: Three obscured photo-multipliers can extract single photo-electron spectra, and a calibrated PIN diode yields an electrical signal proportional to the incident number of photons.

The calibration system was used to derive characteristic parameters of the MAGIC camera: Correction factors to equalize the differences in gain and quantum efficiency between different pixels in the camera and their evolution with time, absolute conversion factors from FADC counts to photo-electrons and photons, correction factors to equalize the signal transit times. A global time resolution of the MAGIC camera is derived and a linearity calibration performed. Finally, the short, medium and long-term evolution of the camera with time is investigated and solutions presented to correct for the found changes.

Analysis Part

Data taken on GRB050713a was analyzed. This burst was detected on July, 13^{th}, 2005 by the BAT instrument onboard the SWIFT satellite, and followed-up by the MAGIC Telescope only 40 seconds after the onset of the burst, but while the burst was still ongoing. As the burst position, seen from the MAGIC Telescope, appeared rather close to the horizon, observational conditions were not optimal and especially the energy threshold came out at least three times higher than the one obtained in common observations at low zenith angles. A parallel test analysis was performed on data taken during an extraordinarily strong flare of the Active Galactic Nucleus (AGN) "Markarian 501", the strongest high-energy gamma ray source at that time. The data of test analysis was taken just 10 days before the GRB050713a data. The test analysis confirmed the gain in sensitivity as well as the lowering of the energy threshold: The spectrum can be extended to energies well below 100 GeV for observations at low zenith angles, with a sensitivity of about 4σ per hour for an equivalent

Crab Nebula flux at a mean energy of 80 GeV.

The GRB050713a data was searched for signals in four ways:

1. Searching the first 90 s of overlap with the prompt emission phase.
2. Searching the first 1000 s.
3. Searching the entire 37 minutes of data taken on GRB050713a.
4. Searching in time bins of 100 s.

None of these four searches yielded a significant excess over background and differential upper limits were derived for each of these searches.

The following differential upper limits (95% CL) on the emission of GRB050713a were obtained, including statistical and systematic uncertainties:

$$< \frac{d\Phi}{dE} >|_{160\,\mathrm{GeV}} < 1.3 \cdot 10^{-8}\ \mathrm{ph/cm^2/TeV/s} \equiv 4.2\ \mathrm{C.U.} \quad \text{first } 90\,\mathrm{s}$$
$$< \frac{d\Phi}{dE} >|_{160\,\mathrm{GeV}} < 3.3 \cdot 10^{-9}\ \mathrm{ph/cm^2/TeV/s} \equiv 1.1\ \mathrm{C.U.} \quad \text{first } 1000\,\mathrm{s}$$
$$< \frac{d\Phi}{dE} >|_{160\,\mathrm{GeV}} < 1.4 \cdot 10^{-9}\ \mathrm{ph/cm^2/TeV/s} \equiv 0.45\,\mathrm{C.U.} \quad \text{entire } 2223\,\mathrm{s}$$
$$< \frac{d\Phi}{dE} >|_{160\,\mathrm{GeV}} < 1.6 \cdot 10^{-8}\ \mathrm{ph/cm^2/TeV/s} \equiv 5.2\ \mathrm{C.U.} \quad \text{any } 100\,\mathrm{s} \text{ interval}$$

$$< \frac{d\Phi}{dE} >|_{280\,\mathrm{GeV}} < 3.0 \cdot 10^{-9}\ \mathrm{ph/cm^2/TeV/s} \equiv 4.1\ \mathrm{C.U.} \quad \text{first } 90\,\mathrm{s}$$
$$< \frac{d\Phi}{dE} >|_{280\,\mathrm{GeV}} < 2.9 \cdot 10^{-10}\ \mathrm{ph/cm^2/TeV/s} \equiv 0.40\,\mathrm{C.U.} \quad \text{first } 1000\,\mathrm{s}$$
$$< \frac{d\Phi}{dE} >|_{280\,\mathrm{GeV}} < 2.6 \cdot 10^{-10}\ \mathrm{ph/cm^2/TeV/s} \equiv 0.36\,\mathrm{C.U.} \quad \text{entire } 2223\,\mathrm{s}$$
$$< \frac{d\Phi}{dE} >|_{280\,\mathrm{GeV}} < 2.8 \cdot 10^{-9}\ \mathrm{ph/cm^2/TeV/s} \equiv 3.8\ \mathrm{C.U.} \quad \text{any } 100\,\mathrm{s} \text{ inverval}$$

with 22 % uncertainty on the determination of the absolute energy scale.

Resumen

Esta tesis consiste en dos partes: Una técnica que describe el telescopio MAGIC, su calibración y la reconstrucción de sus señales; y una parte de análisis resumiendo la primera observación de la emisión inicial de un estallido de rayos gama ("Gamma Ray Burst"), realizada con un telescopio Cherenkov.

Parte Técnica

Después de una introducción a la técnica IACT, se presenta el telescopio MAGIC con su sistema de calibración: un conjunto de "LEDs" ultra rápidos y luminosos en tres colores diferentes. Éste se utiliza para enviar impulsos de luz hacia la cámara, la cual se caracteriza utilizando las señales que recoge de una serie de impulsos de luz que poseen la misma intensidad. Dos dispositivos adicionales miden la cantidad absoluta de luz: fotomultiplicadores oscurecidos, capaces de extraer espectros de fotoelectrones individuales, y un PIN diodo calibrado que produce una señal eléctrica proporcional al número total de fotones incidentes.

El sistema de calibración fue utilizado para obtener parámetros característicos de la cámara: factores de corrección para igualar las diferencias de ganancia y de eficiencia cuántica entre los pixeles de la cámara, así como su evolución temporal. Además se obtuvieron factores de conversión de cuentas de FADC a fotoelectrones y fotones, y factores de corrección para igualar los tiempos de paso. Se obtuvo una resolución de tiempo global y se realizó una calibración de linealidad. Finalmente, se investigó la evolución temporal de la cámara a plazo corto, medio y largo y se presentan soluciones para corregir los cambios encontrados.

Parte de Análisis

En esta parte se analizaron datos de un estallido de rayos gama (GRB), llamado GRB0507013a. Este estallido fue detectado el 13 de julio del 2005, por el detector BAT, integrado al satélite SWIFT, y en seguida observado por el telescopio MAGIC mientras el estallido estaba todavía activo. Como la posición del estallido, vista des del telescopio MAGIC, se encontró cerca del horizonte, las condiciones de observación no eran óptimas. Así, el umbral de energía resultó ser al menos tres veces más alto que el que se habría obtenido en observaciones con ángulo zenital bajo.

Un análisis paralelo fue realizado con datos tomados durante un "flare" extraordinariamente intenso del núcleo activo "Markarian 501", que dio los flujos de rayos gama más intensos en este periodo del año. Estos datos se tomaron 10 días antes de los de GRB050713a. El análisis paralelo confirmó la ganancia en sensitividad como también un umbral de energía más bajo: El espectro de rayos gama de Markarian 501 podía ser extendido hacia energías mucho más bajas que 100 GeV, para observaciones a bajo ángulo zenital. Se obtuvo una sensitividad de cerca de $4\,\sigma$

por hora para un flujo de rayos gama equivalente al flujo de la nebulosa del Cangrejo a energías alrededor de 80 GeV.

Los datos de GRB0507013a fueron analizados de cuatro maneras diferentes:

1. Buscando señal en los primeros 90 segundos de coincidencia con la fase inicial de emisión.
2. Buscando señal en los primeros 1000 segundos de datos.
3. Buscando señal en el conjunto de 37 minutos de datos de GRB0507013a.
4. Buscando señal en bines de 100 segundos.

Ninguna de estas búsquedas reveló un exceso significativo de señal respecto al fondo esperado y se obtuvieron límites superiores sobre el flujo de rayos gama para cada una de estas búsquedas (95% CL):

$$< \frac{d\Phi}{dE} >|_{160\,\mathrm{GeV}} \;<\; 1.3 \cdot 10^{-8}\ \mathrm{fot./cm^2/TeV/s} \;\equiv\; 4.2\ \text{C.U. (primeros 90 s)}$$
$$< \frac{d\Phi}{dE} >|_{160\,\mathrm{GeV}} \;<\; 3.3 \cdot 10^{-9}\ \mathrm{fot./cm^2/TeV/s} \;\equiv\; 1.1\ \text{C.U. (primeros 1000 s)}$$
$$< \frac{d\Phi}{dE} >|_{160\,\mathrm{GeV}} \;<\; 1.4 \cdot 10^{-9}\ \mathrm{fot./cm^2/TeV/s} \;\equiv\; 0.45\,\text{C.U. (completos 2223 s)}$$
$$< \frac{d\Phi}{dE} >|_{160\,\mathrm{GeV}} \;<\; 1.6 \cdot 10^{-8}\ \mathrm{fot./cm^2/TeV/s} \;\equiv\; 5.2\ \text{C.U. (cualquier intervalo de 100 s)}$$

$$< \frac{d\Phi}{dE} >|_{280\,\mathrm{GeV}} \;<\; 3.0 \cdot 10^{-9}\ \mathrm{fot./cm^2/TeV/s} \;\equiv\; 4.1\ \text{C.U. (primeros 90 s)}$$
$$< \frac{d\Phi}{dE} >|_{280\,\mathrm{GeV}} \;<\; 2.9 \cdot 10^{-10}\ \mathrm{fot./cm^2/TeV/s} \;\equiv\; 0.40\,\text{C.U. (primeros 1000 s)}$$
$$< \frac{d\Phi}{dE} >|_{280\,\mathrm{GeV}} \;<\; 2.6 \cdot 10^{-10}\ \mathrm{fot./cm^2/TeV/s} \;\equiv\; 0.36\,\text{C.U. (completos 2223 s)}$$
$$< \frac{d\Phi}{dE} >|_{280\,\mathrm{GeV}} \;<\; 2.8 \cdot 10^{-9}\ \mathrm{fot./cm^2/TeV/s} \;\equiv\; 3.8\ \text{C.U. (cualquier intervalo de 100 s)}$$

Estos límites incluyen incertidumbres estadísticas y sistemáticas, además hay que asumir un 22% de incertidumbre sobre la determinación de la escala absoluta de energía.

1 Introduction

1.1 Cosmic Rays

Ever since in 1912 the Austrian physicist Viktor Hess announced the first experimental evidence that ionizing radiation constantly impinges on the Earth's atmosphere [1], the then newly discovered ***cosmic rays*** have been puzzling physicists and astro-physicists. Due to their spectral behaviour, they must have been emitted by objects which have not had the time to thermalize. For this reason, cosmic rays are considered messengers from the ***non-thermal*** part of the universe, containing as much or even more energy than the ***thermal*** radiation, mainly emitted by the stars. It is still unclear which sources produce the cosmic rays and how, what their composition is over the whole observed energy range and how far they propagate in space.

The measured cosmic rays energy spectrum (figure 2) shows an energy range extending over more than 13 orders of magnitude with fluxes reaching from 1 particle/(cm^{2}s) at energies of 100 MeV to less than 0.01 particles/(km^{2}century) for the highest observed energies. In the region of the energy spectrum which is unaffected by the propagation of particles to the Earth through the solar wind (at energies E greater than 1 GeV), the differential fluxes dN/dE follow a strict power law, $dN/dE \propto E^{-\alpha}$, first with $\alpha \approx 2.7$ and later with $\alpha \approx 3$ [2]. There are structures visible, namely a ***knee*** at $\approx$ 4–5 PeV [1] and an ***ankle*** at $\approx$ 3 EeV [2]. Up to the knee, the chemical composition could be measured directly: About 79 % of the primary nucleons consist of ***protons***, 70% of the rest consists of ***helium nuclei*** and only a small fraction of nuclei of heavier elements [3]. Less than 1 % of the cosmic rays consists of ***electrons and positrons***, the spectrum of which is steeper than the one of protons and nuclei (see figure 3 and [3,4]). Only a tiny fraction of the cosmic rays is made up of ***gamma rays***. While the origin of the low-energy part (below 10 GeV) can be traced back to the Sun, the high-energy part ranging up to the knee is believed to originate from ***Galactic accelerators*** and those at higher energies from ***extra-galactic accelerators***. Cosmic rays up to about 1 EeV are isotropic, while a claim on an-isotropy at higher energies is still under debate [5]. It is believed that cosmic rays are confined in the magnetic field of our Galaxy up to the knee[3].

Figure 1: Viktor Hess in his research balloon. Figure from [2].

[1] 1 PeV $\equiv 10^{15}$ eV

[2] 1 EeV $\equiv 10^{18}$ eV

[3] Abundance measurements of radio-active isotopes, especially of ^{10}Be revealed that cosmic rays are typically confined during 10^7 years in the Galaxy [6].

Because of interaction of the cosmic rays with the interstellar medium, it is believed that the average source spectrum is harder ($\gamma \approx 2.1$) than the locally observed cosmic rays [7].

1.2 Gamma Ray Bursts

Gamma ray bursts (***GRB***) are short, violent outbursts of gamma rays, discovered in 1973 [9] by the VELA spy satellites, launched to survey possible nuclear test detonations in the upper atmosphere, banned by the Partial Test Ban Treaty. Since their discovery, they have created a long history of speculations about their origin. Almost 20 years later, the ***BATSE*** experiment could archive more than 2700 GRBs, having been detected by satellites at a rate of about one burst per day and prove their isotropic distribution on the sky and therewith their extra-galactic origin. This hypothesis was confirmed when the rapid observations of the ***BeppoSAX*** satellite allowed counterpart observations by optical telescopes which detected the GRB ***afterglow***s and could determine the redshifts of some GRB host galaxies [10], centered around $z \approx 1$ [11]. In 2004, a new observational window was opened with the launch of the ***SWIFT*** satellite which combines a wide field-of-view and an increased sensitivity with respect to BATSE and BeppoSAX. Although both the GRB progenitors and the exact emission mechanisms are still under debate, they are thought to be prime candidates for the acceleration of cosmic rays beyond the knee [12, 13]. No GRB could be observed at energies exceeding 20 GeV up to now, an important clue for the hypothesis of cosmic ray acceleration, though.

1.3 Modern Cherenkov Telescopes

Until the 20^{th} century, only the visible part of the electromagnetic spectrum could be used for astronomy. Photons of lower and higher energy were getting accessible to telescopes only then, with gamma astronomy being the last piece of the puzzle. It was not until the 1990's, that photons of the MeV energy range became a useful tool to study the universe. With the launch of the ***CGRO*** satellite, the Universe could be studied in the MeV energy domain. The satellite was equipped, among others, with the ***BATSE*** and EGRET detectors. While the first was dedicated to GRB detections, the last measured the Universe at MeV energies [14].

At the same time, the ground-based ***IACT***-technique established the TeV energy range as a window to the direct observation of the ***non-thermal*** part of the universe [15]. Until now, a last observational energy gap from about 30 to 200 GeV is still about to be covered, a prime target for the ***MAGIC*** telescope.

1.4 This Work

This work presents a detailed study of the main parts of the MAGIC Telescope: its photomultiplier camera, joined to the signal amplification and read-out chain and the calibration system. At the same time, it demonstrates the capabilities of the

new instrument: The follow-up observation of a gamma ray burst during its prompt emission phase for the first time made by an IACT.

As this work might appear quite elaborate for Spanish thesis standards, let me take here the opportunity to give a short list of justifications:

- Many pieces of the MAGIC telescope were built by PhD students. Only one example is the calibration system taken care of by the author of this thesis. As MAGIC is still a young experiment, important parts of the instruments have not yet been published, and PhD theses are one way to document their functionning and analysis. This is also true for the calibration system which finds here a comprehensive documentation.

- Unfortunately also many analysis concepts are not yet standardized inside the collaboration and propositions in this direction are found here. A thorough and critical view at the emerging concepts is an important part of the work of a physics collaboration since many erroneous (e.g. biased) algorithms are quickly invented and may become later a standard because of familiarization. In order to follow these concepts easily, also for a non-expert in Cherenkov telescopy, a glossary is given at the end which I hope will allow a smoother and easier reading of this thesis.

- Many times, I got the impression that a very competitive atmosphere in this field of research has left some of the needed thoroughness on its way. This work is explicitely intended to give an example of how a thorough and honest way of working is possible in such a situation. In this context, credits are intended to be given to all persons who cooperated in parts of this work whenever they appear.

- Finally, the acculturation of the author to physics research in a North-German environment has left traces. Especially, I intend to apply the scientific method in a rather strict interpretation which from my point of view is the only possibility to maintain credibility of scientific research in a public environement otherwise dominated by subtle manipulation of data and deliberate misinterpretations.

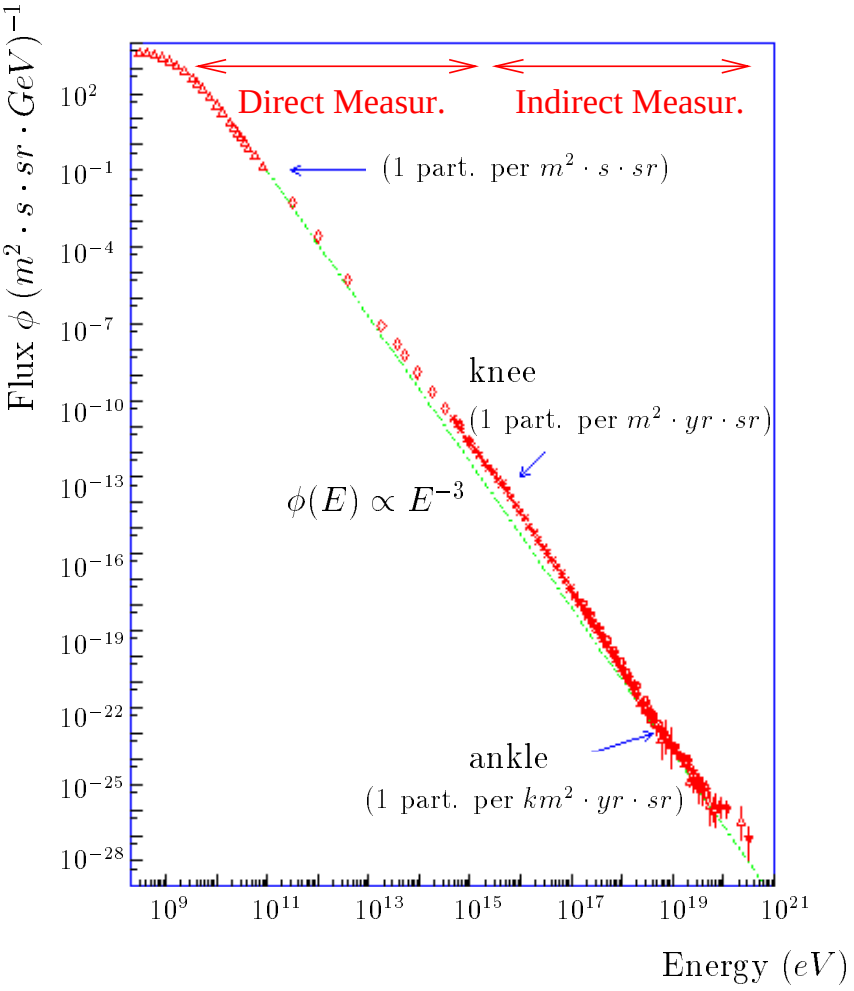

Figure 2: Differential energy spectrum of cosmic rays. Figure from [8].

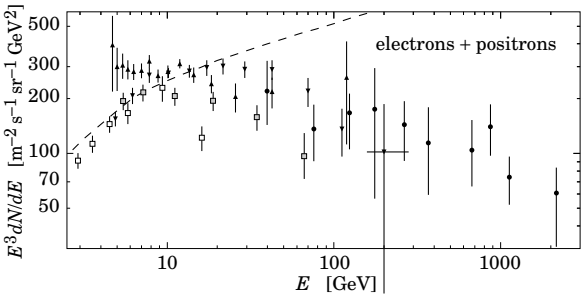

Figure 3: Differential energy spectrum of cosmic ray electrons and positrons, multiplied by E^3. Dashed line: The proton spectrum, additionally multiplied by 0.01. Figure from [3].

2 Creation of Gamma Rays

While charged particles get deflected in the intergalactic and galactic magnetic fields, stable neutral particles, like the ***gamma rays*** and the ***neutrinos*** [16] point back directly to their origins and can be used as ***messenger particles*** for astronomy. By learning about the type of sources, measuring the fluxes and the energy spectra of the gamma rays, models about the acceleration of high-energy particles and especially the ***cosmic rays*** can be tested or refined.

Most of the observed spectra show ***power laws***, as well those of ***cosmic rays*** as those of ***gamma rays***.

Every time, when power law spectra occur, ***non-thermal*** processes are likely to be the reason. When particle densities are low, interactions between them are rare and cannot provide thermal equilibrium. ***Fermi acceleration***, first introduced by Enrico Fermi [17], where particles are reflected stochastically back and forth, e.g. on moving shock waves, can push particles to very high energies and produce a power law spectrum. There is "first order" Fermi acceleration where the energy gain per acceleration cycle is proportional to the velocity β of a particle and "second order" Fermi acceleration where it is proportional to β^2. Both versions stem from different geometries: The first one usually used in shocks, the second in moving plasma clouds. The physical mechanism is the same, however [4]. Alternatively, strong electrical fields can accelerate particles directly to high energies.

Concerning the mechanisms for ***gamma rays*** emission from a (power-law) distribution of accelerated particles, the main physical processes are [19, 20]:

Synchrotron Radiation: Accelerated charges radiate. In the case of relativistic particles, accelerated by magnetic fields, the corresponding radiation is called ***synchrotron radiation***. If E_e is the particle (electron) energy, the radiation is emitted mainly into an angle of $\theta \approx m_e c^2/E_e$ with respect to the velocity vector of the particle. In the case of relativistic electrons, the synchrotron radiation spectrum peaks at an energy of [21]

$$E_\gamma \simeq 1.5 \cdot 10^{-5} \cdot \left(\frac{E_e}{[\mathrm{TeV}]}\right)^2 \cdot \left(\frac{B}{[\mathrm{G}]}\right) \ [\mathrm{GeV}] \ , \tag{1}$$

where B is the magnetic field component perpendicular to the particle velocity. One can immediately see that strong magnetic fields of the order of $10^6\,\mathrm{G}$ [5] and higher are needed in order to push the photon energies into the GeV-range. For power-law distributions of particle energies with spectral index p, the spectral index of the synchrotron radiation α is typically $dN_\gamma/dE \sim E^{-\alpha}$ with $\alpha = (p+1)/2$ [19]. Synchrotron radiation itself modifies the electron energy spectrum: The radiation "cools" the electrons with higher energy and produces a ***cooling break*** in the power-law distribution of electron energies. After the cooling break, the spectrum of the photon emission is usually softer: $\alpha = (p+2)/2$.

[4] It was recently discovered that in ultra-relativistic outflows with high radiation fields, acceleration of order even higher than two can occur [18].

[5] $1\,\mathrm{Gauss} \equiv 10^{-4}\,\mathrm{T}$

Bremsstrahlung: Occurs when a charged particle is accelerated or decelerated in an electric field. In electron-ion collisions, the Coulomb field of the nucleus changes the electron energy. Gamma ray production can occur when relativistic electrons interact with gas. For instance, the major part of the diffuse Galactic gamma radiation up to 100 MeV comes from ***bremsstrahlung*** of cosmic ray electrons on the interstellar medium (***ISM***). The spectrum of bremsstrahlung radiation is flat up to roughly the electron kinetic energy $E_\gamma = (\gamma_e - 1)\, m_e c^2$ [21]. In case of a power law distribution of electron energies, the bremsstrahlung spectra follow the spectral index of the radiating particles. In the gamma ray regime, both electron-electron bremsstrahlung as ion-electron bremsstrahlung are equally important.

Inverse Compton Scattering: Occurs when photons of lower energy get up-scattered through collisions with energetic particles, especially electrons. Gamma ray production can occur when relativistic electrons scatter up photons from interstellar optical, infrared or microwave radiation fields. The average energy of inverse Compton scattered photons, E_γ, can be calculated typically from the average energy of the scattering electrons E_e [21]

$$E_\gamma \simeq 6.5 \cdot 10^3 \cdot \left(\frac{E_e}{[\mathrm{TeV}]}\right)^2 \cdot \left(\frac{E_{ph}}{[\mathrm{eV}]}\right)\ [\mathrm{GeV}]\ , \tag{2}$$

for an ambient photon-field with typical energies of E_{ph} and $E_{ph}E_e \ll (m_e c^2)^2$ (***Thomson regime***). As the original photon energy get multiplied with the square of the Lorentz factor of the electron, photons can be up-scattered to very high energies with this mechanism. For a power law distribution of electrons with spectral index p, the resulting differential gamma ray spectrum follows a power law with a spectral index $\alpha = (p+1)/2$ for the non-relativistic regime ($E_{ph}E_e \ll (m_e c^2)^2$) [22] and $\alpha \approx p + 1 - q$ in the ultra-relativistic (***Klein-Nishina regime***, $E_{ph}E_e \gg (m_e c^2)^2$), where q is the spectral index of the soft photons before being scattered [23]. As in the synchrotron radiation case, ***inverse Compton scattering*** of a population of electrons can cool these and produce ***cooling break***s in the gamma ray spectrum. Inverse Compton scattering is important in regions of high photon densities.

The Synchrotron Self Compton Model: In the class of Synchrotron Self Compton (***SSC***) models, relativistic electrons emit synchrotron radiation and the same population of electrons scatters the synchrotron radiation field up to higher energies. Typical multi-wavelength SSC-spectra show "duplicated" emission features, e.g. power laws joint at break energies.

Neutral Pion Decay: Energetic collisions of protons p with interstellar gas particles (p_i) or a radiation field (γ_i) will produce neutral pions:

$$\begin{aligned} \mathrm{p} + \mathrm{p_i} &\longrightarrow \pi^0 + k \cdot \pi^\pm + \mathrm{X} \\ &\longrightarrow \gamma + \gamma + \mathrm{X}\ , \\ \mathrm{p} + \gamma_i &\longrightarrow \Delta^+ \longrightarrow \mathrm{p} + \pi^0 \\ &\longrightarrow \mathrm{p} + \gamma + \gamma\ , \end{aligned} \tag{3}$$

where the π^0 decays almost immediately into two gamma rays with an energy distribution peaking at a broad maximum at about 70 MeV in the rest frame of the π^0 [6]. In the case of beamed annihilations, the resulting gamma ray energy will be Lorentz-boosted to higher energies. The differential photon energy spectrum obtained from ***neutral pion decay*** produced by non-relativistic peaks thus by 70 MeV, but highly relativistic nucleons with energies distributed by a power law with spectral index p have harder spectra with a spectral index of about $\alpha = p + 1$ [24].

In the following, the principal observation targets for the MAGIC Telescope are described. All these sources can be responsible for part of the cosmic rays acceleration and it is expected that the current generation of Cherenkov Telescopes will contribute significantly to their understanding. A special focus is made on gamma ray bursts since their observation and analysis is part of this thesis.

2.1 Supernova Remnants

Supernovae are stellar explosions occurring at the end of the life of a massive star. An implosion of the star's core, followed by a subsequent explosion, disrupts the star's mantle and accelerates the stellar medium into the surrounding ***ISM***, liberating about 10^{51} erg [6] of explosion energy. In the case of very massive stars, a ***pulsar*** is created in the center while the most massive stars are believed to create ***black hole***s. The material expanding away from the center is called a *supernova remnant* (***SNR***). It forms a shock wave through the ISM which accelerates electrons and protons through first order Fermi acceleration.

Recently, the ***H.E.S.S.*** telescope array could resolve spatially the TeV-emission from the ***SNR*** shell of RX J1713.7-3946 [25] and correlate it with the X-ray emission detected by ***ROSAT*** (see figure 4).

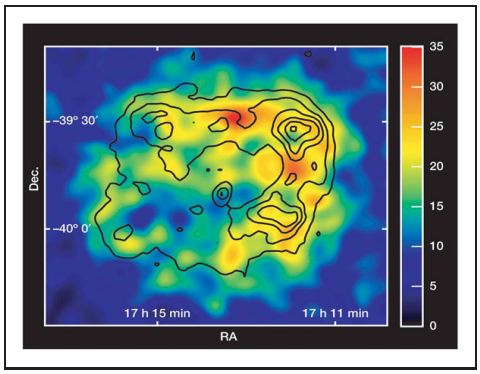

Figure 4: The SNR RX J1713.7-3946 seen in gamma rays (colors) and X-rays (contours). Figure from [25].

Although it is generally believed that ***SNR***s are the source of the ***cosmic rays*** up to the ***knee*** [26], mainly because the total power contained in the cosmic rays matches a few percent of the total mechanical energy released by supernovae in our Galaxy[7], acceleration of hadrons has not yet been observed directly without any doubt. It would manifest itself by a harder emission component in the gamma ray spectrum and/or anti-

[6] $1\,\text{erg} \equiv 10^{-7}\,\text{J}$

[7] The local density of ***cosmic rays*** in the galaxy is $\rho_{CR} \approx 1\,\text{eV/cm}^3$ while the mean life time of cosmic rays in the galactic disk is $\tau_{CR} \approx 6 \cdot 10^6$ yrs. The needed power to generate all cosmic rays in the Galaxy is thus: $L_{CR} = V_D \cdot \rho_{CR}/\tau_{CR} \approx 5 \cdot 10^{40}\text{erg/s}$ where V_D is the Galaxy volume: $V_D = \pi R^2 d \approx \pi \cdot (15\,\text{kpc})^2 \cdot (200\,\text{pc}) \approx 4 \cdot 10^{66}\,\text{cm}^3$. Supposing that a supernova has an acceleration efficiency ϵ_{SNR} of a few percent and a supernova rate of $r_{SN} \approx 0.03\,\text{yr}^{-1}$, the power provided by ***SNR***s reads as: $L_{SNR} = \epsilon_{SNR} \cdot P_{SN} \cdot r_{SN} \approx \epsilon_{SNR} \cdot 10^{51}\,\text{erg} \cdot 10^{-9}\,\text{s}^{-1} \approx \epsilon_{SNR} \cdot 10^{42}\,\text{erg/s}$.

correlation with the X-ray emission regions. Instead, the favored production mechanisms for the gamma radiation are ***SSC*** scattered photons.

According to whether a pulsar or a black hole remains in the center, SNRs are classified into ***shell type***s (nothing in the center), ***plerion***s (interior sub-structure indicating the presence of a pulsar in the center, emitting a "pulsar wind") and composite (appearing like plerions or shell-type, depending on the observed wavelength). Galactic SNRs are ***extended sources*** with a diameter of typically 0.1°.

The first object ever observed by a Cherenkov telescope was the plerion-type SNR ***Crab Nebula*** [15] which is also the strongest steady TeV gamma ray source in the sky. It is nowadays used as a calibration source for all ***IACT***s.

2.2 Pulsars

Pulsars are rapidly rotating objects which were discovered due to their apparent periodic photon emission. It is generally believed that ***pulsar***s are created in core-collapse supernovae or from an accreting white dwarf in a binary system, leaving behind fast spinning ***neutron star***s [27]. Old pulsars having accreted material over a long time period, exhibit pulsed emission periods of typically milliseconds, the so-called *milli-second pulsars*. The pulsed emission is beamed along the magnetic field axis, which itself is mis-aligned with the rotational axis. The emitting region rotates therefore, passing the line-of-sight to the Earth at regular intervals.

Pulsars are believed to produce the strongest magnetic fields in the universe, reaching up to 10^{12} G and have masses between 1.4 and 3 solar masses, comprised in a volume of only 20 km of diameter. Its core density can reach $10^{15}\,\mathrm{g/cm^3}$. About 1 500 pulsars have been detected so far, out of which about 35 in X-rays and 9 in gamma rays. The EGRET detector discovered 7 pulsars with gamma emission above 100 MeV which have all counterparts at other wavelengths (see figure 5 and ref. [28]) No steady pulsed emission has yet been detected in the GeV to TeV energy regime so far.

According to Peter Goldreich and William Julian [29], the rotating magnetic field induces an ***electric field*** which is strong enough to pull particles out of the neutron star's surface. In spite of the intense surface gravity, the pulsar must then possess a dense ***magnetosphere***, containing a plasma surrounding the neutron star, which co-rotates with the star. The magnetosphere is, however confined to a *light cylinder* of radius $R_L \equiv c/\Omega$ past which the particles would otherwise ***co-rotate*** at a speed greater than the ***speed of light*** c (Ω is the rotation speed of the system). Some of the magnetic field lines cannot be closed then because they have to pass through the light cylinder. These field lines start from a (small) region on the surface of the neutron star, called the ***polar caps***.

The ***polar cap model*** [30,31] predicts ***synchrotron radiation*** from accelerated charged particles in the polar caps. The synchrotron photons, in turn, will interact with the strong magnetic field and create electron-positron pairs ($\gamma + B \rightarrow e^+ + e^-$) initiating electro-magnetic cascades. The electrons and positrons can in turn inverse-Compton scatter the synchrotron radiation field.

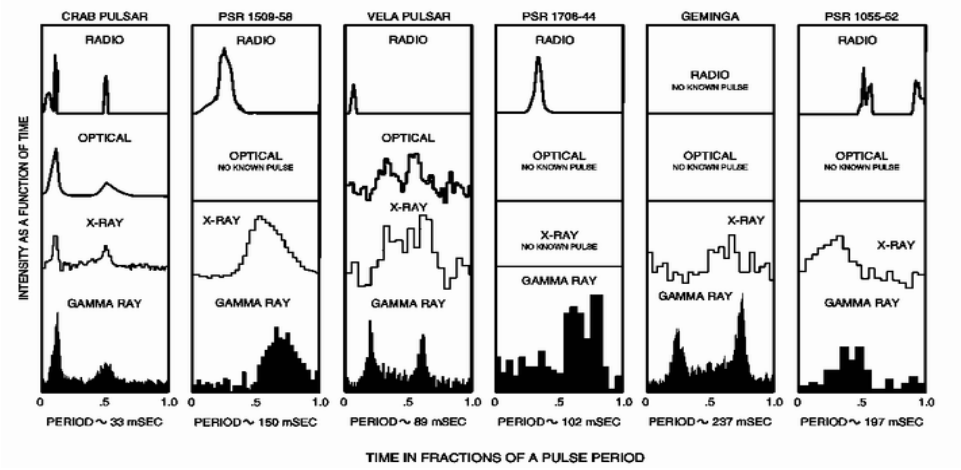

Figure 5: The 7 pulsars detected by the EGRET detector. All have counterparts in other wavelengths, but no common multi-wavelength behaviour can be discerned. "Gamma ray" means here typically MeV-energies.

In the ***outer gap model*** [32, 33], gamma rays of GeV energies are produced further outside in ***vacuum gaps*** in the outer regions of the magnetosphere inside which energetic electrons accelerate infrared and optical photons from regions outside the gap via ***inverse Compton scattering***.

Both models differ mainly in their predictions of the position of a cut-off in the energy spectrum: While the polar cap model does not allow cutoffs beyond 50 GeV, the spectra may extend to 100 GeV in the outer gap model. A Cherenkov telescope is thus an ideal instrument to distinguish between both mechanisms if it is sensitive in the energy region between 50 and 100 GeV.

Pulsars with escaping jets taking away radiation and particles can create ***pulsar wind nebulae***, forming ***plerion***-type SNRs.

2.3 OB-Associations

In 2005, the ***HEGRA*** telescope system discovered serendipitously the unidentified TeV-source TeV J2032+4130 in the Cygnus region [34] which was later confirmed by the ***Whipple*** collaboration [35]. The source was steady in flux over four years, exhibits a hard spectrum and does not coincide with the center of the Cygnus region. It lacks obvious counterparts at radio, optical or X-ray energies, however it coincides with an ***OB-association***, estimated to contain about 2600 ***OB-stars*** [36]. These are young hot stars emitting especially in the O and the B-band (blue).

GeV to TeV gamma radiation can be explained by a combination of SNR shocks of an OB-association (the "Cygnus-OB2" region in this case) which altogether form a so-called ***superbubble***. This large-scale shock front runs into the dense region of winds-rich OB-stars. While low-energy particles are prevented from penetrating into the winds because of convection, protons above a threshold of typically TeV do

so and collide against the interstellar particles to produce gamma rays via ***neutral pion decay*** [37]. This mechanism produces TeV sources without counter-parts in the MeV to GeV energy regime and, if confirmed, would establish OB-associations as an important contribution to the production of cosmic rays.

2.4 Unidentified EGRET Sources

Between 1991 and 1995, the Energetic Gamma Ray Experiment Telescope (***EGRET***) detected 271 sources [14] in the energy range from 100 MeV to 10 GeV, out of which more than 150 remain unidentified (see figure 6). Among the unidentified sources, a clear concentration in the galactic plane can be seen, but also sources from other directions are visible. About 40% of these sources have hard power law spectra which seem to extend beyond 10 GeV.

Recently, the ***Milagro*** collaboration announced the discovery of a steady TeV source [38], spatially coincident with the unidentified source 3EG J0520+2556.

It is still a mystery what the unidentified sources are, but gamma ray observations beyond 10 GeV will probably contribute to reveal the nature of these sources.

2.5 Active Galactic Nuclei

Active galactic nuclei (***AGN***) are a class of galaxies in the core of which masses of 10^6 to 10^9 solar masses are concentrated in a region of the size of the solar system. These central objects must be super-massive ***black hole***s.

In the unified scheme for AGNs, invented in the 1990's by Megan Urry and Paolo Padovani [40] (after already existing supermassive black hole models [41]), the central black hole is surrounded by a rotating luminous ***accretion disk***, heated up to temperatures in the optical and UV [41]. The plasma emits a thermal spectrum peaking in X-rays. A thick dust torus, situated further outside, obscures the emission from the accretion disk and from clouds orbiting above the disk (the so-called ***broad emission line region***). Sometimes, bipolar ***jet***s or blobs emanate from the central ***black hole*** and emit radio through gamma rays, relativistically beamed along the jet axes. Depending on the observation angle with respect to the jet axis, a rich phenomenology of AGNs can be observed leading to many classes and sub-classes of AGNs. For gamma ray astronomy, the most important ones are those where a jet points directly in the direction of the Earth, the so-called ***blazar***s.

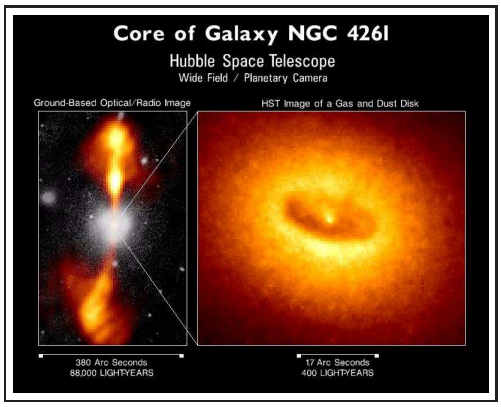

*Figure 7: The AGN NGC4261, as seen by the Hubble Space Telescope. The two **jet**s, the dust torus and the **accretion disk** could be spatially resolved.*

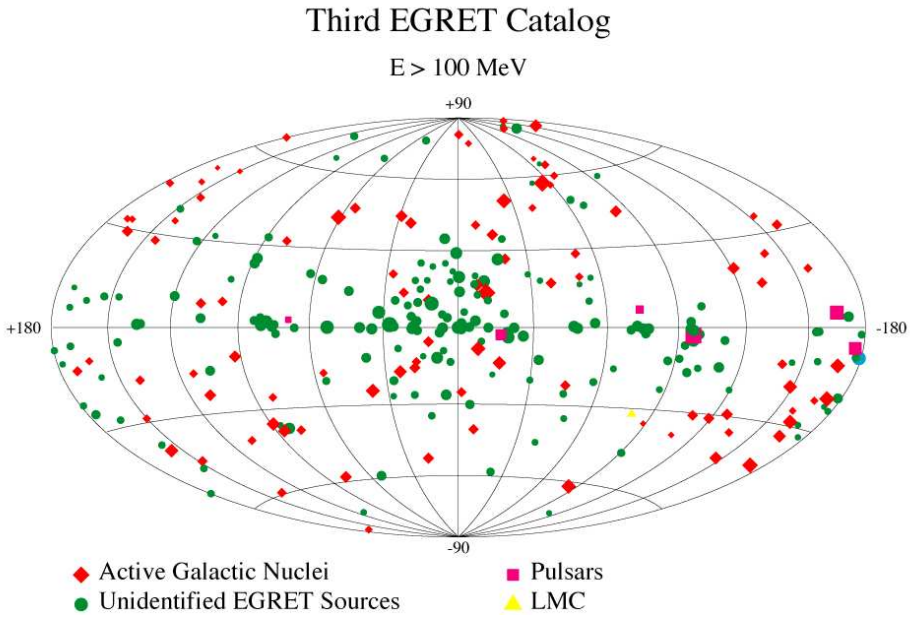

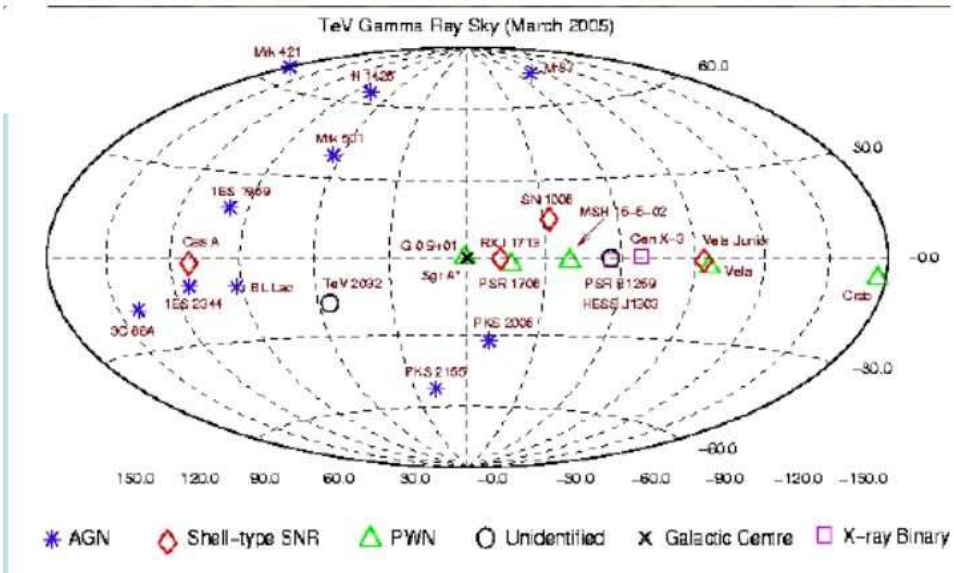

Figure 6: Top: The 271 point sources detected by the EGRET satellite in the energy range from 100 MeV to 10 GeV. The majority of the sources could not be identified with counterparts at other wavelengths. Figure from [14]. Bottom: The 24 TeV-sources known up to date. Figure from [39].

Figure 7 shows an AGN, observed with the Hubble Space Telescope. All ingredients of the unified model, except for ***black hole*** itself, could be spatially resolved: The two ***jet***s, the dust torus and the ***accretion disk***.

Blazars show very variable fluxes from the radio to the TeV regime. The emission can grow by orders of magnitude if the blazar is in ***flaring state***. Otherwise, it is said to be in ***quiet state***. The spectra can be best fitted by power laws with differential spectral indices around $\alpha \approx -2$ and exponential cutoffs in the TeV energy range. The spectra get harder in flaring state [42].

Especially important are the two brightest blazars in gamma rays: ***Mrk 501*** [43] and ***Mrk 421*** which was the first blazar ever observed with a Cherenkov Telescope [44]. Figure 8 shows the light curves of Mrk 501, observed in X-rays and in gamma rays [45]. The detailed physical mechanisms leading to jets or ejected blobs are still not understood, although the existing multi-wavelength data accommodates best with ***SSC*** models. Simultaneous multi-wavelength observations are nowadays the best tool to understand and model the jet formation and photon emission that goes along with it. Even the process of creation of a jet itself is not yet fully understood.

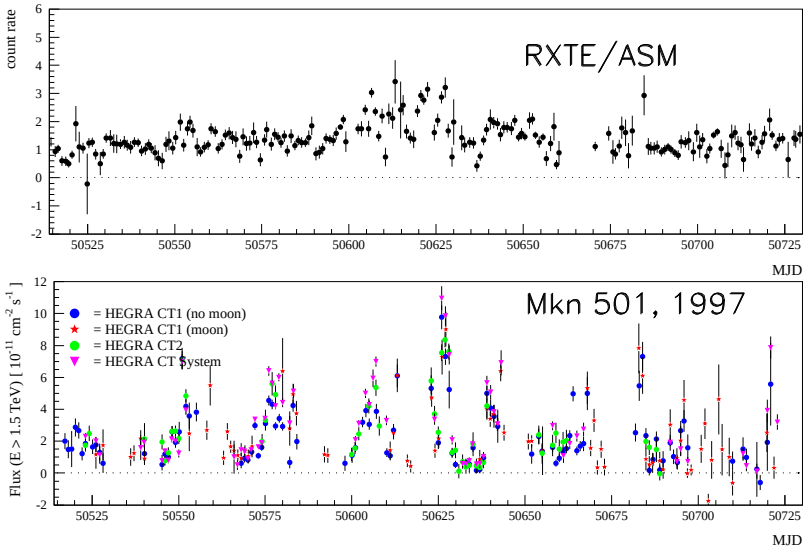

Figure 8: The light curve of Mrk 501 in flaring state, observed with the RXTE-satellite in X-rays (2–10 keV, top) and with the CT1-telescope in gamma rays (1.5–20 TeV, bottom). Figure from [45].

Recently, a first tentative detection of ***M87***, a very close, radio-loud AGN seen off-axis, was performed in TeV gamma rays by the ***HEGRA*** collaboration [46]. This points to the possibility the Cherenkov Telescopes might have become as sensitive as to capture the emission from the torus around the accretion disk.

AGNs are believed to be important sources for the acceleration of the highest-energy ***cosmic rays*** [47, 48].

2.6 Microquasars

A ***microquasar*** is an object of stellar mass which shows some of the properties of an ***AGN*** in miniature, including strong emission over a broad range of wavelengths, rapid variability at high energies and ***jet***s. Microquasars were discovered [49] much later than AGNs.

In the standard microquasar model by Felix Mirabel and Luis Rodriguez [51], a normal star and either a ***black hole*** or a ***neutron star*** orbit around each other in a binary system. The companion star loses matter into an ***accretion disk*** orbiting around the compact object which is heated up to about 10^7 K [41]. High-energy gamma ray emission should take place in the ***jet***s [52].

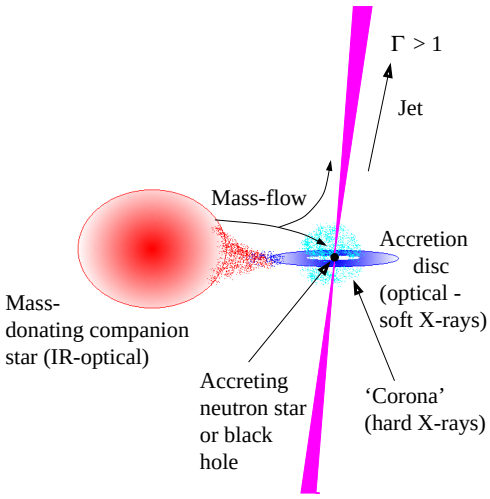

Figure 9: Sketch of a ***microquasar****. Figure from [50].*

The discovery of MeV gamma ray emission from a microquasar [53], associated with a previously unidentified EGRET source, made microquasars prime candidates for at least part of the unidentified EGRET sources, and for associated GeV and TeV gamma ray emission, at least if the observer is situated in the line-of-sight of one of the two jets: the so-called ***Microblazars***. If this hypothesis is true, Microblazars should be observable also in high energy gamma rays, and observations in that energy regime can be used to pin down the fundamental assumptions of the model. Very recently, two microquasars were indeed detected in the hundreds of GeV regime by H.E.S.S. [54] and MAGIC [55], showing predicted periodic emission.

2.7 Starburst Galaxies

Starburst galaxies are young galaxies with a high ***star formation rate***. This implies also a high supernova-rate since massive stars have short life times, compared to less massive stars. The central regions of ***starburst galaxies*** are therefore believed to exhibit a high density of ***cosmic rays*** which might interact with interstellar gas, abundant in large amounts in some starburst galaxies [56]. The resulting high energy photon emission is predicted to extend to TeV energies [57].

In 2002, the ***CANGAROO*** collaboration reported the detection of extended TeV-emission from the direction of the starburst galaxy NGC 253 [58] [8]. In order to test the above assumptions, it would be important to take the gamma ray emission

[8] However, see also the observation campaign of ***H.E.S.S.*** which yields a flux limit below the signal seen by ***CANGAROO*** [59].

spectra from the GeV to TeV energy range.

2.8 Unidentified TeV Gamma Ray Sources

The ***H.E.S.S.***-collaboration discovered recently a new source: HESS J1303-631, an extended TeV-emitter with constant flux and a spectrum following a power-law with differential index $\alpha = -2.44$ [60]. No counterpart to this source has been found up to date. However, in the vicinity of HESS J1303-631, a pulsar is present, which might influence the production mechanism of that source.

From a survey of the galactic plane, another stand-alone TeV gamma ray emitter was announced with the discovery of HESS J1614-518 [61], again with no plausible counterpart at other wavelengths [9].

Sources of this type are especially interesting because they are thought to be hadron accelerators.

2.9 Gamma Ray Bursts

Gamma ray bursts (***GRB***) are short, violent outbursts of gamma rays. The ***BATSE*** detector could archive more than 2700 GRBs, occurring at a rate of about 1 burst per day. It could prove their isotropic distribution on the sky and therewith their extra-galactic origin (see figure 10 and [64]). This hypothesis was confirmed when the rapid observations of the ***BeppoSAX*** satellite allowed counterpart observations by optical telescopes which detected the GRB ***afterglow***s and could determine the redshifts of some GRB host galaxies [10], centered around $z \approx 1$ [11] (for review of the status after ***BeppoSAX***, see ref. [65, 66]). With the launch of the much more sensitive ***SWIFT*** satellite, the mean GRB redshift has been even boosted to $z \approx 2.8$ [67], thus covering any predicted maxima of the ***star formation rate*** (SFR) along redshift.

GRBs are prime candidates for the highest energy ***cosmic rays*** [12, 68], especially are they considered the only accelerators capable to boosting proton energies to $E \geq 10^{20}$ eV [69], like observed in the cosmics rays spectra [12].

2.9.1 Phenomenology

Figure 11 shows a couple of typical light curves taken in the 100 keV energy regime by ***BATSE***. One can see immediately that GRBs can exhibit ***complicated light curves*** and time structures δT much smaller than T, their total duration. The burst morphology can be subdivided into four groups [65]: single-pulsed events, smooth events with well-defined peaks, bursts with distinct, well-separated episodes of emission and finally erratic, chaotic and spiky bursts.

[9] In the same paper, the HESS-collaboration discovered another new source of TeV gamma ray emission: HESS J1813-178 with at first sight no plausible counterparts at other wavelengths. For this source, an X-ray counterpart was found meanwhile [62, 63].

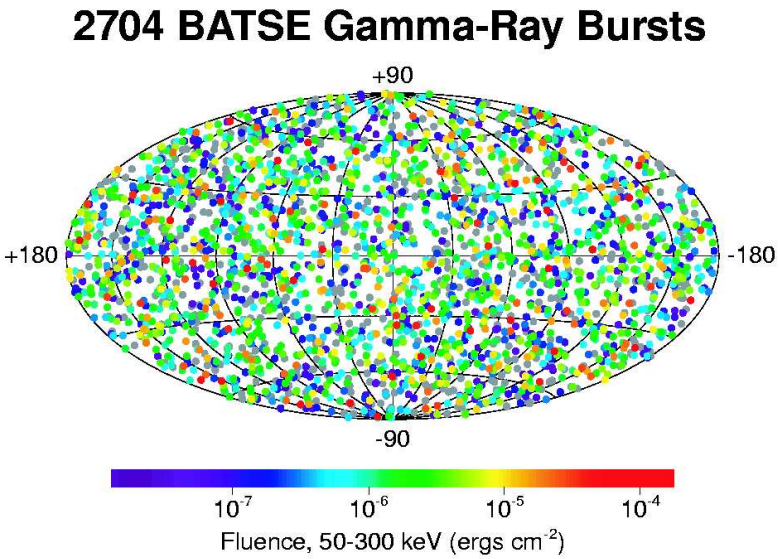

Figure 10: The more than 2 700 GRBs detected by the BATSE satellite. No clustering or asymmetries are seen.

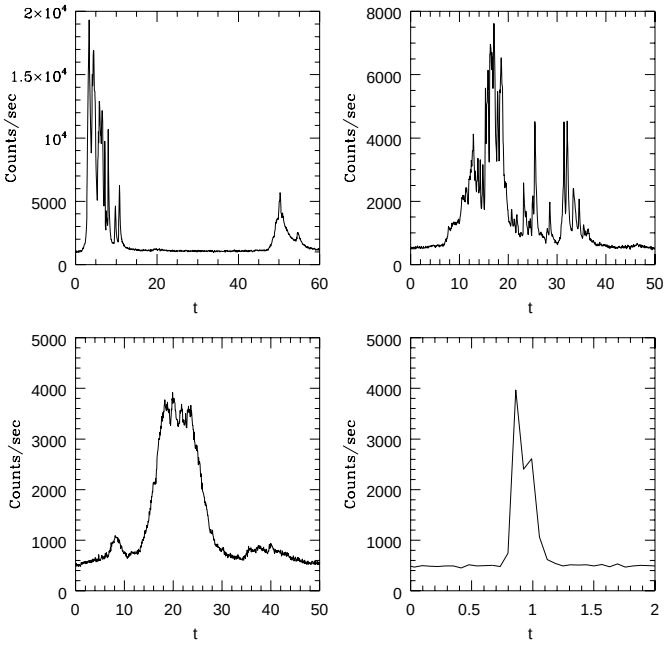

Figure 11: Four typical light curves of GRBs as detected by BATSE. Top left: burst with distinct, well-separated episodes of emission, top right: chaotic, spiky burst, bottom left: smooth event, multi-peaked, bottom right: single-pulsed (here double-pulsed). All times in seconds.

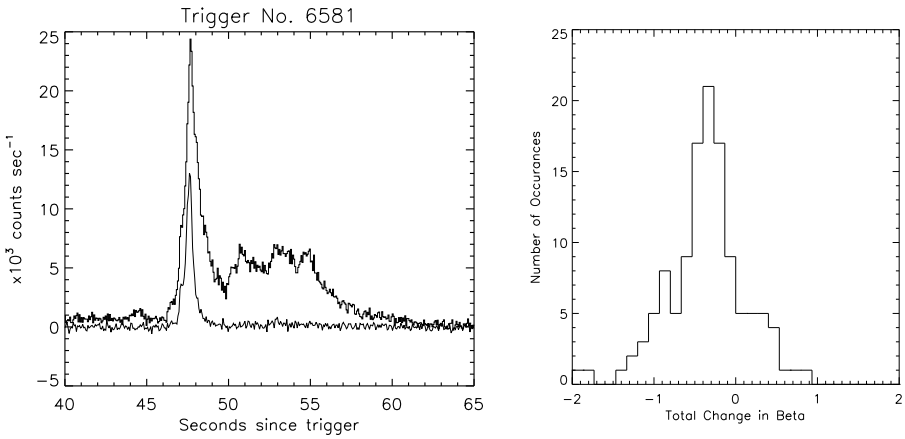

Figure 12: Left: Example of the hard-to-soft spectral evolution seen in many sub-pulses within a GRB: The upper trace is the time profile of 25-50 keV photons while the lower one shows the time profile of the hardest photons with the BATSE large-area detector. The second to fourth sub-pulse of the soft photons were not detectable with the harder photons. Figure from [70]. Right: Histogram of the total change in the high-energy power-law index β during a GRB, obtained from a sample of bright BATSE bursts. The mean change lies at $\Delta\beta \approx -0.3$. Figure from [71].

The shortest rise times recorded are roughly equal to the shortest structures within time histories, namely $\delta T \approx 0.2$ ms. This number constrains severely the size and the speed of the emitting region, since [72, 73]:

$$R_{\text{emission}} < \Gamma^2 \cdot c \cdot \delta\, T_{min} \approx \Gamma^2 \cdot 60\,\text{km} \tag{4}$$

where R_{emission} is the path along which the emission takes place, Γ is the Lorentz factor of the emitting region moving towards the observer and c the speed of light.

Observed GRB durations span at least five orders of magnitude (see figure 13) following a bimodal [75] distribution with peaks at 0.5 and 34 seconds [70]. GRBs can be divided into those with durations smaller than and those greater than 2 seconds (the so-called ***short bursts*** and ***long bursts***). The short bursts have a tendency to harder spectra [75] and have only a few major pulse structures.

The prompt emission spectra of GRBs are simple (no absorption or emission lines) and range out to GeV energies [76]. In general, both the time-integrated spectra and spectra of shorter intervals within a burst, can be well fit with a double power law joined smoothly at a break energy E_b (the so-called ***Band-spectrum*** [77]):

$$N(E) = N_0 \cdot \begin{cases} E^{\alpha}\, \exp(-E/E_b) & \text{for } E < (\alpha-\beta)E_b \\ \left((\alpha-\beta)\, E_b\right)^{\alpha-\beta} E^{\beta}\, \exp(\beta-\alpha) & \text{for } E > (\alpha-\beta)E_b \end{cases} \tag{5}$$

In this model, the ***peak energy*** in the νF_ν representation relates to the ***break***

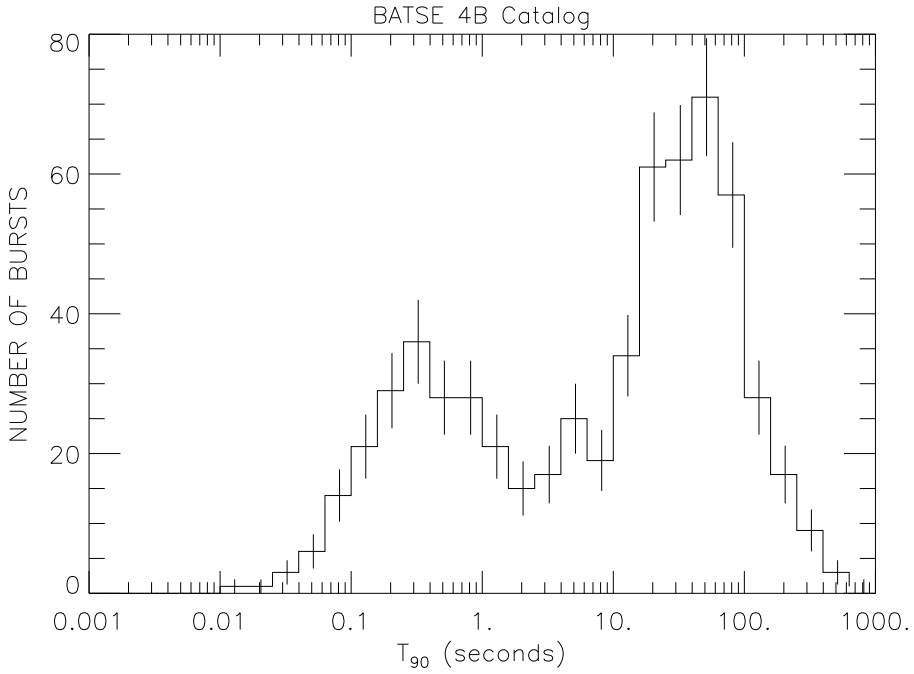

Figure 13: Distribution of burst durations obtained with the BATSE detector

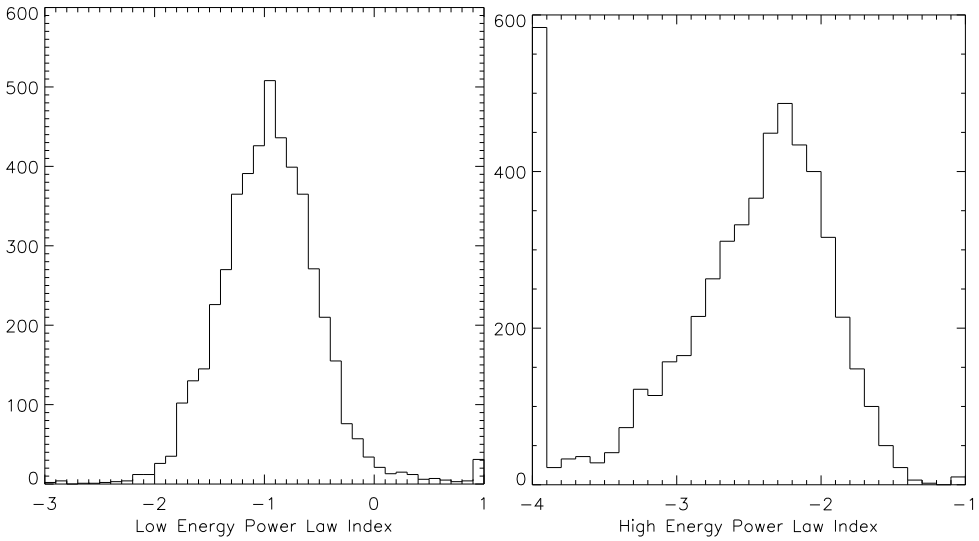

Figure 14: Distribution of the low-energy spectral indices α (left) and high-energy spectral indices β (right), obtained from fits of GRB spectra from the 4^{th} BATSE catalog to the "Band function" (eq. 5). On the right side, all bursts which could not be fitted beyond the break energy or with fit results $\beta < -4$ are included in the first bin. Figure from [74].

energy like: $E_{peak} = (\alpha + 2)E_{break}$. Most bursts have a high-energy spectral index close to $\beta \approx -2.25$ (see figure 14). Spectral softening is usually observed throughout a GRB and in sub-pulses within a burst (see figure 12 and [71]).

On the low-energy side, the spectral indices α are most often centered around $\alpha \approx -1$. The break energies E_b of BATSE bursts are distributed very closely around 200 keV.

Afterglows at longer wavelengths are being observed since the ***BeppoSAX*** satellite has been launched in 1996. As the afterglow light curves decline faster with time than t^{-1}, they do not contribute significantly to the total energy budget of the emission [79,80]. Nevertheless, the ***XRT*** detector on ***SWIFT*** discovered bright X-ray flares [78] in the first two hours after the onset of burst, following by several less energetic flares in the same energy range up to two days after the burst [81]. These flares carry an enormous amount of energy and have been associated with ongoing activity of the inner engine of the burst [23].

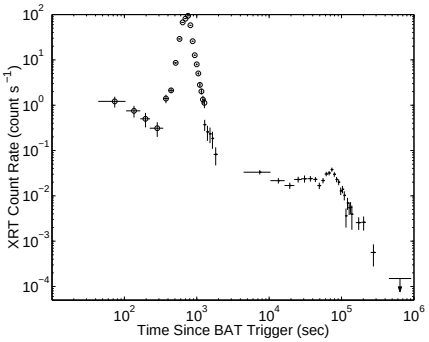

Figure 15: Example 0.2-10 keV band X-ray flare light curve, observed by XRT on SWIFT [78].

Observations of breaks in the afterglow light curves suggest that the gamma ray emission is beamed into solid angles of $\Omega \approx 0.1$ sr [10], where the break happens at the transition from a regime dominated by ***relativistic beaming*** to the one dominated by the intrinsic beaming of the jet itself. With the measured time at which a jet break occurs and general assumptions about the circumburst medium density, the beaming angle θ can be extracted [84]. These breaks led Giancarlo Ghirlanda to discover an important correlation [82] between the bolometric collimation-corrected energy of the bursts $E_\gamma = (1 - \cos\theta) \cdot E_{\gamma,iso}$, with the opening angle θ derived from the afterglow jet breaks, and the peak energy in the GRB rest frame: $E^{obs}_{peak}(1+z) \propto E_\gamma^{0.7}$. This ***Ghirlanda relation*** will allow to use GRB as ***standard candles*** at cosmological distances.

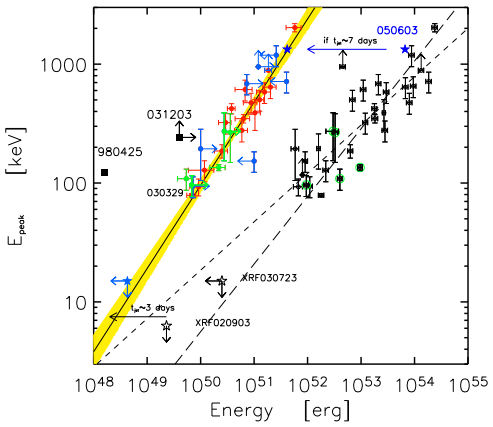

Figure 16: Ghirlanda relation: In black: $E_{\gamma,iso}$ without beaming correction, red and green: bolometric collimation corrected energy (E_γ), blue arrows: upper/lower limits for E_γ due to upper/lower limits on their jet break time. Figure from [82], update from [83].

Some afterglow observations yielded significant (although weak) linear polariza-

tion of the optical emission [85, 86].

2.9.2 Progenitors

Up to date, it is unclear what the progenitors of GRBs are and which event triggers the GRB. However, all hypotheses presented here have in common that the GRB comes together with the creation of a stellar-sized ***black hole***, surrounded by an ***accretion disk***. With an almost maximally rotating black hole, the geometry of the system has two favored directions, identified with the rotation axis of the black hole, where-along emission ***jet***s form.

The ***collapsar***-model, proposed by Sten Woosley in 1993 [87–89], and under the name of ***hypernova*** by Bohdan Paczyński in the same year [90, 91], suggests that GRBs occur when the core of a super-massive star collapses directly to a black hole. This model is favored for the class of ***long bursts***. A variant of the collapsar model has been proposed by Mario Vietri and Luigi Stella in 1998 [92] (the ***supranova*** model): A supernova explosion initially results in the formation of a comparatively massive, very fast rotating ***neutron star***. This neutron star is ***supramassive***: If it were not for its fast rotation, it would immediately collapse to a ***black hole***. Subsequently, the neutron star loses rotational momentum through a ***pulsar wind*** and gravitational waves until it collapses to a black hole and triggers the GRB.

A first hint to a close connection between ***GRB***s and ***supernovae*** came with the observation of GRB980425 [10] [93], the closest burst observed so far (z = 0.0085), spatially coincident with the supernova SN1998bw. However, GRB980425 was a very unusual burst, showing a total energy release of orders of magnitude lower than typical GRBs at higher redshifts.

With GRB030329, a very close and bright burst could be intensely followed by telescopes in all wavelengths. After about 10 days, the optical spectra showed clearly features of a supernova [94], thus confirming the association for at least some long bursts [95].

The ***XMM-Newton*** collaboration found strong emission lines of light elements in the X-ray spectrum of the ***afterglow*** of GRB011211, blue-shifted with respect to the host galaxy with an outflow velocity of one-tenth of the speed of light. These observations also implied that the GRB was probably preceded by a supernova explosion a few days earlier [97].

The ***neutron star-merger*** model, proposed by Bohdan Paczyński and Jeremy Goodman [72, 73, 98, 99], assumes two ***neutron star***s or a neutron star and a black hole or two black holes orbiting around one another. Due to losses of orbital momentum through the emission of gravitational waves, they

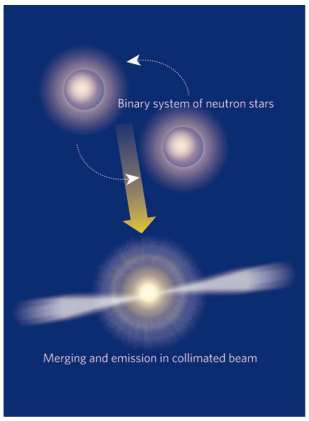

Figure 17: NS-NS merger. Figure from [96].

[10] The naming convention of a GRB follows the rule: GRB YYMMDD. E.g. GRB9804225 has to be read as: The GRB occurring on the 25th of April, 1998.

spiral together and coalesce. At that moment, a ***black hole*** is formed and a GRB emitted. The model makes two key predictions: First, as neutron stars can only be created in supernova explosions, the expulsion of a big part of the stars enveloppe from a point displaced from the center of gravity of the binary system, must transfer momentum to the binary system containing the neutron star remainder (the so-called "momentum kick"). Neutron star or black hole binary systems have life times of typically 10^9 yr and travel 1-100 kpc before merging [100]. Gamma ray bursts in this models should therefore occur mainly outside galaxy cores or star forming regions, just in contrary to the predictions of the collapsar model. Second, because these bursts occur in much less dense regions of the galaxy, their optical afterglows are predicted to be about a factor 1000 dimmer than the ones obtained from supernova models. Exactly these two predictions could be verified on July 9^{th}, 2005, when the ***HETE-2***-II satellite could determine rapidly the position of a short burst [101], and follow-up observations allowed the observation of the optical afterglow of a short burst for the first time [96].

2.9.3 Fireball Model

The ***Fireball Model*** was first introduced by Peter Mészáros and Martin Rees [102, 103] and further developed by Ramesh Narayan and Tsvi Piran [98, 104] following the relativistic generalization of the method to model ***SNR***s.

It assumes that a central object produces a highly variable ultra-relativistic ($\Gamma \gg 100$) outflow of an optically thick plasma shell (the ***fireball***), containing mostly electrons, positrons and gamma rays.

This energy is transported via bulk motion to about 10^{13}–10^{15} cm before the plasma becomes optically thin and radiates the GRB [11]. The baryonic mass of the outflow needs to be below 10^{-4} solar masses to allow these highly relativistic expansion speeds. In order to reconvert the kinetic energy efficiently into radiation, relativistic shocks ($\Gamma > 100$) are required [99, 105], accelerating the ***electrons and positrons*** at very short time scales, compared to the shock expansion timescale [80]. Large-scale ***turbulences*** distribute the energy dissipated in the shock over the shocked gas. Possibly, various such outflows can collide with each other – producing relativistic ***internal shocks*** [103] at about 10^{14}–10^{16} cm from the triggering event – and emit the prompt gamma rays. The observed radiation is then

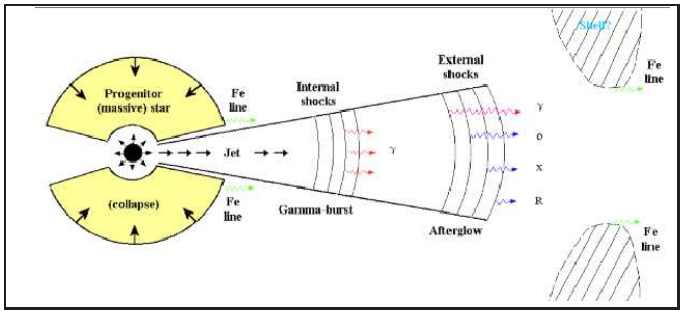

*Figure 18: A sketch of the **fireball** model.*

[11] The supranova model explains naturally this rather unusual baryon-clean environment.

a convolution of contributions from regions of the blast wave emitting at different times and moving with different Lorentz factors and directions with respect to the observer. A fully self-consistent transformation to the observer's frame can hence be done only numericaly.

The internal shocks were shown to be able to produce the complex time-profiles of some bursts [106,107]. At a later stage, the shell impacts on the ***circumburst medium***, a relativistic ***external shock*** [102] is produced which radiates the ***afterglow*** and, depending on the density of the circumburst medium, the smooth GRB time profiles. In both cases, a fraction of electrons is accelerated by repeated diffusion across the shock front, undergoing first order Fermi acceleration. The electrons spiral in the turbulent magnetic fields and radiate ***synchrotron radiation*** (given the observational constraints, a fireball is always in the ***Klein-Nishina regime*** for inverse Compton scattering [108]). At the same time, the electrons "cool" by the their own synchrotron emission. If the primary electron Lorentz-factors are distributed like $f(\gamma) \propto \gamma^{-p}$ in an interval of $(\gamma_{min} < \gamma < \gamma_{max})$, then the resulting photon spectra consist of three parts: $N(E) \propto E^{-2/3}$ before $E = \gamma_{min}^2 \cdot h\nu_B$ ($\nu_B = eB_\perp/2\pi m_e c$ is the gyrofrequency), then $N(E) \propto E^{-(p+1)/2}$ where cooling effects are not yet important and last $N(E) \propto E^{-(p+2)/2}$ after the so-called "cooling break". The hardest possible spectral index of this model if therefore $\alpha \approx -1.5$, in contradiction to some of the spectral fit results, shown in figure 14 (see however [109] and [110] for possible solutions to this problem).

Because the fireball expands relativistically, the observed radiation is blue-shifted. Due to ***relativistic beaming***, only a small fraction of the expanding shock is visible at the beginning and thus the time profile of the arriving gamma rays is not smoothed out by the simultaneous emission from different points in the expanding shell [108, 111]. As long as the jet has an opening angle of $\theta \gg \Gamma^{-1}$, the observed geometry is determined by relativistic beaming. As the Lorentz-factor of the fireball decreases, the beaming angle opens up and the expansion is seen as if it was isotropic. The initial interaction of the fireball ejecta with the surrounding gas produces also a ***reverse shock***.

The strength of the fireball model consisted in predicting very exactly the behaviour of the ***afterglow*** before these could be verified experimentally, assuming only ***synchrotron radiation*** (yielding a power-law spectrum with three breaks [112]). Later, the optical signature of a ***reverse shock***, predicted in 1999 [113], was verified one month later with the ***ROTSE*** telescope [114].

The currently most used formulation of the – nevertheless complex – fireball model can be found in [115,116] [12]. Although the fireball model became widespread and largely accepted, there is still no agreement about its details [80].

Currently, additional thermal components of the spectrum are discussed (see e.g. models by Felix Ryde [117]), dominating the emission at the beginning of the GRB. The (time-resolved) low-energy parts of the spectrum can be well fit to thermal spectra with an evolving "observed temperature" $kT = kT'2\Gamma$. The temperature

[12] However, calculated within the framework of a $\Lambda = 0$ universe.

evolution $kT(t)$ itself can be modelled by a smoothly broken power-law in time with power-law indices expected from emission of the photosphere of the ***optically thick*** fireball before becoming transparent.

2.9.4 Cannonball Model

The ***Cannonball Model*** was invented by Alvaro DeRùjula and Arnon Dar [118–121]. It assumes first a core-collapse ***supernova*** and the creation of a neutron star. About ten days later, the neutron star collapses and bipolar jets of hydrogenous plasma clouds – the so-called ***cannonball***s (CBs) – are ejected. These CBs have Lorentz factors of the order to $\Gamma \sim 10^3$ and consist of baryons and electrons in equal parts.

A CB is emitted, when a part of the accretion disk falls ***abruptly*** onto a compact central object (as observed e.g. in ***microquasar***s). When the CB crosses the ***SNR*** with its large Lorentz factor, its surface becomes heated to keV temperatures due to collisions with the shell particles. It emits thermal ***bremsstrahlung*** radiation as it reaches the transparent outskirts of the shells. This radiation, in turn, is boosted and collimated by the CB's motion and seen like a single pulse in a GRB.

Due to ***relativistic beaming***, GRBs are observable only if the angle θ subtended by the CB's velocity vector and the line of sight to the observer is small: $\theta \sim (1/\Gamma_0)$.

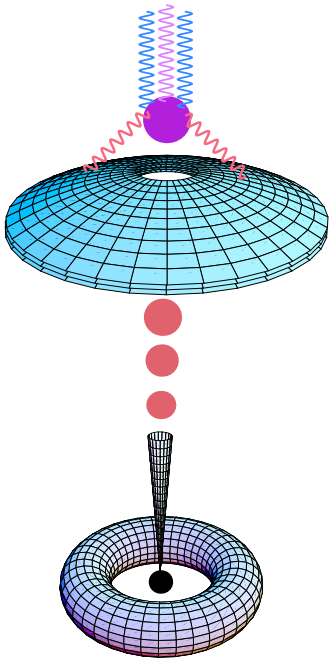

Figure 19: Sketch of the cannonball model. Figure from [118].

2.9.5 Other Models

In the ***Compton Drag Model*** [122], introduced by Davide Lazzati, Elena Rossi, Gabriele Ghisellini and Martin Rees: A massive star collapses and creates a fireball which traverses a funnel inside the (not yet blown away) massive star envelope. The fireball ***inverse Compton scatters*** ambient ***soft photons*** radiated by the walls of the funnel (the so-called ***Compton Drag***) and produces thus the GRB.

Another model was proposed by Boris E. Stern and Juri Poutanen [123], suggesting that a synchtrotron self-Compton mechanism at rather low shell velocities ($\Gamma \approx 30 - 100$) can reproduce the gamma ray and X-ray spectra if the electrons get continuously re-accelerated and heated. In contradiction to the fireball model, the particle acceleration is then not dominated by Fermi acceleration, but instead by other proposed mechanisms which are not further discussed here: Plasma instabilities behind the shock front [124] or magnetic field energy dissipation [125, 126]. The

strength of this model consists in explaining very naturally the hard-to-soft evolution of spectra, as shown in figure 12, and the possibility to reach rather hard values of $\alpha > -1.5$, obtained from Band-function fits (equation 5) of some GRB spectra.

Finally, Vladimir Usov suggested a Poynting flux model from highly magnetized, fastly rotating neutron stars, created in a collapsar [125, 127]. In such a model, a strongly magnetized wind flowing a high Lorentz factors is created. Magnetic reconnection can then transfer magnetic energy to electron-positron pairs in the wind. Later, large-scale electro-magnetic waves can efficiently accelerate parts of the electrons and positrons. The resulting spectra will be again a combination of thermal spectra with non-thermal synchtrotron emission [117].

2.9.6 Emission of GeV and TeV Gamma Rays

Several attempts were made in the past to observe GRBs in the GeV and TeV energy range, each indicating some excess over background but without stringent evidence. The only significant detections were made by the ***EGRET*** detector which could observe seven GRBs emitting gamma rays with energies between 100 MeV and 18 GeV [76,128]. Figure 20 shows the averaged spectrum of the four brightest bursts, observed by EGRET. The continuation of the power law is visible up to the GeV-range, without any apparent cut-off.

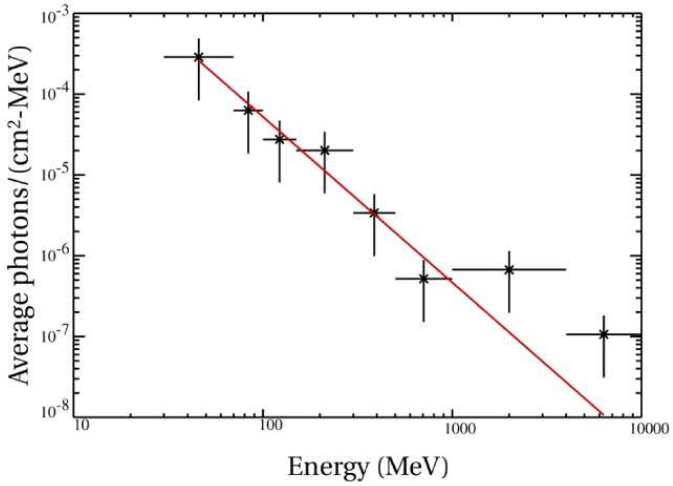

Figure 20: Averaged spectra of the four brightest GRBs observed by EGRET: GRB910503, GRB930131, GRB940217 and GRB940301. Figure from [129].

Especially one burst, GRB940217 [76], showed an event of $E > 18$ GeV more than one hour after the onset of the burst (see figure 21).

Recent results from the ***TASC*** shower counter, part of the ***EGRET*** detector, jointly fit with BATSE data, indicate that the spectrum of GRB941017 contained a very hard, luminous, long-duration component [130]. That data shows a spectral

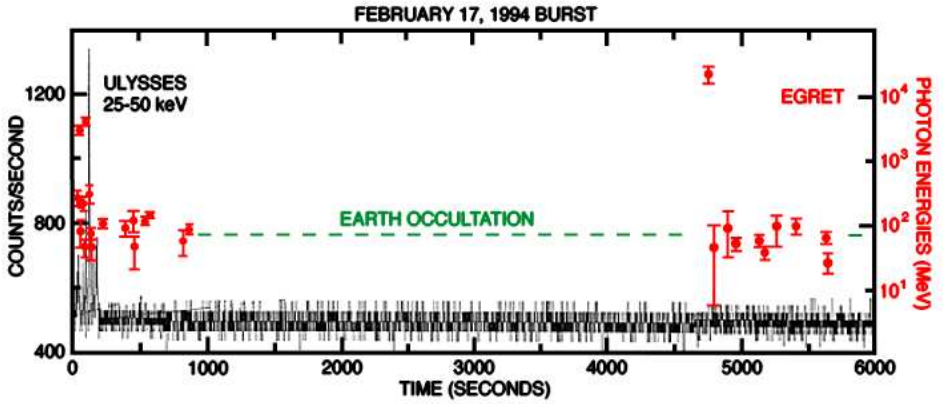

Figure 21: The light curve of GRB940217, as observed by the ULYSSES detector (black lines) and EGRET (red points). In the last case, each point corresponds to one single gamma ray event and the vertical scale is the photon energy (right scale in red). During the time period marked with "earth occultation", the burst was not visible for EGRET. The probability to observe the 10 events after earth occulation from background fluctuations is $6 \cdot 10^{-4}$, the probability to detect one single event with energy $E > 18$ GeV from background is $5 \cdot 10^{-6}$. Figure and numbers from [76].

component presumably due to ultra-relativistic hadrons with a differential photon flux spectral index of $\alpha = -1$ with no cut-off up to the TASC detector energy limit at 200 MeV.

Many other detectors have reported marginal excesses of gamma rays from some GRBs beyond the GeV range, like the ***TIBET*** air shower array [131], the ***Whipple*** Air Cherenkov Telescope [132, 133], the ***HEGRA-AIROBICC*** array [134], the ***Milagrito*** experiment [135] and the ***GRAND*** array [136]. None of these results gave significant excesses over background, though. Lately, the results from a GRB searches above 100 GeV from the full ***Milagro*** detector [13] and the ***STACEE*** Solar Array, presenting upper limits at the level of 2000 [137] and 6 Crab Units [138], respectively. While the first limit applies to the entire prompt emission of GRB010921, the second one is only valid from 3.2 minutes after the occurrance of the corresponding GRB050607.

The ***fireball*** and the ***cannonball*** model allow or predict GeV to TeV gamma ray fluences comparable to or even stronger than the keV to MeV radiation, with durations ranging from shorter than the prompt burst to extended TeV ***afterglow***s [139–142].

In the ***fireball*** model, possible emission mechanisms range from proton-synchrotron emission [24, 143] to photon-pion production [12, 24, 144, 145] and inverse-

[13] Reference [137] gives an upper limit already at 100 GeV, however, this detector deploys its full sensitivity only above the TeV energy range.

Compton scattering in the burst environment [80,112,140,141,146] or in the ***reverse shock*** [147,148]. Even considering pure electron ***synchrotron radiation***, measurable GeV-emission for a significant fraction of GRBs is predicted [141,149].

Since the discoveries of the X-ray flares by ***SWIFT***, Xiang-Yu Wang, Zhuo Li and Peter Mészáros [150] predict that these X-ray flare photons should be Inverse-Compton scattered by the forward-shock electrons from the afterglow, predicting GeV-TeV flares. Also a direct SSC model for the X-ray flares was calculated, predicting observable GeV-TeV flares correlated in time with the X-ray flares. If such high energy gamma ray flares would be observed, the emission mechanism could be restricted already with the use of a simple correlation analysis.

In order to give a feeling about the detection and discrimination potential of the MAGIC telescope with respect to fireball models, the most important theoretical interpretations of the measurements obtained from GRB941017 [130] – explained further above – are displayed in figure 22: Above, an electronic model by Pe'er Asaf and Eli Waxman [148] is shown which assumes that the forward shock electrons inverse Compton scatter optical photons emitted in the reverse shock which traverses the fireball. One can immediately see that the predicted GeV to TeV radiation lies orders of magnitude above the sensitivity of the MAGIC telescope. A concurrent model by Charles Dermer and Armen Atoyan [145], is shown in figure 22 on the next page. It assumes the high-energy tail of GRB941017 being due to an escaping beam of ultra-high-energy ($E \gtrsim 10^{14}$ eV) neutrons which interact with the external radiation field to produce a directed beam of pions. These pions decay into gamma rays, muons and subsequently electrons which themselves emit synchrotron radiation. The resulting spectra follow the observed E^{-1} photon flux spectra between 100 keV and 100 MeV, showing a sharp cut-off at 500 MeV which is due to internal photo-absorption above this energy. Would the MAGIC telescope have been operational when that burst occurred, these two models could have been easily tested.

The ***cannonball*** model predicts narrow GeV emission flares from ***neutral pion decay***, each associated with one of the CBs and arriving about 1 second earlier than the GRB emission (see figure 23).

The ***Compton drag*** model predicts no GeV gamma radiation at all because the plasma is so dense that it opaque to the energetic photons (getting self-absorbed via $\gamma + \gamma \rightarrow e^+ + e^-$) when the GRB is radiated. Figure 24 shows the expected photon spectra obtained from three typical scenarios within the framework of the Compton Drag model. None of the shown scenarios predicts measureable fluxes above 1 GeV photon energy at Earth.

Similarly, the Stern and Poutanen model predicts no measurable gamma ray emission above about 20 GeV as can be seen in typical spectrum displayed in figure 25.

Up to now it cannot even be excluded that GRBs may emit the main part of its energy in form of high-energy ($E > 100\,GeV$) gamma ray emission and simply escaped detection because of the photon absorption on the infrared background radiation (see section 2.12.1 and [152]).

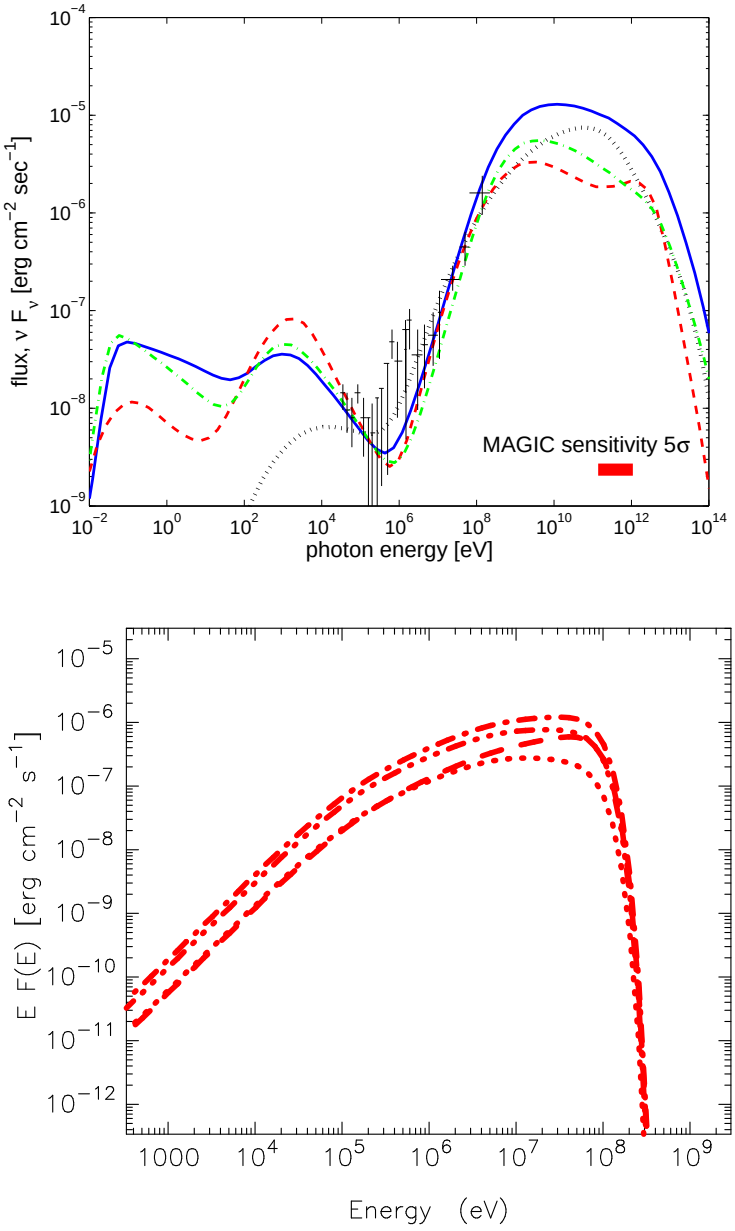

Figure 22: Top: Spectra for four different models developed in [148] for a time interval of T_0+100 s to T_0+200 s after the onset of the burst. Points with error bars are the observed spectrum of GRB941017 [130], the coloured lines shows the predicted spectra of the model obtained with different initial parameters. Also the MAGIC sensitivity is shown as red thick line. Figure from [148]. Bottom: Spectra predicted by the model developed in [145]. In red: four generations (for the time inverval of $T_0 + 100$ s to $T_0 + 200$ s) of the synchortron emission from the decay products of the neutron beam (see text for explanations). Figure from [145].

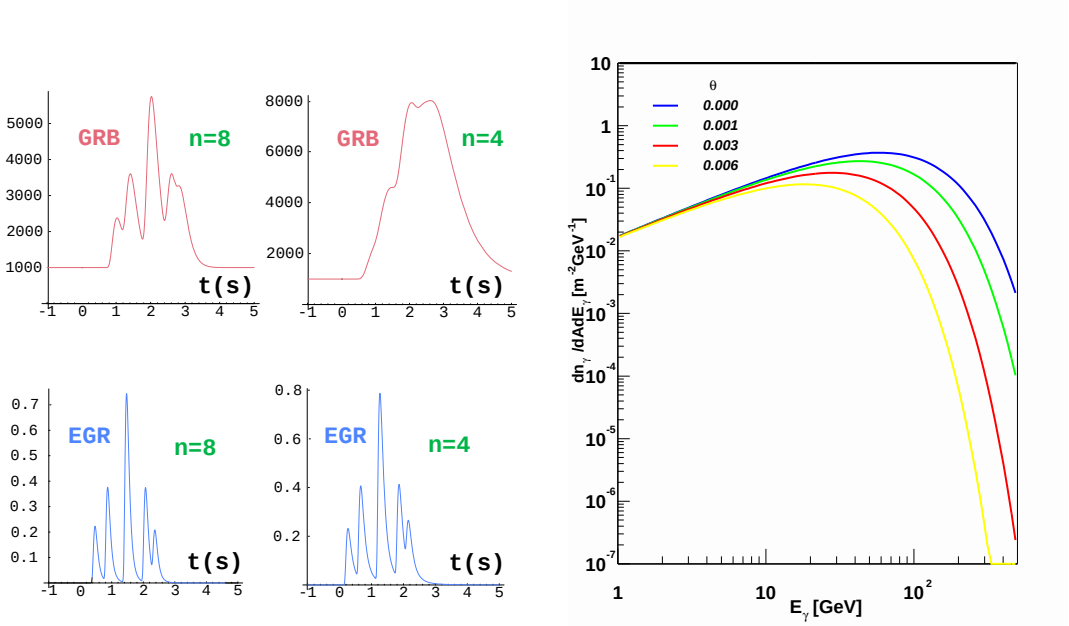

*Figure 23: Left: The light curves of a typical GRB (top red) and their high-energy gamma ray emission - here called "Energetic Gamma Rays" (EGR) - from **neutral pion decay** (bottom, blue). within the framework of the **cannonball** model. The numbers $n = 8$ and $n = 4$ model two typical SNR column density functions (from [151]). Right: The predicted observer spectra of EGR's (formula (44) from [151]) for a GRB situated at $z = 1$. The four lines correspond to different angles between the CB velocity vector and the line-of-sight to the observer.*

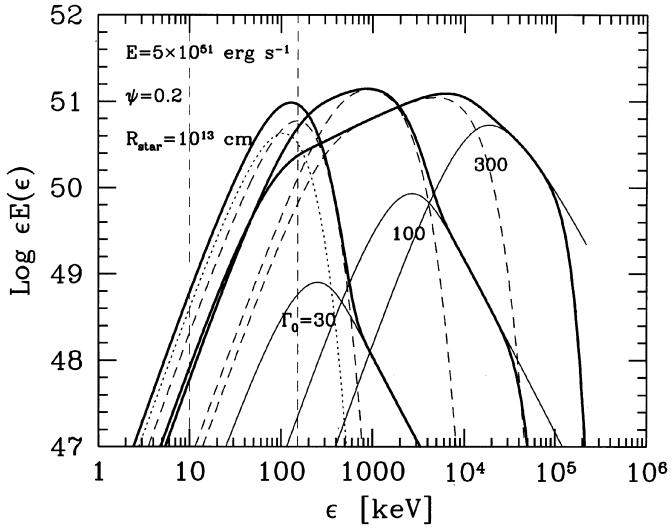

Figure 24: Predicted photon spectra from three scenarios with varying bulk Lorentz factors, predicted by the Compton Drag Model (solid lines, from [122]).

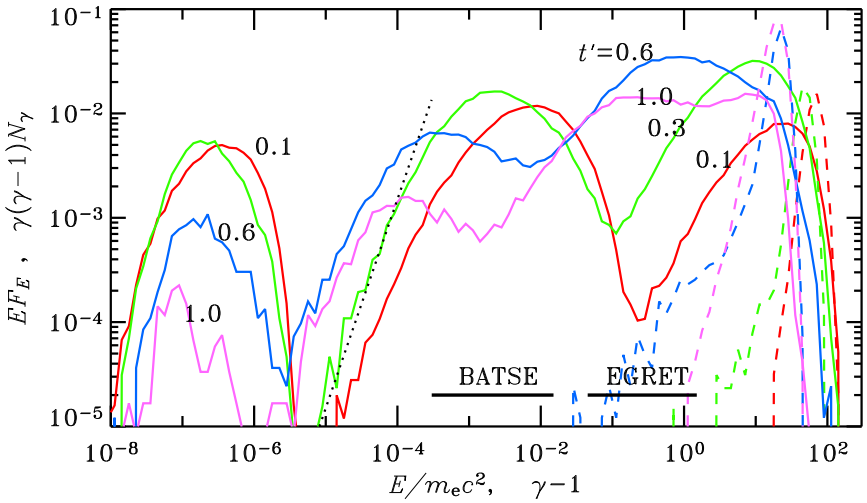

Figure 25: Predicted comoving frame photon spectra in the framework of the model by Stern and Poutanen. The solid lines show the photon spectra at different times during the prompt emission, the dashed lines the electron energy distributions. To retrieve the expected observer spectra, the x-axis values need to be multipied with $m_ec^2 \cdot 2\Gamma/(1+z)$ ($\Gamma \approx 130$ here). The right side would thus correpond to about 20 GeV for a GRB at redshift $z = 1$ (from [123]).

2.10 X-Ray Flashes

While the break energy of gamma rays emitted from the prompt GRBs is situated at 200 keV, X-ray flashes (***XRF***) are characterized by peak energies below 50 keV and a dominant X-ray fluence. Because of similar properties, a connection between ***XRF***s and ***GRB***s is suggested. In the ***fireball*** model, an increase of the baryon load within the fireball itself [153] or low efficiency shocks [154] could produce XRFs. The ***cannonball*** model requires the existence of XRFs, produced from GRBs observed more off-axis [155]. Up to date, no conclusive response has been found about the nature and origin of XRFs, though.

2.11 Soft Gamma Repeaters

Soft gamma repeaters (***SGR***) are believed to be extremely rare strong magnetic ***neutron star***s (so-called ***magnetar***s) which have a rotation period ($\ll$20 ms) so fast that they allow the creation of magnetic fields of greater than 10^{14} G by the dynamo effect. According to a model by Robert Duncan and Christopher Thompson [156], magnetars spin-down at the very fast rate of several thousands of years and heat therewith the interior of the neutron star. The huge magnetic field puts a strong stress on the crust of the magnetar which cracks once in a while. It emits then numerous short-duration (about 100 ms) bursts of hard X-rays. SGR spectra show

no evolution and can be explained by thermal ***bremsstrahlung*** spectra with a temperature of about 30-40 keV [157].

Only four identified SGRs were discovered in the last 20 years: SGR0526-66 [14], situated in the Large Magellanic Cloud (***LMC***), and SGR1806-20, SGR1900+14 and SGR1627-41, situated in our Galaxy. On 27 December 2004, an exceptionally long giant flare from SGR1806-20 could be observed which has become the most luminous transient event, ever observed in our Galaxy [158]. Only one out of these four SGRs (SGR1900+14) is in principal observable by the MAGIC telescope.

2.12 Cosmology and Diffuse Background Radiation

2.12.1 Gamma Ray Horizon

Already in the 1960's, Robert Gould and Gerald Schréder pointed out the possibility that above some critical energy, the visible universe in high energy photons should be limited because of pair production on the cosmological low-energy diffuse and isotropic extragalactic background light (***EBL***), produced by the stars [159].

Given a gamma ray of energy E and a low-energy photon of energy ϵ (e.g. from the EBL), electron-positron pair production ($\gamma_E\,\gamma_\epsilon \rightarrow e^+\,e^-$) can occur above the threshold energy condition:

$$E\,\epsilon\,(1-\cos\theta) > 2\,m_e^2 c^4\ , \tag{6}$$

where θ is the scattering angle between two photons and m_e the electron mass.

Given a certain model about the ***EBL***, the attenuation of a hypothetical mono-energetic flux $\phi(E)$ of emitted gamma rays of energy E from a source situated at redshift z, can be parameterized by the ***optical depth*** $\tau(E,z)$:

$$\phi(E,z) = \phi(E,0)\cdot\exp\left[-\tau(E,z)\right] \tag{7}$$

The condition $\tau(E,z) = 1$ defines a ***Gamma Ray Horizon*** (***GRH***), also known as the ***Fazio-Stecker relation*** (***FSR*** [160]), as the gamma ray energy E at which a fraction of 1/e of the flux $\phi(E)$ gets absorbed after traveling a distance, expressed in redshift z, from the source.

Figure 26 shows the ***GRH*** as computed in [161]. The ***GRH*** has not yet been measured experimentally. Its exact shape and magnitude can be used to measure the ***EBL*** and even to constrain cosmological parameters [162].

An argument for the existence of the ***GRH*** is the fact that in spite of an energy-flux sensitivity superior to EGRET, a much smaller number of sources has been discovered by the Cherenkov Telescopes above 200 GeV. For extragalactic sources, this discrepancy might be either due to internal absorption in the emitting sources or external absorption in the ***EBL***. A detailed measurement of the ***GRH*** [162] with many sources at different redshifts can give an answer to this problem.

[14] In constrast to GRBs, SGRs are identified by their galactic coordinates, i.e.: SGR0526-66 means SGR, situated at RA: $05^{\rm h}.26^{\rm m}$, DEC: -66°

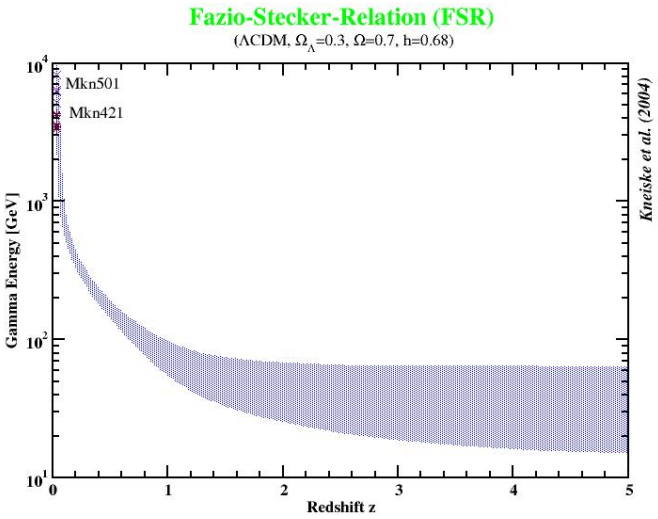

*Figure 26: The **GRH**, as computed in [161]. Different lines correspond to different models of the **EBL**. Also displayed are three AGNs with measured spectra up to the assumed GRH.*

As ***GRB***s are usually located at a very high redshift ($z \approx 1$), energetic gamma rays get absorbed by the ***GRH*** and pose a serious problem to Cherenkov telescopes: From figure 26 follows that no signal will be received above 100 GeV from a source located at $z = 1$. However, the energy threshold of a Cherenkov telescope scales with observation zenith angle like [163]:

$$E_{thr}(\theta) = E_{thr}(0) \cdot (\cos\theta)^{-3} \tag{8}$$

A given energy threshold $E_{thr}(0)$ of a telescope (e.g. 50 GeV for MAGIC) has to be multiplied by a factor $(\cos\theta)^{-3} \approx 4$, if it observes at 50° zenith angle and $(\cos\theta)^{-3} \approx 25$ at 70°.

2.13 Fundamental Physics

2.13.1 Super-symmetric Particles and Dark Matter

For quite some time already, it is known that the galaxies rotation velocities do not match with what one expects from the matter distribution, seen in stars, and Newtonian dynamics [164]. In 2003, the WMAP collaboration established that the main contribution to the matter content of the universe is non-baryonic: Out of its total matter content: $0.127 < \Omega_m h^2 < 0.143$, the baryonic part is only: $0.00217 < \Omega_b h^2 < 0.00232$, the rest not being part of the standard model of particle physics [165] (h is the reduced Hubble constant). This result lead to wide speculation about the nature of the ***dark matter***, however the most favored candidate is the lightest

super-symmetric particle (***LSP***) in the Minimal Super-symmetric extension of the Standard Model of particle physics (***MSSM***), namely the neutralino χ. It was estimated that the continuum gamma ray fluxes due to neutralino annihilations in the center of the Galaxy, if they exist, should be detectable by a Cherenkov Telescope with energy threshold of 100 GeV and 250 hours of observation time [166].

2.13.2 Quantum Gravity Scale

Any quantum theory of gravitation introduces quantum fluctuations at the Planck scale ($E_p \approx 10^{19}\,\mathrm{GeV} \equiv 10^{-33}\,\mathrm{cm}$), which would induce a deformed dispersion relation for photons of the form:

$$\boldsymbol{p}^2c^2 = E^2 \cdot [1 + f(E/E_{QG})] \tag{9}$$

where E is the photon energy, E_{QG} an effective quantum-gravity energy scale (which might be lower than the Planck-scale) and f is a model-dependent function of the ratio E/E_{QG}, $\boldsymbol{p}$ is the photon momentum and c is the velocity of light. At small energies $E \ll E_{QG}$ a series expansion of the dispersion relation can be made:

$$\boldsymbol{p}^2c^2 = E^2 \cdot [1 + \xi E/E_{QG} + O(E^2/E_{QG}^2)] \tag{10}$$

where $\xi = \pm 1$ is a sign ambiguity which is fixed in the given theory. Equation 10 leads then to energy-dependent velocities of the photon:

$$v = \frac{\partial E}{\partial p} \approx c \cdot \left(1 - \xi \frac{E}{E_{QG}}\right) \tag{11}$$

Gamma rays traveling cosmological distances should therefore encounter a "vacuum" energy dispersion $\delta v \approx E/E_{QG}$, violating Lorentz invariance [167]. A gamma ray signal of observed energy E_γ should acquire a time delay with respect to the Lorentz-invariant case, after having traveled a distance L (redshift z) [168]:

$$\Delta t \approx \xi \cdot \frac{E_\gamma}{E_{QG}} \cdot \int_0^z (1+z)\frac{dl}{dz}\,dz \overset{z \ll 1}{\rightarrow} \quad \xi \cdot \frac{E_\gamma}{E_{QG}} \cdot \frac{L}{c}\ , \tag{12}$$

with:

$$\frac{dl}{dz} = \frac{1/(1+z)}{H_0 \cdot [\Omega_M(1+z)^3 + \Omega_K(1+z)^2 + \Omega_\Lambda]^{1/2}} \tag{13}$$

an H_0 being the Hubble constant and Ω_M, Ω_K and Ω_Λ the cosmological parameters.

Gamma rays of different energies being emitted simultaneously should thus reach an observer at different times. In order to use equation 12 to test E_{QG}, a rapidly varying signal is required with typical time intervals δt smaller than the time delay Δt due to the quantum gravity effect and observed simultaneously at two different energies at least.

It has been shown [169] that GRBs are the best suited astronomical candidate sources for these tests because of their cosmological distances (large $L \approx 10^{10}$ light yr) and their possible small time structures $\delta t \leq 0.2$ ms. A photon of 20 MeV energy

would acquire then a time delay of about 0.5 ms while a photon of 100 GeV gets delayed by about 3 seconds, if the quantum gravity scale is the Planck-scale and more, otherwise. Going beyond 100 GeV is unfortunately not plausible because of the absorption of more energetic photons by the ***GRH*** (section 2.12.1, but see also ref. [168]).

In order to disentangle possible energy-dependent time delays in the emission itself, at least two requirements have to be fulfilled:

1. It has to be shown that any measured time delay is un-related to the source physics, i.e. the emission at one "reference" energy comes from the same emission process at the same time as the one observed at the "test" energy.

2. The strict linear dependency of the time delay with energy has to be demonstrated.

In 1999, the ***Whipple*** collaboration published a first bound on E_{QG}, obtained with that technique using a rapid flare ($\delta t \approx 280\,\mathrm{s}$) of Mrk 421 ($z = 0.031$), observed up to 2 TeV energy. The results was $E_{QG}/\xi > 4 \cdot 10^{16}$ GeV at 95 % confidence level [170].

Using the same method for ***GRB***s, much higher sensitivities should be reached since the distances L are usually much larger and typical time intervals δt much shorter. For instance, assuming a GRB at a redshift of $z = 1$, observed simultaneously at 100 GeV and 1 MeV, with a time binning of 1 s, a hypothetical limit of $E_{QG}/\xi > 10^{19}$ GeV should be reached.

However, as emission models are not yet being settled (see section 2.9.3), it will be very difficult to fulfill the first requirement.

3 The Magic Telescope

The MAGIC Telescope was inaugurated in October 2003, and commissioned until 2004 [171]. Before describing the functionning of the telescope, an overview of air shower physics and the IACT-technique is given.

3.1 Air Showers

Cosmic rays hardly ever hit the ground, but instead collide with the nucleons, mainly nitrogen, of the air. In such collisions, new particles are created which themselves interact with the atmospheric atoms, leading to an ***air shower***. Depending on whether the impinging particle is a hadronic (nucleus) or an electromagnetic (electron or gamma ray) particle, one makes the distinction between electromagnetic and hadronic air showers.

Electromagnetic Air Showers

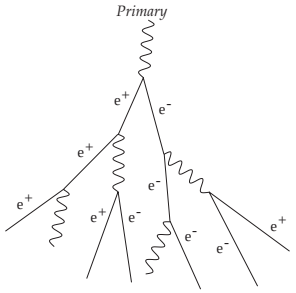

Figure 27: Sketch of electromagnetic shower

Gamma rays above a ***critical energy*** E_c of about 20 MeV lose energy in air primarily through ***pair creation***, electrons and positrons above $E_c \approx 81\,\mathrm{MeV}$ [3] through ***bremsstrahlung***, below through ***ionization*** [172]. The energy loss due to bremsstrahlung is proportional to the energy E_e of the electron ($-dE_e/dx = E_e/X_0^e$) characterized by the ***radiation length*** X_0^e ($37\,\mathrm{g/cm^2}$ in air). Analogously, the ***pair creation*** process by gamma rays can be characterized by a mean free path $X_0^\gamma = 9/7 \cdot X_0^e$ ($47\,\mathrm{g/cm^2}$ in air). The secondary particles created in these processes are again electrons, positrons and photons which can generate secondaries until they reach the respective critical energies. The number of created particles increases exponentially with the shower length until the ***shower maximum*** is reached (when the average energy of the cascade particles is equal to the critical energy) and the shower drops off. Important for Cherenkov telescopes is the development of the number of electrons N_e above a certain energy threshold with the slant depth X in units of the radiation length X_0. It was calculated by Bruno Rossi [173] and Kenneth Greisen [174] (the "Rossi Approximation B"):

$$< N_e(t, E_0) > \;\simeq\; \frac{0.31}{\sqrt{\ln(E_0/E_c)}} \cdot \exp(t - 1.5\, t \ln s)\ , \tag{14}$$

$$\text{with :} \qquad t \;=\; X/X_0 \approx \frac{X_{air}}{X_0 \cdot \cos(\theta_{sh})} \cdot \exp(-\frac{H}{H_0})\ , \tag{15}$$

$$s \;=\; \frac{3t}{t + 2\ln(E_0/E_c)}\ , \tag{16}$$

$$\Delta N_e(s) \;\simeq\; \frac{9}{14}(s - 1 - 3\ln s) \cdot N_e(s)\ , \tag{17}$$

where E_0 is primary particle energy, $X_{air} = 1013\,\mathrm{g/cm^2}$ the column height of air at ground and $H_0 = 8\,\mathrm{km}$ the scale height of the atmospheric pressure. The incidence angle of the shower is denominated θ_{sh} [15]. The ***shower age*** s ranges from 0 to 2, with the ***shower maximum*** $t_{max} = \ln(E_0/E_c)$ found at $s = 1$.

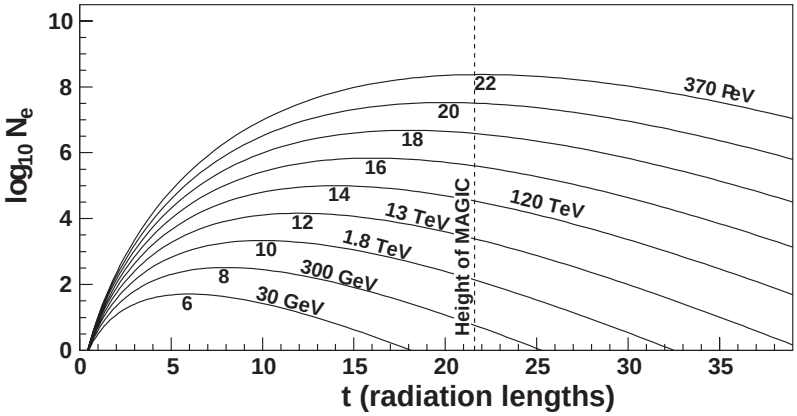

Figure 28: Longitudinal development of an electromagnetic shower: N_e versus the slant depth X, measured in radiation lengths $t = X/X_0$. The lines are calculated for different values of $\ln(E_0/E_c)$.

Most of the information that can be retrieved from equation 14 is highlighted in figure 28: Gamma ray induced air showers in the energy range from 30 GeV to 30 TeV have their shower maximum well above the location of the MAGIC telescope, with more energetic showers reaching deeper into the atmosphere. Below about 100 GeV, the showers die out completely before reaching the ground. Moreover, the distribution is ***asymmetric*** with respect to the shower maximum.

It is useful to invert equation 15:

$$H = H_0 \cdot \ln\left(\frac{R_{air}}{t}\right), \tag{18}$$

with $R_{air} = X_{air}/X_0 = 27.4$ to calculate typical heights H of the shower maxima from figure 28. For instance, at 100 GeV the shower maximum ranges from about 12 km to 10 km a.s.l.

Very important is the fact that there are large fluctuations from shower to shower, even for those of same energy. From eq. 17 follows that the fluctuations are smallest near the shower maximum [16]. At 10 km height, a 100 GeV shower has then: $s = 1.38, \Delta N_e \approx 0.4 N_e$ a 1 TeV shower: $s = 1.18, \Delta N_e \approx 0.2 N_e$. In order to seize all fluctuations correctly, extensive Monte-Carlo simulations are required.

Multiple scattering of the electrons and positrons deflects the secondary particles away from the primary gamma ray direction, the ***shower axis***. The transverse

[15] Note that equation 15 is only approximate and neglects temperature changes and the curvature of the Earth.

[16] However, eq. 17 does not include development fluctuations, i.e. the dependence of s with height.

extension of an electromagnetic shower can be parameterized by the Molière radius R_M [172]:

$$R_M = 21.2\,\text{MeV} \cdot \frac{X_0}{E_c} \approx 9.3\,\text{g/cm}^2 \text{ (in air)} \tag{19}$$

On average, only 10 % of the lost energy lies outside a cylinder with radius R_M ($\approx$ 78 m at sea level, 190 m at 10 km height) and about 99% is contained within $3.5\,R_M$. Traditionally, the lateral spread can be parameterized by the Nishimura-Kamata-Greisen (NKM)-formula [175,176], although only strictly valid between $s =$ 1.0 to 1.4:

$$\rho_e(r) = K \cdot \frac{N_e}{R_M^2} \cdot \left(\frac{r}{R_M}\right)^{s-2} \cdot \left(1 + \frac{r}{R_M}\right)^{s-4.5}, \tag{20}$$

where K is some normalization constant. A more complete parameterization containing all fluctuations and correlations between the parameters has been compiled by Günter Grindhammer and S. Peters [177].

Hadronic Air Showers

A hadronic shower is produced in the collision of a nucleus with another (atmospheric) nucleus, creating mainly pions and Kaons and further nucleons. The last ones and the possible fragments of the original nucleus form part of the ***hadronic core*** of the cascade. The cascade continues to suffer collisions with the air, similar to the first one, until its energy per nucleon falls below the pion production threshold of about 1 GeV.

Hadronic showers have various components:

Hadronic component: The core of energetic hadrons, consisting of nucleons and mesons. As these hadrons are heavy, they can transfer significant transverse momenta to their decay products.

Electromagnetic component: Consists of electrons, positrons and photons from electromagnetic sub-cascades, initiated by the decay of mesons, mainly the neutral pions π^0 [17]. About one third of the collision energy is transferred to the electromagnetic component in each hadronic interaction. This process transfers continuously energy from

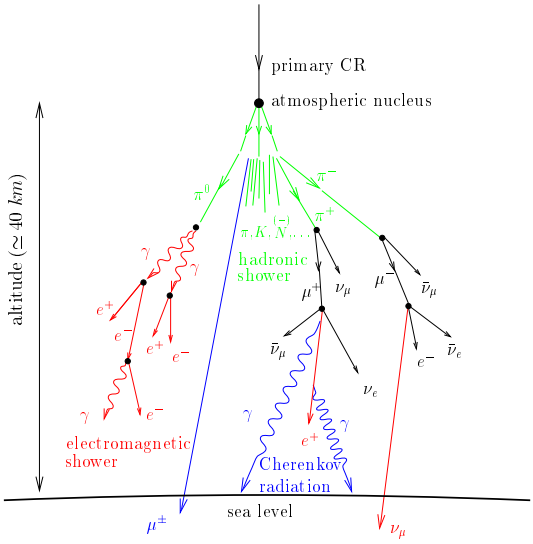

Figure 29: Sketch of the generation of a hadronic air shower. Figure from [8].

[17] The π^0 has a decay time of only $\tau = 8.4 \cdot 10^{-17}$ s, while the $\pi^\pm$ particles decay much slower: $\tau = 2.6 \cdot 10^{-8}$ s [178].

the hadronic to the electromagnetic component which ends up being the dominant one at the shower tail. If occurring at a high transverse momentum, the pure electromagnetic component can resemble a stand-alone electromagnetic shower and produces an irreducible background for Cherenkov Telescopes.

Muonic component: Some of the charged pions and Kaons decay before they interact, most of them into muons and neutrinos [18]. The muons themselves interact almost exclusively by ionization and usually reach the ground before decaying. Single muons with large transversal momenta can travel far from the shower core and are recognized by their clean Cherenkov rings (see e.g. figure 38 right).

Figure 30 shows the vertical fluxes of the most important particles produced by cosmic rays in the atmosphere with energy above 1 GeV.

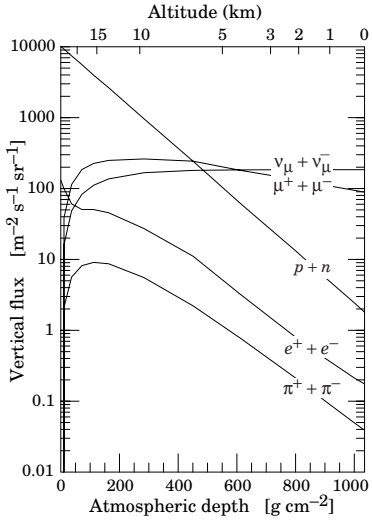

Figure 30: Vertical fluxes of particles in the atmosphere with $E > 1$ GeV. Note that the electromagnetic component is not fully taken into account with this lower energy limit. Figure from [3].

An interaction length can be defined also for hadronic showers: $-dE/dx = E/X_h$, characterized by the hadronic ***radiation length*** X_h (83 g/cm^2 in air for protons and 107 g/cm^2 for pions). The average shower maximum can be expressed as [179]:

$$t_{max} = \ln(\frac{E_0}{AE_c}), \tag{21}$$

with A being the mass number of the primary nucleus. At the maximum of shower development, there are approximately 2/3 particles per GeV of primary energy [3]. For protons, the characteristic interaction length is more than the double of the corresponding electromagnetic interaction lengths, hadronic showers penetrate thus

[18] The neutrino component of the air shower is not visible for Air Cherenkov Telescopes and is further neglected here.

deeper into the atmosphere than electromagnetic ones of the same energy. Moreover, hadronic showers show larger fluctuations from shower to shower, than compared to the electromagnetic case.

3.2 The Imaging Air Cherenkov Technique

Observations of gamma rays using the subsequently produced electromagnetic showers in the atmosphere is possible by detecting the electromagnetic radiation of the secondary shower particles.

Charged particles moving through a dielectric medium of refraction index n with a velocity βc larger than the local phase velocity of light (c/n) generate a photonic shock-wave, called the ***Cherenkov*** [19] ***radiation***. The threshold condition for this type of light emission reads as:

$$\begin{aligned} \beta \cdot n &> 1 \\ E &> m_0 c^2 \cdot \frac{n}{\sqrt{n^2-1}} \end{aligned} \tag{22}$$

with m_0 being the particle rest mass and E the particle energy. Condition 22, translates into an energy threshold for electrons and positrons of about 20 MeV in dry air at 2200 m a.s.l. ($n = 1.0004$ at 400 nm) [20], 40 MeV and 80 MeV at 10 km and 20 km altitude, respectively[21].

Cherenkov light is emitted on a narrow cone around the direction of the emitting particle with an opening angle θ_c of:

$$\cos(\theta_c, \lambda) = \frac{1}{\beta n(\lambda)} \tag{23}$$

The Cherenkov light cone opened by gamma ray induced air showers has an opening angle of typically 1.2° at 2200 m a.s.l., 0.75° and 0.36° at 10 km and 20 km altitude, respectively. From each part of the particle track the Cherenkov light arrives on an ellipse on the ground. As there are many charged particles produced in an air shower, the individual Cherenkov cones

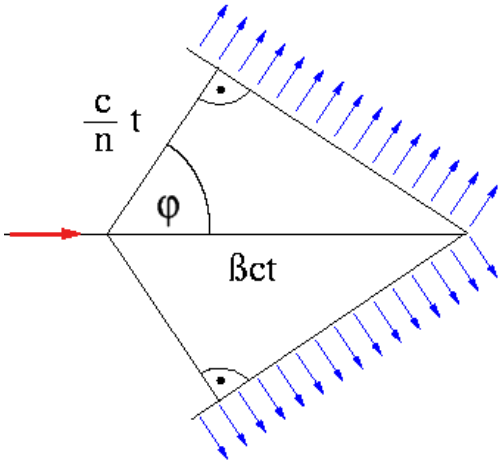

Figure 31: Sketch of Cherenkov light production

[19] Note the standard transliteration to English of the name of the Russian physicist Cherenkov (instead of Čerenkov) who discovered this kind of light emission together with Vavilov in 1934.

[20] In principle, there is also a wavelength-dependency of the refraction index in air. The refractivity $(n-1)$ varies by less than 1% over the visible spectrum and has been neglected here.

[21] According to [180] eq. (1), the refraction index of height z in a U.S. standard atmosphere at a wavelength of 400 nm can be approximated like: $n = 1 + 0.0814 \cdot e^{-z/8}/T$ where z is the atmospheric height in km and T the temperature of air in K, approximated on average as $T(z) = 287 - 6.5z$ for heights smaller than 11 km and $T(z) = 220$ K between 11 and 20 km.

overlap, and the sum of all Cherenkov light photons illuminate uniformly an area of typically 50 000 m^2 at 2200 m a.s.l., called the ***Cherenkov light pool***. This number is almost independent from whether the light has been emitted at 20 km or at 10 km altitude.

The number of photons produced per unit path length of a particle and per unit energy interval of the photons is [172]:

$$\frac{d^2N}{dx\,d\lambda} = \frac{2\pi\alpha}{\lambda^2}\cdot\left(1-\frac{1}{\beta^2 n^2(\lambda)}\right), \tag{24}$$

$$\frac{d^2N}{dE\,dx} \approx 370\,\sin^2\theta_c(E)\ [\mathrm{eV}^{-1}\,\mathrm{cm}^{-1}], \tag{25}$$

where λ is the wavelength of light and $\alpha \approx 1/137$ denotes the fine-structure constant. Both formulations are equivalent for electrons. In an electromagnetic air shower, about 500 Cherenkov photons are created per GeV of incident gamma ray energy in the spectral range between 300 nm and 600 nm. However, a considerable fraction of these photons is lost due to scattering and absorption in the air. Since the involved scattering angles are large compared to the Cherenkov angle, scattered photons are usually lost (as well as absorbed photons) for a Cherenkov telescope. Figure 32 shows the photon spectra before and after atmospheric interactions. The

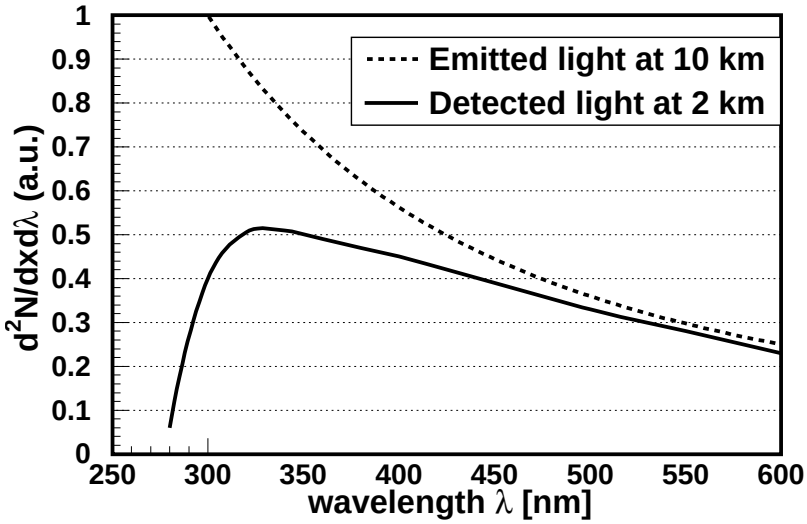

Figure 32: Spectrum of Cherenkov light at the shower maximum (dashed curve) and after traveling down to 2 km altitude (full curve).

cross section of ***Rayleigh scattering*** is proportional to λ^{-4}, thus the UV part of the spectrum is especially affected by the scattering. It is the dominant contribution to the Cherenkov light attenuation under perfect weather conditions. ***Mie scattering*** takes place by particles larger than the photon wavelength: Water droplets, dust and calima. It prevails under poorer weather conditions, its cross section is proportional to $\lambda^{-(1-1.5)}$. At altitudes above 10 km, absorption by ozone may play

a significant role. It affects wavelengths below 400 nm. Wavelengths larger than 800 nm (infrared) are usually absorbed by the H_2O and CO_2 molecules in the air. As the absorption affects especially short wavelengths below 300 nm, it introduces a zenith-angle dependency of the Cherenkov light spectrum: Showers from particles incident at higher zenith angles have spectra shifted toward larger wavelengths (***redder spectra***). Figure 33 shows the simulated average Cherenkov light spec-

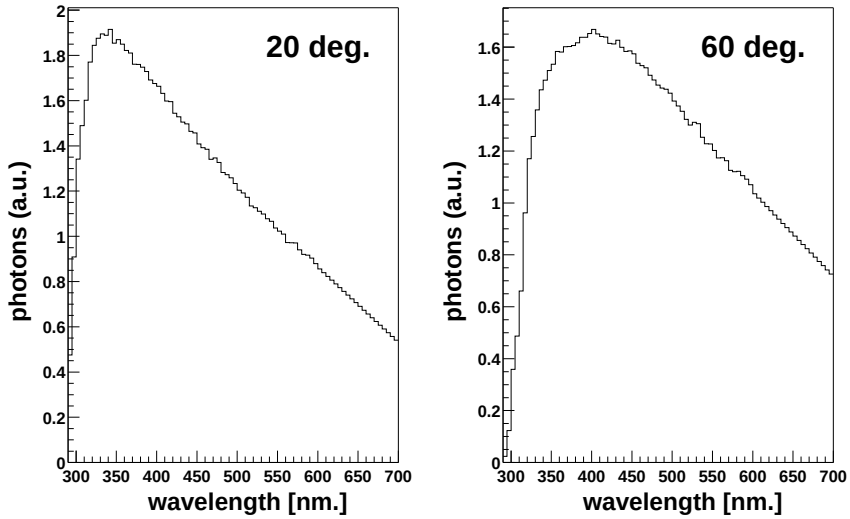

Figure 33: Photon spectrum from simulated Cherenkov showers observed at 20° *(left) and* 60° *(right) zenith angle, simulated for a Crab spectrum between 10 GeV and 30 TeV.*

trum for electromagnetic showers seen from the angles 20° and 60° with respect to vertical incidence. The effect of the wavelength shift can be seen. There is also an energy-dependency of the absorption and scattering: Low-energy showers lose their energy at higher altitudes, the Cherenkov light needs to cross a larger amount of air and is more affected by absorption than showers of higher energy [22].

Figure 34 shows the Cherenkov light photon density for different primary energies and various primary particle types. The photon density has been averaged over an area of 50 000 m^2. One can see that the main contribution from the hadronic air showers comes from single protons with energies greater than 100 GeV. Helium cores contribute only above primary energies of about 300 GeV, apart from the fact that they are already much less abundant in the cosmic rays. Gamma ray induced showers produce an almost constant fraction of their energy in form of Cherenkov

[22] Ref. [181] dedicates two pages about the effect of Cherenkov light absorption by ozone at altitudes between 10 and 40 km. These effects are particularly difficult to simulate since they depend much on the geographical latitude, season and on how much solar irradiation has occurred during the day.

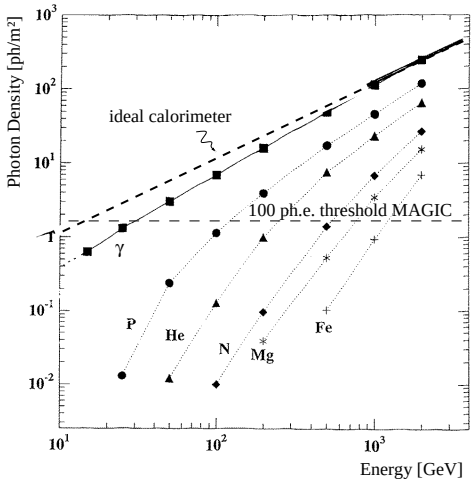

Figure 34: Average photon density of Cherenkov light between 300 and 550 nm from different incident particles vs. the incident energy. Plotted is the mean Cherenkov photon density within 125 m of the shower core for vertically incident showers. The flux numbers have been integrated within a 10 ns window around the peak arrival time. Figure from [181, 182]. The thin line represents roughly the MAGIC trigger threshold for vertical particle incidence.

light (compare to the dashed line "ideal calorimeter"): The number of collected photons by a Cherenkov telescope is roughly proportional to the primary gamma ray energy. Cherenkov light is thus a good ***measure*** of the incident particle ***energy*** [23].

The numbers in figure 34 have to be compared with a typical ***night-sky photon flux*** of about $\boldsymbol{2\ ph/m^2}$ in the same wavelength range [183], seen e.g. by the MAGIC camera during the time of the Cherenkov light flash. Even at full moon, the scattered photon flux increases not more than a factor 10 [181]. The most important background for gamma ray astronomy above 100 GeV is therefore cascades initiated by hadronic particles.

Figure 35 shows the average radial Cherenkov light photon density for vertically incident 100 GeV gamma ray and 400 GeV proton induced showers. The values have been averaged over all azimuth angles. One can see that the ***radial light density*** is almost constant up to about 130 m impact distance for the electromagnetic shower (called the ***shower core***), with a slight enhancement at about 80–120 m and a consecutive steep fall beyond 125 m. There is even light emission beyond 200 m impact distance, called the ***shower halo***. With the mirror area of the MAGIC telescope, shown as a dashed line, effective collection areas of $\pi \cdot (180\ \mathrm{m})^2 = 10^6\ \mathrm{m}^2$ should

[23] Although below 100 GeV the proportionality gets lost and fluctuations in the shower itself become visible on the ground. The uncertainty in the number photons due to the shower fluctuations increases well beyond the square root of the number photons.

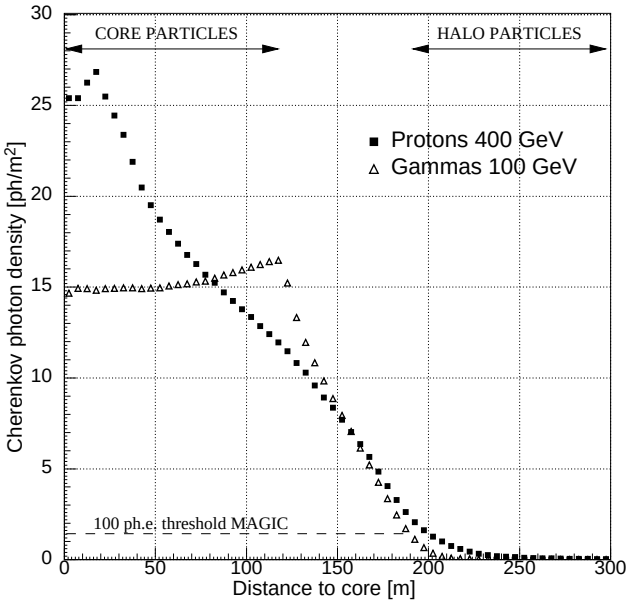

Figure 35: Lateral distributions of Cherenkov photon densities for 100 GeV gamma ray and 400 GeV proton induced showers at an altitude of 2200 m a.s.l. for vertical incidence. Figure from [181].

thus be reached. Figure 36 shows the locations of Cherenkov photons hitting the ground at 2200 m a.s.l. from simulated 300 GeV and 100 GeV gamma ray showers. While the 300 GeV ***Cherenkov light pool*** is filled out uniformly, at 100 GeV the individual ring structures become visible.

Proton showers show their brightest average emission at 20 m impact parameter, steeply falling down beyond. However, local fluctuations (not shown in figure 35) are much bigger for hadronic showers, due to the Cherenkov emission of penetrating single pions and Kaons, and the muons produced in the respective decays. For the same reason, light can be spread to larger distances from the shower core.

Figure 37 shows the locations of Cherenkov photons hitting the ground at 2200 m a.s.l. from a simulated 1 TeV proton shower. The non-uniformity of Cherenkov light reaching the ground and the impact of single energetic electrons and muons can be discerned.

While the hadronic cascades are isotropic in arrival directions, a Cherenkov telescope searches for an enhancement of electromagnetic showers from a hypothetical source direction. Only with the invention of the Imaging Atmospheric Cherenkov Telescope (***IACT***) by the Whipple collaboration in 1989 [15] (using a 37 pixel ***PMT*** camera), the hadronic background could be reduced to such an extent that the first TeV gamma rays from the Crab Nebula could be detected.

An IACT uses the on average statistically different shapes of images from hadronic and electromagnetic showers to differentiate between both. Since electromag-

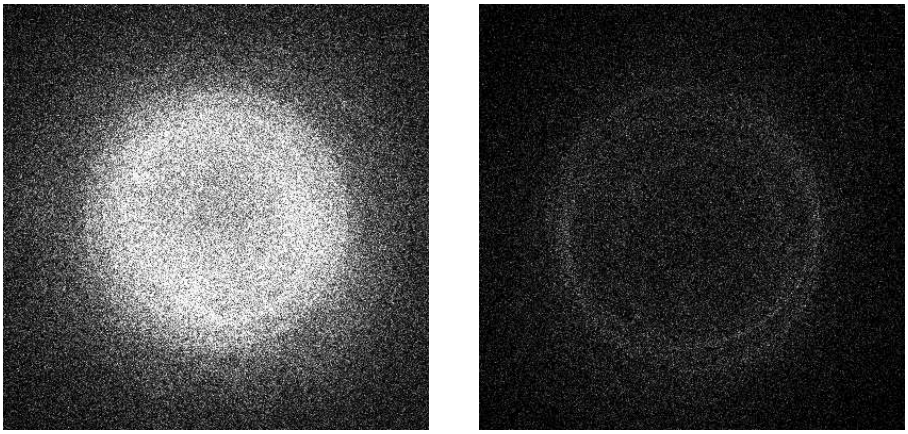

Figure 36: Examples of the lateral distribution of Cherenkov light from simulated vertically incident gamma showers on ground at 2200 m a.s.l. The area displayed covers 400×400 m with the shower core at the center. Atmospheric extinction has not been taken into account. Left: 300 GeV gamma ray, right: 100 GeV gamma ray. Figures from [184].

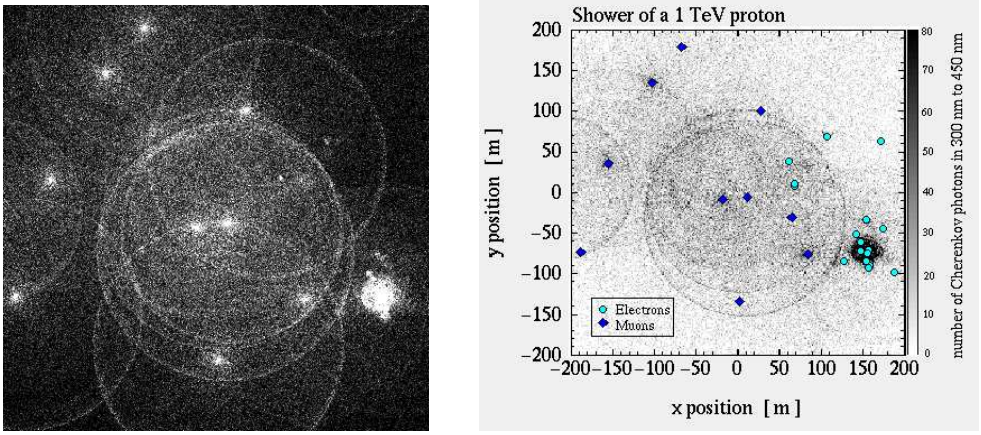

Figure 37: Example of the lateral distribution of Cherenkov light from a simulated 1 TeV vertically incident proton shower on ground at 2200 m a.s.l. The area displayed covers 400×400 m with the shower core at the centre. Atmospheric extinction has not been taken into account. Left: Only Cherenkov photons, right: Impact points of all electrons and muons reaching the ground displayed. Figures from [184].

netic showers are narrower and better confined than hadronic showers, their images can be reduced to a couple of statistical parameters (the so-called ***Hillas parameters*** [185]) which in turn are used to suppress more than 99% of the unwanted hadronic background. Figure 38 shows three typical examples of such shower images in the camera of MAGIC.

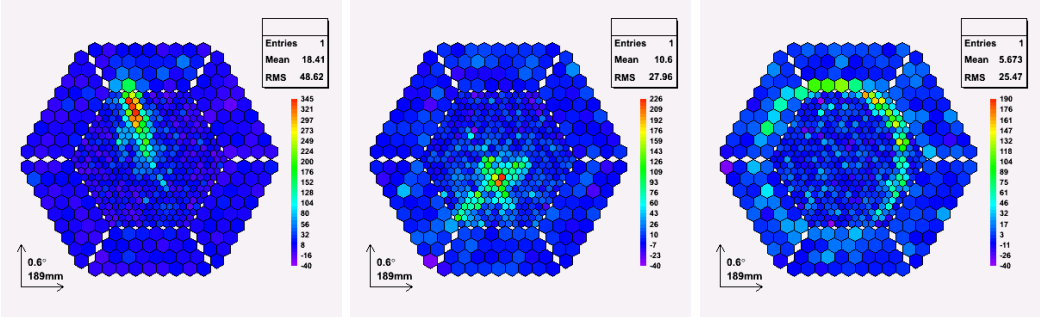

Figure 38: Example of the three different types of shower images recorded by the MAGIC camera: Left: gamma-like shower, center: hadronic shower, right: single muon.

Two other differences between gamma ray and hadron induced showers concern the distributions of arrival times of the Cherenkov photons on ground [186–188]: The first show shorter photon arrival time spreads of typically 1–2 ns while the latter may exhibit large tails.

3.3 Site

The MAGIC Telescope has been built on the Observatory ***Roque de los Muchachos*** on the Canarian Island of La Palma (28.75°N, 17.89°W), 2200 m above sea level. The Instituto de Astrofśica de Canarias (***IAC***) and the Roque de los Muchachos provide an excellent infrastructure for the observations. Already the precursor telescopes CT1 and the CT-system had been run there successfully (see e.g. [42]). The site makes possible more than 2000 hours of good observation conditions per year [181].

Figure 39 shows a picture of the MAGIC telescope as of 2005.

3.4 Drive System

The telescope [189] has an ***alt-azimuth-mount***, placed on a circular rail of 18 m diameter. The telescope frame, constructed by the German company MERO, is made of carbon fiber-epoxy composite tubes which are especially light-weight and weigh less than 20 t. The rest of the support is made of aluminum with a total moving weight less than 60 t [190]. The telescope can move from $-80°$ to $105°$ in zenith and $400°$ in azimuth. The telescope is moved by two 11 kW motors in azimuth direction and one 11 kW motor in the elevation. The angular position is controlled by 14-bit shaft encoders with an accuracy of $0.022°$.

Figure 39: Left: The Observatory Roque de los Muchachos at La Palma, right: View of the MAGIC Telescope.

The support structure was designed to react quickly to ***GRB*** alerts from satellites. The design goal was to turn the telescope toward the burst position within 30 s [181,191], in order to detect a burst when the prompt γ–emission is still ongoing.

Until mid-2005, the drive engines could be used at 70% of their full power with which it was possible to move the telescope 180° in azimuth in less than 22 s [190]. Efforts to improve this number are still going on.

3.5 Star-guider

In order to monitor the tracking system online, a sensitive CCD-camera (0.0003 lx) of type Watec WAT902H has been installed in the center of the mirror dish. Is has a $4.6° \times 4.6°$ field-of-view and image the sky in the telescope pointing direction as well as part of the PMT camera. It delivers 25 frames per second which are getting integrated over 5 seconds to achieve a better signal-to-noise ratio [192]. Six reference points (red LEDs) on the camera frame indicate the position of camera while individual stars get recognized by a dedicated analysis software and compared to starfield catalogs. With this information, the real pointing position of the telescope can be retrieved.

3.6 Reflector

Reflectors of Cherenkov telescopes follow either a ***Davies-Cotton*** [193] or a ***parabolic*** layout. In the first case, all reflector facets have the same focal length $\boldsymbol{f}$, which in turn is the same of the telescope as a whole. The facets are arranged on a sphere of radius $\boldsymbol{f}$. In the parabolic layout, the ***spherical mirror facets*** are arranged on a ***paraboloid*** $z = r^2/(4f)$, and the focal length of the mirrors varies with the distance from the optical axis. Assuming small and perfect mirror facets, both approaches provide a more or less point-like focus for light rays parallel to the optical axis. While the parabolic layout suffers from slightly larger ***aberration***s than the Davies-Cotton one (increasing linearly with the angle to the optical axis), the first

one is ***isochronous***, i.e. a plane incident wavefront results in practically no photons arrival time spread in the camera.

The MAGIC Telescope has a parabolic reflector [194] of a diameter of 17 m, tessellated in 956 square mirror elements of 49.5×49.5 cm size, each of spherical shape. The mirrors are made of 5 mm thick AlMgSi1.0 alloy plates glued to an aluminum honeycomb inside a thin Al-box, with front plates coated with a transparent protective quartz layer. The mirrors were diamond milled in order to achieve the spherical reflecting surface, with curvature radii ranging from 34.1 m at the center to 36.6 m at the rim [195]. Figure 40 shows the reflectivity of the MAGIC mirros. The relative reflectivity never drops below 80% in the wavelength range from 280–650 nm and the average reflectivity lies around 85%.

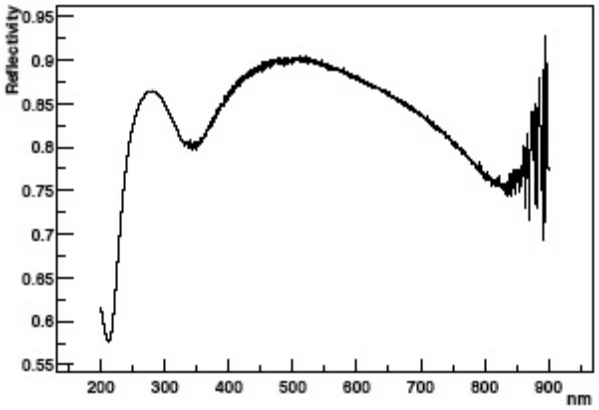

Figure 40: Reflectivity of the MAGIC mirrors. Figure from [194].

Three or four mirrors are grouped onto one ***panel***. The mirror panels are staggered yielding an overall isochronousy of about 0.8 ns. Each panel has an integrated print circuit board heating system. In order to compensate for distortions of the mirror panel caused by gravity at different tracking positions of the telescope, an active mirror control (***AMC***) has been implemented [196], consisting of three mechanical actuators (stepping motors) per panel, which re-position every mirror panel whenever an optical adjustment is desired. These motors are controlled by micro-controllers, driven by a central AMC computer via ***RS-485*** communication. The minimum displacement is 10 µm which corresponds to a transverse focal displacement in the camera plane of about 1.6 mm [196]. The alignment of the mirrors is performed with an artificial light source at a distance of 980 m (the ***Roque lamp***), with a displaced camera to match the focal length for this procedure[24]. In the center of each mirror panel, a red laser (685 nm) points towards the camera. The position of the laser spot of each mirror on the camera is recorded as a result of the alignment procedure with the Roque lamp. With the recorded individual laser spot positions

[24]In the spring of 2005, a sensitive ***CCD***-camera was installed on the telescope watching the MAGIC camera in order to allow mirror alignments with bright stars.

as a reference, the mirrors can be re-aligned in a couple of minutes. Usually, the mirrors are re-aligned before starting to track a new source. The full alignment needs about 220 s [196], however the step motor positions are filled into a database after every alignment. At the occurrence of a ***GRB***, the mirrors get adjusted directly from the database information, taking only a couple of seconds for the adjustment.

The reflector is usually focused to 10 km because this corresponds to the typical height of the shower maximum for 100 GeV gamma ray induced showers at low zenith angle observations (see figure 28 and eq. 18).

From geometrical arguments follows that a mirror dish of diameter D "sees" the shower until a maximum height of $H > (d_\perp - D/2)/\tan(\theta_c)$, where $d_\perp$ is the maximum possible impact parameter $d_\perp \approx 65\ m$. Even in the "worst case" – a shower occurring at the maximum impact parameter – the shower is imaged up to a height of $H \approx 3.3$ km from the telescope. This number corresponds to about 14 electromagnetic radiation lengths for a vertically incident gamma ray. From figure 28 follows that showers below 100 GeV are practically always fully contained in the camera image. Until the highest imaged gamma ray energies of 20 TeV, at least the shower maximum is always fully contained.

The MAGIC reflector had a point spread function (***PSF***) of about 0.08° ***FWHM*** in 2005, corresponding to about 2.4 cm [190].

3.7 Camera

The MAGIC camera serves to capture the Cherenkov light images with the help of photomultiplier tubes (***PMT***s), amplify them and transmit them to the control house by optical fibers.

Gamma ray induced showers of 30–200 GeV energy have their shower maximum at an altitude of about 8–11 km (6–8 radiation lengths), far away from the telescope. In this case, the camera will record a rather concentrated image in its inner part, with the trigger area restricted to a small disk around the camera center. In order to distinguish these images from those triggered by hadronic showers, a fine pixelization is needed in this part of the camera.

Larger showers above 200 GeV have their shower maximum at about 10 km – much closer to the ground – and images tend to extend to the outer parts of the camera. As the photon statistics is much higher in this case, requirements for the pixel sizes are not so strict there. For these reasons, the MAGIC camera was built with two pixel sizes: An inner hexagonal area composed of 397 ***inner pixels*** of type ET9116 with 1″ diameter and 0.1° ***FOV***, surrounded by an area of 180 ***outer pixels*** of type ET9117 with 1.5″ diameter and 0.2° ***FOV***. These PMTs provide signals with rise times of about 700 ps and less

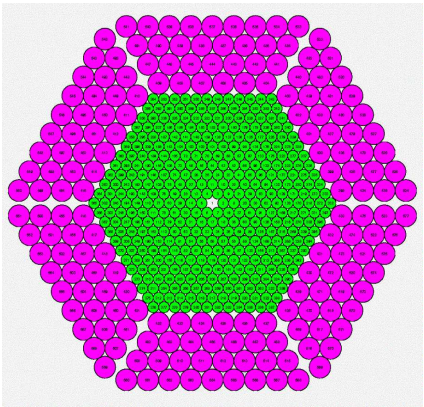

Figure 41: Sketch of MAGIC camera

than 1–1.2 ns ***FWHM*** pulse widths [197]. They have a hemispherical bialcali photocathode and 6 dynodes out of which the first is stabilized by a Zener diode to a fixed value of 350 V with respect to the photocathode. Figure 42 shows the after-pulse probability measured as function of different first dynode voltages. One can see that up to 350 V, the probability is less than 0.002 for a threshold of 10 photo-electrons. After-pulses occur with a time delay of 350–400 ns[25] [197]. Dynodes 2-4 are regulated with classical voltage divider resistances, while dynodes 5 and 6 are fixed to −375 V and −175 V with respect to the anode by an ***active load***. The last has been introduced to avoid non-linearities of the signal amplification at high currents. Two active loads for each dynode supply one half of the entire camera, each. Every couple of months, the camera gets ***flat-fielded***: The total voltage drop in the photomultipliers get adjusted such that the response to a uniform pulsed light source is the same. Inner pixels are then usually run at 1100–1300 V voltage drop from cathode to anode, outer pixels at 950–1050 V. These high voltages and the anode currents are monitored at a rate of 10 Hz using 12 bit ***ADC***s, multiplexed in groups of 96. The gain of the photomultiplier lies around 20 000 for the inner pixels and around 10 000 for the outer pixels.

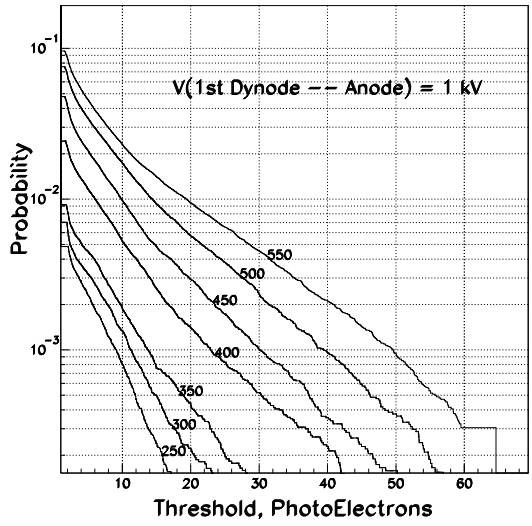

*Figure 42: Probability to observe after-pulses caused by a single photo-electron as function of a preset threshold for the ET9116A. The numbers at the plotted lines indicate the voltage between photocathode and first dynode. The MAGIC camera runs the **PMT**s with 350 V. Figure from [197].*

Each PMT is connected to an AC-coupled ultra-fast low-noise trans-impedance preamplifier using RF low noise bipolar transistors (AT41533) [198] with a gain of about 400. The photocathode quantum efficiency is enhanced using a ***PTP***

[25] Primarily caused by ions traveling back to the photo cathode and hitting out electrons.

wavelength shifter in a mixture, invented by David Paneque [199, 200]. The applied mixture is called ***coating***.

Figure 43 (left) shows a profile of the different quantum efficiency spectra obtained from the coated MAGIC PMTs. A quantum efficiency of about 30 % is reached at the maximum [201], with a spread of about 10 % from pixel to pixel. On the right side of figure 43, the spatial response uniformity after coating is shown. It was measured scanning the coated photomultiplier with respect to the photon incidence angle on the photocathode. At the highest incidence angle possible with the MAGIC reflector, $theta_{max} = 27°$, losses of maximal 20% with respect to vertical incidence can occur.

Photo-electrons are not relativistic, though they can possess a seizable tranverse momentum with respect to the direction in which they get accelerated and hence miss the first dynode. The probability to capture the electron is called the ***collection efficiency*** which is wavelength-dependent and differs according to the light incidence angle. Its absolute value has never been measured to better than 5% so far for any Cherenkov telescope and causes currently the main systematic uncertainty in the absolute energy scale determination [202]. For this work, an average collection efficiency of 0.9±0.05 was assumed for an incident Cherenkov light spectrum.

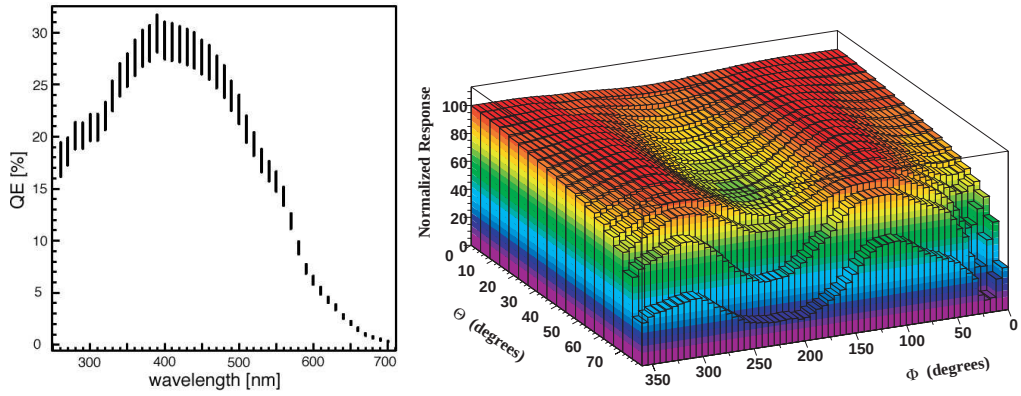

*Figure 43: Left: profile of the different quantum efficiency spectra of the MAGIC **PMT**s. The spread is about 10% at the maximum. Right: spatial uniformity of a coated ET9116A **PMT**: θ corresponds to the photon incidence angle with respect to vertical incidence, ϕ is the azimuth angle. The PMTs were illuminated with a blue LED peaking at 470 nm. In the MAGIC camera, incidence angles of only up to 27° can occur. Figures from [200].*

The dynode system of the PMTs is surrounded by a diamagnetic μ-metal cylinder in order to protect the amplified electrons from the magnetic field of the Earth. The overall time response of the coated PMT is < 1.3 ns, including the decay time of the wavelength shifter [197, 199].

The photomultipliers were selected by their quantum efficiencies in the blue part

of the spectrum in order to maximize their response to gamma ray showers of small energies. Figures 44 and 45 show the distribution of ***corning blue (CB)*** and

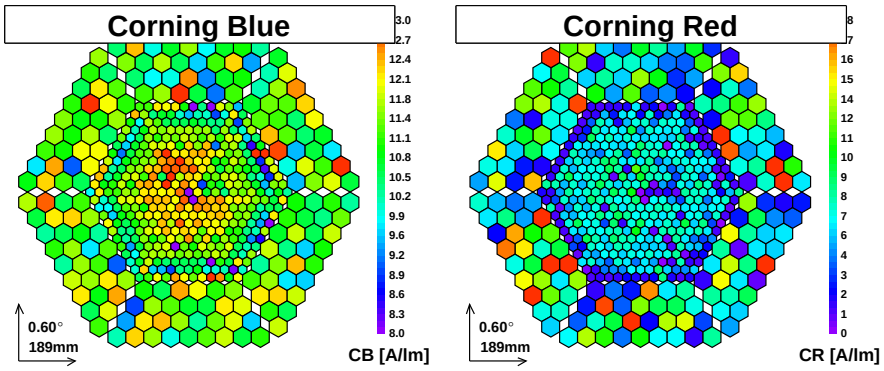

*Figure 44: Values of corning blue and corning red of the MAGIC **PMT**s*

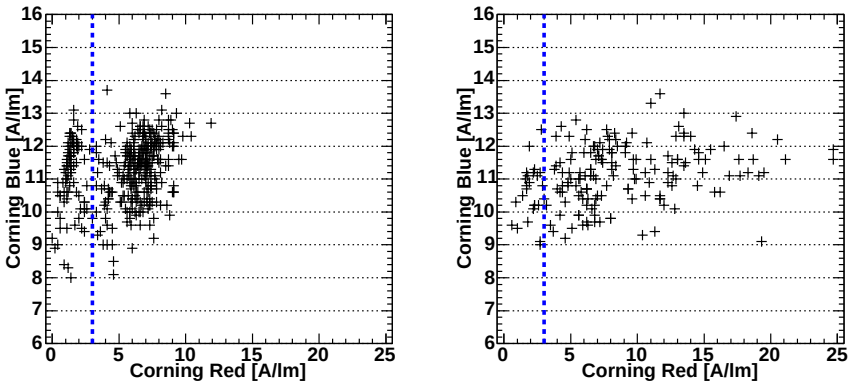

Figure 45: Values of corning blue vs. corning red of the MAGIC inner pixels (left) and outer pixels (right).

corning red (CR) of the photomultipliers used in the MAGIC camera. One can distinguish the preference of high corning blue values towards the camera center and further ***two classes of PMTs*** according to their ***corning red (CR)*** values: The outmost ring of the inner camera and some photomultipliers further inside have very low quantum efficiencies in the red part of the visible spectrum: These photomultipliers correspond to a different production cycle and have slightly different properties [203] [26].

[26] All spare PMTs belong to the second class of low ***corning red (CR)*** values. As the photomultipliers have to be replaced with time, the camera becomes more and more blind to the red end of the spectrum.

Temperature and humidity are monitored at three points in the camera and can be controlled using a water-based cooling system. Until March 2005, the camera was only cooled before and during operation, leading to a temperature increase during the first hour of observation. Afterwards, the camera was heated to the desired working temperature before operation and stabilized there using a feedback system.

The MAGIC camera is equipped with non-imaging ***light concentrators*** in front of the PMTs. They reduce dead areas between the round photomultiplier cathodes and limit the solid angle viewed by a PMT reducing noise coming from stray light from the ground. The light concentrators were designed by Daniel Ferenc [204] and made from a plastic material with aluminized Mylar foil of about 85% reflectivity. They follow a hexagonal approximation to the Winston cone design [205]. The light guides used for outer pixels cover exactly four times the area of those used for the inner pixels.

Figure 46 shows the normalized photo-electron spectra including ***coating*** and ***light guides*** for the telescope observation angles: 20° and 60°. The average quantum efficiency amounts to 0.208 for the case of 20° zenith angle and to 0.198 for the case of 60° zenith angle.

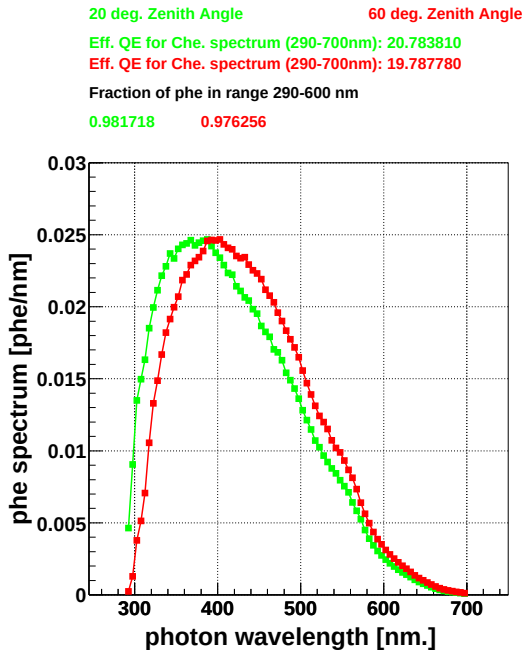

Figure 46: Normalized photo-electron spectrum in the coated MAGIC PMT with light guides for gamma ray induced air showers. Green points: 20°, red points: 60° zenith angle. Figure provided by Jürgen Gebauer.

Ideal Winston cones show a sharp angular cutoff at $\sin(\theta_{max}) = D_{out}/D_{in}$ if D_{out} is the entrance diameter and D_{in} the exit diameter. Figure 47 shows the behavior of the actual light guides: There is a cutoff at $\theta_{max} = 27°$, although not as sharp as the one that would have been obtained with perfect Winston cones. There is also an

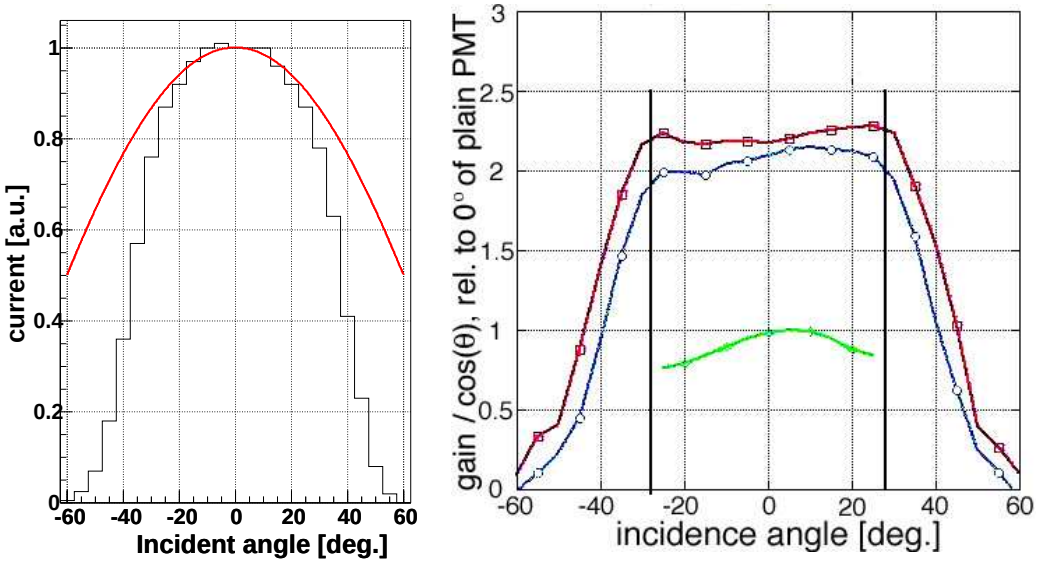

Figure 47: Left: Relative angular response of the MAGIC PMT, equipped with light guides (normalized to 0° incidence angle). The plain red line shows a $\cos(\theta)$ curve corresponding to the available solid angle. Right: Relative gain of the coated MAGIC PMT with aluminized Mylar light guide (middle curve) with respect to a plain PMT, operated without light guide and coating and illuminated through a 22 mm diaphragm (lowest curve) at 0° incidence angle. All curves were corrected for the $\cos(\theta)$-dependent solid angle reduction. Also displayed is a measurement using a new foil from 3M (top curve) which was not yet available when the telescope was built. All three measurements were performed with a blue LED. The indicated limit of angular acceptance is the maximum incidence angle from the MAGIC mirrors.

asymmetric response with respect to positive or negative illumination angles which is due to the position of the first dynode. It becomes clear that the light guides "smear out" the non-uniform behaviour leaving an asymmetry of less than 4 %.

In front of the light guides, the MAGIC camera is protected by a ***plexiglass*** with uniform transmission over all wavelengths down to 300 nm where it drops down (see figure 48).

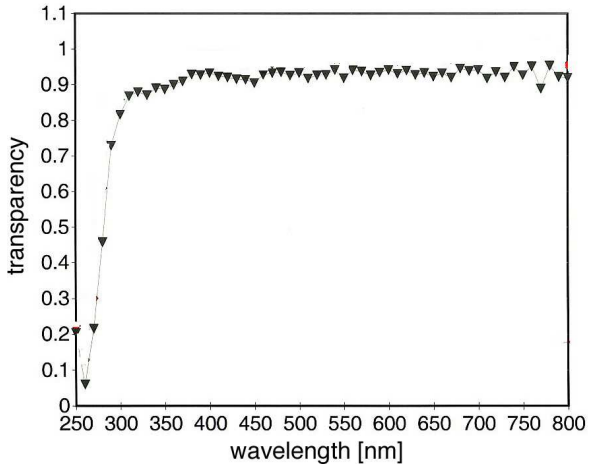

Figure 48: Transmission of the plexiglass in front of the light guides. Figure provided by Eckart Lorenz.

3.8 Signal Transmission and Processing Chain

The pre-amplified PMT signals are transmitted over 162 m long ***optical fibers*** [27] to the central data acquisition building (the ***control house***) using fast current driver amplifiers coupled to vertical cavity laser diodes (***VCSEL***s) [207] [28]. The VCSELs (Honeywell multi-mode HFE4080-321) are pre-biased at around 5 mA and emit at 850 nm wavelength [200]. They are grouped into ***optical transmitter boards***. Figure 49 shows a photograph of such an optical transmitter board. The connection between the VCSEL and the optical fiber is facilitated with a spherical lens which focuses the light into the 50 µm core of the optical fiber. This optical signal transmission system is able to transmit the short PMT signals with practically no pulse form distortion [200].

Unfortunately, the optical transmitters are affected by non-negligible noise and gain drifts. The VCSELs were selected [200] according to their noise behaviour upon which the following choices were made: About 7% of the VCSELs was rejected at all, while the remaining ones were divided into a group of 397 with the lowest noise

[27] The technique to transmit photomultiplier signals over large distances via optical fibers was first developed by the AMANDA collaboration [206].

[28] Commercialized in 1996 for digital communications applications, MAGIC is the first instrument to use these devices in analog mode.

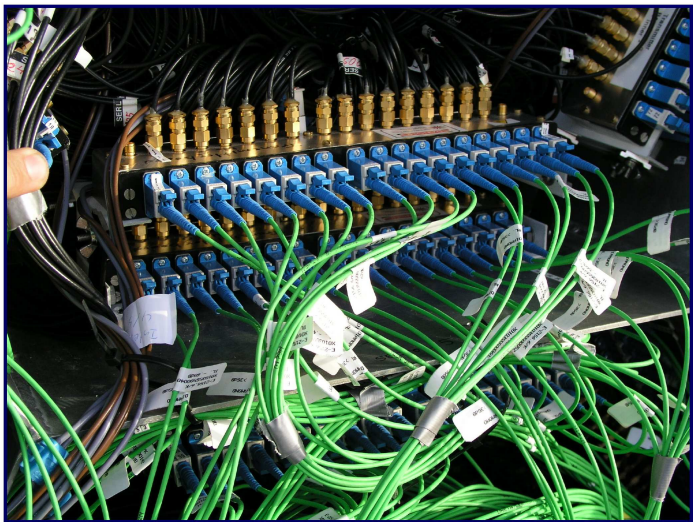

*Figure 49: Photograph of two transmitter boards in the camera of MAGIC: The black coaxial cables with gold-plated **SMA** connectors transport the signal from the PMT bases to the optical transmitter boards (blue). The optical signals are then transported through optical fibers (green). Photo from [200].*

characteristics, used for the inner pixels, and a group of more than 200, used for the outer pixels or as spares. Figure 50 (left) shows the relative standard deviation of the output pulse obtained after transmitting a series of stable input pulses through the optical transmission chain in a long time test. The ***VCSEL***s used for the inner pixels fluctuate on average by only 2% while the ones used for the outer pixels do so by up to 8% and more. Because of the stochastic character of sudden noisy periods of the transmission, a second estimator was introduced: The maximum of a set of relative standard deviations, calculated in periods of five minutes, called the ***maximum relative noise***. Figure 50 (right) shows the behaviour of the ***VCSEL***s with respect to this parameter: The ones used for the inner pixels can fluctuate up to about 8% in certain five-minutes periods while the ones selected for the outer pixels do so by up to 12%.

Additionally, gain drifts were observed in the transmission behaviour of the ***VCSEL***s. Figure 51 (left) shows the average gain behaviour of a test channel during a long-time test. A relative sudden change in gain of up to 30% can occur. Ref. [200] estimates however, that the relative RMS can be reduced to an overall $< 3\,\%$ above signals from 10 photoelectrons for the inner pixels and $< 5\,\%$ for the outer pixels if the gains get re-calibrated every five minutes (figures 51 right and figure 52).

At the other end of the optical fiber, the signals are received using a fast GaAs ***PIN photodiode*** (Mitel 1A446). The signal is further split into two branches: one ***trigger line*** and a ***signal line***. The first goes to a discriminator and further to the trigger system, while the last gets ***shaped to about 6.3 ns FWHM*** and digitized

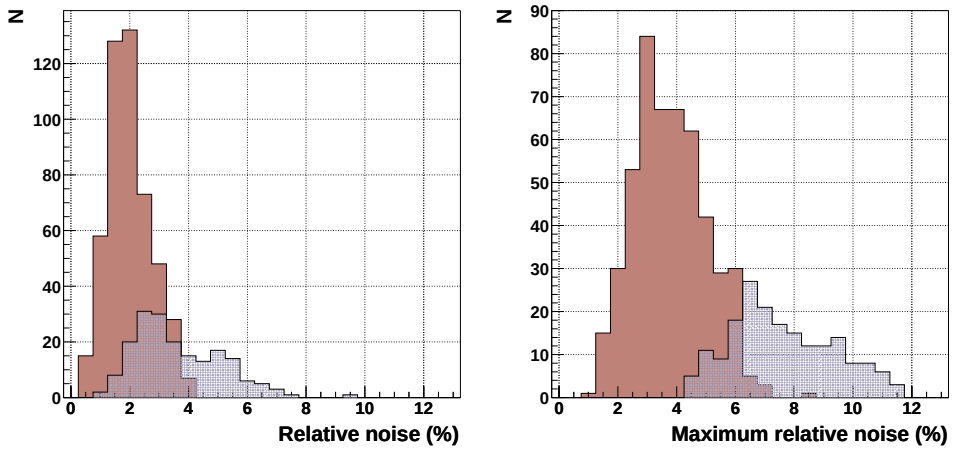

Figure 50: Noise in the optical transmitter boards after selection. Left: Relative noise, right: maximum relative noise (see text for explanation). Brown histogram: inner pixels, blue histogram: outer pixels. Figures from [200].

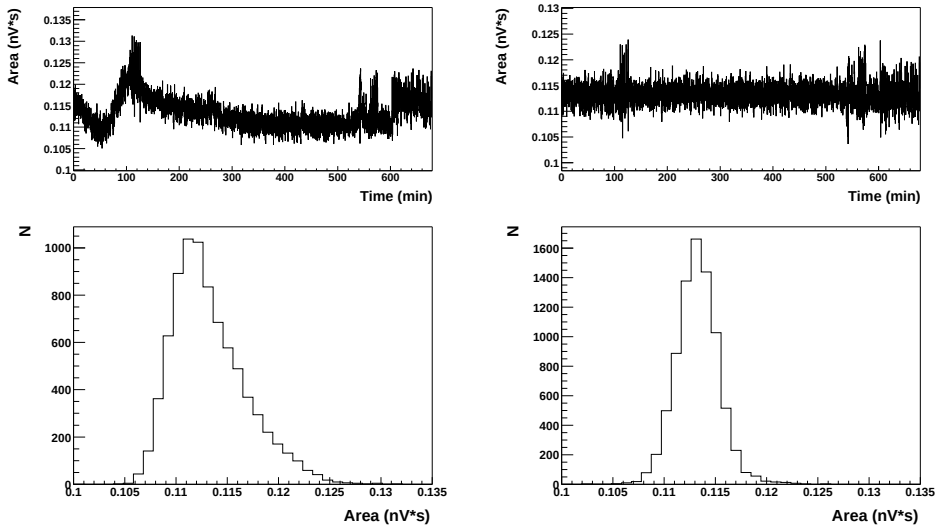

Figure 51: Top left: Long-term behaviour of the output pulse area vs. time obtained from a stable input pulse and transmitted via the optical transmission chain. Bottom left: Projected distribution of the output pulse areas. Right: Same as left, with re-calibration every five minutes (see text). Figures from [200].

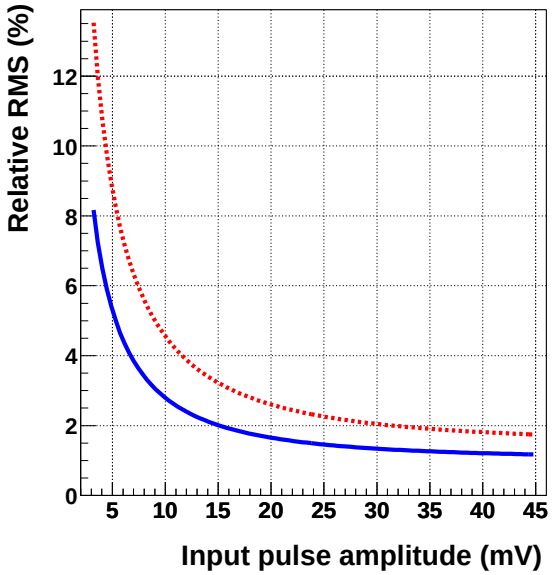

*Figure 52: Parameterization of the relative RMS vs. amplitude of the input pulse after re-calibration. 1 mV input pulse corresponds to the signal produced by about 1 photoelectron after amplification by the **PMT** and the preamplifier. Blue: inner pixel, red: outer pixels. Figure from [200].*

by the FADC system. Because only 8-bit FADCs are used, the signal is further split into a ***high-gain*** part (amplified by an additional factor 10) and a ***low-gain*** part (delayed by a passive 55 ns delay line). If the signal exceeds a preset threshold, corresponding to signal height obtained from about 50 photoelectrons, both lines are combined using a fast ***GaAs***-switch and digitized. In the other case, only the high-gain line is processed.

3.9 Trigger

The triggering of a Cherenkov telescope must make use of the extremely short duration of the Cherenkov light signals from air showers which are typically of a few nanoseconds. A typical trigger condition requires that a minimum number (e.g. four) neighboring pixels exhibit a signal larger than a given threshold of a few photoelectrons within a short time window.

The trigger signals transmitted from the optical receiver board run into a ***discriminator*** which issues a digital signal (5.5 ns FWHM) whenever the pulse exceeds the equivalent of about 10 (for extra-galactic sources) or 12 (for galactic sources) photoelectrons. The discriminator thresholds are set by an 8-bit ***DAC*** which is controlled by a ***PC***. The thresholds can be modified during telescope operation. The individual trigger rates are monitored by 100 MHz scalers and used to dynamically adapt the discriminator thresholds further if the rate exceeds a certain level. With

this individual pixel rate control (***IPR***), stars brighter than magnitude 4 in the field of view of the inner camera are effectively taken out of the trigger. The digital signals have individual computer-adjustable time delays to match the intrinsic time-offsets between the different readout channels from the camera. The discriminator level is sometimes referred to as ***trigger level 0***.

Further, two trigger levels are applied:

Level-1 Trigger

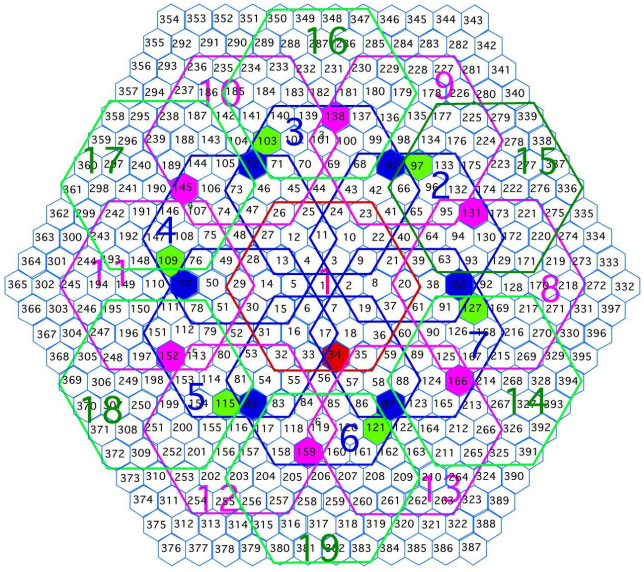

Figure 53: The 19 active trigger regions in the inner camera.

The level-1 trigger (***L1T***) applies a simple N-next-neighbor logic during a few nanoseconds in one of the 19 hexagonal overlapping regions of 36 pixels (***trigger cells***). The multiplicity of the cluster of next neighbors can be set by a ***PC*** during telescope operation. Usually, a four-fold coincidence is required. The L1T is active on 325 inner pixels (see figure 53).

Level-2 Trigger

The level-2 trigger (***L2T***) is widely programmable and can perform a rough ***topological analysis*** of the event images [208]. The L2T decision is coded in an 8-bit word which is sent to the FADC system for event acquisition. The 8-bit word reflects the combination of trigger decisions which had been programmed. With this feature, it is possible to select different ***event types*** (e.g. calibration, pedestal, low-energy, etc.) already at the trigger level. It is also possible to make topological cuts at this stage, a feature which has not yet been used for the data analyzed in this thesis. The L2T contains also a ***prescaler*** board allowing to prescale each of

the trigger lines individually. The L2T can handle a trigger rate of up to 1 MHz. In cases of high-frequency triggers of interest (e.g. in the case of a GRB), a second ***high-frequency*** trigger line can be used to send topological event information to the digital modules (DMs) of the FADC system.

The trigger rate is typically dominated by (hadronic air-shower) background events, additional to single muons passing close to the telescope. It is usually 250 Hz for extragalactic sources and 200 Hz for galactic sources (using the increased thresholds) [190].

3.10 Data Acquisition

Figure 54 gives an overall sketch of the data stream of the MAGIC telescope.

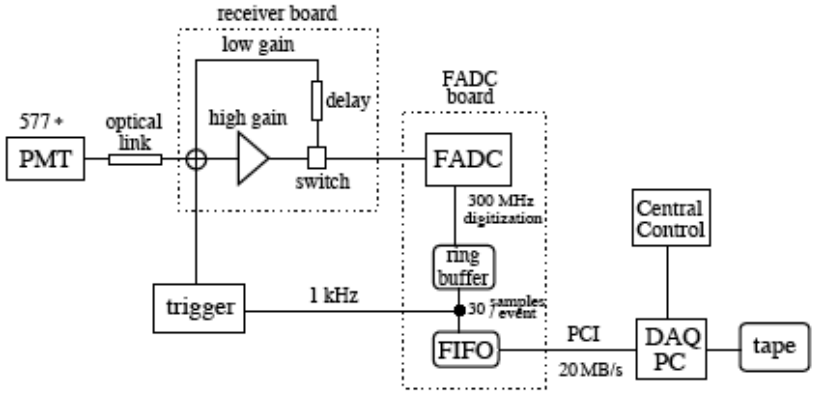

Figure 54: Sketch of the data stream. Figure from [209].

Because Cherenkov light pulses are so short (1–2 ns), a fast pulse digitization is required. To do so, the pulses are stretched to about 6 ns FWHM and then recorded by 300 MSamples/s Flash ADCs (***FADC***s). This procedure ensures that usual Cherenkov light pulses are always sampled at four or more points.

The data acquisition (***DAQ***) of MAGIC consists of 18 crates containing each 4 electronic boards equipped each with 8 FADC chips. The FADCs were designed and produced by Ralf Stiehler [210]. Each of the 8-bit FADCs has a 500 MHz bandwidth digitizing at a speed of 300 MSamples/s using fast comparators [209]. The digitized signals get continuously stored into a 32 kB ring buffer. Whenever a trigger signal arrives, ***30 FADC samples*** are written to a 512 kB long ***FiFo*** buffer (at a maximum rate of 80 MB/s). The readout of the ring buffer introduces a dead time of about 25 µs [190, 211]. The data is further saved to a RAID0 disk system at a rate of up to 20 MB/s controlled by an ***FGPA*** chip on a ***PCI*** card [29] in a dual processor PC running on a multi-threaded C++ readout program. The data taken during one night can amount to 800 GB. During day-time, the data is written to

[29] produced by the company "MicroEnable".

tape and, since May 2005, also analyzed at La Palma. The readout has an overall dynamic range of more than 1300 and was shown to be linear in a dynamic range of >800 [209]. It has a dead time of 25 µs, additionally 80 µs are artificially generated by the prescaler of the ***L2T*** [211].

3.11 The GRB Alert System

The GRB Alert System (called ***gspot***) was written by Nicola Galante [212]. It performs a full-time survey of alerts provided by the GRB Coordinates Network (***GCN***) [213] through a ***TCP/IP*** connection to a computer at the Goddard Space Flight Center (***GSFC***). These alerts include all real-time GRB alarms provided by the GRB-satellites (***SWIFT***, ***Integral*** and ***HETE-2***) and include the ***UTC***, the GRB ***coordinates***, ***intensity*** and additional information depending on the kind of burst and satellite.

In case of an alert, ***gspot*** enters an ***alarm state***. It remains there as long as the following requirements are fulfilled:

- The Sun has to have a zenith angle larger than 108° (below the astronomical horizon).
- The GRB zenith angle has to be smaller than 65°. In case of moon shine, the maximal zenith angle is reduced to 60°.
- The angular distance from the GRB to the Moon has to be at least 30°.

Moreover, each alert sends out an e-mail to an internal mailing list and updates the ***GRB Alert System web page***: `http://www.magic.iac.es/site/grbm/`.

Gspot consists of a core program written in *c* which continuously monitors the GCN and communicates its status to the ***Central Control*** interface (see below). It runs in stand-alone mode and is fully automatic.

3.12 Software Packages

The software packages used (and partly developed) for this work, can be divided into two parts:

Telescope Control Software:

The control system of the telescope is split up into functional units which correspond to the independent ***subsystems*** of the telescope [214]. Two control software packages, written in ***Labview 6i***, steer and coordinate the individual subsystems and provide the common user interfaces: The ***Central Control*** (called "Arehucas") and the ***Camera Control*** (called "La Guagua"). Further subsystems have individual steering software (usually written in C/C++), interfaced by the ***Central Control*** via the ***TCP/IP*** protocol: The ***DAQ***, the ***Camera***, the ***HV Regulators*** in the camera, the camera ***Cooling System***, the camera ***Lid***, the ***calibration system***,

the ***Drive System***, the ***L2T***, the ***AMC***, the ***Weather Station*** and ***gspot***. The central control and the camera control store control information to disk at a rate of about 22 kB/s.

Monte Carlo (*MC*) Simulation Software:

For the simulation of air showers, the ***CORSIKA*** 6.019 package [215–217] was taken using ***VENUS*** [218] for hadronic interactions and the ***US*** standard atmosphere. All ***Cherenkov photons*** around the telescope location are stored in intermediate files. Maximum ***impact parameters*** of 300 m for gamma ray showers and 400 m for hadronic showers were used. The reflector simulation reads these files, simulates the Cherenkov ***light absorption and scattering*** in the atmosphere and performs the reflection on the mirror dish. Location and arrival times (plus additional information) of the photons in the camera plane are again stored in an intermediate file. In a last step, the camera simulation program simulates the ***photomultiplier response***, ***signal transmission***, the ***trigger*** and the ***FADC*** digitization. Each photon gets simulated individually and the electronic signals overlaid and noise added. It is possible to add additional noise from the night sky background (***NSB***) or from ***stars*** in the FOV of the camera in a subsequent step. An overview of the performance of the MC simulation software can be found in [219].

Analysis Software:

The MAGIC Analysis and Reconstruction Software (***MARS***) [220] is a ***ROOT***-based [221] collection of C^{++} classes and macros. It reads ***MC*** and ***data*** files, performs a ***signal extraction*** and subsequent ***calibration***, calculates ***image parameters*** and performs a ***flux*** and ***energy determination***. The signal extraction and calibration steps were mainly written by the author and will be explained in more detail in the following chapters.

4 The Calibration System

The MAGIC calibration system was first designed by ***Thomas Schweizer*** in cooperation with Eckart Lorenz, Manel Martínez, Alexander Ostankov and David Paneque [222].

The main components of the MAGIC calibration system are: a ***pulser box*** which houses ***pulsed LED***s providing ultra-fast light pulses in three different colors with intensities variable by a factor greater than 300 in order to calibrate the whole dynamic range of the camera and the readout chain. The absolute light flux, in turn, is calibrated using additional devices: three ***blinded pixel***s in the MAGIC camera and a calibrated ***PIN diode***, situated between the camera and the pulser box. At the same time, a ***continuous light source*** in four different colors and variable intensities is available to simulate star and moon light. The calibration system provides, in addition, a sophisticated ***trigger system*** which allows to pulse the LEDs at almost any frequency smaller than 4.5 kHz and to fire trains of pulses at a second frequency.

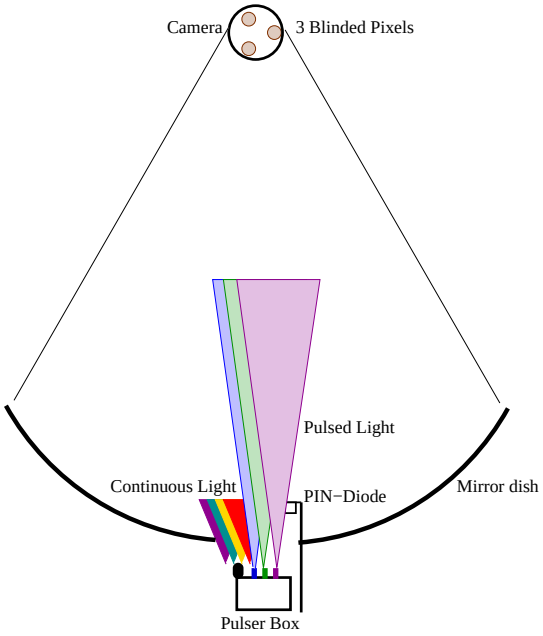

Figure 55: Components of the calibration system

In this work, an upgraded and finalized version of the calibration system is presented which is currently installed at the telescope and has been working on-site for the last one and a half years. Some parts of the hardware were taken over directly from the preparatory work of Thomas Schweizer [222] (like the pulser board), others needed to be finalized (like the periphery of the pulser board), again others were completely revised and modified in essential parts (like the PIN diode and the blinded pixels) and finally, some pieces had to be built up from scratch by the author (like the trigger system). The hardware of the calibration system was supervised by ***Manel Martínez*** and ***Eckart Lorenz***, and parts of the CAN-bus communication and the trigger system were built in cooperation with ***Javi Lopez*** and ***Jose Flix***.

A detailed description of the calibration system hardware can also be found in [223].

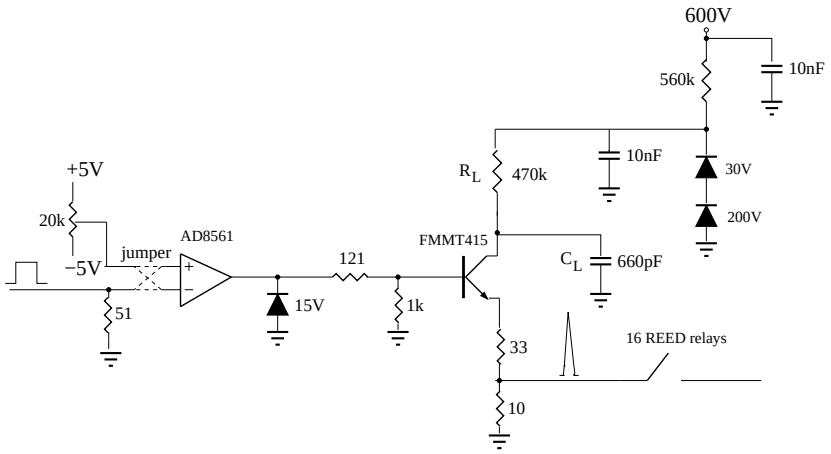

*Figure 56: Schematic of the circuit used to trigger the avalanche transistor circuit: A **TTL** signal (left) causes the comparator AD8561 to issue a digital signal which switches the avalanche transistor FMMT415 with collector voltage 230 V (Zener diodes). The capacitor C_L discharges creating a fast signal of about 1–2 ns with a peak current of tens of ampere. Part of the energy is lost to microwave radiation while this trigger signal travels to the 16 pulsed LEDs slots. The LEDs fire depending on whether the corresponding relay is open or closed.*

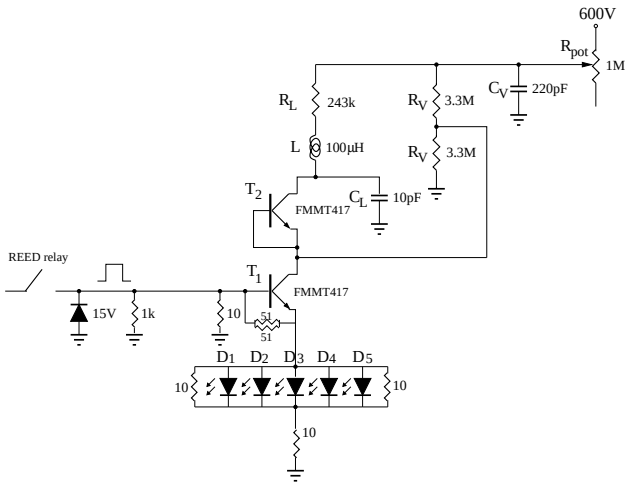

Figure 57: Schematic of the avalanche transistor circuit (one slot): a fast signal (left) switches the avalanche transistor T_1 with collector voltage 300 V (voltage divider R_V). The switch causes T_2 to break through and discharge capacitor C_L. The discharge current flows through the load resistance R_L and through the LEDs D_1 to D_5 (in some slots, only 1,2 or 4 LEDs are placed). The response time of transistor T_2 depends on the collector voltage and can be adjusted with R_{pot}.

4.1 Pulsed LEDs

The heart of the calibration system consists of fast and ultra-bright blue and green (NISHIA single quantum well (SQW) InGaN/GaN ***LED***s [224] [30]) and UV (NISHIA, NSHU590) ***pulsed LED***s which are driven by an electronic circuit using ***avalanche transistors*** [225] of type FMMT415 and FMMT417, manufactured by ZETEX. These transistors are run in ***avalanche mode***, i.e. the collector-emitter voltage is so high that a current flowing through the base causes a (fast) break-down of the collector and the transistor becomes almost instantaneously conducting. An ordinary transistor is considered broken at this stage, however the avalanche transistor recovers completely and can be used again under the same conditions [31]. This technique allows thus very fast trigger edges at high currents, in our case it provides a peak current of about 6 A traversing the LEDs during 2–3 ns (see schematic figures 56 and 57 and a picture of the electronic board, figure 59).

Figure 58 shows the electrical pulse traversing the LEDs, probed with 1 MΩ, and the optical signal registered by a photo-multiplier. One can see the 2 ns FWHM electrical pulse width. The FWHM of the optical pulse amounts to 4–5 ns. This number is smaller than the shaping time of the optical receivers circuit (6.3 ns), however a small secondary pulse at about 8 ns from the pulse maximum is sometimes present.

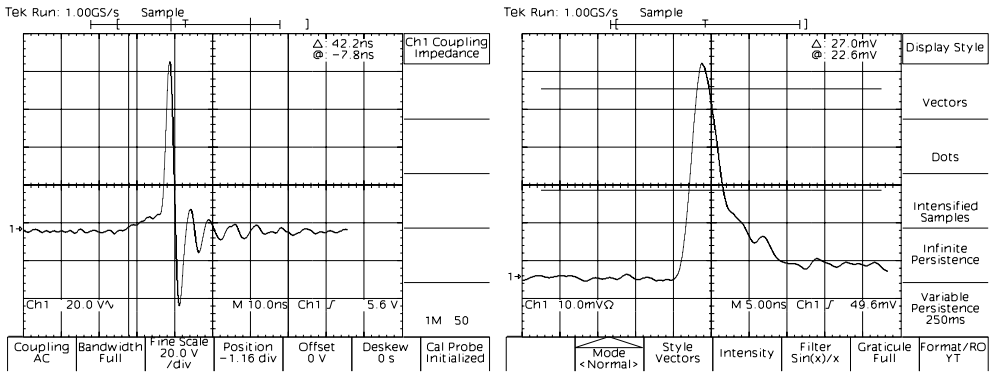

Figure 58: Probes of the pulses traversing one slot with 5 UV LEDs (left) and the slightly amplified signal at the anode of an inner pixel (right). Note that the vertical scale is 20 V per box in the left display. At these frequencies, the oscilloscope probe forms an inductance itself and influences the registered signal. Especially the large overshoot observed in the left picture is visible because of the finite resistance of the probe. The horizontal scale is 10 ns per box in the left shot while it is 5 ns per box in the right one.

The LEDs are placed in 16 ***slots*** which can switched on and off individually.

[30] Type NSPB300, "old" type, produced before 1999

[31] For a theoretical explanation of the avalanche transistor phenomenon, see [226].

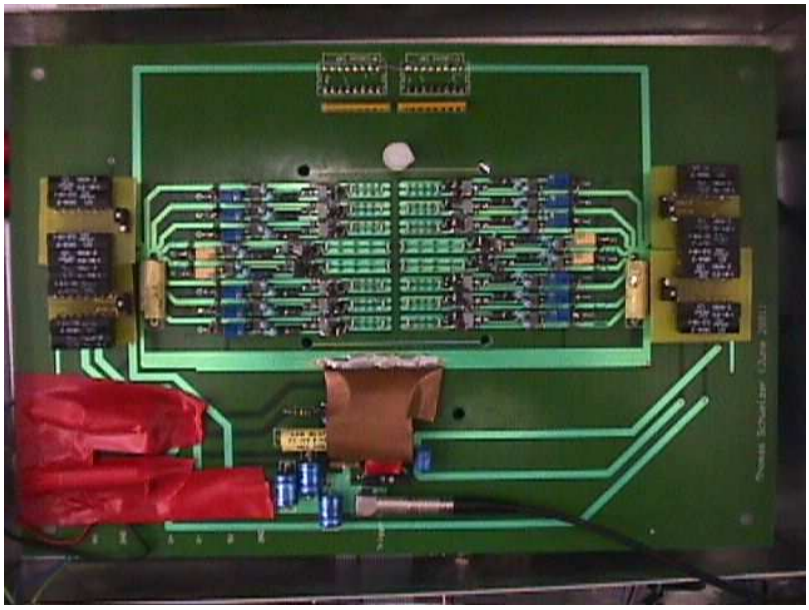

Figure 59: The pulser board from behind: one can distinguish the 16 slots, grouped in two side containing 8 each. The two central ones from each side drive the UV-LEDs with slightly higher currents than the rest, the remaining 12 ones are used for blue and green LEDs.

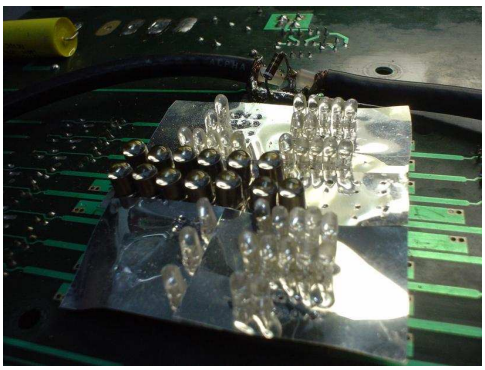

Figure 60: A picture of the pulsed LEDs set in place. Dismounted and not shown are the continuous light LEDs and the diffuser plate on top.

All LEDs situated in one same slot are driven in parallel while one slot can contain a maximum of 5 LEDs (see figure 60). One slot may contain LEDs of one of the three possible colors: UV (375 nm), blue (445 nm) or green (505 nm). In total, four slots contain green LEDs, four slots UV-LEDs and the remaining 7 slots blue LEDs (one slot is broken). The light intensity emitted in one slot depends on the number of LEDs in that slot. As the transistors are used in the avalanche mode, one slot yields always the same light intensity, once equipped with LEDs. Additionally, different slots can be switched simultaneously, and therefore the possible combinations of light intensities enlarged.

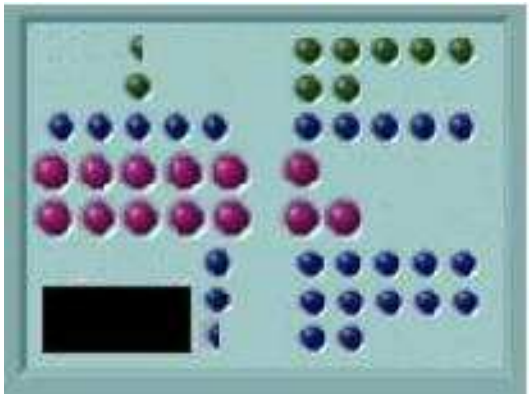

Figure 61: Configuration of the pulsed LEDs: 375 nm (UV), 445 nm (blue) and 505 nm (green). The two LEDs shown as halves depict slots with an additional small diffuser plate acting as an additional absorber. The black box symbolizes the continuous light LEDs.

The avalanche transistor circuit allows also to fine-tune the launch time of the light pulses in each individual slot, because the response time of the transistors depends slightly on the applied collector voltage which can be adjusted with a potentiometer (see schematic figure 57). In this way, the 16 slots were time-adjusted to better than 500 ps precision relatively to each other before installing the system at the telescope.

Table 1 gives a global overview of the most important characteristics of the pulser system, as currently used in the telescope: The mean peak wavelengths (see a more detailed treatment in the following section), minimum and maximum available signal strengths in the camera (given in mean number of photo-electrons per pulse per inner pixel) and information about the pulse form. Besides slightly different pulse widths, the blue and green LEDs show also small secondary pulses at about 7–10 ns. The corresponding implications for the signal extraction will be treated in section 5.7.

4.1.1 Spectra of the Pulsed LEDs

An important characteristic of the Nishia LEDs is the variable spectrum depending on temperature and applied forward current. Figure 63 shows the dependency of the peak wavelength vs. ambient temperature and figure 64 the peak wavelength vs. applied forward current, as provided by the manufacturer. One can see considerable shifts between 1 and 100 mA forward current, especially for the green LEDs. As the LEDs are driven with peak currents of about 6 A, when operated in pulsed mode, the light spectra are expected to show even stronger shifts toward shorter wavelengths and were therefore measured in a dedicate campaign at IFAE, in collaboration with

Light Pulser Characteristics					
color	peak wavelength [nm]	min. nr. phe's inner pixel	max. nr. phe's inner pixel	secondary pulses	FWHM Pulse [ns]
green	∼505	6	120	yes	3–4
blue	∼445	6	600	yes	3–4
UV	∼375	3	50	no	2–3

Table 1: The most characteristics of the light pulser system: Peak wavelength, intensity range and pulse forms.

Figure 62: The LED pulser box, seen from the direction of the camera.

Manel Errando.

We used a CVI-Laser monochromator of type CM110 with a grating of about 8 nm width [32], increased in steps of 4 nm. The grating had been calibrated with a red laser and later with various emission lines of a Neon lamp. A more detailed description of the setup can be found in the diploma thesis of Manel Errando [227]. In a first step, the spectrum was measured with LEDs operated with a continuous current of 20 mA applied to the LEDs. After passing the monochromator, the light was captured with a calibrated photo-diode of type S1337-1010DQ from Hamamatsu and read out with a Keithley picoampere-meter of type 6517A. Figure 67 shows the resulting spectra together with double-Gaussian fits. Similar to what is announced in the data sheets, the spectra are not purely Gaussian, but have instead large tails. Within the precision of the setup, the resulting peak wavelengths agree with the predictions from the manufacturer, except for the blue LED which was measured to an 8 nm smaller peak wavelength.

To test possible calibration errors of the monochromator, we tried therefore to reproduce the peak-wavelength vs. forward current dependency, shown in figure 65. A common global shift of 5 nm towards shorter wavelengths is visible for the blue and of ±10 nm for the green LEDs whereelse the UV spectra show shifts of 3–5 nm towards longer wavelengths. The reason for this discrepancy is not yet understood: unfortunately, the data sheet does not provide an estimate of the accuracy of the measurement, figure 64. Another possible explanation might be differences in the warm-up time of the LEDs (not provided by the manufacturer) which can cause shifts of up to 5 nm. To be conservative, we conclude that the above numbers reflect the systematic accuracy of our setup and will be included in later calculations.

In a second step, the LEDs were operated in pulsed mode, the light pulses trasmitted to the monochromator with the help of a UV-trasparent optical fiber (type ThorLabs, BFH22-910) and registered with a calibrated MAGIC PMT. The anode pulses were then amplified with the standard pre-amplifier, which is also used for the front-end amplification of the PMT signals in the camera, and further read out with a digital oscilloscope. The last was adjusted to measure the mean pulse amplitude and a mean pulse integral per wavelength slot. One can see in figure 68 that the obtained spectra peak at shorter wavelengths than if operated in continuous mode, just as expected. Moreover, the spectra appear much broader in pulsed mode. Both peak position and pulse width differ between the two pulse analysis modes of the oscilloscope. The reason for this difference is not yet understood. Since we could not be sure to reproduce exactly the same electrical pulse traversing the LEDs, compared to the one used in the calibration box at the telescope, we decided to include the difference as an additional systematic uncertainty of the peak wavelengths and widths.

Table 2 summarizes the main results of the spectrum measurements, including the global systematic uncertainties. Main results are: a stable peak wavelength for

[32] DK121260 ruled grating for green and blue pulses and DK241220 for the UV pulses, both 1200 grooves/mm.

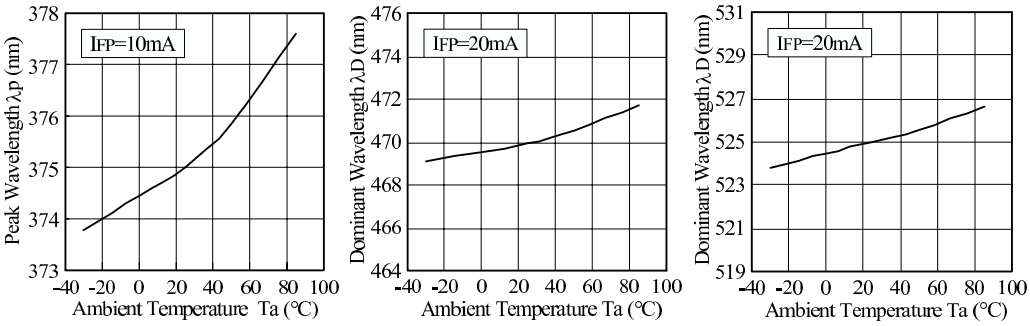

Figure 63: Dependency of the peak wavelength vs. temperature for the three pulsed LEDs, as provided by the manufacturer. Left: NSHU590 (UV), center: NSPB310A (blue), right: NSPG300A (green).

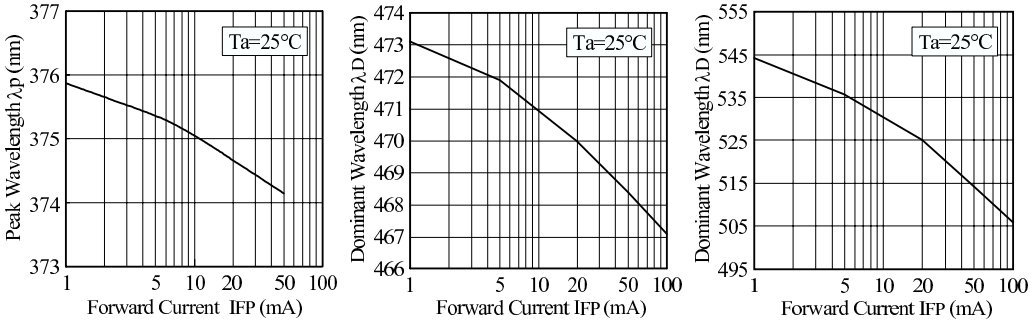

Figure 64: Dependency of the peak wavelength vs. continuous forward current for the three pulsed LEDs, as provided by the manufacturer. Left: NSHU590 (UV), center: NSPB310A (blue), right: NSPG300A (green).

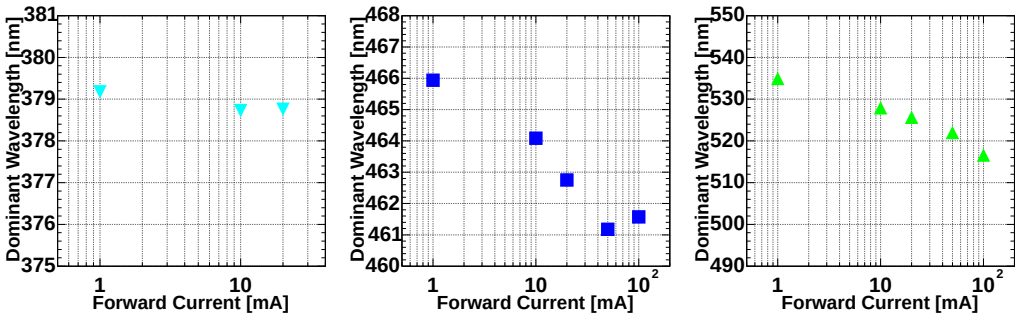

Figure 65: Dependency of the peak wavelength vs. continuous forward current for the pulsed LEDs, as measured at IFAE (at 20 °C): Left: NSHU590 (UV), center: NSPB310A (blue), right: NSPG300A (green).

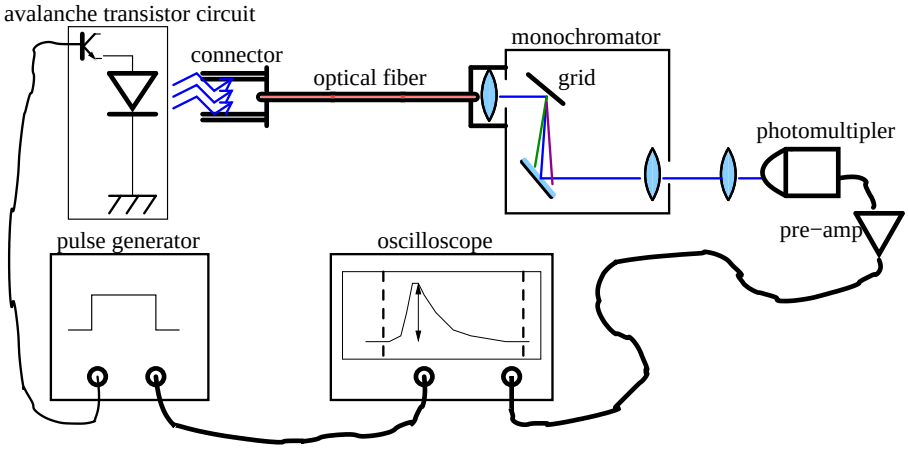

Figure 66: Sketch of the spectrum measurements setup

the UV LEDs, shifted peak wavelengths for blue and green LEDs and a general broadening of the spectra in pulsed mode. Moreover, the systematic uncertainties on both peak wavelength and FWHM could be evaluated.

LED color	Data Sheet peak w.l. λ_p [nm]	Data Sheet FWHM $\Delta\lambda$ [nm]	Continuous Mode peak w.l. λ_p [nm]	Continuous Mode FWHM $\Delta\lambda$ [nm]	Pulsed Mode peak w.l. λ_p [nm]	Pulsed Mode FWHM $\Delta\lambda$ [nm]
UV	375±3	12	378±4	16±3	375±4	32±5
Blue	470	26	462±7	27±2	445±7	35±4
Green	525	36	524±8	38±2	503±9	47±3

Table 2: Spectral characterization of the pulsed LEDs in continuous and pulsed mode. All values for the continuous mode apply to a forward current of 20 mA and 25 °C temperature. The values for the pulsed mode include the difference between pulse amplitude and integral readout (see text). The uncertainties are both statistical and systematic. (In some cases, the manufacturer did not provide uncertainty estimations.)

For all following considerations, the light spectra of the LEDs will be parameterized as

$$N_{\mathrm{ph}} \frac{dn_{\mathrm{ph}}}{d\lambda} \qquad \text{with :} \qquad \int_{-\infty}^{+\infty} \frac{dn_{\mathrm{ph}}}{d\lambda}\, d\lambda = 1 \ , \tag{26}$$

where N_{ph} is the light fluence in number of photons per solid angle segment, spectrally distributed like $dn_{\mathrm{ph}}/d\lambda$. Following the fits, displayed in figures 67 and 68, the spectral part of eq. 26 will be further parameterized as:

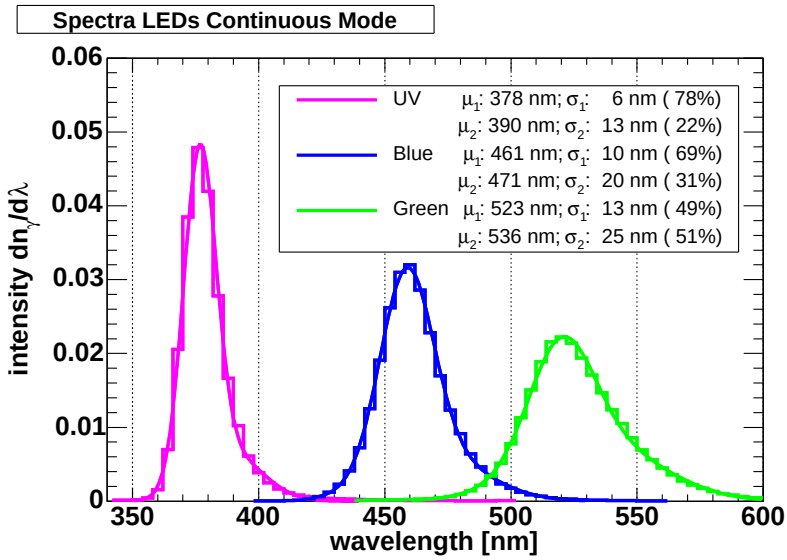

Figure 67: Spectra of the pulsed LEDs in continuous mode, including corrections for the quantum efficiency of the S1337-1010DQ PIN diode, the grating efficiency of the monochromator and an offset of 240 pA of the Keithley picoampere-meter. The legend shows the results of a double Gauss fit.

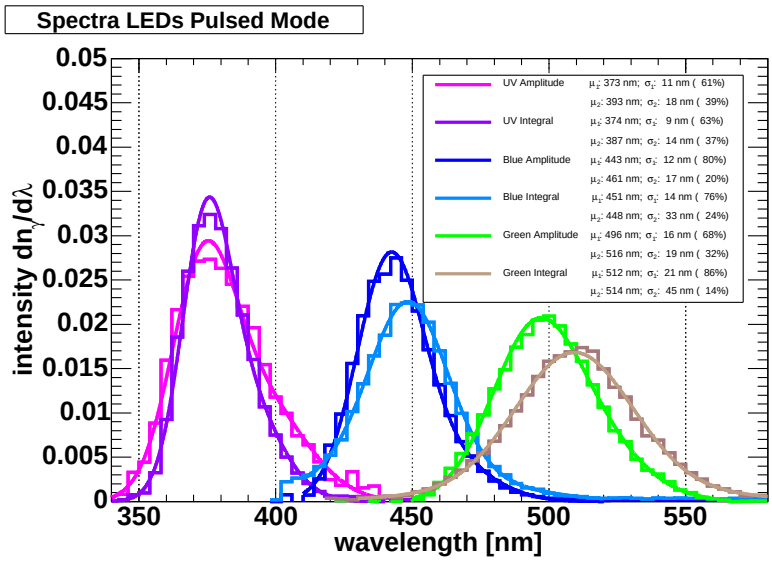

Figure 68: Spectra of the pulsed LEDs operated pulsed mode. The light pulses were registered by an ET9116 PMT and a common digital oscilloscope, measuring once average pulse amplitudes (lines denoted as "amplitude") and full pulse integrals (lines denoted as "integral"). The legend shows the results of a double Gauss fit.

$$\frac{dn_{\mathrm{ph}}}{d\lambda} = \frac{A_1}{\sqrt{2\pi\sigma_1^2}} \exp\big(-\frac{(\lambda-\mu_1)^2}{2\sigma_1^2}\big) + \frac{A_2}{\sqrt{2\pi\sigma_2^2}} \exp\big(-\frac{(\lambda-\mu_2)^2}{2\sigma_2^2}\big)$$

$$\text{with :} \qquad A_1 + A_2 = 1 \ . \tag{27}$$

In following calculations, all systematic uncertainties will be applied simultanesouly to the parameters μ_1 and μ_2 for simplicity.

4.1.2 Peripheries for the Pulsed LEDs

The LED pulser board with all peripheries is housed in a water-tight ***pulser box***, situated about 1 m behind the center of the mirror dish, 18.3 m from the camera (see figure 62).

The light pulses from the pulsed LEDs exit the pulser box via a diffuser, in order to homogenize the light flux and a subsequent glass window to protect the electronics from water and dust. The window has an incorporated heating system, consisting of high-power resistances and a ventilator, which prevents the glass from condensation of humidity inside the box.

The pulser box provides integrated power supplies, especially the ***600 V collector voltage*** for the avalanche transistors is generated on-place. The combination of slots is set via ***CAN-bus*** and can be steered by PC in the control house.

The output voltage of the 600 V supply has a ripple of only 30 mV ($\sim 5 \cdot 10^{-5}$), but a sizeable time dependency ranging from 607 V at switch-on time to 616 V after about one hour (see figure 69). Later, the change is less than 0.2%. For this reason, the 600 V supply has to be switched on about one hour before taking the first calibration run.

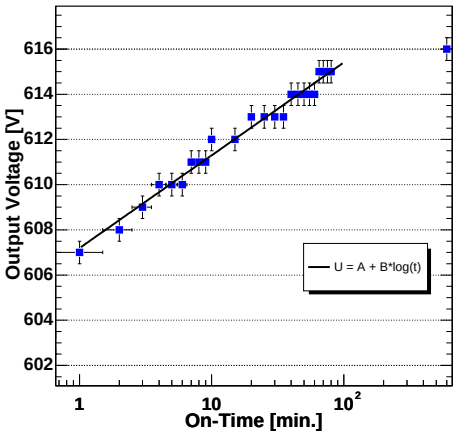

Figure 69: Measurements of the time dependency of the output voltages from the 600 V supply.

The ***trigger*** for the pulsed LEDs is generated in the control house, the signal being transmitted via optical fibers. Because of the avalanche transistor design, only one trigger pulse amplitude is required (however the combination of slots is set every time via the CAN-bus).

4.1.3 Spatial Uniformity of the Pulsed Light

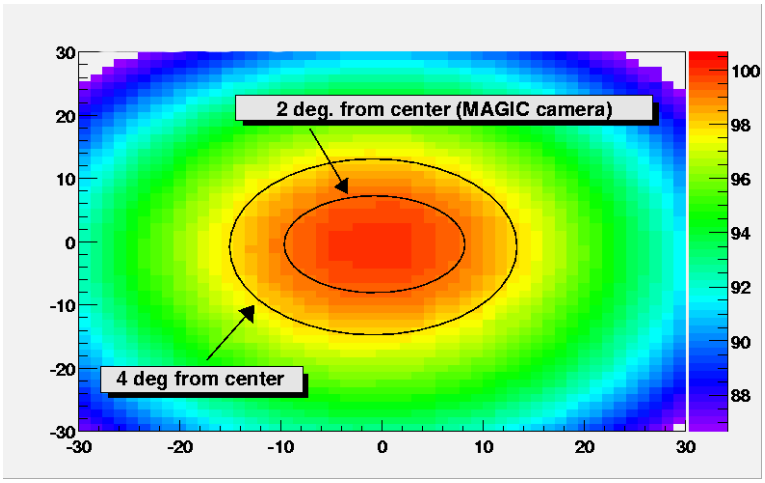

Figure 70: Uniformity of the emitted light from the pulsed LEDs. Figure from [222].

After traversing the diffuser plate, the emitted light has been shown to be uniform to about 1% in a cone of 2° radius from the center in a measurement performed by Thomas Schweizer (see figure 70). The uniformity cone covers the entire camera (which itself extends over 1.8° if looked at from the pulser box). The uniformity has been re-estimated from calibration pulses of different colours and by comparing results obtained with the pulsed LEDs and the CT1 pulser. These measurements and a small correction to the alignment of some LEDs were performed in collaboration with Michele Doro and are described in detail in his diploma thesis [203]. A very loose global upper limit to the uniformity of about 8% can be additionally extracted from the spread of conversion factors in the camera, after having been flat-fielded with the CT1-pulser.

Including the spatial distribution of light into the parameterization of the emitted light pulses (eq. 26) and neglecting emission outside the 2° cone of uniform emisssion, we obtain thus:

$$\begin{aligned} N_{\mathrm{ph}} \cdot \frac{dn_{\mathrm{ph}}}{d\Omega\, d\lambda} \qquad &\text{with :} \qquad 2\pi \cdot \int_{-2^\circ}^{2^\circ} \int_{-\infty}^{+\infty} \frac{dn_{\mathrm{ph}}}{d\Omega d\lambda}\, d\lambda\, \sin\theta d\theta = 1 \\ = N_{\mathrm{ph}} \cdot \frac{dn_{\mathrm{ph}}}{\Omega_{tot}\, d\lambda} \qquad &\text{with :} \qquad \Omega_{tot} = 4\pi \cdot (1 - \cos(2^\circ)) = 0.00766 \text{ sr} \,, \end{aligned} \tag{28}$$

where N_{ph} represents now the totality of photons emitted into the 2° uniformity cone. In now place throughout this work, light emitted outside the cone of uniform emission, will be used.

4.2 The CT1-Pulser

In order to cross-calibrate some systematic effects of the standard pulsed LEDs and for use as a backup calibrator, the ***CT1-pulser*** from the previous ***CT1*** was installed in the center of the mirror dish. Figure 71 shows a picture of the CT1-pulser. It drives 10 UV LEDs in parallel, of the same type as the ones used for the MAGIC pulsed LEDs (NISHIA NSHU590), but the transistors in the electronic circuit are not switched in avalanche mode, hence driving less current through each individual LED. This configuration allows to fire the same LEDs with variable intensities, depending on the amplitude of the supply voltage. That, in turn, is generated in the ***Control House*** and transferred to the pulser electrically via a coax-cable together with the trigger pulse. In contrast to the standard light pulser, the CT1-pulser setup does not allow to trigger the camera readout from outside, except for using the general majority trigger launched by a multiple-fold of photo-multiplier signals.

Figure 71: The CT1-pulser Box.

4.3 Continuous Light Source

The ***continuous light source*** is designed to simulate ***star light*** and the night sky background at different wavelengths and intensities.

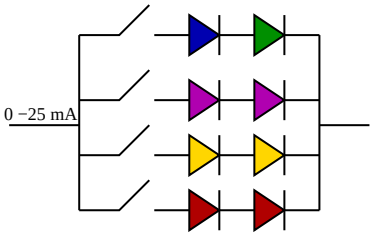

Figure 72: Sketch continuous light LEDs

Four pairs of LEDs are used providing peak wavelengths at 615 nm (red), 590 nm (amber), 525 nm and 470 nm (green-blue) and 375 nm (UV) (see table 3). Each of the four pairs can be switched on and off independently, hence allowing combinations of colors. In practice, only one pair at a time has been used so far. The continuous light LEDs are driven by a current-supply circuit which provides stable currents between 0 and 25 mA, depending on the voltage level provided by a small ***DAC***. The DAC, in turn, can be steered by CAN-bus from the computers in the control house.

Type	typ. wavelength max. [nm]	LED colour	peak wavelength [nm]
A	300–390	UV	375
F,G	390–580	green-blue	525 and 470
K	580–830	amber	590
		red	615

Table 3: Spectral types of stars and the continuous light colours

Figure 73 shows the current traversing the continuous light LEDs depending on the input DAC value, measured at different times after switching on the system. As the pulsed LEDs and the continuous light LEDs are alimented from the same power supplies, there is a small dependency of the current on whether the 600 V supply is switched on or not.

The continuous light source serves also to calibrate the camera currents readout at different wavelengths.

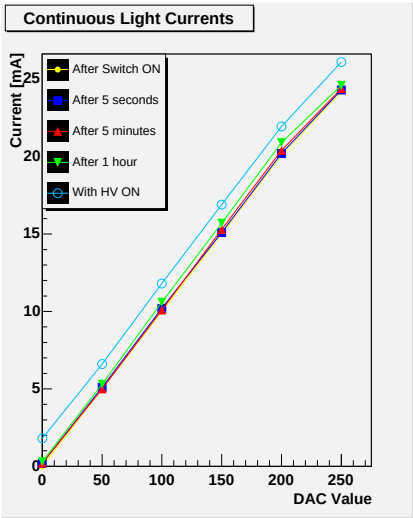

Figure 73: Current vs. DAC value for the continuous light source.

4.4 The Blinded Pixels

Three selected ***inner pixels*** with accurately measured quantum efficiencies (see [201]) were installed in the camera of the telescope and ***blinded with filters*** in order to reduce the number of photo-electrons per pulse in a controlled way and ***extract single photo-electron spectra***.

As the number of photo-electrons, n, collected by a blinded pixel in the course of one calibration pulse, follows a Poisson distribution [33],

$$P(n) = \frac{e^{-\mu_{\text{p.e.}}} \cdot \mu_{\text{p.e.}}^{n}}{n!} \ , \tag{29}$$

the mean number of photo-electrons per pulse,

$$\mu_{\text{p.e.}} = \frac{N_{\text{ph}} \cdot A_{\text{bp}}}{D_{\text{bp}}^2 \cdot \Omega_{tot}} \cdot T_{\text{plex}} \cdot \overline{QE} \cdot \eta_{\text{coll}}(\overline{\lambda}) \ , \tag{30}$$

can be extracted from the statistical distribution of anode signals. Here, N_{ph} is the total number of photons, emitted by the light pulser into the 2° uniform emission cone, $A_{\text{bp}} = 1\,\text{cm}^2$ is the geometrical area of a diaphragm, placed in front of the photo-cathode, $D_{\text{bp}} = 18.260 \pm 0.03\,\text{m}$ is the distance of the blinded pixel to the light diffuser plate, T_{plex} the transmission coefficient of the plexiglas in front of the camera, $\overline{QE}$ the effective acceptance of the photo-cathode (including the filter in front) and $\eta_{\text{coll}}(\overline{\lambda})$ the mean collection efficiency of the photo-electrons to the first dynode. $\overline{QE}$ has to be calculated for each of the light pulser colors separately:

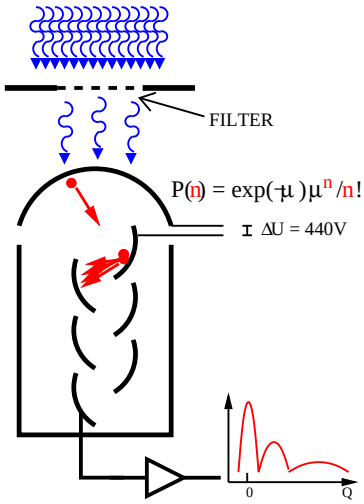

Figure 74: Sketch of a blinded pixel.

$$\overline{QE} = \int_{-\infty}^{+\infty} \frac{dn_{\text{ph}}}{d\lambda} \cdot QE(\lambda) \cdot T_{\text{filt}}(\lambda)\, d\lambda \ , \tag{31}$$

where $QE(\lambda)$ is the quantum efficiency of the photo-cathode and $T_{\text{filt}}(\lambda)$ the (wavelength-dependent) transmission coefficient of the filter. The integration goes over the entire wavelength-spectrum $dn_{\text{ph}}/d\lambda$ (figure 68) for every of the three possible light pulser colors (see eq. 27).

If the mean photo-electron fluence is low ($\mu_{\text{p.e.}} \ll 1$), mainly events with $n = 0$ and $n = 1$ contribute to the distribution of registered signals, eq. 29. In a good photo-multiplier, these two types of events have usually well distinguishable anode signals, even if the intrinsic noise of the photo-multiplier is taken into account. A fit to distribution eq. 29, folded with the noise distribution of the PMT, yields then a measurement of the mean photo-electron fluence $\mu_{\text{p.e.}}$. Inverting equation 30, the

[33] The number of photons emitted by a LED per fixed time interval follows a Poisson distribution, while the conversion of photons to photo-electrons is a random binary process. The convolution of a Poisson with a binary process yields again a Poisson distribution.

total amount of photons $N_{\rm ph}$, emitted by the light pulser into the 2° cone of uniform emission, can be retrieved if also $T_{\rm plex}$, $\overline{QE}$ and $\eta_{\rm coll}$ are known to sufficient precision:

$$
\begin{aligned}
N_{\rm ph} &= \mu_{\rm p.e.} \cdot C_{\rm bp} \qquad\qquad \text{with :} \\
C_{\rm bp} &= D_{\rm bp}^2 \cdot \Omega_{tot} / (A_{\rm bp} \cdot T_{\rm plex} \cdot \overline{QE} \cdot \eta_{\rm coll}(\overline{\lambda})) \ , \qquad (32) \\
\frac{\Delta N_{\rm ph}}{N_{\rm ph}} &= \sqrt{(\frac{\Delta \mu_{\rm p.e.}}{\mu_{\rm p.e.}})^2 + (\frac{\Delta C_{\rm bp}}{C_{\rm pd}})^2} \qquad \text{with :} \qquad (33) \\
\frac{\Delta C_{\rm bp}}{C_{\rm bp}} &= \sqrt{(\frac{2\Delta D_{\rm bp}}{D_{\rm bp}})^2 + (\frac{\Delta A_{\rm bp}}{A_{\rm bp}})^2 + (\frac{\Delta T_{\rm plex}}{T_{\rm plex}})^2 + (\frac{\Delta \overline{QE}}{\overline{QE}})^2 + (\frac{\Delta \eta_{\rm coll}}{\eta_{\rm coll}})^2} \\
&\quad + \Delta(\frac{dn_{\rm ph}}{d\Omega}) \ , \qquad (34)
\end{aligned}
$$

where the last contribution $\Delta(\frac{dn_{\rm ph}}{d\Omega})$ to the uncertainty of the conversion factor $C_{\rm bp}$ stems from the precision of the uniformity measurement (section 4.1.3) and is asymmetric. Table 4 lists all those parameters and their uncertainties, which have been measured before installing the blinded pixels on the telescope.

The three blinded pixels are situated just outside the last ring of outer pixels in the camera, each 120° from the two others, at a distance of about 60 cm from the camera center. They lie still inside the 2° cone of uniform illumination by the pulsed LEDs.

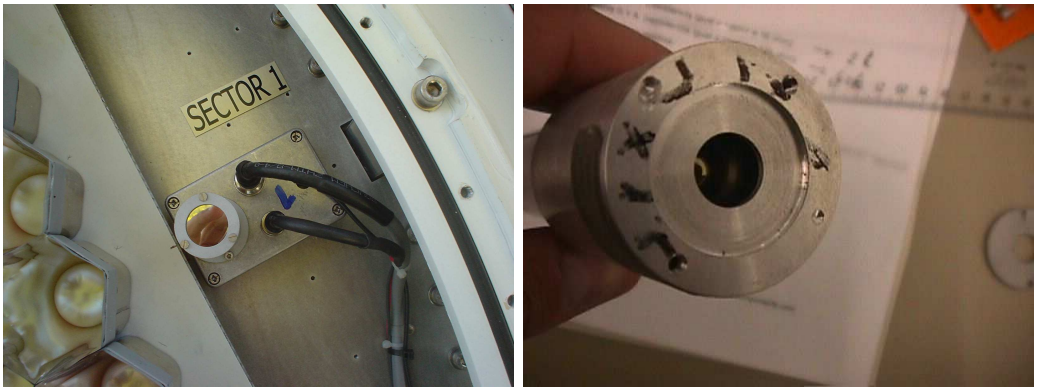

Figure 75: Left: blinded pixel #1 placed in the camera. Right: the diaphragm of the blinded pixel

Apart from the light filters, a diaphragm of exactly 1 cm^2 area covers the photocathode at a distance of about 0.5 cm in order to reduce the dependencies of the quantum and collection efficiency, QE and η_{coll}, on the impact distance from the central

	Blinded Pixels parameters			
	UV	Blue	Green	comments
T_{filt} (BP#1)	0.0111	0.0110	0.0108	Oriel 50550
T_{filt} (BP#2)	$(1.00 \pm 0.05) \cdot 10^{-3}$			Edmunds NT47–212
T_{filt} (BP#3)	$(1.96 \pm 0.08) \cdot 10^{-3}$			diaphragm
$\overline{QE}$ (BP#1)	0.00306	0.0028	0.00206	incl. T_{filt} (BP#1)
$\overline{QE}$ (BP#2)	0.00026	0.00024	0.00018	incl. T_{filt} (BP#2)
$\overline{QE}$ (BP#3)	0.00051	0.00042	0.00028	incl. T_{filt} (BP#3)
T_{plex}	0.91	0.92	0.92	
η_{coll}	0.91	0.93	0.97	estimations
C_{bp} (BP#1)	$1.01 \cdot 10^7$	$1.07 \cdot 10^7$	$1.39 \cdot 10^7$	
C_{bp} (BP#2)	$1.18 \cdot 10^8$	$1.24 \cdot 10^8$	$1.59 \cdot 10^8$	
C_{bp} (BP#3)	$6.04 \cdot 10^7$	$7.11 \cdot 10^7$	$1.02 \cdot 10^8$	
	accuracy estimations			
	[%]	[%]	[%]	
$\Delta\overline{QE}/\overline{QE}$(BP#1)	2.5	$^{+3}_{-3.5}$	7	asymm. in blue
$\Delta\overline{QE}/\overline{QE}$(BP#2)	5	5.5	8.5	
$\Delta\overline{QE}/\overline{QE}$(BP#3)	5	5.5	9	
$\Delta A_{\text{bp}}/A_{\text{bp}}$	< 0.1	< 0.1	< 0.1	
$\Delta D_{\text{bp}}/D_{\text{bp}}$	< 0.2	< 0.2	< 0.2	
$\Delta T_{\text{plex}}/T_{\text{plex}}$	2	2	2	
$\Delta\eta_{\text{coll}}/\eta_{\text{coll}}$	5	4	$^{+1}_{-3}$	
$\Delta\frac{dn_{\text{ph}}}{d\Omega}/\frac{dn_{\text{ph}}}{d\Omega}$	$^{+0}_{-1}$	$^{+0}_{-1}$	$^{+0}_{-1}$	asymm.
$\Delta C_{\text{bp}}/C_{\text{bp}}$(BP#1)	$^{+7}_{-6}$	$^{+7}_{-7}$	$^{+8}_{-7}$	
$\Delta C_{\text{bp}}/C_{\text{bp}}$(BP#2)	$^{+8.5}_{-7.5}$	$^{+8}_{-7}$	$^{+9.5}_{-8.5}$	
$\Delta C_{\text{bp}}/C_{\text{bp}}$(BP#3)	$^{+8.5}_{-7.5}$	$^{+8}_{-7}$	$^{+10}_{-9}$	

Table 4: Averaged combined efficiencies $\overline{QE}$ of the blind pixels assembly (see equation 33) for the three possible light pulser colors UV, blue and green. The uncertainties have been obtained by varying the spectral parameters, as obtained in section 4.1.1, including systematic uncertainties in the overall estimation of the blind pixels quantum efficiency (1%) and the transmission coefficients of the filters. The large relative uncertainty in the green is mainly due to the falling blinded pixels quantum efficiency spectrum and the uncertainty about the peak wavelength.

axis of the photomultiplier (recall figures 43 and 47). Especially the wavelength-dependency of the collection efficiency $\eta_{coll}(\lambda)$ is reduced this way. Figure 75 shows two photographs of one blinded pixel with the diaphragm and the filter set in place. The blinded pixels have no light guides.

Actually ,only two blinded pixels carry absorption filters, while the third one has instead a diaphragm of 0.5 mm diameter. Table 4 lists also the transmission coefficients $T_{\rm filt}$ of the three blinded pixels which are approximately uniform over the used wavelengths. Figure 76 shows the measured quantum efficiency $QE(\lambda)$ of blinded pixel #1 and the combinated photo-electron emission probability $QE(\lambda) \cdot T_{\rm filt}(\lambda)$ including the absorption by the filter, while figure 77 shows the quantum efficiency of blinded pixel #3.

The voltage between the photo-cathode of the blinded pixel and its first dynode was raised to 440 V (instead of the 360 V applied to the other PMTs), in order to decrease the statistical variance of the amplified signal to a minimum. A dedicated copper shielding was placed around the photo-cathode and dynode system to shield the blinded pixel especially well against electric fields.

The readout of the blinded pixels has been modified such that the anode signals get amplified about a factor four higher than in a common inner pixel. The nominal cathode voltage of the blinded pixel is 1550 V, about 20% higher than the common voltage of the inner pixels.

Figure 78 shows two recorded signal pulses: one obtained when the "blinded" pixel was illuminated with an intense pulsed light source without filter and a second one when the filter was properly set in place and the blinded pixel was illuminated with a weak pulsed light source and the – sporadically ocurring – single photo-electron pulse was recorded with the MAGIC FADCs. The FWHM of the single photo-electron pulse is about 7–8 ns after shaping, larger than the one obtained from an ordinary inner pixel, due to the limited bandwidth of the pre-amplifer, now operated at a higher gain.

4.4.1 Statistical Description of the Blinded Pixel

As the Blinded Pixel method relies upon the precise modelling of the statistical processes which generate the distribution of signals, a description of the individual steps will be presented here following a model developped by Bellamy et al. [228].

The Ideal PMT

If the secondary electron multiplicity of the first dynode is large enough [34] ($\gtrsim 4$), the response of the dynode system to a single photo-electron can be approximated by a Gaussian distribution

$$G_1(x) = \frac{1}{\sigma_1\sqrt{2\pi}} \exp\Big(- \frac{(x-Q_1)^2}{2\sigma_1^2}\Big) \ , \tag{35}$$

[34] We estimate the secondary electron multiplicity of our blinded pixels to about 10–12.

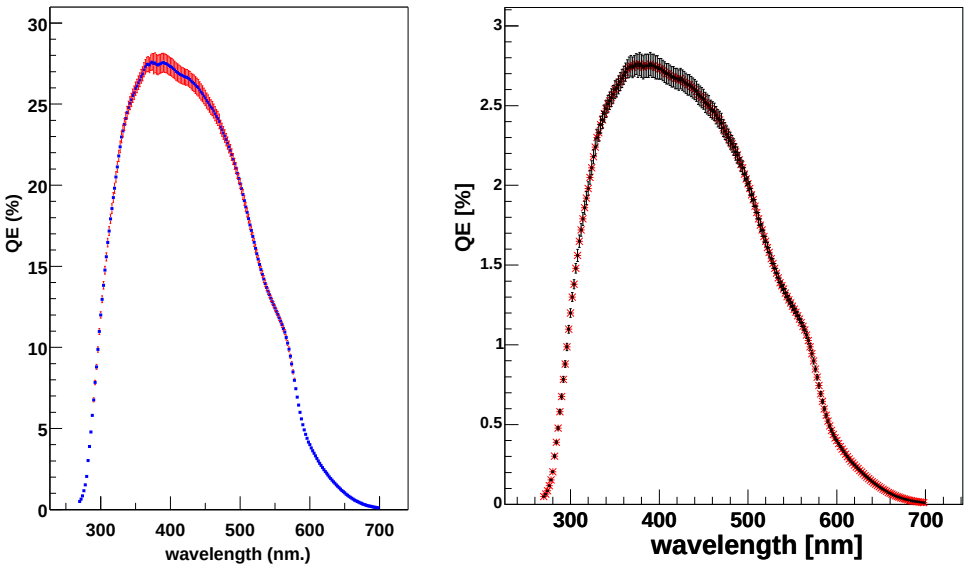

Figure 76: Left: quantum efficiency of blinded pixel #1 (data provided by David Paneque). Right: combined photon detection efficiency, with filter included. Error bars show the systematic uncertainty.

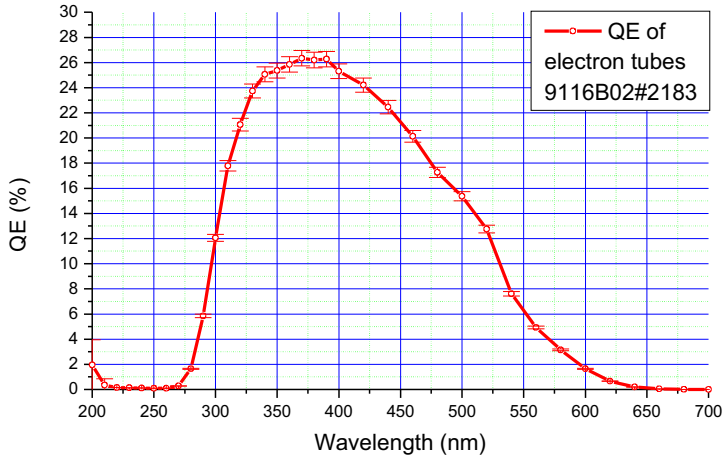

Figure 77: Quantum efficiency of blinded pixel #3 (data provided by Razmik Mirzoyan).

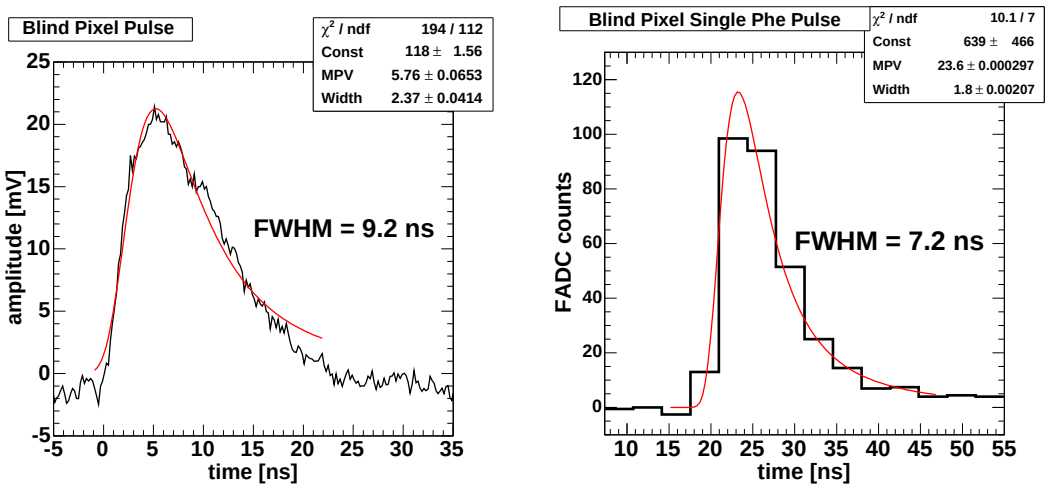

Figure 78: Electronic pulse forms of blinded pixel #1 after transmission through the optical fibers and shaping within the optical receiver board. Left: without filter, illuminated with an intense light pulse and pulse shape recorded with an oscilloscope. The red line shows the result of a Landau-function fit to the recorded amplitudes. A FWHM of 9.2 ns is observed. Right: with filter, illuminated with a weak light pulse. A single photo-electron pulse is shown, recorded with the MAGIC FADCs. A FWHM of 7.2 ns is observed.

where x is the variable charge, Q_1 the average charge at the PMT output, when one electron is collected by the first dynode, and σ_1 is the corresponding standard deviation. Assuming that the amplification process for the charges, initiated by multiple photo-electrons, is a linear superposition of the one photo-electron case, the response to n photo-electrons can be expressed as

$$G_n(x) = \frac{1}{\sigma_1\sqrt{2\pi n}} \exp\Big(-\frac{(x-nQ_1)^2}{2n\sigma_1^2}\Big) \ . \tag{36}$$

An ideal noiseless PMT would yield thus a distribution obtained from the convolution of eq. 29 with eq. 36:

$$S_{ideal}(x) = \sum_{n=0}^{\infty} \frac{e^{-\mu_{\mathrm{p.e.}}} \cdot \mu_{\mathrm{p.e.}}^n}{n!} \frac{1}{\sigma_1\sqrt{2\pi n}} \exp\Big(-\frac{(x-nQ_1)^2}{2n\sigma_1^2}\Big) \ . \tag{37}$$

Background Processes

In a real PMT, various background processes are always present which can be classified in three categories:

1. Processes which are also present in the absence of calibration pulses, like: thermo-electron emission from the photo-cathode and/or the dynode system,

leakage current in the anode circuit, electronic noise in the amplification chain. Out of these processes, the last one is the most important in our case. These processes generate in first order Gaussian spectra.

2. Secondary processes generated by the incident light flux, like: photo-emission from the dynodes, photo-electrons missing the first dynodes, but hitting one of the subsequent dynodes, photo-electrons back-scattered from the first dynode and being multiplied by the subsequent dynode stages, etc. The amplitudes of the signals obtained from these processes is expected to decrease exponentially. As in our case, the amplification adds additional noise, the exponential is blurred by the Gaussian obtained from process #1.

3. Additionally, Poissonian processes occur, like external and internal radio-activity, light from the night-sky background, etc.

In summary, when no primary photo-electron is emitted, the obtained charge distribution can be parameterized with the following function:

$$B(x) = \begin{cases} (1 - w_E - w_P) \cdot \frac{1}{\sqrt{2\pi}\sigma_0} \exp\left(- \frac{x^2}{2\sigma_0^2}\right) & \text{(process \#1)} \\ +w_E \cdot \frac{1}{\sqrt{2\pi}\sigma_0} \int_0^x \alpha \, \exp(-\alpha \, x') \exp(-\frac{(x-x')^2}{2\sigma_0^2}) \, dx' & \text{(process \#2)} \\ +w_p \cdot \frac{1}{\sqrt{2\pi}\sigma_p} \exp(-\frac{x-Q_{p1}}{2\sigma_p^2}) & \text{(process \#3)} \end{cases}$$

with :

$$\sigma_p = \sqrt{\sigma_0^2 + \sigma_{p1}^2}$$

and

$$w_p \approx \mu_p \cdot \exp(-\mu_p) \tag{38}$$

where σ_0 is the standard deviation of the type #1 background distribution, w_E is the probability that a measured signal is accompanied by a type #2 background process and α is the coefficient of the exponential decrease of this type of background. The Poisson background, parameterized by the mean emission probability μ_p, is assumed to be very small, hence only the case of multiplicity one is taken into account, with the mean charge at Q_{p1} and a width of σ_{p1}.

The Realistic PMT

Background processes #1 and #2 are usually present either in the case of single or multiple photo-electron emission, therefore a convolution of the ideal PMT spectrum (eq. 37) has to be made with the background charge distribution (eq. 38 #1 and #2)

and added to the Poissonian background. The resulting model for the realistic PMT then reads as [35]

$$
\begin{aligned}
S_{real}(x) &= \int S_{ideal}(x')B(x-x')\,dx' \\
&= e^{-\mu_{\text{p.e.}}} \cdot \left\{ \begin{array}{l} \frac{1-w_E-w_p}{\sqrt{2\pi}\sigma_0} \cdot \exp(-\frac{(x-Q_0)^2}{2\sigma_0^2}) \\ + w_E \cdot \frac{\alpha}{2} \exp(-\alpha(x-Q_0-\frac{\alpha\sigma_0^2}{2})) \cdot \left[1-\text{erf}(\alpha\sigma_0^2-x)\right] \\ + \sum_{n=1}^{\infty} \frac{\mu_{\text{p.e.}}^n}{n!} \left[(1-w_E-w_p)G_n(x-Q_0) + w_E\, I(x-Q_0)\right] \end{array} \right. \\
&\quad + w_p \cdot \frac{1}{\sqrt{2\pi}\sigma_p} \exp(-\frac{x-Q_{p1}}{2\sigma_p^2})
\end{aligned}
$$

with :

$$
I(x-Q_0) = \left\{ \begin{array}{ll} 0 & \text{for} \quad x <= Q_0 \\ \frac{\alpha}{2} \exp[-\alpha(x-Q_n-\alpha\sigma_n^2/2)] & \\ \times \left[\text{erf}\left(\frac{x-Q_n-\alpha\sigma_n^2}{\sigma_n\sqrt{2}}\right) - \text{erf}\left(\frac{Q_0-Q_n-\alpha\sigma_n^2}{\sigma_n\sqrt{2}}\right)\right] & \text{for} \quad x > Q_0 \end{array} \right.
$$

and :

$$
\begin{aligned}
Q_n &= Q_0 + nQ_1 \\
\sigma_n &= \sqrt{\sigma_0^2 + n\sigma_1^2} \\
\sigma_p &= \sqrt{\sigma_0^2 + \sigma_{p1}^2}
\end{aligned} \tag{39}
$$

Model 39 has ten free parameters out of which five (Q_0, σ_0 and the Poisson background μ_p, Q_{p1} and σ_{p1}) can readily be measured taking pedestal runs just before the calibration with pulsed light. Two parameters (w and α) describe the discrete background and two more (Q_1, σ_1) the response of the PMT to an incident photo-electron. These parameters are expected to change only slowly with time and can be fixed rather tightly during the fit, once established. Finally, the last free parameter $\mu_{\text{p.e.}}$ is proportional to the intensity of the pulsed LEDs.

Figure 79 gives an example of the procedure to fit a single photo-electron spectrum with a blinded pixel: first, a pedestal run is taken, yielding an estimate of Q_0 and σ_0, and fixing the Poissonian background (which results to about what is expected from photons of the night sky background). Second, the calibration run

[35] Note that this function differs from formula 8 of Bellamy et al. [228] in three ways: first, a small error ocurred in formula 8, subtracting $\alpha\sigma_n^2$ in the exponential instead of $\alpha\sigma_n^2/2$. Second, Bellamy et al. had an almost noiseless amplification scheme and did not need to fold the exponential distribution into any electronics noise which is the case here. Third, the Poissonian background was neglected there, because obviously no night sky backgrounds were present in their setup and radioactivity low.

yields a single photo-electron spectrum which is fitted to function 39. One can see that acceptable χ^2 values are obtained and the mean number of photo-electrons per pulse, $\mu_{\text{p.e.}}$, is obtained with a precision of about 3%.

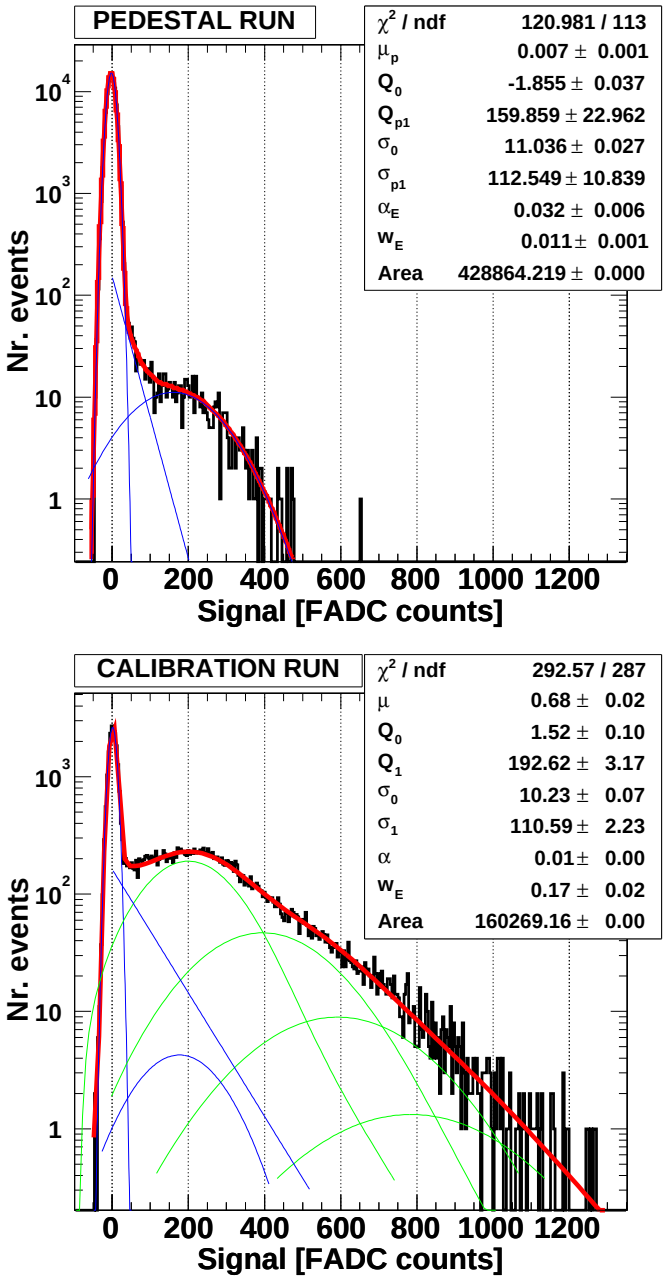

Figure 79: Example of a single photo-electron fit procedure to the blinded pixel signal. Top: pedestal run yielding the three types of background (see text). Bottom: Calibration run with Poissonian background fixed. Blue: individual background contributions; Green: individual contributions due to single or multiple photo-electrons; Red: complete fit. In both fits, the area is not a free parameter, but fixed by the integral of the histogram.

4.5 The PIN Diode

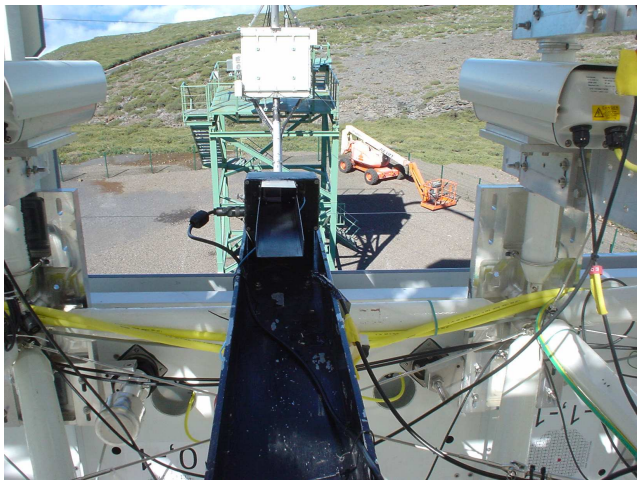

Figure 80: The aluminium box housing the PIN diode set in place.

The blinded pixel and the ordinary PMTs of the MAGIC camera have several systematic uncertainties in common, among which the insufficienct knowlegde of the ***collection efficiency*** of the PMTs and the long-term variations of the transmission coefficient of the plexiglas (due to dust and sporadic cleaning [36]) stand out with the largest uncertainty. It is therefore desirable to have an additional device to measure the absolute light flux, independent from these effects. Such a device can be a calibrated ***PIN diode*** (see figure 55).

The MAGIC telescope houses a PIN diode, situated between the calibration pulser box and the camera, at about 1 m from the pulser box outside the light cone which illuminates the camera, but still inside a viewing angle of 4 degree where the light flux is stable to 2% (recall figure 70). Measuring the number of incident photons per calibration pulse at that viewing angle and distance, an extrapolation to the expected photon fluence in the camera can be made and the result cross-checked with those obtained from the blinded pixel and the rest of the camera. The MAGIC PIN diode is housed in a double aluminium box, with a glass window opening the sight to the calibration box (see fig. 80 and 81). Between two glass plates, a mesh of gold wires of 10 µm thickness and 1 mm distance is placed to protect the hole against electronic noise. The distance of the PIN diode to the light diffuser in the pulser box has been measured with a *DISTO* device [37] from Leica [229] to 1.139±0.005 m.

Photodiodes are semiconductor light sensors which generate a current when the *p*–*n* junction is illuminated by light. Compared with a PMT, it has the advantages of higher quantum efficiency, no photo-electron collection losses, lower working voltage

[36] Unfortunately, I note that every time when I come to La Palma, the plexiglas has got more scratches because people used inadequate cleaning methods

[37] Device accuracy: ±1.5 mm, available at MPI from Razmik Mirzoyan.

and insensitivity to magnetic fields. Its main disadvantage is higher dark noise in relation to the signal, because the created charges are not getting amplified as in the case of a photo-multiplier [38].

The silicon PIN diode consists of a boron-doped $p-$layer silicon material of about 1 µm thickness, followed by a neutral $i-$layer, called the depletion region. The size of this region depends on the applied reverse voltage and reaches 265 µm in saturation. The PIN diode forms now an effective capacitance of about 40 pF. On the other end, a much thicker $n-$layer is installed.

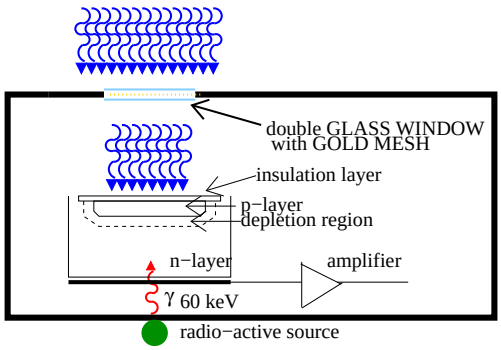

Figure 81: Sketch of the PIN diode.

As the resolution of such a device is always much lower than using the equivalent photo-multiplier tube [230], ***single photo-electron counting*** is ***impossible*** with a PIN diode, and the signals from the pulsed LEDs would be too small if recorded at the distance of the camera. Therefore, the PIN diode was placed between the pulser box and the camera, at a distance of $D_{\rm pd} = 1.139$ m from the diffuser in front of the pulsed LEDs. This choice requires an additional absolute calibration of the PIN diode itself, since there is no low-rate Poisson spectrum to allow the extraction of a Poisson mean. This dedicated ***PIN diode calibration*** was performed using two radio-active γ-emitters: ^{241}Am and ^{133}Ba. A light pulse emitted by the pulsed LEDs, with fluence $N_{\rm ph}\,\frac{dn_{\rm ph}}{d\Omega\,d\lambda}$ (see definition eq. 28) will then create on average a number of photo-electrons $< N_{\rm p.e.} >$ in the PIN diode:

$$\begin{aligned} < N_{\rm p.e.} > &= \frac{N_{\rm ph}\cdot A_{\rm pd}}{D_{\rm pd}^2\cdot\Omega_{tot}}\cdot\int_{-\infty}^{+\infty}\frac{dn_{\rm ph}}{d\lambda}\cdot QE(\lambda)\cdot T_{\rm glass}(\lambda)\cdot\eta_{\rm mesh}\,d\lambda \\ &= \frac{N_{\rm ph}\cdot A_{\rm pd}}{D_{\rm pd}^2\cdot\Omega_{tot}}\cdot\overline{QE} \end{aligned} \tag{40}$$

where $A_{\rm pd} = 63.52 \pm 0.1$ mm^2 is the geometrical area of the diaphragm in front of the PIN diode, $\eta_{\rm mesh} = 0.98 \pm 0.005$ the transparency coefficient of the gold wire mesh, $QE(\lambda)$ the quantum efficiency of the PIN diode (figure 84) and $T_{\rm glass}(\lambda)$ (figure 82) the transparency coefficient of the protecting glass plates. The averaged acceptancies of the PIN Diode assembly, $\overline{QE}$, have been evaluated for each of the three pulser colors and are listed in table 5.

With this information, the total amount of photons $N_{\rm ph}$, emitted by the light pulser into the 2° cone of uniform emission, can be calculated if the mean number of photo-electrons, $< N_{\rm p.e.} >$, created in the PIN Diode, is known:

[38] This limitation is not valid any more in the case of a so-called Avalanche Photodiode where intrinsic amplification takes place, like in the case of a photo-multiplier.

$$
\begin{aligned}
N_{\rm ph} &= < N_{\rm p.e.} > \cdot C_{\rm pd} \qquad \text{with :} \\
C_{\rm pd} &= D_{\rm pd}^2 \cdot \Omega_{tot}/(A_{\rm pd} \cdot \overline{QE}) \qquad (41) \\
\frac{\Delta N_{\rm ph}}{N_{\rm ph}} &= \sqrt{(\frac{\Delta N_{\rm p.e.}}{N_{\rm p.e.}})^2 + (\frac{\Delta C_{\rm pd}}{C_{\rm pd}})^2} \qquad \text{with :} \\
\frac{\Delta C_{\rm pd}}{C_{\rm pd}} &= \sqrt{(\frac{2\Delta D_{\rm pd}}{D_{\rm pd}})^2 + (\frac{\Delta A_{\rm pd}}{A_{\rm pd}})^2 + (\frac{\Delta \overline{QE}}{\overline{QE}})^2} \\
&\quad +\Delta(\frac{dn_{\rm ph}}{d\Omega}) \ , \qquad (42)
\end{aligned}
$$

where the last contribution $\Delta(\frac{dn_{\rm ph}}{d\Omega})$ to the uncertainty of the conversion factor $C_{\rm pd}$ stems from the precision of the uniformity measurement (section 4.1.3) and is asymmetric. Table 5 lists all those parameters and their uncertainties, which have been measured before installing the PIN Diode at the telescope. All systematic uncertainties which have to do with PIN Diode itself, will be included in the uncertainty of $< N_{\rm p.e.} >$ and will be explained in more detail later.

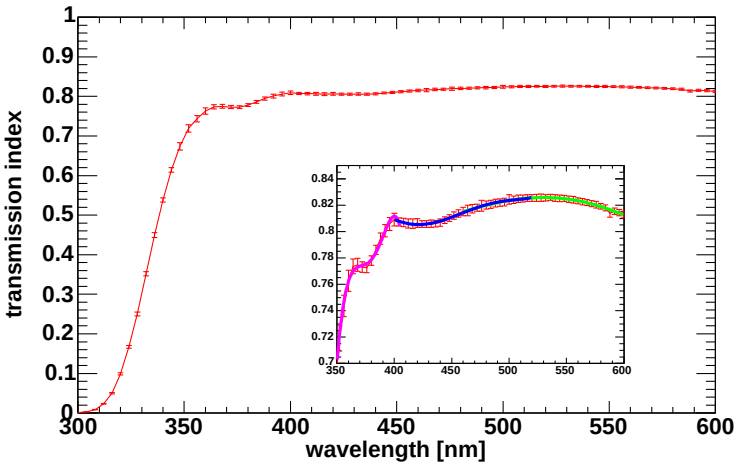

Figure 82: Transmission coefficients of the double PIN diode box glass window. The inset shows the wavelength region illuminated by the pulsed LEDs. Measurements performed in collaboration with Manel Errando.

With the signal recorded by a characteristic gamma-ray emission lines of energy E_γ the obtained number of photo-electrons $\mu_{\gamma-{\rm cal}}$ can be calibrated:

$$
n_{\gamma-{\rm cal}} = \frac{E_\gamma\,[{\rm eV}]}{3.62\,[{\rm eV/phe}]} \qquad (43)
$$

	PIN Diode parameters			
	UV	Blue	Green	comments
$\overline{QE}$	0.3	0.55	0.645	incl. T_{glass}
C_{pd}	521	284	242	
	accuracy estimations			
	[%]	[%]	[%]	
$\Delta\overline{QE}/\overline{QE}$	$^{+5}_{-7}$	3.5	3	asymm. in UV
$\Delta A_{\text{pd}}/A_{\text{pd}}$	< 1	< 1	< 1	
$\Delta D_{\text{pd}}/D_{\text{pd}}$	< 0.5	0.5	0.5	
$\Delta\frac{dn_{\text{ph}}}{d\Omega}/\frac{dn_{\text{ph}}}{d\Omega}$	$^{+0}_{-2}$	$^{+0}_{-(2-3)}$	$^{+0}_{-(2-3)}$	asymm.
$\Delta C_{\text{pd}}/C_{\text{pd}}$	$^{+9}_{-5}$	$^{+6}_{-3.5}$	$^{+5.5}_{-3}$	

Table 5: Averaged combined efficiencies $\overline{QE}$ of the PIN Diode assembly (see equation 42) for the three possible light pulser colors UV, blue and green. The uncertainties have been obtained by varying the spectral parameters, as obtained in section 4.1.1, including systematic uncertainties in the overall estimation of the PIN Diode quantum efficiency and the transparency of the protection glass. The large relative uncertainty in the UV is mainly due to the steeply rising PIN Diode quantum efficiency spectrum. The larger uncertainty in spatial uniformity for blue and green LEDs is due to their position on the pulser board.

The principal functioning of the method was shown in [231–233] and using the MAGIC calibration system in [222]. In order to explain the functionning of the radio-active source calibration, first an introduction to the interaction mechanisms of particles with the silicon material will be given.

4.5.1 Interaction of Gamma-Rays with Silicon

A photon in the optical and near-infrared range, which strikes the PIN diode, will excite electrons in the crystal structure of the silicon. If its energy is above the band gap energy of the silicon (1.115 eV $\equiv$ 1105 nm), the excited electron gets pulled up into the conduction band of the semiconductor, leaving a hole in the valence band. These electron-hole pairs (also called: "photo-electrons") occur throughout the $p-$, $i-$ and $n-$layer materials, but in the depletion region the electrons are accelerated by the electric field towards the $n-$layer, the corresponding holes to the $p-$layer.

Incident X-rays and γ-rays (below about 1 MeV) instead can interact with the silicon material of the PIN diode via photo-absorption, Compton scattering and coherent (Raleigh) scattering (see figure 83). Pair production hardly occurs below 1 MeV γ-ray energy.

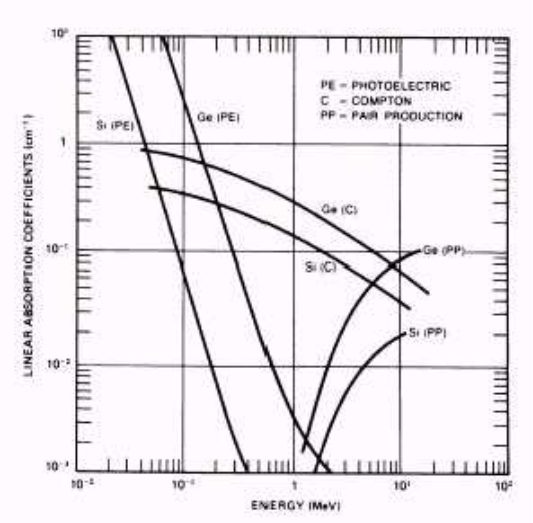

Figure 83: Absorption Coefficients of Silicon and Germanium

Photo-Absorption

Below about 55 keV photon energy, the X-ray is most probably absorbed by a bound electron (mostly from the K shell) of the silicon atom which is kicked out of the atom. The energy of the created fast electron equals the energy of the photons minus the binding energy E_b of the electron (1.8 keV for a K-shell electron). As a result of this process, the atom is left with a vacancy in the K shell, resulting in the emission of another X-ray with about E_b, emitted from the recombination of outer electrons with the vacant whole. Typical mean free paths are 1.9 cm for an 80 keV X-ray and 1.3 µm for the K shell photons. As the depletion region is two orders of magnitude larger than the mean free path of the K-shell X-ray, in total all the energy of the primary photon is converted into fast electrons.

Compton Scattering

Compton scattering is the most probable interaction process of X-rays above 55 keV in silicon [234]. In this case, the X-ray gets scattered by an electron with a partial energy loss. The recoil electron energy E_e can be calculated from the incident X-ray energy E_0 with the following formula [230]:

$$E_e = E_0 \cdot \frac{\alpha \cdot (1 - \cos\theta)}{1 + \alpha \cdot (1 - \cos\theta)} \ , \qquad \alpha = \frac{E_0}{m_e c^2} \ . \tag{44}$$

The amount of transmitted energy depends thus on the scattering angle θ. An upper limit to the transferred energy can be obtained for the (most probable) case of complete backward scattering leading to about 6 keV electron energy for the 60 keV photon or 19 keV electron energy for the 80 keV photon.

Coherent Scattering

Coherent scattering happens when the photon scatters with the atom as a whole maintaining practically all its energy but changing its direction. This process is not relevant here since it does not deposit energy in the PIN diode.

4.5.2 Interaction of Electrons with Silicon

Fast electrons ionize the material, creating on average one electron-hole pair per 3.62 eV of lost energy [124, 231] (note however that H. Spieler gives the same parameter as 3.67 eV at room temperature [235]. Moreover, there is however some temperature dependency, e.g. the same value rises to 3.72 at 80 K). This energy is higher than the band-gap energy E_b of silicon because of the involved phonon-creation required by angular momentum conservation. The exact details of the ionization process are still not exactly understood [230], but the average energy necessary to create an electron-hole pair seems to be independent of the type and energy of radiation.

If an electron of energy E_e is fully stopped within the active region of the PIN diode, the collected number of electron-hole pairs $n_{e,h}$ is then given by the relation:

$$n_{e,h} = E_e[\text{eV}]/3.62 \tag{45}$$

The statistical variance of this number $n_{e,h}$ is smaller than would be expected by a pure Poissonian process since not all events along the track of the ionizing particle are independent. The actual statistical variance $\text{Var}(n_{e,h})$ is reduced by the Fano factor F which is about 0.1 in silicon [236].

$$\text{Var}(n_{e,h}) = F \cdot n_{e,h} \tag{46}$$

In the case of the PIN diode, electronic noise in the readout causes much higher variances of the registered signal, though.

Minimum ionizing particles crossing the PIN diode (e.g. a muon from an air shower), create about 20000 electron-hole pairs via the same mechanism.

4.5.3 The HAMAMATSU PIN Diode S3590-08

In the MAGIC telescope, a silicon PIN diode of type S3590-08 from HAMAMATSU was used. It has an exact area of 1 cm^2, diminished by a diaphragm to 63.517 mm^2 effective area and is operated at 70 V reverse voltage. Then, it forms then an effective capacitance of about $C = 40$ pF. Using the standard relation between a capacitor's distance d, its area A and the material's dielectric permittivity ϵ and its capacitance,

$$d_{depletion} = \frac{\epsilon_{silicon} \cdot A}{C} \ , \tag{47}$$

one can derive the effective thickness of the depletion region to about 265 µm. With the knowlegde of the electrons and holes mobilities $\mu_{e,h}$ (1350 cm^2/Vs for electrons, 480 cm^2/Vs for holes at 300 K [230]) and the applied counter voltage V, one

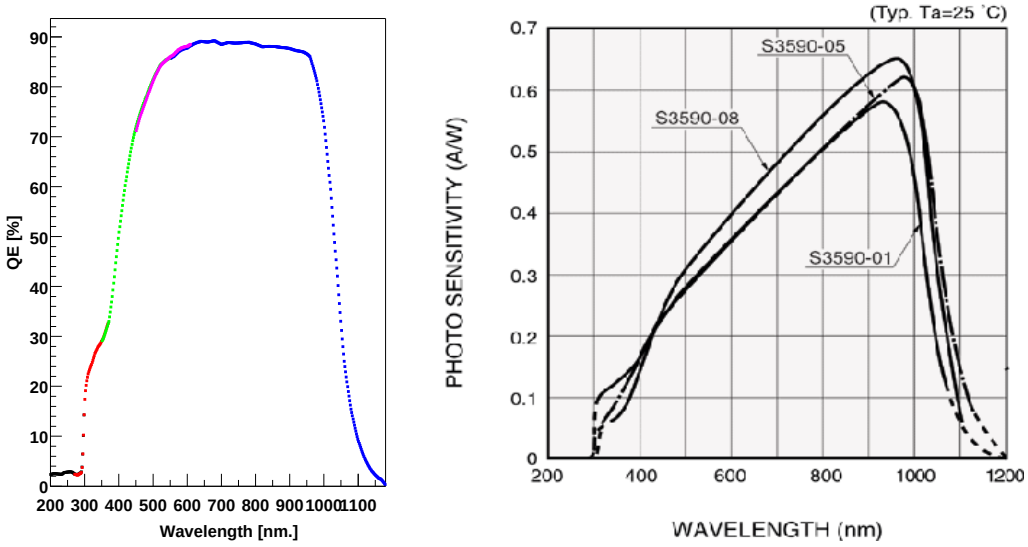

Figure 84: Left: the quantum efficiency of the PIN diode, measured at IFAE by David Paneque with 1% accuracy. Right: the photo-sensitivity of the PIN diode provided from the data-sheet, estimated accurary: 5%.

can also estimate the maximum time that the particles need to drift through the material:

$$t_{e,h} = \frac{d^2_{depletion}}{\mu_{e,h} \cdot V} \tag{48}$$

The resulting maximal collection times are 7.5 ns for the electrons and 21 ns for the holes. Figure 84 shows the quantum efficiency measured at IFAE by David Paneque and the photo-sensitivity of the PIN diode, as provided in the data-sheet. The two quantities can be translated into one another using the following relation:

$$QE = \frac{S \cdot 1240}{\lambda} \cdot 100\,[\%]\ . \tag{49}$$

Here, S is the photo-sensitivity in (A/W) and λ the photon wavelength in (nm).

4.5.4 The ^{241}Am Calibration Source

^{241}Am is an α-emitter decaying into ^{237}Np with a half life time of 432 years. The decay product ^{237}Np itself has a life time of greater than 10^6 years. The ^{241}Am decay can leave the ^{237}Np in a great number of possible excited states, however largely favoured the ground state. In about 36% of the cases, the Np nucleus emits additionally a 60 keV gamma ray and all further gamma emission is strongly suppressed (see table 6). For this reason, ^{241}Am is widely used as a calibration source because

the simplicity of its first order gamma ray energy spectrum. In 38% of the cases, re-configuration of the electrons around the new Np nucleus leads to emission of mostly L shell X-rays of about 20 keV (see figure 85).

The ^{241}Am source was used for part of the measurements, but is not continuously installed on the telescope. For this reason, only cross-check were made using this source.

γ-emission ^{241}Am					
E_γ [keV]	ΔE_γ [keV]	Compton edge [keV]	prob. emission [%]	λ_{abs} [cm]	$\lambda_{Compton}$ [cm]
26.3448	0.0002	2	2	0.3	3.0
59.5412	0.0001	11	36	3.5	2.8

Table 6: The most important γ-ray emission lines of ^{241}Am. Not shown are gamma rays with emission probabilities less than 0.2%. The typical interaction lengths were calculated for silicon. Energies and probabilities from [237], absorption lengths from [234].

γ-emission ^{133}Ba					
E_γ [keV]	ΔE_γ [keV]	Compton edge [keV]	prob. emission [%]	λ_{abs} [cm]	$\lambda_{Compton}$ [cm]
53.16	0.05	9	2	2.4	2.8
79.61	0.05	19	3	8.76	2.9
80.998	0.008	19	34	9.33	2.9
276.40	0.01	144	7	429	3.9
302.85	0.01	164	18	536	4.1
356.01	0.02	207	62	858	4.3
383.85	0.02	231	9	1073	4.4

Table 7: The most important γ-ray emission lines of ^{133}Ba. Not shown are gamma rays with emission probabilities less than 1%. The typical interaction lengths were calculated for silicon. Energies and probabilities from [237, 238], absorption lengths from [234]

Figure 85 gives an example of the spectrum obtained with a high-resolution state-of-the-art Si-detector while figure 90 shows the spectrum obtained with a test setup at IFAE. One can clearly distinguish the prominent 59.6 keV peak.

The ^{133}Ba Calibration Source

^{133}Ba is a β- and γ-emitter decaying into the stable ^{133}Cs with a half life time of 10.6 years. The ^{133}Cs nucleus can be created in a stable or four excitated energy levels, thus a variety of possible γ-emission lines are observed, the most important of which are listed in table 7, together with their interaction lengths in silicon. The most prominent features of a ^{133}Ba spectrum are an absorption peak at 81 keV and a Compton edge at 207 keV. With thick detectors, the absorption peaks of the four energetic gamma rays are also prominent parts of the spectrum. Moreover, the reconfiguration of the electronic shell of the Cesium leads to K shell X-rays, mostly with energies between 30 and 35 keV. Figure 86 gives an example of a ^{133}Ba spectrum, obtained with a high-resolution Germanium detector. Besides the various absorption peaks, the Compton edge at 207 keV is clearly visible.

In the PIN diode setup, the interaction lengths of the energetic ($E_\gamma > 300$ keV) gamma rays are so small that the corresponding absorption peaks are not distinguishable any more.

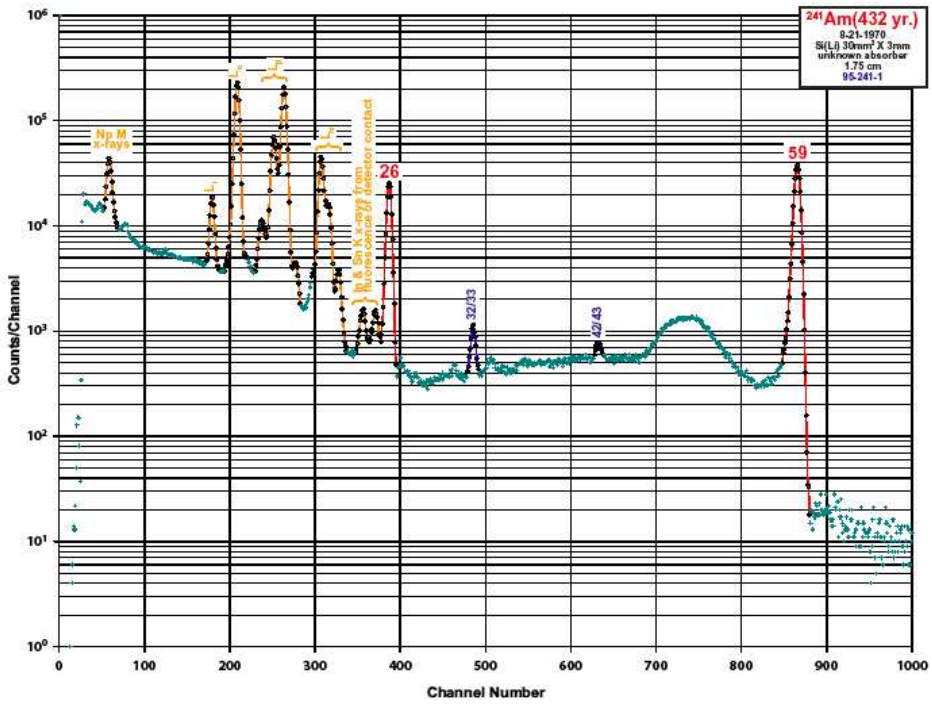

Figure 85: Spectrum photon emission of ^{241}Am

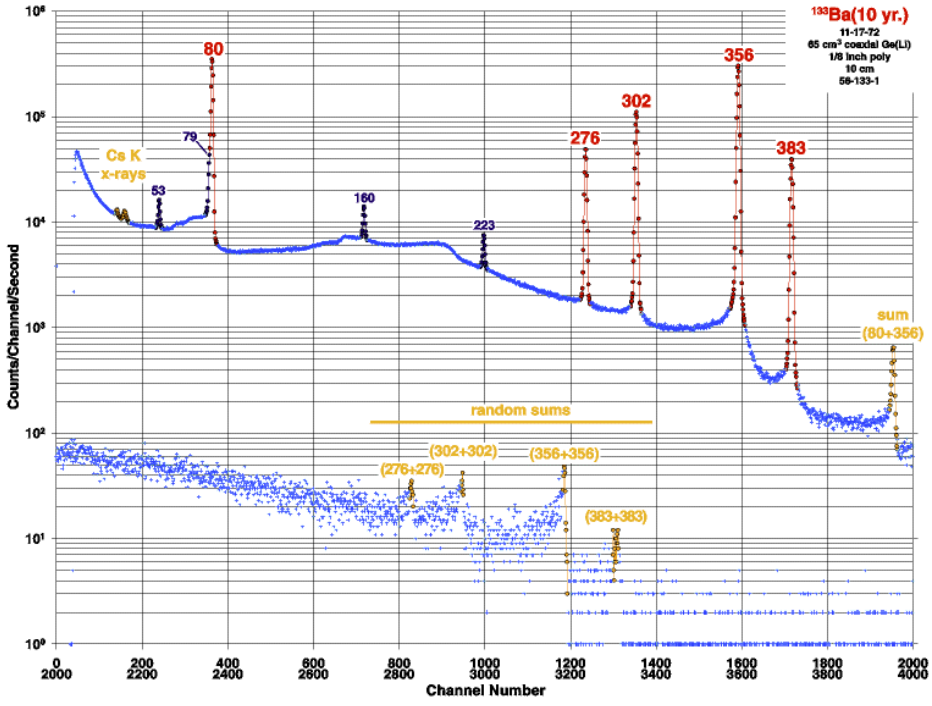

Figure 86: Spectrum photon emission of ^{133}Ba

4.5.5 Noise Behaviour of the PIN Diode

As dark noise is the limiting factor to the charge resolution obtained with a PIN diode, a closer look at the individual contributions to the intrinsic noise is useful. Figure 87 shows a simplified version of the readout circuit of the PIN diode. Using a pulse shaper with characteristic time T_S, the following noise contributions can be identified:

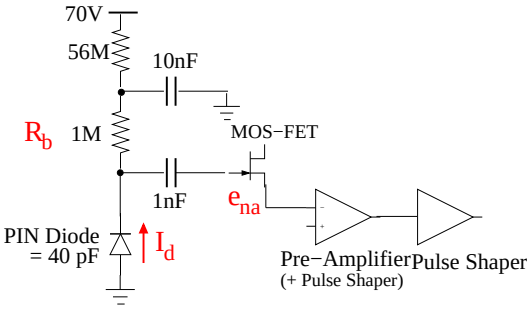

Figure 87: Simplified schematics of the PIN diode readout circuit

• Shot noise due to the residual leakage current I_d in the PIN diode. Its variance is proportional to the leakage current (Poissonian statistics) which in our case has been measured to about 5 nA at room temperature. The equivalent noise charge of this contribution amounts to

$$(Q_n/e)^2 \approx \frac{2I_d}{e} \cdot T_S \qquad \approx 13 \cdot \left(\frac{I_d}{[\mathrm{nA}]}\right) \cdot \left(\frac{T_S}{[\mathrm{ns}]}\right) , \tag{50}$$

where e is the electron charge. Note that the reverse bias current depends strongly on the temperature, namely as [235]

$$\frac{I_d(T_2)}{I_d(T_1)} = \left(\frac{T_2}{T_1}\right)^2 \cdot \exp\left[-\frac{E_g}{2k}\left(\frac{T_1 - T_2}{T_1 T_2}\right)\right] , \tag{51}$$

where E_g is the band gap energy (1.2 eV) and k the Boltzmann constant. Cooling the setup from 25 °C to 0 °C yields then a factor 10 reduction of I_d.

• Noise from the bias resistor R_b. Its variance is linearly proportional to the temperature T and inversely proportional to the resistance.

$$(Q_n/e)^2 \approx \frac{4\,kT}{e^2 R_b} \cdot T_S \qquad \approx 630 \cdot \left(\frac{T}{[290\ \mathrm{K}]}\right) \cdot \left(\frac{[\mathrm{M\Omega}]}{R_b}\right) \cdot \left(\frac{T_S}{[\mathrm{ns}]}\right) , \tag{52}$$

• Amplifier noise e_{na}^2. Both the currently used MOS-FET 2SK322 as the subsequent low-noise amplifier CLC425 have a voltage noise coefficient e_{na} of about $1\,\mathrm{nV}/\sqrt{\mathrm{Hz}}$. The equivalent noise charge depends on the sum of capacitances C_d at the input which are about 40 pF for the PIN diode, and 9 pF at the input of the MOS-FET, thus $C_d \approx 50$ pF. Note that a MOS-FET has a negligible gate current ($I \ll 1$ nA) and is neglected here.

$$(Q_n/e)^2 = \frac{e_{na}^2 C_d^2}{e^2} \cdot \frac{1}{T_S} \qquad \approx 1 \cdot 10^8 \left(\frac{C_d^2}{[(50\ \mathrm{pF})^2]}\right) \cdot \left(\frac{[\mathrm{ns}]}{T_S}\right) , \tag{53}$$

• Trapping and de-trapping processes in the PIN diode and the resistors and capacitors can introduce additional non-white noise fluctuations. This noise usually exhibits a 1/f power spectrum. It contributes to the "parallel" noise e_n and can be

parameterized by a device specific constant A_f which amounts to about $10^{-12}\,\mathrm{V}^2$ for the MOS-FET and yields

$$(Q_n/e)^2 = \frac{A_f C_d^2}{e^2} \qquad \approx 1 \cdot 10^5 \left(\frac{C_d^2}{[(50\ \mathrm{pF})^2]}\right) . \tag{54}$$

In total, the equivalent noise charge Q_n can be estimated in the following form:

$$Q_n/e \approx \sqrt{(13 + 630) \cdot \left(\frac{T_S}{[\mathrm{ns}]}\right) + 10^8 \cdot \left(\frac{[\mathrm{ns}]}{T_S}\right) + 10^5} \tag{55}$$

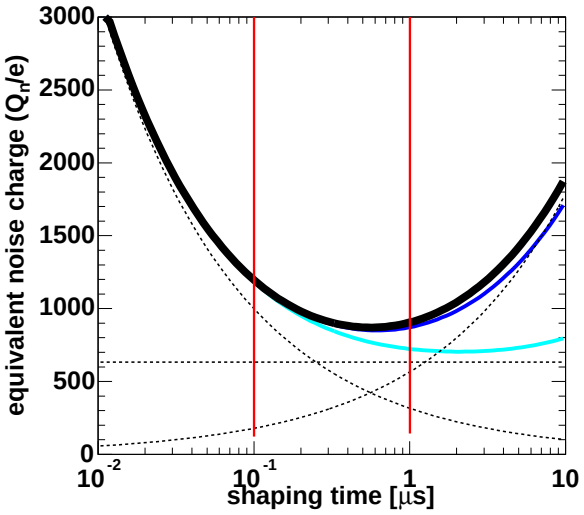

Figure 88: Equivalent noise charge vs. shaping time for the PIN diode front end electronics (eq. 55). As dotted lines, the individual components are drawn, in blue the total noise charge for the case of 0 °C *outside temperature. In light blue, if PIN diode and pre-amplifiers are getting cooled to* −30 °C *and the bias resistor raised by a factor 10. In red, the chosen shaping times for two measurements of the absolute light flux (see text).*

One can see that the "series" noise contributions (first term) increase with shaping time T_S and the "parallel" noise contributions (second term) decrease with shaping time. The specific form of the pulse shaper adds factors of order unity to the individual terms (0.5 for series noise, 1.0 for the parallel nosie and 4 for the constant term in the used differentiator-integrator setup [236]). These numbers have been included in figure 88). Moreover, the parallel noise contribution largely out-ranges the series one at low shaping times. A broad minimum is reached below about 1 µs. Equation 55 gives an estimate of the noise introduced in the front-end electronics and represents thus a lower limit to the recorded noise of the registered signals. Figure 88 displays eq. 55 with the three components shown separately as dotted lines.

Two measurements of the absolute light flux were performed, one without limitations of the readout, where an optimal shaping time of 1 µs was chosen, and another

one performed with the MAGIC FADCs where a maximum shaping time of only 100 ns was allowed. These two numbers are marked as red lines in figure 88.

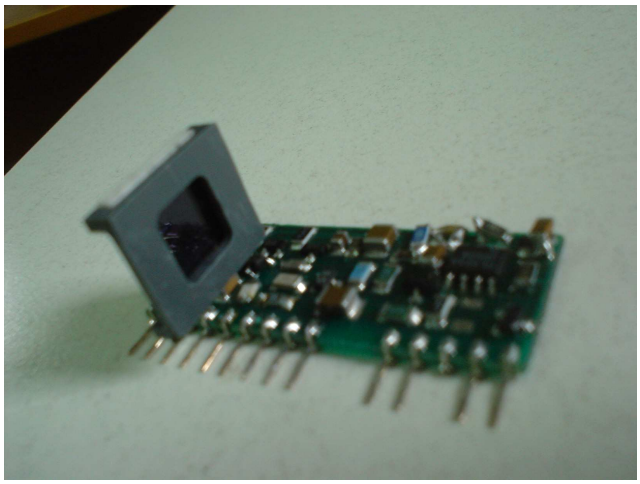

Figure 89: The PIN diode mounted on the pre-amplifier. The diaphragm is visible and the front-end amplifiers and shapers.

4.5.6 PIN Diode Readout

The PIN diode signal after the front-end amplifiers is converted to an analog optical signal by an optical LED transmitter (type HFBR-1406). The optical signal travels to the Control House via 150 m of optical fiber and gets converted back to an analog electrical signal via a low-noise, amplifying fiber optic receiver (type HFBR-2406). The signal was then recorded by a *QVT*-multi-channel analyzer (LeCroy) during a testing phase in May, 2005 and later by the MAGIC FADCs. In both cases, the PIN diode signal is split into two parts, one used to self-trigger the FADC readout while the other one gets then recorded in the correct time interval. In this way, the signals from the radio-active source can trigger the telescope readout during normal data taking, at a usual rate of about 7 Hz for the ^{133}Ba source.

Figure 90 gives an example of various spectra which were obtained with the *QVT*-multichannel analyzer. One can see the 60 keV peak of the ^{241}Am source and several features of the ^{133}Ba spectrum, among which the absorption peak at 81 keV can be most easily discerned. Also the spectra of two typical intense blue light pulses are shown. Figure 91 shows the PIN diode self-calibration result using these spectral features. A precision of better than 1% could be achieved. Using the MAGIC FADC system, the emission peak of the ^{133}Ba can still be recognized with enough precision to perform an online self-calibration of the PIN diode, every time when desired.

After installing the system at the telescope, a series of systematic studies were performed during June, 2005. Especially, a PIN diode self-calibration was performed every night using the ^{133}Ba source. Figure 93 shows the evolution of the fitted peak positions of the 81 keV absorption line during the month of June, 2005 and

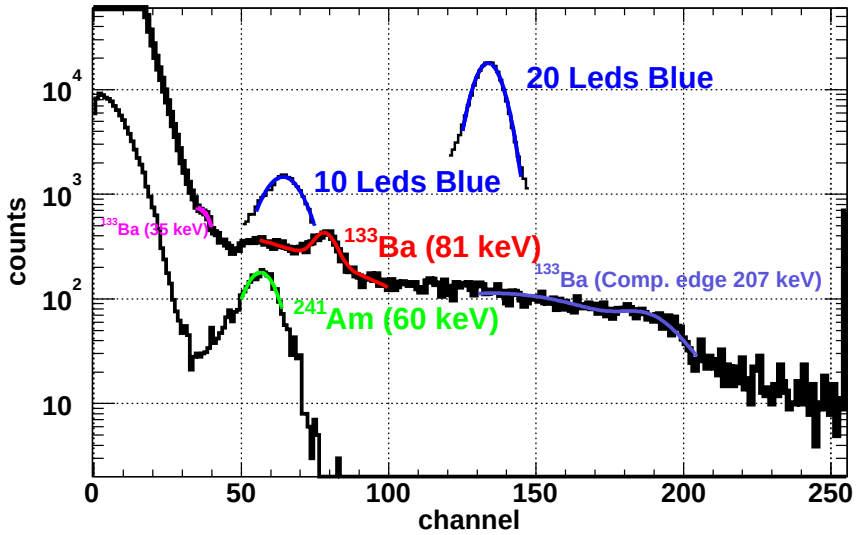

Figure 90: Various spectra taken with the PIN Diode and read out with a LeCroy QVT multi-channel analyzer. Bottom green: ^{241}Am with a 60 keV photon emission line, center red: ^{133}Ba with a photon emission line at 81 keV and a Compton egde at 207 keV, top blue: the spectrum obtained from blue light pulses with two intensity combinations.

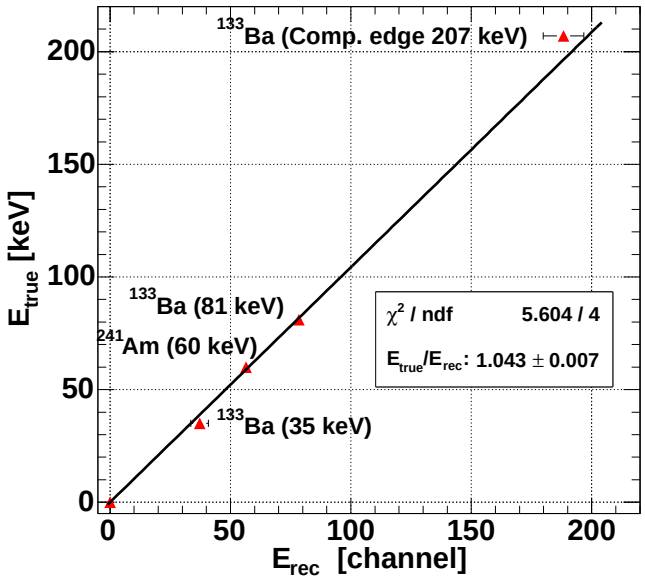

Figure 91: Calibration results from fitted spectra of figure 90.

in February, 2006. One can see an amplification drop around run 58300 and in 2006. Most probably, these drops can be attributed to a loss of reverse voltage, either by switching off the voltage or due to a loss of the battery power. Note that no maintainence access has been made to the calibration system since May, 2005. However on medium time scales, the position of the peak does not vary by more than 2%, with an RMS of less than 1%. At the same time, the peak width (figure 94) lies stably around 1000-1200 photo-electrons, except for the time periods showing the amplification drop where it is lightly higher. The average peak width value coincides nicely with the expected values (compare also with figure 88).

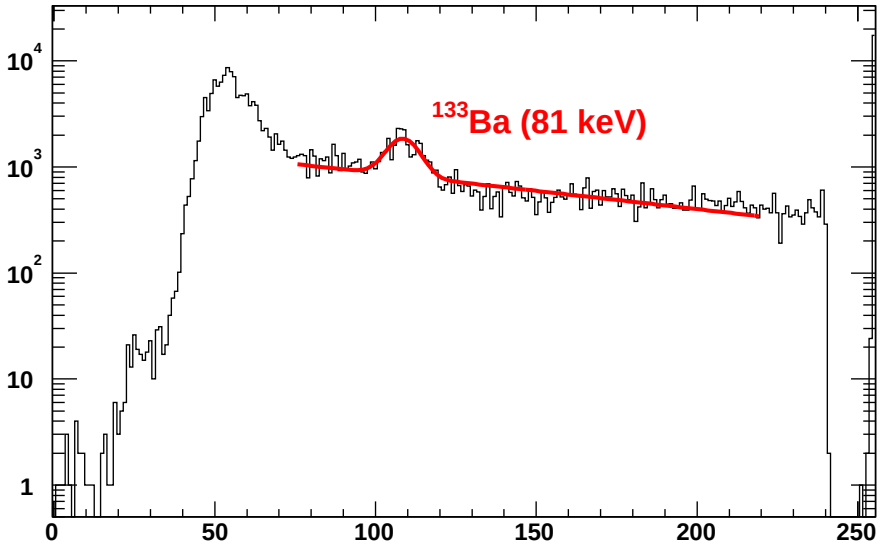

Figure 92: The ^{133}Ba spectrum, taken with the PIN Diode and read out with the MAGIC FADCs at La Palma. In red, a combined fit to the 81-keV emission peak and the combination of Compton edges from higher energy X-rays.

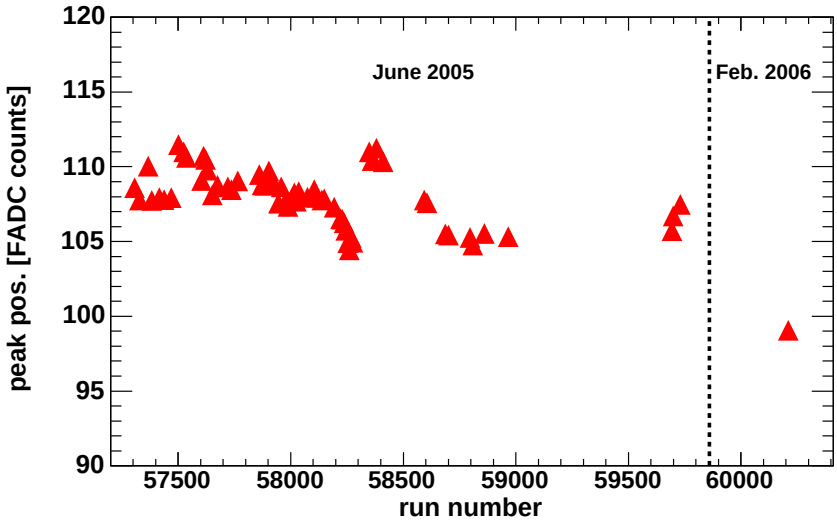

Figure 93: Positions of the ^{133}Ba 81 keV absorption peak vs. run number. The left side corresponds to the beginning of June, 2005, the right side to one month later. A possible explanation of the drop around run 58300 can be found in the text.

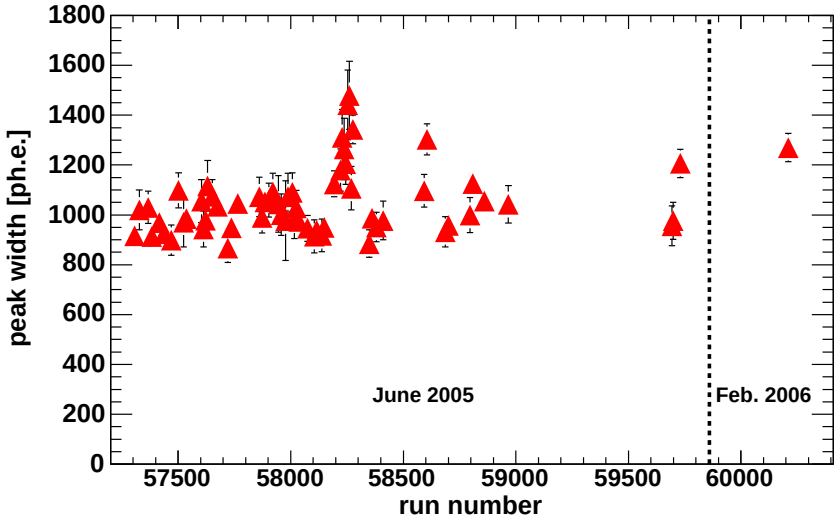

Figure 94: Widths of the ^{133}Ba 81 keV absorption peak (in photo-electrons) vs. run number.

4.6 The Camera

Besides the Blinded Pixels and the PIN Diode, the ***camera*** itself can be used to measure the absolute amount of photons emitted by the light pulser.

As the MAGIC PMTs are operated at a relatively low gain, single photo-electron spectra (like in the case of the Blinded Pixels) are too poor to extract mean numbers of photo-electrons. However, at higher photo-electron fluxes, the spectra can be fitted well to Gaussian distributions: if the noise intensity is sufficiently low and the mean number of photo-electrons large $\mu_{\text{p.e.}} \geq 10$, the photo-multiplier response function (eq. 39) can be simplified, assuming that the Poisson distribution of photo-electrons goes over to a Gaussian with standard deviation $\sqrt{\mu_{\text{p.e.}}}$ [228]:

$$S_\infty(x) \propto \exp\Big(-\frac{(x-Q_0-Q_{sh}-\mu_{\text{p.e.}}Q_1)^2}{2\,(\sigma_0^2+\sigma_\eta^2+\mu_{\text{p.e.}}(\sigma_1^2+\sigma_{\text{VCSEL}}^2+Q_1^2))}\Big)$$

with :

$$\begin{aligned}
\sigma_{\text{VCSEL}} &\approx 0.02\cdot Q_1 \qquad \text{(inner pixels)} \\
&\approx 0.04\cdot Q_1 \qquad \text{(outer pixels)} \\
\sigma_\eta &= \sqrt{(\text{Var}(\eta)/\eta^2}\cdot\mu_{\text{p.e.}}Q_1 \approx 0.01\cdot\mu_{\text{p.e.}}Q_1 \\
Q_{sh} &\approx w/\alpha \ll \mu_{\text{p.e.}}\cdot Q_1\ ,
\end{aligned} \tag{56}$$

where the exponential background was assumed to be small ($1/\alpha \ll Q_1$) and manifests itself as an effective spectrum shift Q_{sh}. While the photo-multiplier produces the noise contribution σ_1, an additional component comes from the optical transmitter (VCSELs) which is denoted with σ_{VCSEL} (see figure 50 for the estimation of the absolute values). The term σ_η^2 denotes the additional variance due to inhomogeneous photon detection effiencies, depending on where and under which angle the photo-electrons are kicked out [239]. We assume here an uncertainty of about 1–3% for the combination of both cases (see figures 43 and 47). While this contribution to the variance of the signal was negligible for the blinded pixels, mainly because of the diaphragm in front and the low mean number of photo-electrons, it cannot neglected here.

The Gaussian distribution allows to extract a mean signal μ_{gauss} and its standard deviation σ_{gauss}:

$$\begin{aligned}
\mu_{gauss} &= \mu_{\text{p.e.}}Q_1 + Q_{sh} \\
\sigma_{gauss} &= \sqrt{\sigma_0^2+\mu_{\text{p.e.}}\cdot(\sigma_1^2+\sigma_{\text{VCSEL}}^2+Q_1^2)+\sigma_\eta^2}\ .
\end{aligned} \tag{57}$$

If the background noise σ_0 is known (e.g. from direct measurement close in time), the mean number of photo-electrons can be calculated:

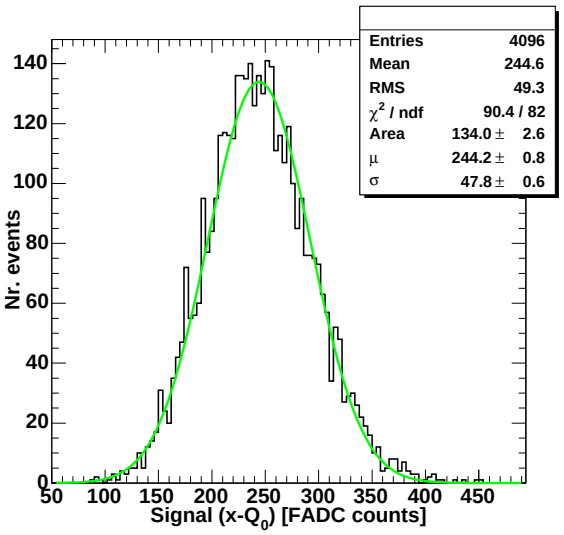

Figure 95: Example of a Gaussian fit to a distribution of charges, obtained with a typical inner pixel and a typical calibration run. The mean number of incident photo-electrons is assumed to about 35 in this case.

$$\mu_{\text{p.e.}} \approx F^2 \cdot \frac{(\mu_{gauss} - Q_{sh})^2}{\sigma^2_{gauss} - \sigma^2_0 - \sigma^2_\eta} \tag{58}$$

with :

$$F = \sqrt{1 + \frac{\sigma_1^2 + \sigma^2_{\text{VCSEL}}}{Q_1^2}}\,, \tag{59}$$

where F is the so-called ***excess-noise factor***, an intrinsic parameter of a the amplification chain. It consists of a contribution from the photo-multiplier itself ($F_{\text{PMT}} = \sqrt{1 + \sigma_1^2/Q_1^2}$) and the additional excess noise from the optical transmitters ($\sigma^2_{\text{VCSEL}}/Q_1^2$). The excess-noise factor of the photo-multiplier can be measured beforehand and changes slowly, but gradually with time. Typical values are $\sigma_1^2/Q_1^2 \approx 0.32$ for the PMTs installed in the MAGIC camera. Compared to this number, $\sigma^2_{\text{VCSEL}}/Q_1^2 \lesssim 0.001$ is really small and can usually neglected [39]. This does neither hold for the sporadically occurring "mode-hopping" of the VCSels nor for so-called "ringing" PMTs. These cases, if happening, need special care and are treated in a later chapter. Figure 96 shows an extreme case of such a behavior.

The contribution of the non-uniform quantum efficiency, characterized by σ_η, and further unknown contributions to the signal variance, can by tested by using the

[39] In fact, this term was only included here to demonstrate that the **short-term** fluctuations of the optical transmitters do not affect the calibration with the F-Factor method, a concern sometimes raised in the collaboration.

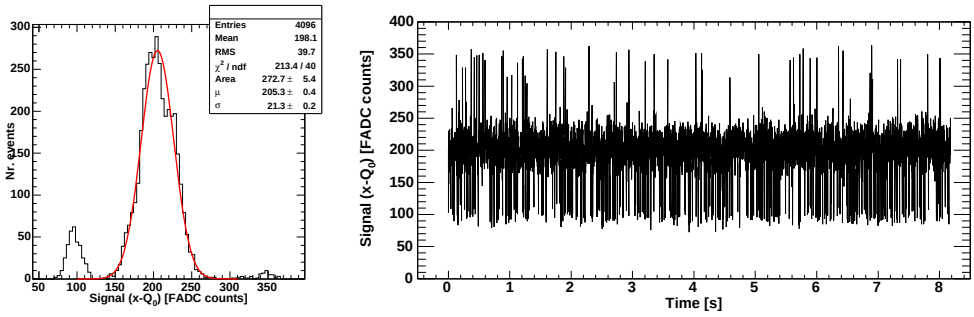

Figure 96: Left: example of a Gaussian fit to a distribution of charges, obtained from a "ringing" pixel, right: the time-line of the extracted charges.

linearity of the photomultiplier and the signal transmission chain (eq. 57) and the definition of the excess-noise factor (eq. 58):

$$\frac{\sigma^2_{gauss} - \sigma^2_0 - \sigma^2_\eta}{\mu^2_{gauss}} \approx (F^2 \cdot Q_1)/\mu_{gauss} \ , \tag{60}$$

where the quantity $F^2 \cdot Q_1$ is a constant, once the photo-multiplier ramped up to its nominal voltage and the transmission chain having reached stability. Illuminating the camera with different intensities of pulsed light and plotting $(\sigma^2_{gauss} - \sigma^2_0 - \sigma^2_\eta)/\mu^2_{gauss}$ against $1/\mu_{gauss}$ should then yield a straight line through the origin, with a slope $F^2 \cdot Q_1$. Physically speaking, this means that in the limit $\mu_{\text{p.e.}} \to \infty$, the relative variance of the (Poissonian) signal vanishes, leaving only contributions which do not decrease with the number of photo-electrons. Thus, if the fitted line does not pass through the origin, probably a further contribution σ_{missing} to σ_{gauss} exists and has not been taken properly into account [40]. Figures 97 gives an example of such a test plot for the high-gain and the low-gain channel of a same pixel. One can see that the fit shows a good precision and the fitted slope agrees well between the two readout channels. This is not the case for the offsets, as will be further explained in the next chapter. Generally, the low-gain readout with signals from a higher numbers of photo-electrons yield offsets of much better precision. Figures 98 show therefore the results of fitted offset σ_{missing} to test plots for all pixels, with different contributions of σ_η, extracted from the low-gain channel. One can see that an upper limit of about 1% contribution of σ_η can be set, but the spread of the fit results themselves yield about $\sigma_{\text{missing}}/\mu_{gauss} \approx 2\,\%$.

In the beginning of the life-time of a Cherenkov telescope, the ***Excess-Noise Factor Method*** can be used to calibrate the camera, but the unknown degradation of the photo-multipliers and therewith increase of the excess noise with the years introduces a gradual worsening of the precision of this method. A more detailed description of the excess noise factor method can be found in [239, 240].

[40] In the collaboration, this plot has become to be known as the "Razmick"-plot, since first proposed by Razmick Mirzoyan.

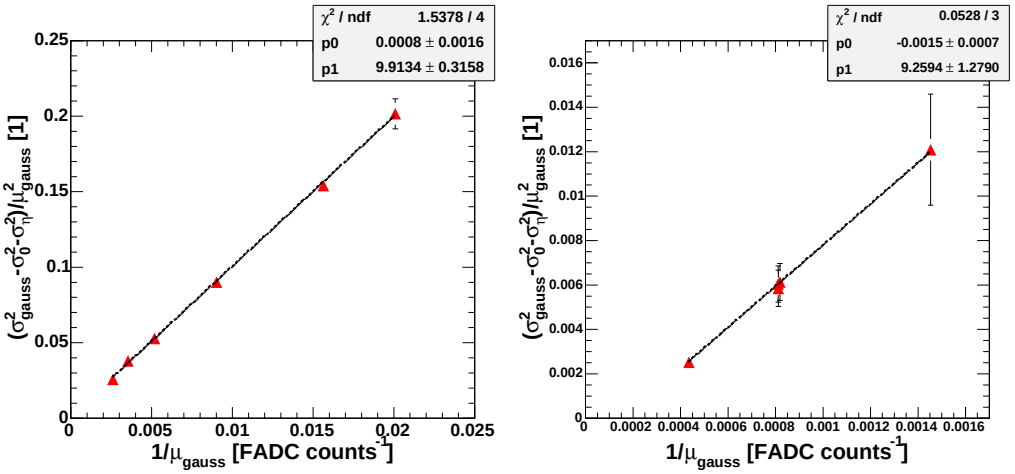

Figure 97: Examples of the $(\sigma^2_{gauss} - \sigma^2_0 - \sigma^2_\eta)/\mu^2_{gauss}$ vs. $1/\mu_{gauss}$ test plots, obtained with various intensities and for one test pixel. Left: high-gain channel, right: low-gain channel.

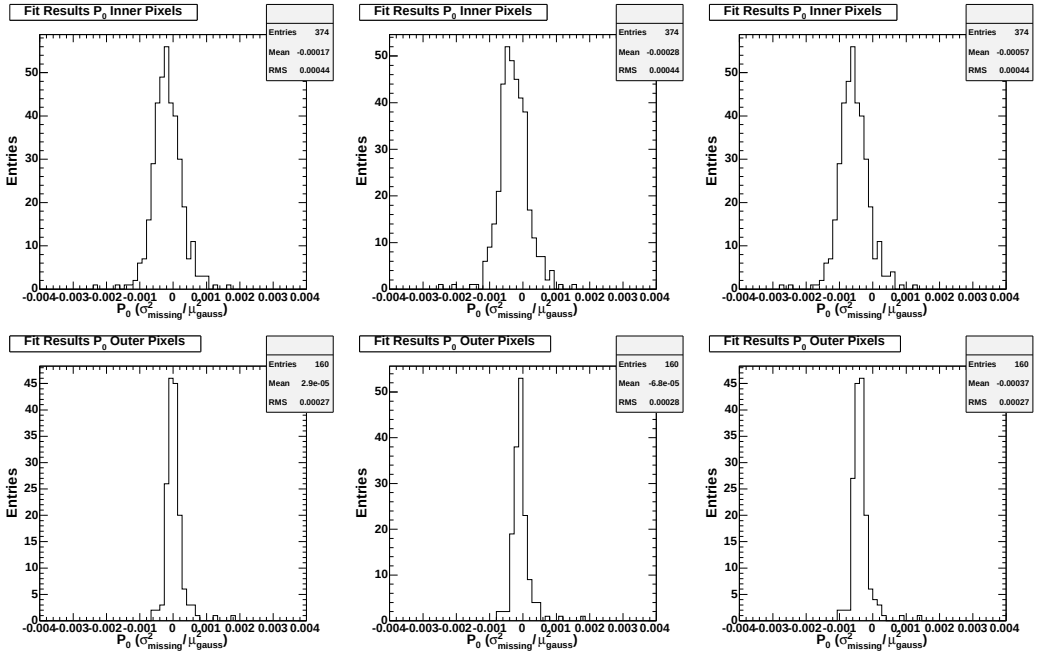

Figure 98: Offsets from line fit to the $(\sigma^2_{gauss} - \sigma^2_0 - \sigma^2_\eta)/\mu^2_{gauss}$ vs. $1/\mu_{gauss}$ test plots, obtained with various intensities and the low-gain readout channel. Top: all inner pixels, bottom: all outer pixels, left: without correction σ_η, center: with a 1% correction, right: with a 2% correction of σ_η applied.

The advantage of this method lies in the fact that the average number of photo-electrons can be calculated for every photomultiplier individually, at least in the inner part of the camera, and the result averaged over all N photo-multipliers of a same size and quantum efficiency. To be robust against outliers, e.g. the median can be calculated:

$$< \mu_{\text{p.e.}} >= \text{median}[\mu_{\text{p.e.}}] \tag{61}$$

Statistical uncertainties get thereby reduced by a factor $\sqrt{2N/\pi}$, usually about 15 in our case. Because the statistical errors on μ_{gauss} and σ_{gauss} are small anyhow, this mean in fact that the excess noise factors of the individual pixels get averaged and one global ***average excess noise factor*** $< F >$ can be used. Systematic degradations of the quality of the photo-multipliers apply then to $< F >$.

From the averaged quantum efficiency spectrum of all measured photo-multipliers $< QE(\lambda) >$ (figure 43) and the measurements of the efficiency of the light guides (figure 47), one can define an averaged quantum efficiency of the combination photo-multiplier and light guides:

$$\overline{QE} = \int_{-\infty}^{+\infty} \frac{dn_{\text{ph}}}{d\lambda} \cdot < QE > (\lambda) \cdot \eta_{\,\text{lightguide}}\, d\lambda \ . \tag{62}$$

The integration goes over the entire wavelength-spectrum $dn_{\text{ph}}/d\lambda$ (figure 68) for every of the three possible light pulser colors (see eq. 27).

Subsequently, the total amount of photons, N_{ph} emitted by the light pulser into the 2° uniformity cone, can be retrieved:

$$\begin{aligned}
N_{\text{ph}} &= < \mu_{\text{p.e.}} > \cdot C_{\text{cam}} && \text{with :} \\
C_{\text{cam}} &= D_{\text{cam}}^2 \cdot \Omega_{tot} / (A_{\text{pix}} \cdot T_{\text{plex}} \cdot \overline{QE} \cdot \eta_{\,\text{coll}}(\overline{\lambda})) \ , && (63) \\
\frac{\Delta N_{\text{ph}}}{N_{\text{ph}}} &= \sqrt{(\frac{\Delta < \mu_{\text{p.e.}} >}{< \mu_{\text{p.e.}} >})^2 + (\frac{\Delta C_{\text{cam}}}{C_{\text{cam}}})^2} && \text{with :} \\
\frac{\Delta C_{\text{cam}}}{C_{\text{cam}}} &= \sqrt{(\frac{2\Delta D_{\text{cam}}}{D_{\text{cam}}})^2 + (\frac{\Delta A_{\text{pix}}}{A_{\text{pix}}})^2 + (\frac{\Delta T_{\text{plex}}}{T_{\text{plex}}})^2 + (\frac{\Delta \overline{QE}}{\overline{QE}})^2 + (\frac{\Delta \eta_{\,\text{coll}}}{\eta_{\,\text{coll}}})^2} && (64)
\end{aligned}$$

where $D_{\text{cam}} = 18.24 \pm 0.01$ m is the distance of the light diffuser plate from the light guides of an inner pixel in the camera, $A_{\text{pix}} = 779.4\,\text{mm}^2$ the geometrical area of the light guides, T_{plex} the transmission of the plexiglas (figure 48) and $< \eta_{\,\text{coll}}(\overline{\lambda}) >$ the mean collection efficiency of the photo-electrons from the photo cathode to the first dynode.

	Averaged Inner Pixel parameters			
	UV	Blue	Green	comments
$\overline{QE}$	0.271	0.258	0.205	incl. $\eta_{\text{lightguide}}$
$\eta_{\text{lightguide}}$	0.94	0.94	0.94	assume 85% refl. and 37% of light hitting light guides
T_{plex}	0.91	0.92	0.92	
η_{coll}	0.90	0.90	0.93	estimations
C_{cam}	$1.47 \cdot 10^4$	$1.53 \cdot 10^4$	$1.86 \cdot 10^4$	
	estimates			
	[%]	[%]	[%]	
$\Delta\overline{QE}/\overline{QE}$	3.5	3.5	8	incl. 3% $\Delta\eta_{\text{lightguide}}$
$\Delta A_{\text{cam}}/A_{\text{cam}}$	< 0.1	< 0.1	< 0.1	
$\Delta D_{\text{cam}}/D_{\text{cam}}$	< 0.1	< 0.1	< 0.1	
$\Delta T_{\text{plex}}/T_{\text{plex}}$	2	2	2	
$\Delta\eta_{\text{coll}}/\eta_{\text{coll}}$	5	5	5	
$\Delta C_{\text{cam}}/C_{\text{cam}}$	6	6	9.5	

Table 8: Averaged combined efficiencies $\overline{QE}$ of the camera average (see equation 64) for the three possible light pulser colors UV, blue and green. The uncertainties have been obtained by varying the spectral parameters, as obtained in section 4.1.1, including systematic uncertainties in the overall estimation of the blind pixels quantum efficiency (1%) and the transmission coefficients of the filters. The large relative uncertainty in the green is mainly due to the falling blinded pixels quantum efficiency spectrum and the uncertainty about the peak wavelength.

5 Signal Extraction

The goal for an optimal signal reconstruction algorithm is to compute an unbiased estimate of the strength and arrival time of the Cherenkov signals with the highest possible resolution for all signal intensities. Furthermore, the algorithm must be stable with respect to changes in observation conditions and background levels and between signals obtained from gamma or hadronic showers or from muons. Last, the needed computing time has to be kept within acceptable limits.

5.1 Review Signal Acquisition

The PMT signals of the MAGIC camera are getting amplified and transmitted over about 160 m of optical fiber to the Control House where they are transformed back to electrical signals (see chapter 3.8). At that stage, typical pulses of signals from captured gamma-ray showers have about 2.2 ns FWHM and rise and fall times of about 1 ns. In order to sample these short pulse shapes with the 300 MSamples/s FADC system, the pulse gets stretched explicitly with an RC-CR integrator-differentiator component. Mathematically speaking, the original pulse is folded with a stretching function of 6 ns leading to an outgoing asymmetric pulse with a FWHM greater than 6 ns.

Because the MAGIC FADCs have a resolution of 8 bit only, the signals are getting split into two branches with gains differing by about a factor 10. The ***low-gain*** branch gets delayed by 55 ns with respect to the ***high-gain*** one, then both branches are multiplexed and subsequently read out by one FADC (see chapter 3.10). The limited bandwidth of the passive delay line introduces an additional pulse stretching of about 7 ns FWHM to the low-gain branch and the GaAs switch produces a characteristic ***switching noise*** lasting about 5–10 ns, before the low-gain pulse arrives. Figure 99 shows the reconstructed pulse shapes of an electronic test pulse of about 2 ns FWHM, ressembling typical MAGIC PMT signals. The test pulses were passed through the entire MAGIC signal transmission and acquisition chain, the signals were reconstructed from the registered FADC samples, normalized to the same amplitude and shifted in time such that all signals start at the FADC slice number. The resulting average pulse shape yields a FWHM of 6.3 ns for the high-gain part and about 10 ns for the delayed low-gain part. About 2–3 FADC slices before the start of the low-gain pulse, the (averaged) switching noise contribution is visible.

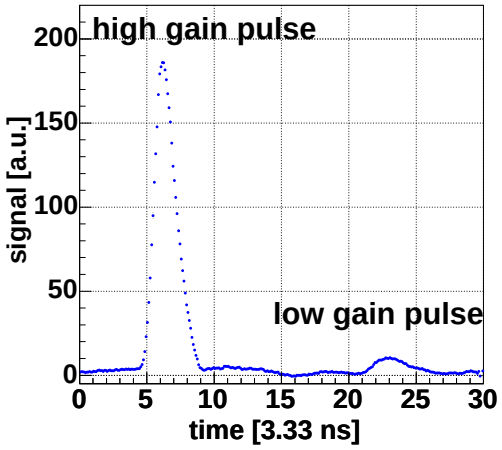

Figure 99: Average reconstructed pulse shape from test pulses. Figure from Hendrik Bartko.

Figure 100 shows typical average normalized pulse shapes, normalized to the same area: high-gain and low-gain pulses from cosmics, the pulse shape implemented in the MC simulation and those obtained from calibration runs with UV and green LEDs. One can observe that the calibration pulse shape obtained from UV LEDs ressembles very well the one obtained from cosmics while the green (and blue) LEDs yield slighty broader pulses (6.5 ns FWHM) and have a pronounced tail. Especially the (averaged) contribution of the ***secondary pulse*** at about 8 ns from the pulse maximum can be discerned.

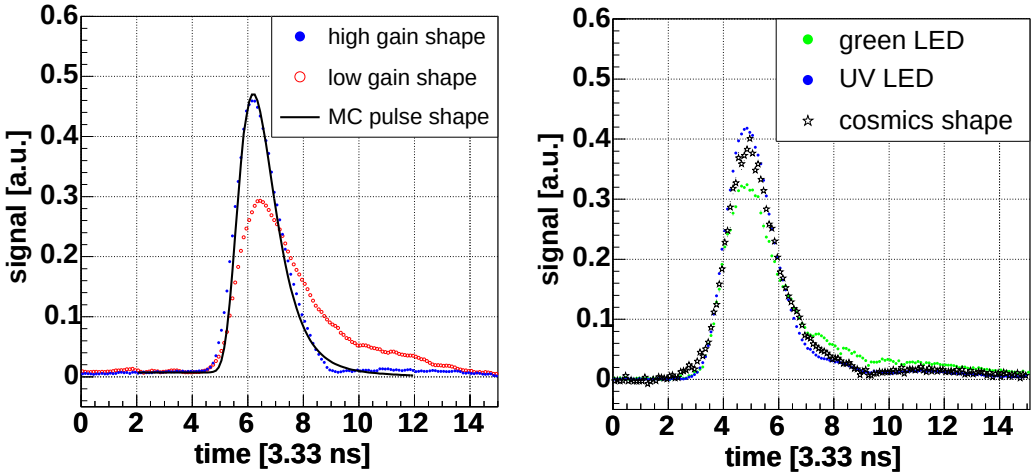

Figure 100: Average normalized reconstructed pulse shapes. Left: high gain (blue, FWHM 6.3 ns) and low gain (red, FWHM 10 ns) pulse shapes from test pulses. The black line corresponds to the high-gain pulse shape implemented in the MC simulations. Right: high gain pulse shapes from calibration pulses with UV and green LEDs (FWHM: 6.5 ns), compared with the average high gain pulse shape from cosmics. Figures from Hendrik Bartko.

5.2 Statistical Properties of Signal Extractors

In the following, a brief introduction to common signal extraction theory is given and criteria for an optimal signal reconstruction algorithm will be developped. Most of the presented theory can be found in [241] and was adapted for the case of the MAGIC Telescope data acquisition.

Consider a large number of identical signals, corresponding to a fixed number of photo-electrons: N_{phe}. By applying a signal extractor, a distribution of estimated signals $\widehat{N}_{\mathrm{phe}}$ is obtained (for fixed N_{phe} and fixed background fluctuations BG). The deviation between true and reconstructed value is defined as:

$$X = \widehat{N}_{\mathrm{phe}} - N_{\mathrm{phe}} \tag{65}$$

Any signal extractor is called ***consistent*** if the quantity X converges to zero as the amount of data increases. Consistency is the most important requirement of an extractor. It requires that the reconstructed signal is proportional to the number of photo-electrons, amplified by the PMT. However, deviations from linearity can be obtained in the following cases:

- At very low signals, a possible bias can cause too high reconstructed signals (positive X).
- At very high signals, the FADC system goes into saturation and the reconstructed signal becomes too low (negative X).
- Any error in the inter-calibration between the high- and low-gain acquisition channels yields an effective deviation from linearity by a constant offset above the low-gain threshold.
- The extraction of the low-gain pulse can be critical: The time delay between high-gain and low-gain pulse is small, therefore mis-interpretations between the tail of the high-gain pulse and the low-gain pulse might occur for large pulses. Moreover, the total recorded time window is relatively small and late pulses might already reach out of the recorded FADC window.

The distribution of the quantity X has a mean B and a variance V defined as:

$$B = < X > = < \widehat{N}_{\mathrm{phe}} > - N_{\mathrm{phe}} \quad (66)$$

$$V = < (X - B)^2 > = \mathrm{Var}[\widehat{N}_{\mathrm{phe}}] \quad (67)$$

$$RMSE = \sqrt{< X^2 >} = \sqrt{V + B^2} \quad (68)$$

The parameter B is also called the ***bias*** of the estimator. If known, it can be subtracted from $\widehat{N}_{\mathrm{phe}}$ to yield a new estimate $\widehat{N}'_{\mathrm{phe}} = \widehat{N}_{\mathrm{phe}} - B$.

The ***root-mean-squared error*** $RMSE$ combines resolution and bias. Both depend generally on N_{phe} and the background fluctuations: $B = B(N_{\mathrm{phe}}, BG)$ and $V = V(N_{\mathrm{phe}}, BG)$. The ratio of $1/V$ to its maximal possible value is also called ***efficiency***.

Typically, one can measure easily the variance, but needs the $RMSE$ for statistical analysis (e.g. in the image cleaning). Only in case of a vanishing bias, the two numbers are equal. Otherwise, the bias has to be known beforehand. Degradations of the efficiency are due to limited intrinsic signal extractor precision and to physical background fluctuations, like electronic noise and the PMT response to light of the night sky.

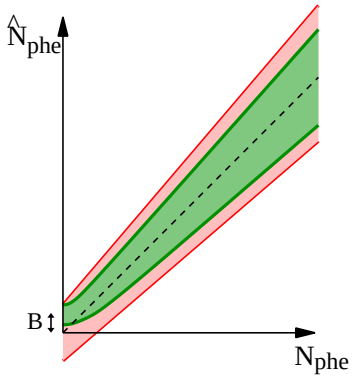

Figure 101: Fixed window (red) and sliding window (green) extractors

The latter consists of amplified photo-electrons and is therefore undistinguishable from very low-intensity Cherenkov shower signals. Every algorithm which actively searches for signals inside a global time window (a so-called ***sliding window algorithm***) will have thus a bias, especially at low or vanishing N_{phe}. Only a reduction of the global time window reduces that bias. In case of no Cherenkov signal, such an algorithm will reconstruct the largest noise pulse which it can find. A signal reconstruction algorithm without bias (a so-called ***fixed window algorithm***) has in many cases a bigger *RMSE*. Figure 101 gives a sketch of typical reconstructed signals from fixed and sliding window extractors.

Finally, the signal extractor has to be ***robust***, i.e. insensitive to departures from assumptions in the pulse shape owing to factors such as noise, intrinsic signal time spreads, etc. This applies especially to pulses with different intrinsic shapes and backgrounds [41]:

- Signals from gamma, hadronic and muonic showers
- Calibration pulses from different LED color pulsers
- Pulse generator test pulses

An important point is the difference between the pulse shapes of the calibration and the Cherenkov shower signals. It has to be ensured that the computed calibration factor between the reconstructed charge in FADC counts and photo-electrons for calibration events is valid for signals from Cherenkov photons.

5.3 Considerations Based on the MAGIC Readout System

Apart from considerations typical for Cherenkov telescopes or FADC pulse reconstruction, the following characteristics of the MAGIC readout system have to be taken into account:

***Inner and outer pixels*:** The outer pixels have a factor four bigger area than the inner pixels. Taking into account the different sizes of the light guides, their (quantum-efficiency convoluted) effective area is slightly less than a factor three higher. As the camera is flat-fielded to yield similar pulse amplitudes for same photon fluences per pixel, the inner pixels are operated at a three times higher gain than the outer ones. This results in lower effective noise charges from the night sky background for the outer pixels. Moreover, due to the lower PMT gain, the amplified electrons of outer pixels have a 1.5 ns longer transit time than the ones from inner pixels.

[41] Unfortunately, the intrinsic small differences in pulse shapes cannot yet be used to discriminate between signals from different types of air showers. This will become possible only with the installation of the next generation DAQ using GHz FADCs.

***AC-coupling*:** The PMT signals are AC-coupled at various places in the signal transmission chain. Adding up a constant number of FADC slices, the contribution of PMT pulses due to the light of night sky is then on average zero, only its RMS depends on the intensity of the background light. In moonless nights, observing an extra-galactic source, a background rate of about 0.13 photo-electrons per nano-second per inner pixel can be assumed. Multiplying this number with the width of an FADC time slice (3.33 ns), a lower limit to the background of $BG \gtrsim \sqrt{0.13 \cdot 3.33} = 0.65$ photo-electrons per FADC slice can be assumed.

***Clock noise*:** The MAGIC 300 MHz FADCs have an intrinsic clock noise of a few least significant bits (LSBs) occurring at a frequency of 150 MHz. This clock noise produces an AB-pattern superimposed on the electronic noise. The amplitude of the clock noise can be measured in pedestal runs and later subtracted from the registered FADC slice values. This is possible because the DAQ stores information about the phase of the AB-pattern.

***Pulse shaping*:** The optical receiver boards shape the pulse with shaping times of about 6 ns, much larger than the typical intrinsic pulse widths. As the shaping time is larger than the width of a single FADC slice, strong correlation of noise between neighbouring FADC slices is expected.

***Momentaneous amplitudes*:** The MAGIC FADCs consists of a series of small comparators which measure the momentaneous amplitude of a pulse at a time. No charge integration over the duration of a time slice is performed by the FADCs. Therefore, pulse structures are lost which have a higher frequency than the 300 MHz of the FADC.

***Trigger jitter*:** As the FADC clock is not synchronized with the trigger, the positions of recorded FADC samples vary uniformely by one FADC slice from event to event. This behaviour does not affect the relative positions of signals between different readout channels within one event.

***DAQ jumps*:** Additionally to the trigger jitter, a time glitch of typically two FADC slices can occur in the readout. This problem affects randomly about 1% of the readout channels. It was repaired mid-2005.

The noise contribution – mainly clock-noise amplitude and pedestal offset – get usually measured directly from late FADC samples, if the signal in the trigger region is not too high, that is: if the low-gain switch has not been applied and hence only high-gain samples stored. In cases where the signal amplitudes are always high, e.g. in calibration light pulser runs, dedicated noise runs (so-called "Pedestal Runs") are taken as close as possible in time.

Figure 102 shows the amplitudes of the mean pedestal offset, the AB-noise amplitude and the pedestal RMS over about one night of data taking with switched-off

camera. One can see the overall stability of mean pedestal and RMS, but large changes in the AB-noise amplitude.

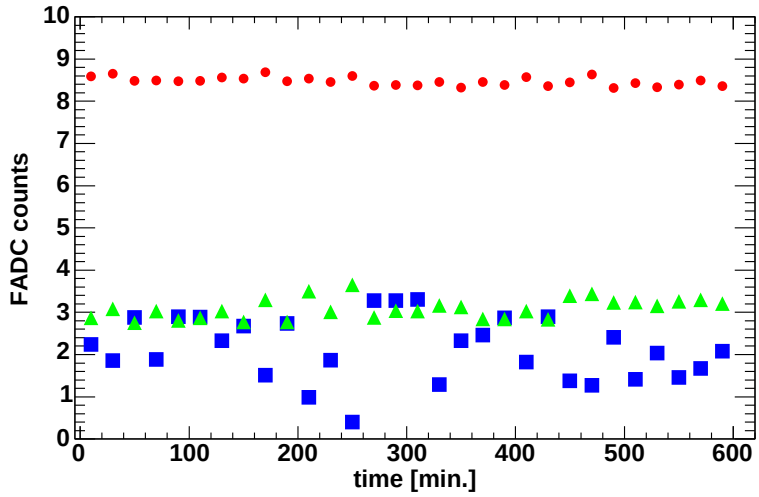

Figure 102: Evolution of pedestal parameters with time. Red circles: Mean pedestal offset, green triangles: pedestal RMS, blue squares: clock-noise amplitude.

The correlation of the noise contributions of FADC slices b_i and b_j can be expressed in the noise auto-correlation matrix $\boldsymbol{B}$:

$$B_{ij} = \langle b_i b_j \rangle - \langle b_i \rangle \langle b_j \rangle \ . \tag{69}$$

Figure 103 shows a typical noise auto-correlation matrix, obtained with 400 000 FADC samples and open camera. As expected for typical signal shaping times, used in the MAGIC readout, neighbouring FADC time slices show a strong correlation, while small further correlation is visible up to time intervals of ±30 ns. The correlation modifies the naive expectation from Poissonian statistics that the RMS of integrated FADC time slices from noise runs scales with the square root of the integration time. Instead, figure 104 shows the corresponding relations for various operation conditions and background light intensities. For any use of the RMS in later analysis, it is therefore mandatory to choose

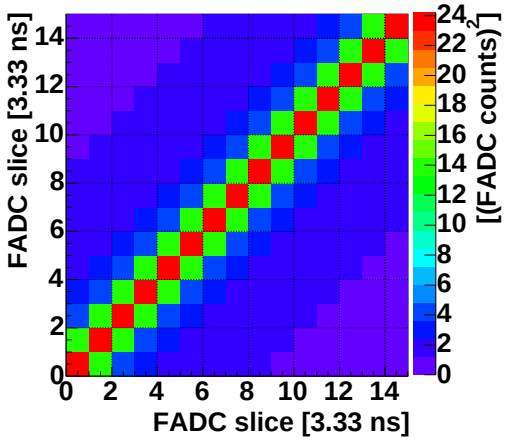

Figure 103: Example noise auto-correlation matrix $\boldsymbol{B}$

beforehand, over how many FADC slices the signal will be extracted and calculate the corresponding "pedestal RMS" integrating over exactly the same number of time slices.

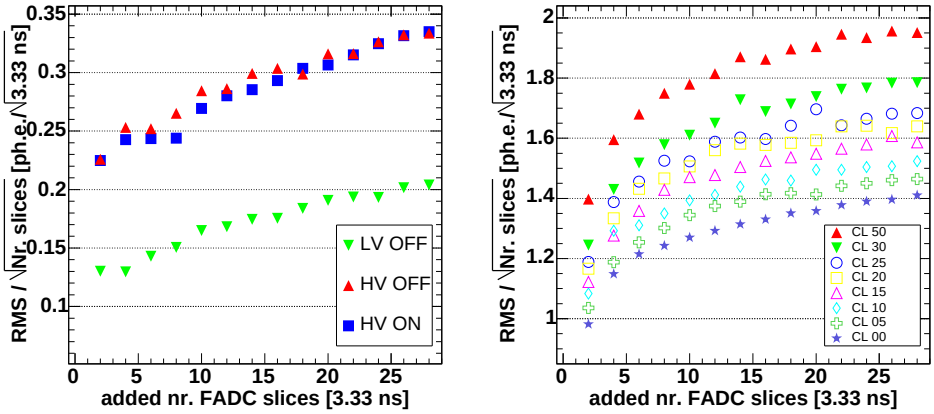

Figure 104: Pedestal RMS per square root of integration time for various background light conditions adding up different numbers of FADC slices under various conditions. Left: switchted off camera (green triangles), closed camera without PMT HV (red triangles), closed camera with PMT HV (blue squares). Right: fully operating open camera and various background light intensities (generated with the continuous light source). The condition "CL 00" (blue) corresponds to the normal observation conditions.

Despite the AC-coupling, the voltage offset at the FADC readout depends slightly on the type of electronics device, placed at the other end of the optical transmission chain. Figure 105 shows the mean pedestal per FADC slice as a function of the number of summed FADC slices for various parts of the camera equipment switched on and off. In case the whole camera is switched on, different intensities of the light of night sky do not modify the mean offset any more, if the downward fluctuations are not getting limited by the incapacity of the FADC to measure negative voltages.

5.4 Signal Extraction Algorithms

In the following, four different signal extraction algorithms are presented and later compared to each other with respect to their statistical properties.

All extractors have in common that they correctly take care of the ***clock noise***, either by summing up only even numbers of FADC slices (and therefore effectively removing the effect) or by correcting each FADC slice value explicitely with the previously measured clock-noise amplitude. Further, all extractors test if the signal has entered saturation by demanding that no FADC slice value exceeds 250 FADC counts (out of a maximum of 256). In case the ***high-gain*** signal saturates, the

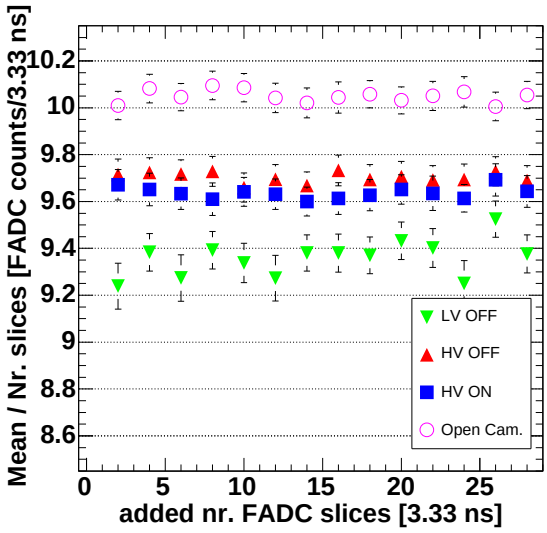

Figure 105: Mean sum of FADC slices (in photo-electrons per FADC slice) obtained from adding up different numbers of FADC slices under various conditions: switchted off camera (green triangles), closed camera with PMT HV switched off (red triangles), closed camera with PMT HV switched on (blue squares) and fully operating open camera (pink circles).

low-gain signal is taken, instead. No combination of high-gain and low-gain signals is performed, mainly because the dynamic range between the low-gain treshold and the high-gain saturation is very small [42].

The most simple extractor is not able to retrieve the arrival time of the pulse while the more sophisticated ones all do so.

5.4.1 Fixed Window

This extractor adds the – pedestal-subtracted – FADC slice contents of a fixed range of consecutive FADC slices. The summation window has to be chosen large enough to cover the complete pulse, otherwise jitters in the pulse position with respect to the FADC slice numbering would lead to integration of always different parts of the pulse. Therefore, the fixed window algorithm always adds up more noise than the one expected from the pure amplitude jitter of the pulse and the FADC digitization noise. Due to the AC-coupling of the readout chain, the reconstructed signals have no bias.

In the here presented implementation, the fixed window extractor does not calculate pulse arrival times.

[42] This is different for other Cherenkov telescopes, see e.g. [25]

5.4.2 Sliding Window with Amplitude-weighted Time

The disadvantages of the previous extractor are overcome by an extractor which searches the maximum integral content of a fixed window of (clock-noise and pedestal-corrected) FADC slice contents within a larger global time window. The amplitude-weighted arrival time is calculated from the window with the highest FADC slice contents integral using the following formula:

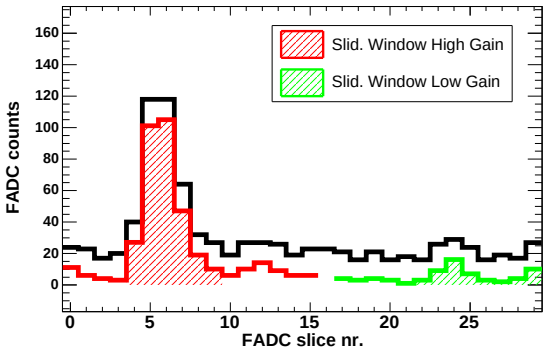

Figure 106: Example sliding window extractor.

$$t = \frac{\sum_{i=i_0}^{i_0+ws-1} s_i \cdot i}{\sum_{i=i_0}^{i_0+ws-1} i} \tag{70}$$

where i denotes a the FADC slice index, starting from slice i_0 and runs over the sliding window size ws. The s_i are the pedestal-corrected FADC slice contents at slice position i.

Figure 106 shows the FADC slice contents, obtained from a typical calibration pulse, together with the pedestal-subtracted FADC values and the maximizing sliding window (in black the pure FADC slice contents, in shaded red and shaded green the pedestal-corrected high-gain and low-gain parts). Figure 109 (top) shows a corresponding high-intensity calibration pulse which saturates the high-gain channel.

As the sliding window algorithm does not include any assumptions of the expected pulse shape, the variance of its reconstructed signal is dominated noise contributions and the FADC digitization jitter. At very small amplitudes, signal pulses are only hardly distinguishable from background fluctuations.

5.4.3 Cubic Spline with Sliding Window or Amplitude Extraction

The limitations of the previous signal extractors are overcome by the cubic spline extractor which interpolates the (pedestal-subtracted) FADC slice contents using a cubic spline algorithm, adapted from [242]. In a second step, it searches for the position of the spline maximum. From then on, two possibilities are offered for the charge reconstruction:

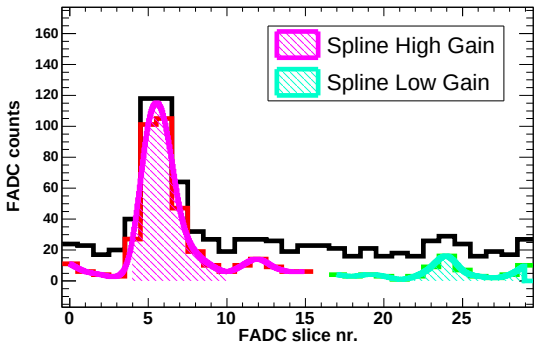

Figure 107: Example spline extractor.

Amplitude: The amplitude of the spline maximum is taken as reconstructed signal.

Integral: The spline is integrated in a window of fixed size, with integration limits determined with respect to the position of the spline maximum.

The pulse arrival times can be computed in two ways:

Pulse Maximum: The position of the spline maximum determines the arrival time.

Pulse Half Maximum: The position of the half maximum at the rising edge of the pulse determines the arrival time.

Figure 107 shows the FADC slice contents, obtained from a typical calibration pulse (in black), together with the pedestal-subtracted FADC values (in red and green) and the interpolating spline. The shaded areas show typical spline integration ranges. Especially in this figure, one can see that the spline correctly raises the pulse maximum, which appeared cut by the limited bandwidth of the FADCs. Figure 109 (center) shows a corresponding high-intensity calibration pulse which saturates the high-gain channel.

The major disadvantages of the cubic spline interpolation are the CPU time required to perform the interpolation and the search for the spline maximum. Moreover, pulses with distorted pulse forms, e.g. due to noise, are not recognized as such.

5.4.4 Digital Filter

The limitations of the previous signal extractors are overcome by an algorithm known as the ***digital filtering method*** [243–245], introduced in the MAGIC analysis by Hendrik Bartko. This algorithm makes a fit to a standard pulse form and can be used if the following three assumptions apply:

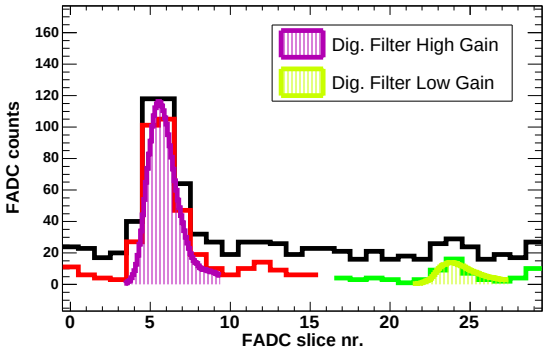

Figure 108: Example digital filter extractor.

1. The normalized signal ***shape*** has to be independent of the signal amplitude and arrival time.

2. The noise properties have to be independent of the signal amplitude.

3. The noise auto-correlation matrix does not change its form significantly with time and operation conditions, i.e. the noise is stationary.

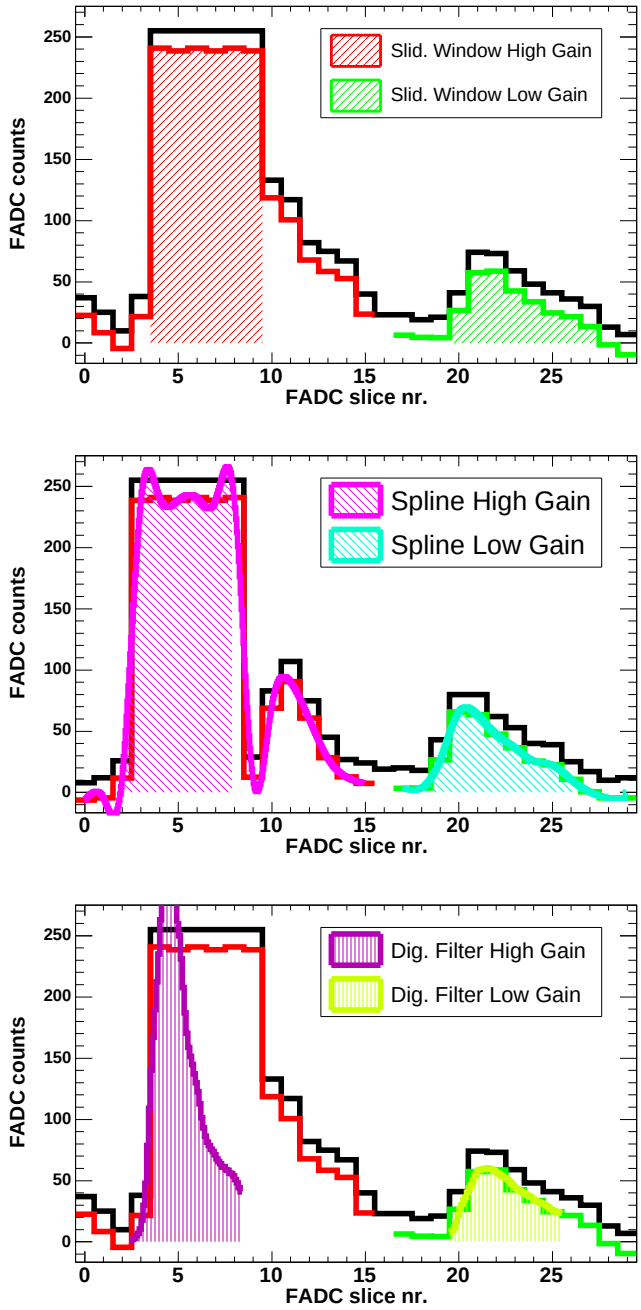

Figure 109: Examples a high intensity calibration pulse, reconstructed with various signal extractors: Top: sliding window, center: spline, bottom: digital filter. The black histograms shows the pure FADC slice values, the colored ones with pedestals subtracted. The shaded areas show the reconstructed charges. One the left side, the (saturated) high-gain pulse is visible while on the right side, the delayed low-gain shows up. In these cases, only the low gain pulse is used for further analysis.

As the pulse shape is mainly determined by the artificial pulse stretching on the optical receiver board, the first assumption holds to a good approximation for all pulses with intrinsic signal widths much smaller than the shaping constant. This will be shown later explicitely. Also the second assumption is fulfilled: Signal and noise are independent and the measured pulse is a linear superposition of the signal and noise contributions. The validity of the third assumption is discussed below, especially for different light of night sky background conditions.

In an ideal amplification chain without noise and using assumption nr. 1, a moving pulse with pulse form $y(t)$ can be parameterized by the normalized signal shape pattern $g(t)$ (e.g. from figure 100), the signal amplitude E and the momentaneous position of the pulse τ, with respect to a norm position:

$$y(t) = E \cdot g(t - \tau) \ , \tag{71}$$

According to assumption nr. 2, a time-dependent noise contribution, $b(t)$, can be added,

$$y(t) = E \cdot g(t - \tau) + b(t) \ , \tag{72}$$

Considering for the moment only time shifts τ smaller than one FADC time slice, equation 72 can be linearized:

$$y(t) = E \cdot g(t) - E\tau \cdot \dot{g}(t) + b(t) \ , \tag{73}$$

where $\dot{g}(t)$ is the time derivative of the normalized pattern signal shape. Discrete FADC measurements y_i of the signal at FADC time slices i ($i = 1, ..., n$) are then expected to have the form:

$$y_i \approx E \cdot g_{i-t_0} - E\tau \cdot \dot{g}_{i-t_0} + b_i \ , \tag{74}$$

where t_0 denotes the N_{t_0} possible (discrete) time offsets at which the pulse may start to appear. In general, t_0 does not need to have the same discretization steps as the FADC time slice. In our case, steps of 330 ps have been chosen for t_0.

The signal amplitude E, and the product of amplitude and time shift $E\tau$, can then be estimated from the given set of FADC contents $\boldsymbol{y} = (y_1, ..., y_n)$ by minimizing the deviation from the pattern pulse shape with respect to the known noise autocorrelation matrix B_{ij}:

$$\chi^2(E, E\tau, t_0) = \sum_{i,j} (y_i - Eg_{i-t_0} - E\tau\dot{g}_{i-t_0})(\boldsymbol{B}^{-1})_{ij}(y_j - Eg_{j-t_0} - E\tau\dot{g}_{j-t_0}) \tag{75}$$

$$= (\boldsymbol{y} - E\boldsymbol{g}_{t_0} - E\tau\dot{\boldsymbol{g}_{t_0}})^T \boldsymbol{B}^{-1}(\boldsymbol{y}_{t_0} - E\boldsymbol{g}_{t_0} - E\tau\dot{\boldsymbol{g}_{t_0}}) \ , \tag{76}$$

where the last expression uses the matrix formalism. $\chi^2(E, E\tau, t_0)$ is a discrete function of t_0 and a continuous function of τ. If the shape of B does not change with time (assumption nr. 3), i.e. different levels of night sky background reflect

themselves only in a multiplicative factor: $B_{ij}^{\text{high NSB}} = c \cdot B_{ij}^{\text{low NSB}}$, the position of the minimum does not depend on the multiplicative constant c and only one standard matrix $\boldsymbol{B}$ can be used. To illustrate this assertion, figure 110 gives an example of the noise auto-correlation matrix, obtained from two different telescope pointing situations: A galactic source (left) and an extra-galactic source (center). On the right side, the ratio between both can be seen which shows structures at the 20% level if the full FADC samples range is taken into account. If a typical pulse of only 4 FADC slices is considered, the magnitude of the systematic effect gets reduced to about 5% which is only slightly higher than the statitical precision of this measurement (3%, see later in this chapter). In this sense, assumption nr. 3 is approximately valid.

In the low-gain FADC samples, the correlated noise of the night sky background is of the same order of magnitude as the electronic and digitization noise. Unfortunately, the noise auto-correlation for the low gain samples cannot be determined directly from the data. The low gain is only switched on if the pulse exceeds a preset threshold and leaves open only a window as wide as the low-gain pulse itself [43]. For this reason, there is no trustable pedestal being calculated in the low gain. The noise auto-correlation is therefore determined from MC simulations and shown in figure 111.

The miminum of $\chi^2(E, E\tau, t_0)$ can be readily calculated:

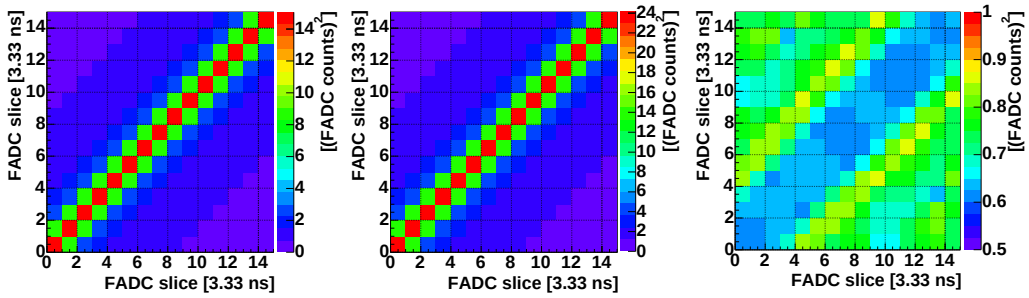

Figure 110: Noise auto-correlation matrix $\boldsymbol{B}$ for the high-gain readout channel and two different intensities of night sky background. Left: $\boldsymbol{B}^{\text{low NSB}}$ obtained with camera pointing off the galactic plane (and low night sky background fluctuations), center: $\boldsymbol{B}^{\text{high NSB}}$ with camera pointing to the galactic plane (high night sky background), right: ratio between both.

$$\frac{\partial \chi^2(E, E\tau, t_0)}{\partial E} = 0 \qquad \text{and} \qquad \frac{\partial \chi^2(E, E\tau, t_0)}{\partial (E\tau)} = 0 \; . \tag{77}$$

Taking into account that $\boldsymbol{B}$ is a symmetric matrix, this leads to the following $2\,N_{t_0}$ equations for the estimated amplitude $\overline{E}$ and the estimation for the product

[43] This has to be considered a design flaw of the data acquisition!

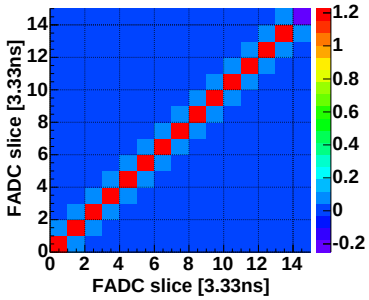

Figure 111: Noise auto-correlation matrix $\boldsymbol{B}$ for the low-gain readout channel, evaluated from MC simulations.

of amplitude and time offset $\overline{E\tau}$:

$$0 = -\boldsymbol{g}_{t_0}^T \boldsymbol{B}^{-1}\boldsymbol{y} + \boldsymbol{g}_{t_0}^T \boldsymbol{B}^{-1}\boldsymbol{g}_{t_0}\overline{E} + \boldsymbol{g}_{t_0}^T \boldsymbol{B}^{-1}\dot{\boldsymbol{g}}_{t_0}\overline{E\tau} \quad (78)$$

$$0 = -\dot{\boldsymbol{g}}_{t_0}^T \boldsymbol{B}^{-1}\boldsymbol{y} + \dot{\boldsymbol{g}}_{t_0}^T \boldsymbol{B}^{-1}\boldsymbol{g}_{t_0}\overline{E} + \dot{\boldsymbol{g}}_{t_0}^T \boldsymbol{B}^{-1}\dot{\boldsymbol{g}}_{t_0}\overline{E\tau} \ . \quad (79)$$

Solving these equations, one gets the following N_{t_0} solutions:

$$\overline{E}(t_0) = \boldsymbol{w}_{\rm amp}^T(t_0)\boldsymbol{y} \quad \text{with} \quad \boldsymbol{w}_{\rm amp} = \frac{(\dot{\boldsymbol{g}}_{t_0}{}^T \boldsymbol{B}^{-1}\dot{\boldsymbol{g}}_{t_0})\boldsymbol{B}^{-1}\boldsymbol{g}_{t_0} - (\boldsymbol{g}_{t_0}^T \boldsymbol{B}^{-1}\dot{\boldsymbol{g}}_{t_0})\boldsymbol{B}^{-1}\dot{\boldsymbol{g}}_{t_0}}{(\boldsymbol{g}_{t_0}^T \boldsymbol{B}^{-1}\boldsymbol{g}_{t_0})(\dot{\boldsymbol{g}}_{t_0}{}^T \boldsymbol{B}^{-1}\dot{\boldsymbol{g}}_{t_0}) - (\dot{\boldsymbol{g}}_{t_0}{}^T \boldsymbol{B}^{-1}\boldsymbol{g}_{t_0})^2} \ , \quad (80)$$

$$\overline{E\tau}(t_0) = \boldsymbol{w}_{\rm time}^T(t_0)\boldsymbol{y} \quad \text{with} \quad \boldsymbol{w}_{\rm time} = \frac{(\boldsymbol{g}_{t_0}{}^T \boldsymbol{B}^{-1}\boldsymbol{g}_{t_0})\boldsymbol{B}^{-1}\dot{\boldsymbol{g}}_{t_0} - (\boldsymbol{g}_{t_0}^T \boldsymbol{B}^{-1}\dot{\boldsymbol{g}}_{t_0})\boldsymbol{B}^{-1}\boldsymbol{g}_{t_0}}{(\boldsymbol{g}_{t_0}^T \boldsymbol{B}^{-1}\boldsymbol{g}_{t_0})(\dot{\boldsymbol{g}}_{t_0}{}^T \boldsymbol{B}^{-1}\dot{\boldsymbol{g}}_{t_0}) - (\dot{\boldsymbol{g}}_{t_0}{}^T \boldsymbol{B}^{-1}\boldsymbol{g}_{t_0})^2} \ . \quad (81)$$

Thus $\overline{E}$ and $\overline{E\tau}$ are given by a weighted sum of the discrete measurements y_i with the weights for the amplitude, $w_{\rm amp}(t_0)$, and time shift, $w_{\rm time}(t_0)$.

As the pulse shapes in the high-gain and the low-gain channel – and for cosmics and calibration events – are somewhat different, dedicated digital filter weights are computed for these event classes, shown in figure 112.

The reconstructed signal E is then the one which maximizes the sum:

$$E(i_0, t_0) = \sum_{i=i_0}^{n-i_0} w_{\rm amp}(i - i_0 + t_0) y_i \ , \quad (82)$$

out of all (possible) FADC start slice values i_0 and weights offsets t_0, yielding maximum positions I_0^{max} and t_0^{max}. Of course, the sums can be first calculated in a (fast) scan over only i_0 and later in a fine scan over a limited range of t_0's, taking advantage of the calculated arrival time:

$$(E\tau)(i_0^{max}, t_0^{max}) = \sum_{i=i_0}^{n-i_0} w_{\rm time}(i - i_0^{max} + t_i^{max}) y_i \qquad \tau = \frac{(E\tau)(i_0^{max}, t_0^{max})}{E(i_0^{max}, t_0^{max})} \ . \quad (83)$$

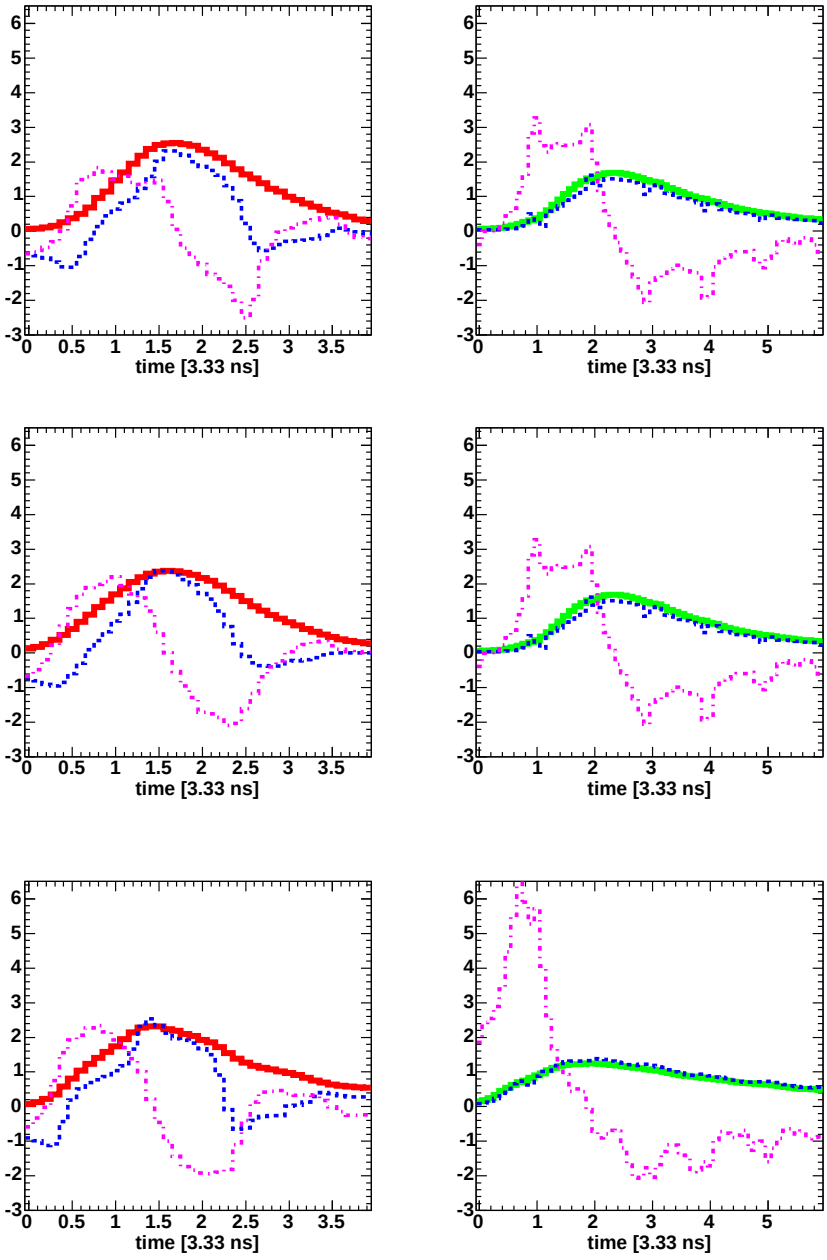

Figure 112: Examples of digital filter weights. Top: cosmics pulses, center: UV calibration pulses and bottom: blue and green calibration pulses. On the left side, the high gain pulse is shown, one the right side, the low-gain. Full lines show the normalized signal shapes $g(t)$ (multiplied with 5 for better visibility), dashed lines the amplitude weights $w_{\mathrm{amp}}(i_0)$, and dotted-dashed lines the time weights $w_{\mathrm{time}}(i_0)$.

5.5 Statistical Parameters from MC Simulations

Some characteristics of the extractor can only be investigated with the use of Monte-Carlo simulations [44] of signal pulses and noise. While under real conditions, the signal can only be obtained in a Poisson distribution, simulated pulses of a specific number of photo-electrons can be generated. Moreover, The same pulse can be studied with and without added noise, where the noise level can be deliberately adjusted.

Nevertheless, there are always systematic differences between the simulation and the real detector. In our case, e.g. no switching noise due to the low-gain switch has been simulated and the total dynamic range of the entire signal transmission chain was set to infinite, thus the detector has been simulated to be completely linear.

For the subsequent studies, the following settings have been used:

- The conversion of total integrated charge to photo-electrons was set to be 7.8 FADC counts per photo-electron, independent of the signal strength.
- The trigger jitter was set to be uniformly distributed over 1 FADC slice only.
- Only one inner pixel has been simulated.
- The night sky background was simulated about 20% lower than under extra-galactic source observation conditions.

5.5.1 Bias

The signal were simulated with noise and extracted using the different signal extractors. Thereby, each extraction window was allowed to move freely within 5 FADC slices, independently of the window size. The extracted signal was then converted back to units of photo-electrons, using a fixed conversion factor, and the bias calculated for each value of simulated numbers of photo-electrons N_{sim}:

$$B =< \widehat{N}_{rec} - N_{sim} > \tag{84}$$

Figure 113 shows the results for some tested extractors, with different initializations.

As expected, the fixed window extractor does not show any bias up to statistical precision. All sliding window extractors however, do show a bias. Usually, the bias vanishes for signals above 5 photo-electrons, except for the sliding window. There, the bias only vanishes for signals above 12 photo-electrons. The best extractors have no bias above 3 photo-electrons and less than 1 photo-electron in the case of no signal ($N_{sim} = 0$).

[44] provided by Abelardo Moralejo

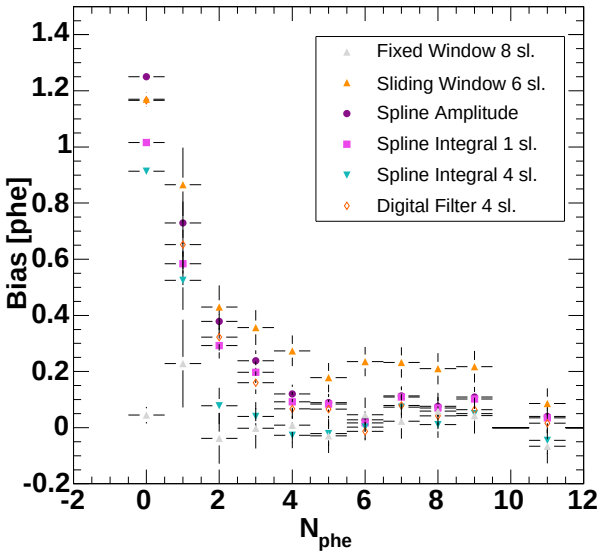

Figure 113: Biases B, obtained from MC simulations of fixed numbers of photo-electrons and fully simulated electronic noise plus light of the night sky. Above 12 photo-electrons, the bias vanishes for all signal extractors.

5.5.2 Root Mean Square Error

In order to obtain the uncertainty of a given extractor, we calculated the relative *RMSE*:

$$\text{Rel. } RMSE = \sqrt{V + B^2}/N_{sim} \ , \tag{85}$$

where $\widehat{N}_{rec}$ is the reconstructed charge, calibrated to photo-electrons with the conversion factors obtained from the un-biased part of signal intensities.

Figure 114 shows the results for the high-gain and low-gain part separately. Also the square root of the relative variance of the number of simulated photo-electrons ($\sqrt{1/N_{sim}}$) is shown which would correspond to the intrinsic fluctuations of the signal coming from air showers, following Poissonian statistics. One can see that for small numbers of photo-electrons N_{sim}, small extraction windows or the digital filter yield smaller *RMSE*, but the difference is only important below about 5 photo-electrons above which all extractors have crossed the black line, i.e. are being more precise than the intrinsic fluctuations of the signal. This is also true for the entire low-gain extraction range.

The best results are always obtained with the digital filter or a spline integrating over 1 FADC slice.

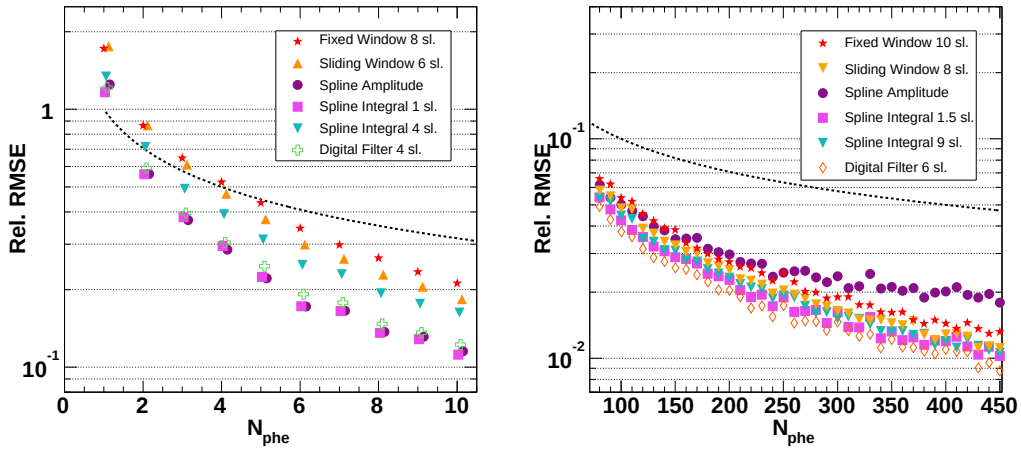

Figure 114: Relative RMSE, obtained from MC simulations of fixed numbers of photo-electrons and fully simulated electronic noise plus light of the night sky. Left: high-gain, right: low-gain. The black dashed line shows the square root of the relative variance of the incoming numbers of photo-electrons, would they fluctuate like Poissonian.

5.5.3 Decomposition of Variance

We are now interested in the reconstructed signal variance $\mathrm{Var}[\widehat{N}_{rec}]$ (eq. 67) at a mean signal intensity of N_{sim}. The simple assumption will be made that $\mathrm{Var}[\widehat{N}_{rec}]$ is a linear superposition of the intrinsic precision of the extraction algorithm and the contribution due to background fluctuations. Thereby, the first is assumed to be independent of the background level while the last is independent of the signal strength:

$$\begin{aligned} \mathrm{Var}[\widehat{N}_{rec}] &= \mathrm{Var}[\widehat{N}_{num}] + \mathrm{Var}[\widehat{N}_{BG}] \\ & \qquad \text{with :} \\ \frac{\partial \mathrm{Var}[\widehat{N}_{intrinsic}]}{\partial N_{BG}} &= 0 \qquad \sqrt{\mathrm{Var}[\widehat{N}_{intrinsic}]} = c_{intrinsic} \cdot N_{\mathrm{phe}} \\ \frac{\partial \mathrm{Var}[\widehat{N}_{BG}]}{\partial N_{\mathrm{phe}}} &= 0 \end{aligned} \tag{86}$$

From eq. 86 follows that one can retrieve the proportionality constant $c_{intrinsic}$ from MC events simulated without noise, and calculate $\mathrm{Var}[\widehat{N}_{BG}]$ directly from pedestal events at $N_{phe} = 0$.

Figure 115 shows the two contributions, obtained from MC simulations, and the difference between $\sqrt{\mathrm{Var}[\widehat{N}_{rec}]}$ and $\sqrt{\mathrm{Var}[\widehat{N}_{intrinsic}] + \mathrm{Var}[\widehat{N}_{BG}]}$. One can see that $\sqrt{\mathrm{Var}[\widehat{N}_{intrinsic}]}$ depends linearly on the number of photo-electrons, while eq. 86

seems to be valid to statistical precision of this measurement for the digital filter and the spline extractors, and to a precision of less than 0.5 photo-electrons for all other extractors.

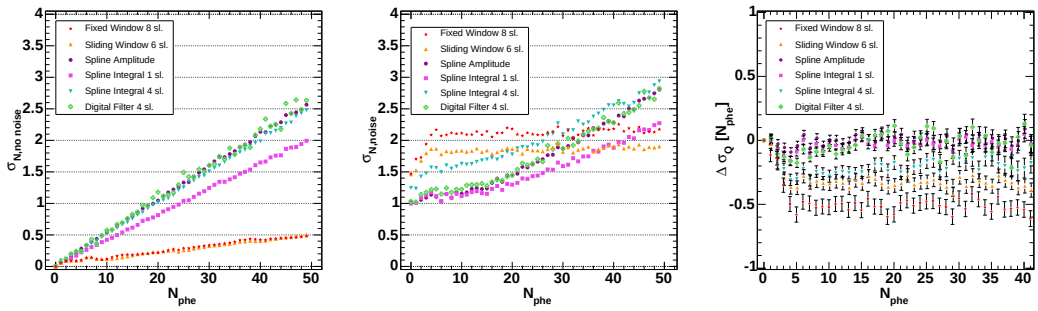

Figure 115: Contributions to the RMSE, obtained from MC simulations of fixed numbers of photo-electrons. Left: $\mathrm{Var}[\widehat{N}_{intrinsic}]$*, obtained with no noise simulated, center:* $\mathrm{Var}[\widehat{N}_{rec}]$ *with fully simulated noise, right:* $\sqrt{\mathrm{Var}[\widehat{N}_{intrinsic}] + \mathrm{Var}[\widehat{N}_{BG}]\Big|_{N_{phe}=0}} - \sqrt{\mathrm{Var}[\widehat{N}_{rec}]}$.

5.6 Statistical Parameters from Pedestal Runs

The background (pedestal) can be completely described by the noise-autocorrelation matrix $\boldsymbol{B}$ (eq. 69), where the square root of the diagonal elements give what is usually denoted as "pedestal RMS" in a Cherenkov telescope analysis. By definition, $\boldsymbol{B}$ and thus the pedestal RMS are independent of the signal extractor.

However, in the previous chapter calibration methods were introduced which rely on the knowledge of the variance of the signal extractor $\mathrm{Var}[\widehat{N}_{rec}]$ to the variance of the extracted signal (e.g. σ_0 in eq. 58). Moreover, in the image cleaning the *RMSE* in the case of no signal ($N_{\mathrm{phe}} = 0$) is of interest.

One can determine $\mathrm{Var}[\widehat{N}_{rec}]$, at least for the case of no signal, by applying the signal extractor with a **fixed window** to pedestal events, where the bias vanishes and measure $\mathrm{Var}[\widehat{N}_{rec}]\Big|_{N_{phe}=0}$, which in general is different from the diagonal elements of the noise auto-correlation matrix B_{ii}.

In order to calculate the statistical parameters, we proceed in the following ways:

1. Determine $\mathrm{Var}[\widehat{N}_{rec}]\Big|_{N_{phe}=0}$ by applying the signal extractor to a fixed window of pedestal events.

2. Determine B, $\mathrm{Var}[\widehat{N}_{rec}]\Big|_{N_{phe}=0}$ and *RMSE* from pedestal events by applying the full signal extractor, including sliding windows.

Note that these methods are only feasible in the high-gain channel. Table 9 shows the square roots of $\mathrm{Var}[\widehat{N}_{rec}]\Big|_{N_{phe}=0}$, obtained by applying an extractor to a

fixed extraction window, for the inner and outer pixels, respectively, for four different typical background conditions: Closed camera, star-field of an extra-galactic source observation, star-field of the Crab-Nebula observation and observation with the almost full moon at an angular distance of about 60° from the telescope pointing position.

The entries belonging to the rows denoted as "Slid. Win." are by construction identical to those obtained by simply summing up the FADC slices (th pedestal RMS). Like expected, the digital filter yields much smaller values of $\mathrm{Var}[\widehat{N}_{rec}]$ than the "sliding windows" of a same window size. This characteristic shows the "filter"–capacity of that algorithm. It effectively "filters out" up to 50% of the night sky background photo-electrons. Moreover, one can see that the ratio between the pedestal RMS of outer and inner pixels is around a factor 3 for the closed camera and then 1.6–1.9 for the other conditions.

$\sqrt{\mathrm{Var}[\widehat{N}_{rec}]}$ for pedestal events and fixed window (units in N_{phe})								
	Closed camera		Extra-gal. NSB		Galactic NSB		Moon	
Extractor	inner	outer	inner	outer	inner	outer	inner	outer
Sliding Win. 2 sl.	0.3	0.9	1.2	2.0	1.5	2.4	3.0	5.3
Sliding Win. 4 sl.	0.4	1.2	1.6	2.7	2.0	3.3	3.9	7.3
Sliding Win. 6 sl.	0.5	1.6	2.0	3.5	2.4	4.3	4.7	9.0
Sliding Win. 8 sl.	0.6	2.0	2.3	4.1	2.9	5.0	5.3	10.1
Spline Amp.	0.3	0.8	1.0	1.8	1.2	2.2	2.5	4.9
Spline Integ. 1 sl.	0.3	0.7	0.9	1.6	1.1	1.9	2.5	4.6
Spline Integ. 2 sl.	0.3	0.9	1.2	2.0	1.5	2.4	3.0	5.3
Spline Integ. 4 sl.	0.4	1.2	1.6	2.8	1.9	3.4	3.6	7.1
Spline Integ. 6 sl.	0.5	1.6	1.9	3.6	2.4	4.2	4.3	8.7
Digital Filter 6 sl.	0.3	0.8	1.0	1.6	1.2	1.9	2.8	4.3
Digital Filter 4 sl.	0.3	0.7	0.9	1.6	1.1	1.9	2.5	4.3

Table 9: $\sqrt{\mathrm{Var}[\widehat{N}_{rec}]}$ *for different extractors applied to a fixed window of pedestal events. Four different conditions of night sky background are shown: Closed camera, extra-galactic star-field, galactic star-field and almost full moon at 60° angular distance from the pointing position. With the first three conditions, a simple RMS of the extracted signals has been calculated while in the fourth case, a Gauss fit to the high part of the distribution has been made. The obtained values can typically vary by up to 10% for different channels of the camera readout.*

By applying the signal extractor with a global extraction window to pedestal events, allowing it to "slide" and maximize the encountered signal, the bias and the *RMSE* for the case of no signal ($N_{phe} = 0$) can be determined.

Table 10 shows the bias, the square root of $\mathrm{Var}[N_{rec}]$ and the *RMSE* for all

extractors using a sliding window. In this sample, every extractor had the freedom to move 5 FADC slices, i.e. the global window size was fixed to five plus the extractor window size. The first line shows the resolution of the smallest existing robust fixed window algorithm in order to give the reference value of 2.5 and 3 photo-electrons RMS for an extra-galactic and a galactic star-field, respectively.

One can see that the bias typically decreases with increasing sliding window size, while the variance increases with increasing window size, except for the digital filter. The root-mean-square-error reaches its lowest values if the lowest sliding window sizes are used. The extractor with the smallest *RMSE* is the digital filter fitting a pulse width of 4 FADC slices. All sliding window extractors have a smaller *RMSE* than the RMS of the signal, obtained with the fixed window reference extractor. This shows that the global uncertainty of the sliding window extractors is smaller than the one of the fixed window extractor even if the first ones have a bias.

Another important information (e.g. for the image cleaning, see section 7.3), is the number of photo-electrons above which the probability to obtain a noise fluctuation is smaller than a certain threshold. For demonstration reasons, a typical value of $3\,\sigma$ (0.3% probability) was chosen here and that number approximated with the formula:

$$N_{\mathrm{phe}}^{\mathrm{thres.}} \approx B + 3 \cdot \sqrt{V} \ , \tag{87}$$

where V is the variance of the extracted signal (eq. 67). Table 10 shows the obtained values of $N_{\mathrm{phe}}^{\mathrm{thres.}}$ for the tested signal extractors. Again, most of the sliding window algorithms yield a smaller signal threshold than the fixed window ones, although the first have a bias. The lowest threshold of only 4.2 photo-electrons for the extra-galactic star-field and 5.0 photo-electrons for the galactic star-field is obtained with the digital filter fitting 4 FADC slices. This is almost a factor 2 lower than the fixed window results. Also the spline integrating 1 FADC slice yields almost comparable results. Shown in table 10 are also the corresponding values, obtained from MC simulations. Here, one has to take into account the slightly lower level of simulated night sky background. We expect thus about 20% lower values than the with real data. This is indeed the case if one takes into account the statistical uncertainties of about 10%.

Statistical Parameters for $N_{\mathrm{phe}} = 0$														
	Closed camera			MC-simulation			Extra-galactic NSB				Galactic NSB			
Name	$\sqrt{\mathrm{Var}[N_{rec}]}$	B	$RMSE$	$\sqrt{\mathrm{Var}[N_{rec}]}$	B	$RMSE$	$\sqrt{\mathrm{Var}[N_{rec}]}$	B	$RMSE$	$N_{\mathrm{phe}}^{\mathrm{thres.}}$	$\sqrt{\mathrm{Var}[N_{rec}]}$	B	$RMSE$	$N_{\mathrm{phe}}^{\mathrm{thres.}}$
Fixed Win. 8	1.2	0.0	1.2	1.5	0.0	1.5	2.5	0.0	2.5	7.5	3.0	0.0	3.0	9.0
Slid. Win. 2	0.5	0.4	0.6	1.1	1.0	1.5	1.4	1.2	1.8	5.4	1.6	1.5	2.2	6.1
Slid. Win. 4	0.8	0.5	0.9	1.4	1.1	1.8	1.9	1.2	2.2	6.9	2.3	1.6	2.8	7.5
Slid. Win. 6	1.0	0.4	1.1	1.8	1.0	2.1	2.2	1.1	2.5	7.7	2.7	1.4	3.0	9.5
Slid. Win. 8	1.3	0.4	1.4	2.1	0.8	2.2	2.5	1.0	2.7	8.5	3.2	1.4	3.5	10.0
Spline Amp.	**0.4**	0.4	0.6	1.1	1.1	1.6	1.2	1.3	1.8	4.9	1.4	1.6	2.1	5.8
Spline Int. 1	**0.4**	0.3	**0.5**	1.1	0.8	1.4	1.2	1.0	1.6	4.6	**1.3**	1.3	1.8	5.2
Spline Int. 2	0.5	0.3	0.6	1.2	0.9	1.5	1.4	0.9	1.7	5.1	1.6	1.2	2.0	6.0
Spline Int. 4	0.7	**0.2**	0.7	1.3	0.8	1.5	1.7	**0.8**	1.9	5.3	2.0	1.0	2.2	7.0
Spline Int. 6	1.0	0.3	1.0	1.7	0.8	1.9	2.0	**0.8**	2.2	6.8	2.5	**0.9**	2.7	8.4
Dig. Filt. 4	**0.4**	0.3	**0.5**	1.0	1.3	1.6	**1.1**	0.9	**1.4**	**4.2**	**1.3**	1.1	**1.7**	**5.0**
Dig. Filt. 6	0.5	0.4	0.6	1.1	1.3	1.7	1.3	1.3	1.8	5.2	1.5	1.5	2.1	6.0

Table 10: The statistical parameters bias B, square root of reconstructed signal variance $\mathrm{Var}[N_{rec}]$ and $RMSE$ for the tested signal extractors, applied to pedestal events. The first line displays the resolution of the smallest robust fixed–window extractor for reference. All units are in reconstructed numbers of photo-electrons, statistical uncertainty: about 0.1 photo-electrons. All extractors were allowed to move 5 FADC slices plus their window size. The extractors yielding the smallest values for each column are marked in red.

5.7 Statistical Parameters from Calibration Runs

Figure 116 gives examples of the smallest and the largest pulses, as registered by the FADCs and which can be obtained with the calibration system. Whereas the UV-pulse is rather stable, the green and blue pulses can show smaller secondary pulses after about 8 ns from the main pulse. Whereas the stable UV-pulses are only available in such intensities as to not saturate the high-gain readout channel, the brightest combination of light pulses easily saturates all high-gain channels in the camera, but does not yet reach a saturation of the low-gain readout.

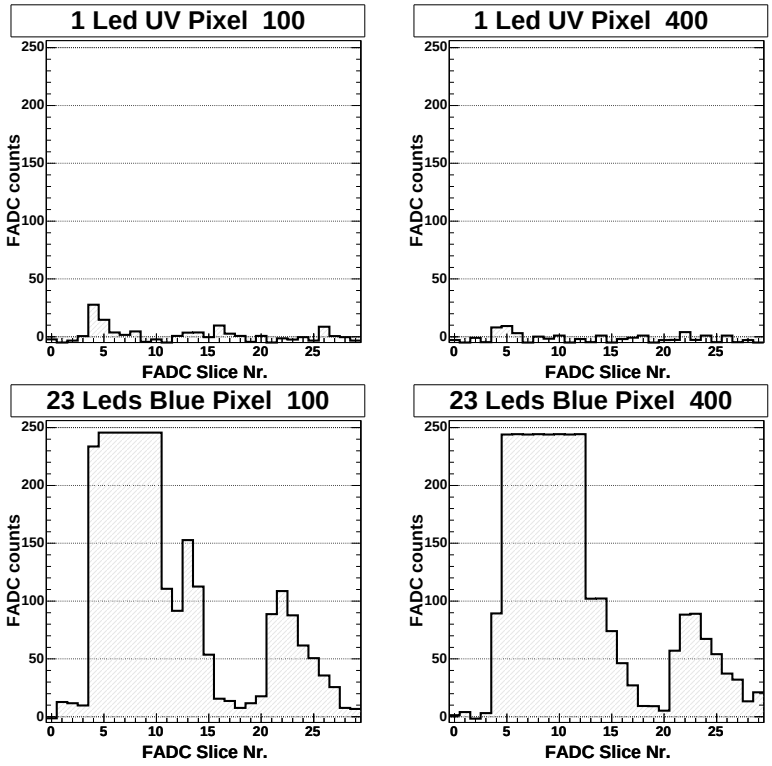

Figure 116: Example of a calibration pulse from the lowest (top) and highest (top) available mono-chromatic intensity. Left: a typical inner pixel, right: a typcial outer pixel. Note that in the upper plots, the pulse height fluctuates much more than suggested from these pictures. Especially, a zero-pulse is also possible. In the lower plots, the (saturated) high-gain channel is visible at early times, while from FADC slice 20 on, the delayed low-gain pulse appears.

Analogue to the procedure introduced in chapter 4.6, the camera was illuminated with sequences of light pulses of increasing intensity of pulsed light. For every sequence of a same light intensity, the signals were extracted from the FADC samples and a Gauss-fit was made to the distribution of reconstructed charges. Then, the quantity $(\sigma^2_{gauss} - \sigma^2_0)/\mu^2_{gauss}$ was plotted vs. $1/\mu_{gauss}$, and fitted to a straight

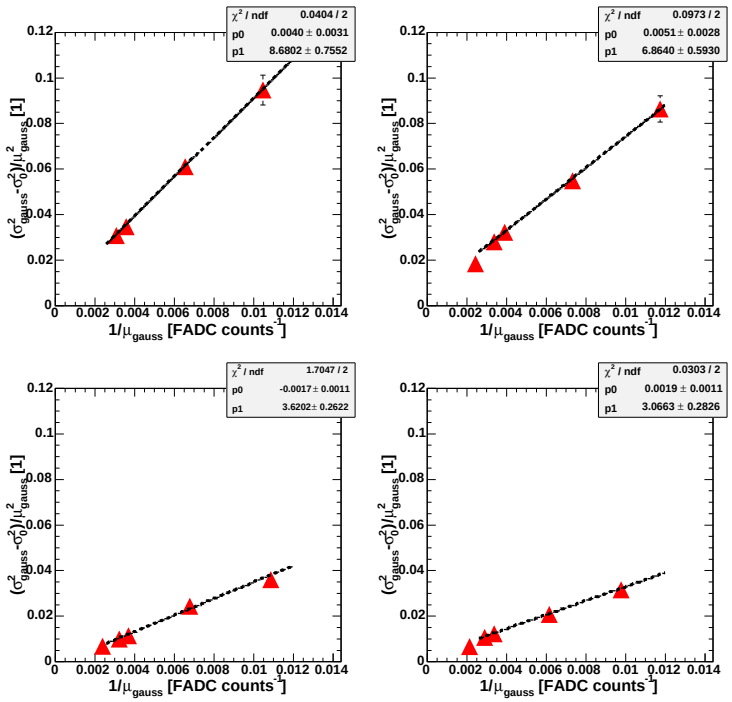

Figure 117: Examples of the $(\sigma^2_{gauss} - \sigma^2_0)/\mu^2_{gauss}$ vs. $1/\mu_{gauss}$ test plots, obtained with various intensities of UV light and for two examplary inner and outer pixels.

line (see figure 117 for examples). The quantity σ_0 is thereby the square root of $\mathrm{Var}[\widehat{N}_{rec}]\big|_{N_{\mathrm{phe}}=0}$, taken from a pedestal run and introduced in section 5.6. Special care has to be taken to set the fit range such that points affected by a bias (recall figure 113) are not included in the fit. If the background contribution of the signal detection chain to the variance of the extracted signal consists only of σ_0 (derived from the case of no light pulses), the fit should yield a straight line through the origin and the slope $F^2 \cdot Q_1$, where F denotes the excess noise factor of the readout chain and Q_1 the extracted signal per photo-electron. If the line does not go through the origin, probably a further contribution $\sigma_{\mathrm{missing}}/\mu_{gauss}$ exists and has not yet been taken into account.

Typical distributions of the fit results are shown in figure 118, showing a bigger statistical spread of $\sigma_{\mathrm{missing}}/\mu_{gauss}$ for the inner pixels than for the outer ones. This is expected since the outer pixels have accumulated a larger number of photo-electrons per reconstructed charge and should show thus less intrinsic fluctuations. There is also a small correlation visible between the fitted offsets and the slopes, illustrating the limits of this procedure. It seems however that the precision of the median value of $\sigma_{\mathrm{missing}}/\mu_{gauss}$ of a large number of channels is still good enough to draw conclusions on the quality of a signal extractor. The median values of the fitted offsets are displayed in figure 119 for different signal extractor configurations. One can see that

the sliding window and the spline amplitude yield a stable, window-size independent contribution of about 2% of additional relative fluctuation. The integrating spline extractors show fluctuations of smaller size, compatible with zero. The same applies to the digital filtering method, if only the inner pixels are considered. Outer pixels yield a larger contribution, of the same size as the sliding window extractor, which might be explained by the fact that the sample pulse forms were obtained by fitting averaged pulses from inner pixels instead of outer ones. Doing so, a small bias towards inner pixels' characteristics might have been introduced [45].

The same measurements, if applied to the low-gain signals, yield results compatible with zero, and only upper limits of about 1% additional relative fluctuation could be obtained (see also section 4.6).

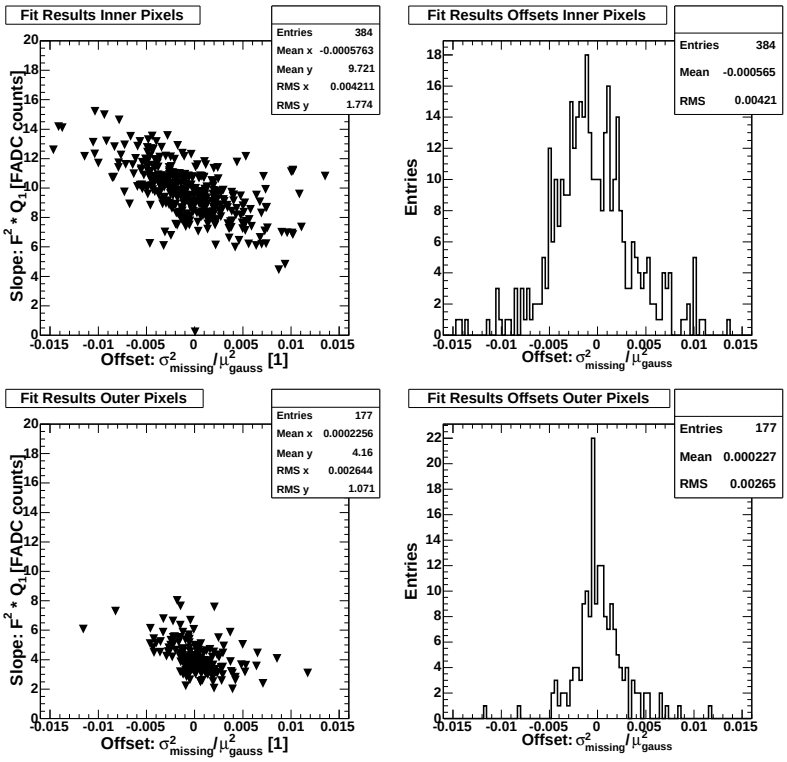

Figure 118: Examples of fit results to the $(\sigma^2_{gauss} - \sigma^2_0)/\mu^2_{gauss}$ vs. $1/\mu_{gauss}$ test plots. Top: inner pixels, bottom: outer pixels.

5.7.1 Numbers of Photo-electrons

In this section, the mean number of photo-electrons μ_{phe} was calculated for a sequence of calibration pulses of same intensity, following the prescription of eq. 58 and

[45] The slightly worse noise behaviour of the optical links used for the outer pixels, as a reason for the additional contribution to the variance at higher intensities, has already been excluded in section 4.6.

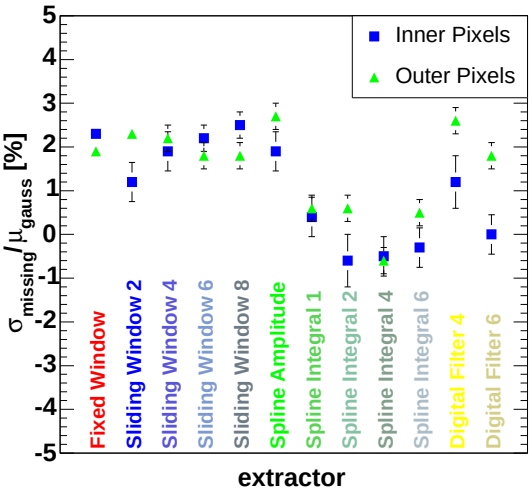

Figure 119: Fit offsets to the $(\sigma^2_{gauss} - \sigma^2_0)/\mu^2_{gauss}$ vs. $1/\mu_{gauss}$ test plots for various extractors. The averaged results of four calibration runs with different intensities and pulser colour are displayed here.

using different signal extractor configurations. If the signals are extracted correctly, the resulting number of photo-electrons should not depend on the signal extractor!

In our case, an additional complication arises from the fact that the green and blue colored light pulses can show secondary pulses after about 8 ns from the primary emission peak which may introduce a dependency of the reconstructed number of photo-electrons on the extraction time-window size (recall fig. 100). The signal extractors will have to be grouped into those being affected by the secondary pulses and those being immune to this effect.

Figure 120 shows the average number of photo-electrons for the standard calibration pulse, emitted from 10 LEDs UV. One can see that a rather good stability is obtained, the results of different signal extractors differ by less than 5%. Adding the corrections on the reduced variances, obtained from MC simulations (displayed in figures 115), bring down the spread in results to less than 4%, but raises the average number of photo-electrons by 3% and 6% in the case of the inner and the outer pixels, respectively. The application of the corrections shown in figure 119 do not have any effect on the spread of $< \mu_{\mathrm{phe}} >$, though.

On the contrary, a typical green pulse yields time-window size dependent numbers of photo-electrons, as shown in figure 121. The obtained spread in number of photo-electrons lies around 15%, due to that dependency. Applying corrections to the variance does not reduce the spread considerably. The digital filter reconstructs thereby the same number of photo-electrons as the other extractors using small window sizes, i.e. the secondary pulses are efficiently filtered out.

A similar behaviour can be seen in the third example of an intense blue calibra-

tion pulse (figure 122): A spread of about 12% is obtained, independently whether corrections are applied or not. Here, the digital filter yields results comparable to medium window sizes of other extractors, most probably because the secondary pulses influence already the overall pulse form, due to the limited bandwidth of the passive delay line.

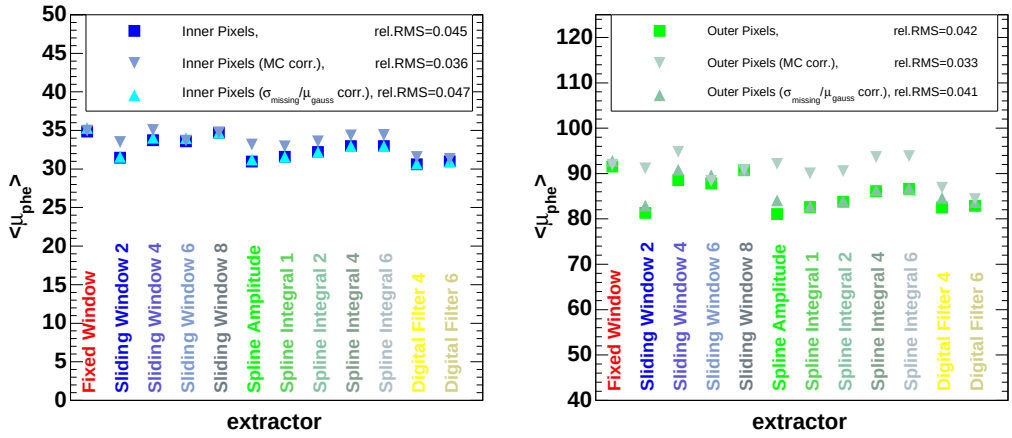

Figure 120: Number of photo-electrons from the standard calibration pulse, emitted by 10 UV LEDs, reconstructed with different signal extractors. Left: inner pixels, right: outer pixels. Shown are also obtained corrections from figures 115 (MC) and figure 119 (real data).

5.8 Robustness Tests

Typically two sources of degradations of the signal extraction quality are of concern for the MAGIC data: ***variations of the pulse form*** and possible ***early or late pulse positions within the recorded FADC samples***.

Variations of the pulse form have a physical reason: average Cherenkov pulses from hadronic showers are usually broader than those from electromagnetic ones, additionally there are differences between the pulse form of calibration pulses and those of cosmics. These variations affect mainly signal extractors which integrate parts of a pulse or perform fits to a sample pulse form. In order to quantize the magnitude of the effect, table 11 lists the part of the pulse which is contained in typical time windows around the pulse maximum, for various pulse forms. While the amplitude extraction or integration of only 1 FADC slice around the maximum yield differences of as much as 10%, the uncertainty is reduced to about 5% if two or more FADC slices are getting integrated. Further deviations, characterized by the blue LEDs calibration pulse, yield an even stronger discrepancy.

In order to test the robustness of the digital filtering method with respect to deviations from the fitted pulse shape, the standard UV calibration pulse was extracted

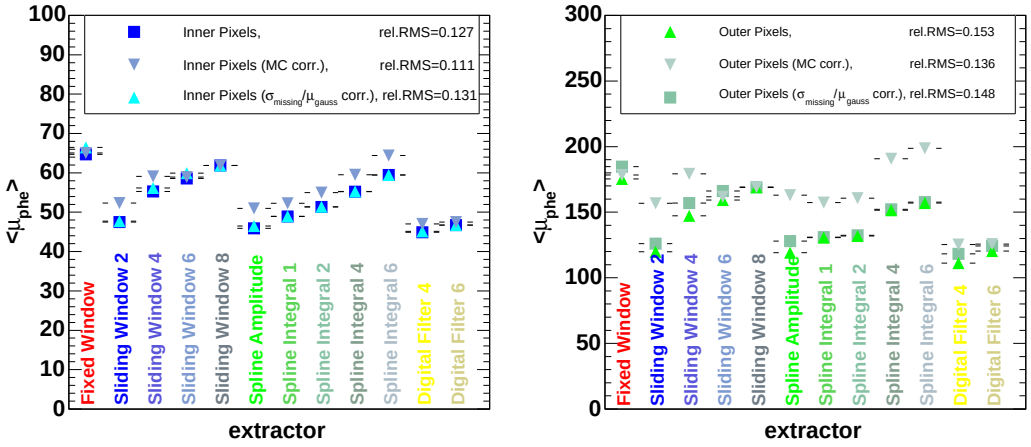

Figure 121: Number of photo-electrons from calibration pulses, emitted by 5 green LEDs, reconstructed with different signal extractors. Left: inner pixels, right: outer pixels. Shown are also obtained corrections from figures 115 (MC) and 119 (real data).

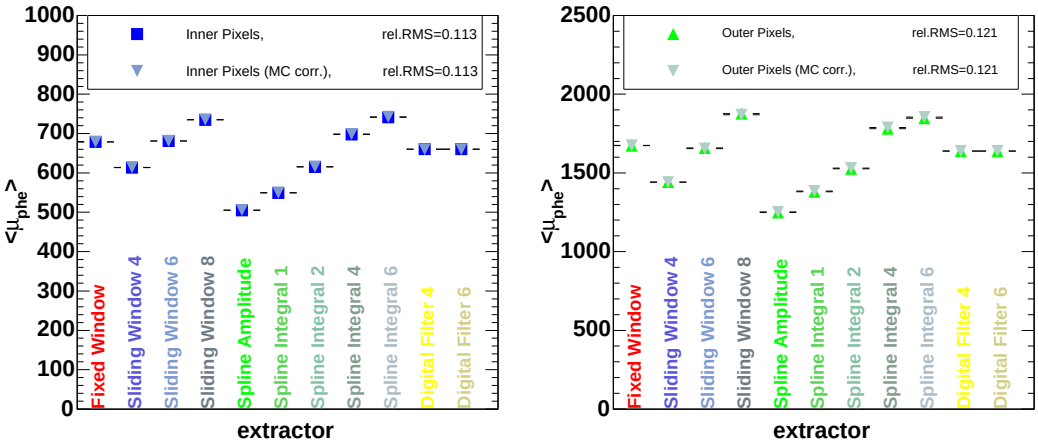

Figure 122: Number of photo-electrons from intense calibration pulses, emitted by 20 blue LEDs, reconstructed with different signal extractors. Only the low-gain amplification channel was used here. Left: inner pixels, right: outer pixels. Shown are also obtained corrections from figure 115 (MC).

Pulse Form Dependency of Integration Windows						
Window Size (FADC slices around maximum)	High Gain				Low Gain	
	MC	Cosmics	Calib. UV	Calib. Blue	Cosmics	Calib. Blue
	(percentage of complete pulse integral)					
Maximum	5.4	5.0	4.5	4.1	3.4	2.5
1 slice	54	50	46	41	35	27
2 slices	78	76	71	66	60	48
4 slices	97	98	95	89	90	82

Table 11: Pulse form dependency of integration windows: Shown is the part of the signal (in percent of the complete pulse integral), contained in different time windows around the pulse maximum for different pulse shapes.

using different weights functions, i.e. fitted to different pulse forms. The results are displayed in figure 123 showing variations of about 8% in the reconstructed signal and 3% in the number of photo-electrons.

In conclusion, all signal extractors which do not integrate the whole pulse, may show systematic deviations of up to 8% due to variations of the exact pulse shape.

A second kind of reconstruction uncertainty is due to the spread of pulse positions within the recorded FADC samples. There is a physical spread of about 2.5 FADC samples RMS, due to the time spread of showers and to the trigger jitter of about one FADC slice. An additional offset of about 5 ns occurred in one trigger cell, due to hardware problems, which were cured only in September, 2005 and affect all data taken before. Taking together these numbers, the position of a pulse from an air shower may vary within 7–8 FADC slices, within one data run. If the readout is adjusted such that the ***mean pulse position*** is too early or too late, a considerable part of the signals cannot be extracted any more because the pulses may reach out of the registered FADC window. This problem affects above all extractors which use large extraction windows, especially the standard digital filter fitting the low-gain pulse to a sample of 6 FADC slices. Figure 124 shows an example of a low-gain signal which has been mis-reconstructed this way.

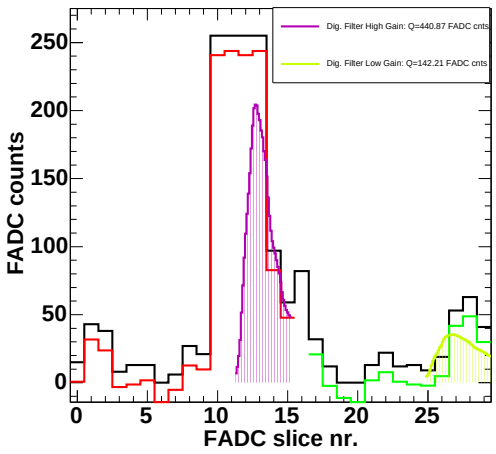

Figure 124: Example of a late pulse position: The digital filter (yellow) cannot extract the low-gain signal correctly.

Unfortunately, the mean pulse position varies quite considerably over the year

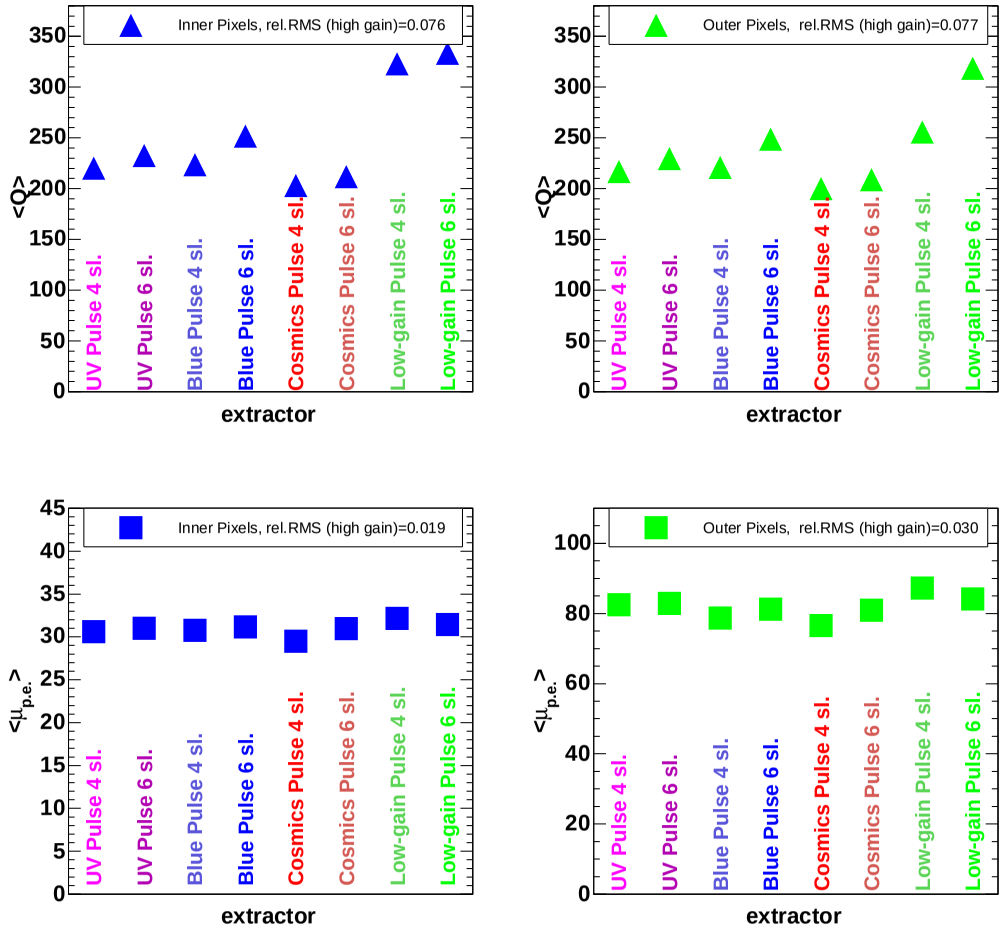

Figure 123: Mean reconstructed charge (top) and number of photo-electrons (bottom) from the standard UV calibration pulses, fitted to different pulse forms using the digital filter. Important for calibration errors is the ratio between both. Left: inner pixels, right: outer pixels. The relative RMS was calculated for the first six (high-gain) pulse forms.

2005, although the problem was known already in January of that year. Figure 125 shows the mean pulse position over the whole year of 2005, with red lines indicating the range where the digital filter can still successfully extract the signal. All data taken outside of the red shaded area, must be extracted using different algorithms, e.g. the cubic spline integrating a small time-window around the pulse maximum.

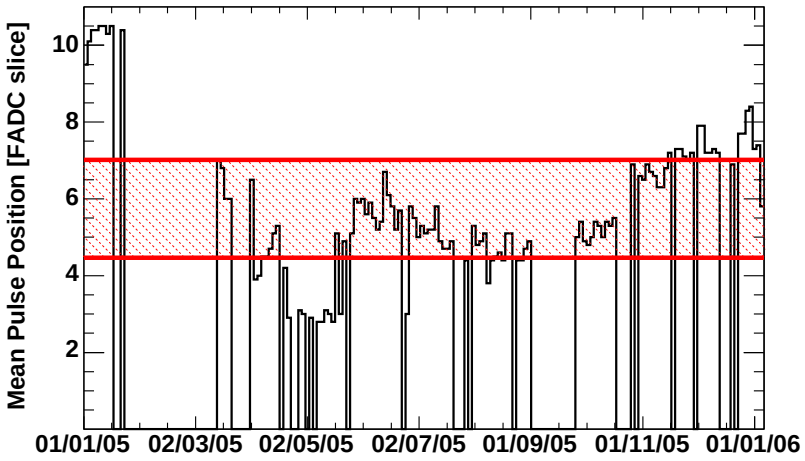

Figure 125: Mean pulse positions for cosmics in the 2005 data. Only the data inside the red shaded area can be extracted robustly using the standard digital filter.

5.9 Time Resolutions

As the calibration LEDs deliver fast-rising pulses, which have a FWHM only slightly larger than those of cosmics, they can be used to test the time resolution of signal extractors and to obtain upper limits on the time resolution of the camera as a whole. The calibration light pulses arrive uniformly over the camera in signal size as well as in time.

Since the calibration system does not deliver a precise enough absolute arrival time stamp, a measurement of the relative arrival time δt has to be made for every channel, with respect to a stable reference channel (usually pixel no. 1)

$$\delta t_i = t_i - t_1 \tag{88}$$

where t_i denotes the reconstructed arrival time of pixel number i and t_1 the reconstructed arrival time of the reference pixel no. 1. During one calibration pulse sequence, histograms of δt_i are filled, and subsequently fitted to the expected Gaussian distribution. The fits yield a mean, $\mu(\delta t_i)$, comparable to systematic delays in the signal travel time, and a width, $\sigma(\delta t_i)$, a measure of the combined time resolu-

tions of pixel i and pixel 1. Assuming that the photomultipliers and readout channels are of a same kind, an approximate time spread of pixel i is obtained:

$$t_i^{res} \approx \sigma(\delta t_i)/\sqrt{2} \tag{89}$$

F igure 126 show distributions of δt_i for an inner pixel and the standard calibration pulse in UV and a high-intenstiy calibration pulse of blue light, obtained with four different arrival time extractors.

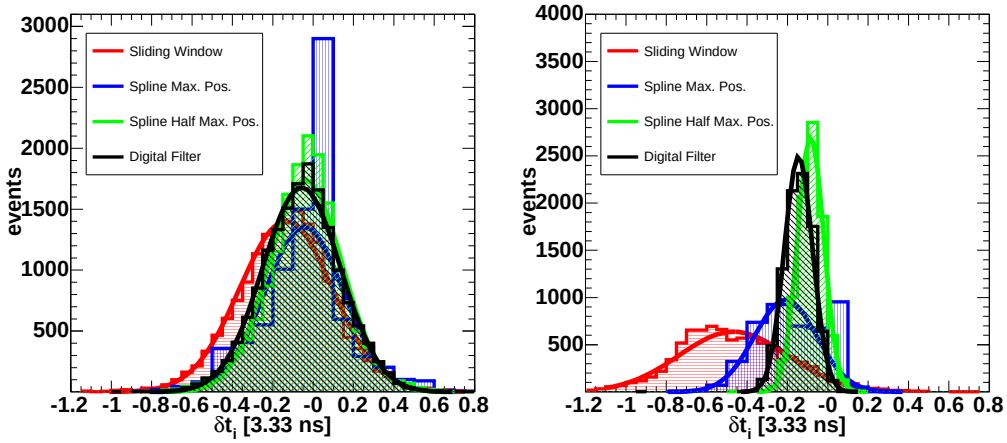

Figure 126: Examples of distributions of relative arrival times (δt_i) for an inner pixel and the four arrival time extractors: Sliding Window with weighted mean position (red), maximum position of the interpolating spline (blue), half maximum position at rising edge of an interpolating spline (green) and a digital filter fitting the pulse position (black). Left: medium sized UV pulse, extracted from the high-gain channel, right: intense blue pulse, extracted from the low-gain channel.

Figure 127 shows the obtained average time resolutions $< t^{res} >$ for various calibration runs, taken with different colors and light intensities, as a function of the mean number of photo-electrons and for three different time extractors: a Sliding Window of 6 FADC slices with amplitude-weighted time (section 5.4.2), the Cubic Spline with the position of the half-maximum at the rising edge of the pulse (section 5.4.3) and the digital filter (section 5.4.4). One can see that the time spread is inversely proportional to the signal intensity, as expected, and a time resolution of better than 1 ns can be obtained for all pulses above a threshold of 5 photo-electrons. At the largest signals, a time resolution of as good as 200 ps can be reached. In order to understand the exact behavior of the time resolution, a short revision of its main contributions is listed here:

1. The intrinsic arrival time spread of the photons on the PMT: This time spread can be estimated roughly by the intrinsic width δt_{IN} of the input light pulse.

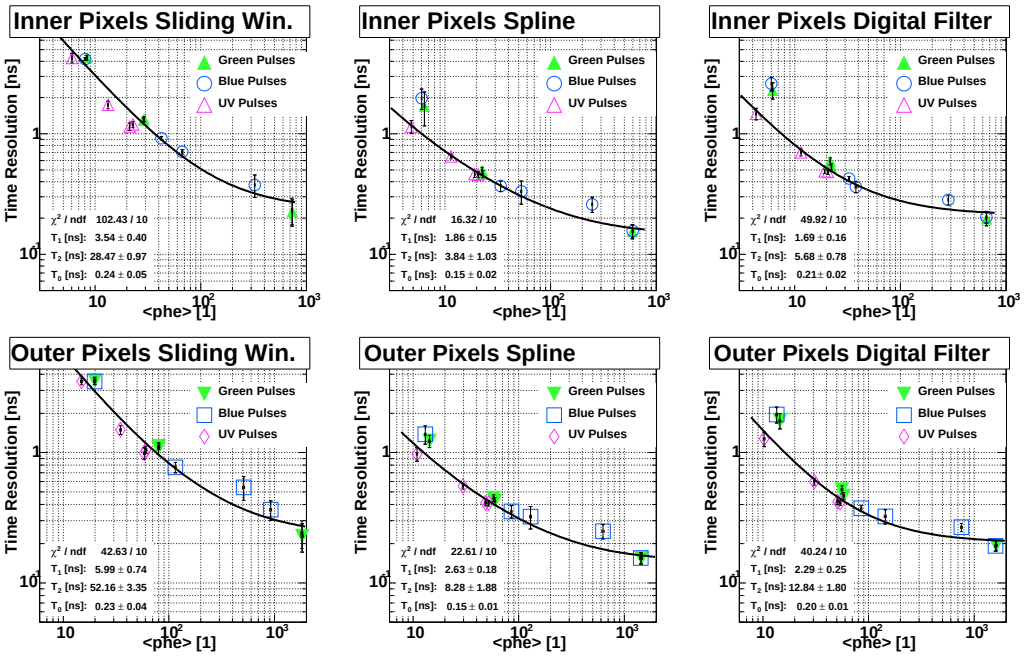

Figure 127: Reconstructed mean arrival time resolutions as a function of the extracted mean number of photo-electrons for the weighted sliding window with a window size of 6 slices (left), the half-maximum searching spline (center), the digital filter with correct pulse weights over 6 slices (right). Error bars denote the spread (RMS) of time resolutions of the investigated channels. The marker colors show the applied pulser colour, except for the last (green) point where all three colors were used.

The resulting time resolution is given by:

$$\Delta t \approx \frac{\delta t_{\mathrm{IN}}}{\sqrt{N_{\mathrm{phe}}}} \tag{90}$$

The width δt_{IN} is about 1 ns for gamma pulses, a few ns for hadron pulses, for muons a few hundred ps and about 2–4 ns for the calibration pulses (see table 1).

2. The transit time spread *TTS* of the photo-multiplier which can be of the order of a few hundreds of ps per single photo electron, depending on the wavelength of the incident light. As in the case of the photon arrival time spread, the total time spread scales with the inverse of the square root of the number of photo-electrons:

$$\Delta t \approx \frac{\delta t_{\mathrm{TTS}}}{\sqrt{N_{\mathrm{phe}}}} \tag{91}$$

3. The reconstruction uncertainty due to the background noise and limited extractor resolution: This contribution is inversely proportional to the signal to square root of background light intensities.

$$\Delta t \approx \frac{\delta t_{\mathrm{rec}} \cdot R}{N_{\mathrm{phe}}} \tag{92}$$

where $R = \sqrt{\mathrm{Var}[\widehat{N}_{\mathrm{phe}}]}$ is the square root of the extractor variance (eq. 67) which depends only very weakly on the signal intensity (compare figure 115 center).

4. A constant offset due to the residual FADC clock jitter or the MC-simulation time steps.

$$\Delta t \approx \delta t_0 \tag{93}$$

In total, the time spread can be expressed as:

$$\Delta T = \sqrt{\frac{T_1^2}{N_{\mathrm{phe}}} + \frac{T_2^2}{N_{\mathrm{phe}}^2} + T_0^2}\ , \tag{94}$$

where T_1 contains the contributions of δt_{IN} and δt_{TTS}, T_2 the contribution of δt_{rec} and T_0 the offset δt_0.

The measured time resolutions in figure 127 were thus fit to equation 94, with the fit results summarized in table 12. The low fit probabilities are partly due to the systematic differences in the pulse forms in intrinsic arrival time spreads between pulses of different LED colors. Nevertheless, all calibration colors had to be included in the fit to cover the full intensity range. In general, the time resolutions for the UV pulses are systematically better than for the other colors which can be attributed to the fact that these pulses have a smaller intrinsic pulse width – very close to pulses from cosmics. There are clear differences between the studied time extractors, especially the sliding window extractor yields poor resolutions. The spline and the digital filter are compatible within the uncertainties.

In order to get an upper limit for the reconstructed arrival time resolution of cosmics pulses, the effect of the mirrors has to be included. Although the MAGIC mirrors have been built in a parabolic shape, and are thus isochronous, the staggering of the mirrors in a chess-board manner introduces an additional, binomial distribution, of arrival times, separated by about 700 ps. Taking into account this effect, the expected time spread for inner pixels and cosmics pulses can thus be conservatively estimated to:

$$\Delta T_{\mathrm{cosmics}} \approx \sqrt{\frac{4.5}{N_{\mathrm{phe}}} + \frac{20}{N_{\mathrm{phe}}^2} + 0.04}\ \ \mathrm{ns}\ . \tag{95}$$

Time Resolutions Fit Results				
Signal Extractor	T_1	T_2	T_0	χ^2/NDF
	Inner Pixels			
Sliding Window	3.5 ± 0.4	29 ± 1	0.24 ± 0.05	10.2
Spline Half Max.	1.9 ± 0.2	3.8 ± 1.0	0.15 ± 0.02	1.6
Digital Filter	1.7 ± 0.2	5.7 ± 0.8	0.21 ± 0.02	5.0
	Outer Pixels			
Sliding Window	6.0 ± 0.7	52 ± 4	0.23 ± 0.04	4.3
Spline Half Max.	2.6 ± 0.2	8.3 ± 1.9	0.15 ± 0.01	2.3
Digital Filter	2.3 ± 0.3	13 ± 2	0.20 ± 0.01	4.0

Table 12: . The fit results obtained from the fit of eq. 94 to the time resolutions obtained for various intensities and colors. The fit probabilities are very small mainly because of the different intrinsic arrival time spreads of the photon pulses from different colors.

5.10 CPU Requirements

The number of executed events per second using the individual extractor algorithms was measured on an Intel Pentium IV, 2.4 GHz CPU machine at IFAE. Table 13 shows the obtained results whereby the individual measurements could easily differ by about 20% from one try to another (using the same extractor). The numbers in this list have to be compared to the I/O speed of about 400 evts/s of the data reading tasks which perform the reading (and de-compression) of the root-files in the standard reconstruction software MARS. For the time being, every signal extractor being faster than this reference number, does not limit the total event reconstruction speed. Only some of the integrating spline extractor configurations lie below this limit and would need to be optimized further.

5.11 Results

Based on the previous investigations, the obtained results are summarized in table 14. The following criteria are used to compare the extractors:

- The extractor should yield stable results against slight modifications of the pulse shape, i.e. not deviate by more than 5% due to typical pulse form differences. This requirement excludes extractors which integrate only small portion of the pulse, especially the amplitude sensing cubic spline extractor.
- The extractor must yield a stable low-gain pulse extraction. This means that apart from being robust against modifications of the pulse shape, the extractor has to be stable against variations of the pulse within the recorded FADC

Measured Extraction Speed		
Name	Events/sec. (CPU)	comments
Fixed Window 14 slices	2700–3300	no time
Sliding Window 2 slices	400–700	
Sliding Window 4 slices	500–800	
Sliding Window 6 slices	1000–1300	
Sliding Window 8 slices	1100–1400	
Spline Amplitude	700–1000	
Spline Integral 1 sl.	300–500	
Spline Integral 2 sl.	200–400	
Spline Integral 4 sl.	150–200	to be optimized
Spline Integral 6 sl.	80–120	to be optimized
Digital Filter 6 slices	700–900	
Digital Filter 4 slices	700–900	

Table 13: The extraction speed measured for different signal extractor configurations.

samples. This criterion excludes the fixed window extractor since typical arrival time jitters are bigger than the time window between the tail of the high-gain pulse and the beginning of the low-gain pulse. In certain data taking periods of the year 2005, also extractors using large sliding windows, are excluded by this criterion.

- The *RMSE* of the reconstructed charge for the case of no signal should not exceed 2 photo-electrons under no-moon conditions and the *RMSE* of the reconstructed charge for air shower signals should never exceed the intrinsic Poissonian signal fluctuations above 5 photo-electrons. This low-energy analysis condition discards the large sliding windows and the fixed window extractor. It is not critical for high-energy analyses, however.

- For analyses around the energy threshold, an extractor should have a small or negligible bias, discarding again the amplitude sensing cubic spline extractor.

- The time resolution should not be worse than 1 ns at a signal strength of 10 photo-electrons. Also this condition applies above all to low-energy analyses where the arrival time information is needed to discriminate between signal and noise. All fixed window and all simple sliding window extractors are excluded by this condition.

- The needed CPU-time should not exceed the one required for reading the data

into memory and writing it to disk. Unless further effort is made to speed up the integrating spline, this extractor is excluded if used with a large integration window.

Tested Signal Extractor Characteristics							
Extractor Configuration	robust-ness pulse form high gain	robust-ness pulse form low gain	robust-ness pulse position	*RMSE*	bias	time spread	Speed
Fixed Window 14 sl.	**BEST**	**OK**	**NO**	**NO**	**BEST**	**NO**	**BEST**
Sliding Window 2 sl.	**NO**	**NO**	**OK**	**OK**	**OK**	**NO**	**OK**
Sliding Window 4 sl.	**OK**	**NO**	**NO**	**NO**	**OK**	**NO**	**OK**
Sliding Window 6 sl.	**OK**	**OK**	**NO**	**NO**	**OK**	**NO**	**OK**
Sliding Window 8 sl.	**OK**	**BEST**	**NO**	**NO**	**OK**	**NO**	**OK**
Spline Amplitude	**NO**	**NO**	**BEST**	**OK**	**NO**	**OK**	**OK**
Spline Integral 1 sl.	**NO**	**NO**	**OK**	**OK**	**OK**	**BEST**	**OK**
Spline Integral 2 sl.	**NO**	**NO**	**OK**	**OK**	**OK**	**BEST**	**OK**
Spline Integral 4 sl.	**OK**	**NO**	**NO**	**OK**	**OK**	**BEST**	**NO**
Spline Integral 6 sl.	**OK**	**OK**	**NO**	**NO**	**OK**	**BEST**	**NO**
Digital Filter 4 sl.	**OK**	**OK**	**NO**	**BEST**	**OK**	**OK**	**OK**
Digital Filter 6 sl.	**NO**	**OK**	**NO**	**OK**	**OK**	**OK**	**OK**

Table 14: The tested characteristics for every extractor. See text for descriptions of the individual columns. **OK** *means, the extractor has passed the test,* **NO** *that the extractor failed and* **BEST** *that the extractor has succeded a particular test as best of all.*

Table 14 shows which extractors fulfill the above criteria. One can see that there is no signal extractor without problems. However, the digital filter fitting four FADC slices can be used always for the high-gain extraction, and the digital filter fitting six FADC slices for the low-gain extraction, whenever the mean pulse position is not critical. This combination has been chosen as the standard extractor for all MAGIC data. It has turned out to be robust, except for the data affected by the pulse position problem.

For the critical data, only the cubic spline algorithms integrating 1–2 FADC slices are left which might nevertheless yield systematic differences due to the instability with respect to deviations of the pulse form. In fact, data taken in January and February of 2005 had to be extracted this way.

If efficiencies at low energies are not critical, i.e. a high image cleaning level is used and timing is not an issue, the sliding window extractor can be used in

configurations which cover the entire pulse. This extractor turns out to be especially robust (whenever the mean pulse position is not critical). Because of this quality, all further measurements done for the absolute calibration, were performed using this extractor.

5.12 Outlook

Parts of the difficulties to find a suitable signal extractor (reflected in table 14) stem from the fact that the MAGIC signals are shaped just as long as to cover about four FADC slices. This choice "washes out" the intrinsic pulse form differences between gamma-like and hadron-like showers, and prevents the analysis therefore from using this information in the gamma-hadron discrimination. On the other side, the shaping time is not big enough to safely extract the amplitude of the (shaped) signal.

These problems will be overcome with the installation of the new 2 GHz FADC system in the middle of 2006, which have been designed to reduce any pulse form deformation to the minimum. It can be expected that the individual pulse forms are then directly recognized as such, e.g. with a digital filter using two sample pulse forms (a gamma-like and a hadron-like) and discriminating between both with the help of the calculated χ^2. These FADCs have a 10-bit dynamic range and do not need a separate low-gain channel any more. This choice will call for some adaptations of the extractors for the case of saturated signals, on the other side remove a lot of sources of instabilities from to the low-gain extraction. It can be expected that the signal extraction will become robuster, besides extracting a wealth of additional information about the shower characteristics.

6 Characterization of the Telescope Using the Calibration System

6.1 High-gain vs. Low-gain Inter-calibration

The signals from the MAGIC telescope camera get split into two branches – the "high-gain" channel and the "low-gain" channel. The first amplifies the signals about a factor 10 higher than the second one. Additionally, the low-gain signal gets delayed by 55 ns and obtains thus a different shape due to the limited dynamic range of the passive delay line (see section 3.8).

In order to combine the signals from both high-gain and low-gain correctly, an inter-calibration is necessary. One can make the following ansatz:

$$\widehat{Q}^i_{HG} = \widehat{Q}^i_{LG} \cdot f^i_A \cdot f_E \ , \tag{96}$$

where $\widehat{Q}^i_{LG}$ is the extracted signal from the low-gain channel i, $\widehat{Q}^i_{HG}$ the equivalent signal that would have been obtained from the high-gain channel N. f^i_A is the (hardware) amplification ratio between high-gain and low-gain for channel i. A constant factor f_E comes from possible different normalizations of the signal extractors for both pulse shapes which is independent of the individual readout channel. By selecting events which have both a non-saturation high-gain signal $\widehat{Q}^i_{HG}$ and an extractable low-gain signal $\widehat{Q}^i_{LG}$ and assuming linearity of both the hardware amplification chain and the signal extractor, the proportionality factors $(f^i_A \cdot f_E)$ can be retrieved for every channel individually:

$$R^i_E = \frac{\widehat{Q}^i_{HG}}{\widehat{Q}^i_{LG}} \equiv f^i_A \cdot f_E \ . \tag{97}$$

The ratios R^i_E are in general different for every channel i and for every signal extractor E.

The high-gain vs. low-gain inter-calibration was performed with cosmics data taken in September and December 2004. An event selection was made requiring that the highest FADC slice content is higher than 180 FADC counts, but does not exceed 240 FADC counts. This selection ensures that the signals do not yet saturate the high-gain channel, but are intense enough to trigger the low-gain switch of the electronics. The signal reconstruction bias was assumed to be negligible in any low-gain event above the chosen threshold (see e.g. figure 113).

Figure 128 shows distributions of the obtained ratios R_E. One can see that the mean conversion factors $< R^i_E >$ are not always centered at the hardware value of 10. The spread over the pixels is about 10% for the sliding window extractor, 8% for the digital filter and even lower for the spline extractors. Figure 129 shows the distribution of the constants R^i_E over the MAGIC camera. One can clearly distinguish clusters of eight pixels which correspond to one same optical receiver board.

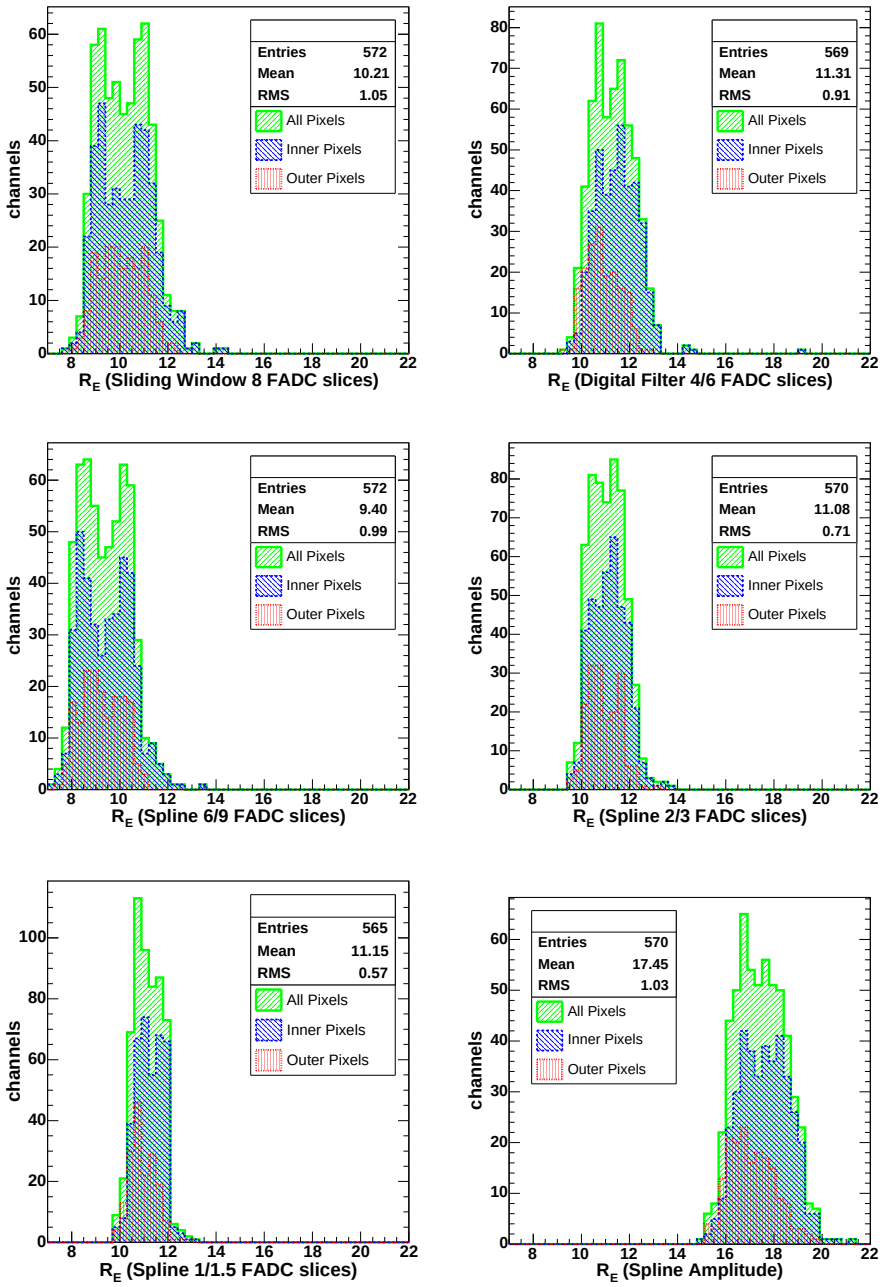

Figure 128: Distributions of the high-gain vs. low-gain signal ratios R_E^i, calculated with typical signal extractor configurations. The first number refers to the high-gain sliding window, while the last number of the low-gain window. E.g. "Spline 1/1.5" means a cubic spline extractor integrating 1 FADC slice around the high-gain spline maximum and 1.5 FADC slices around the low-gain maximum.

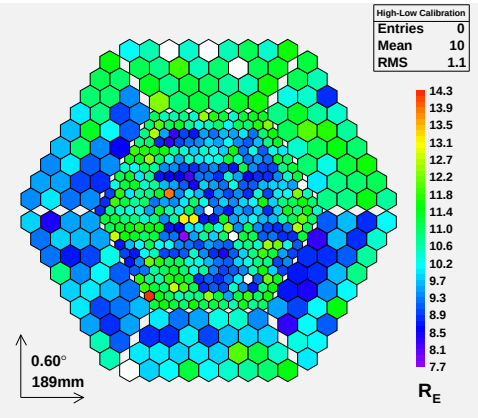

Figure 129: Distributions of the calibrated high-gain vs. low-gain signal ratios R_E, calculated with a sliding window summing 8 high-gain and 8 low-gain FADC slices in the MAGIC camera. Many of the constants R_E^i cluster in groups of eight corresponding to the individual optical receiver boards.

Figure 130 shows the correlation of the amplification ratios obtained with one signal extractor against those obtained with another extractor. In all cases, a clear correlation is visible which confirms the assumption that the differences in amplification ratios between different readout channels are mainly due to hardware differences whereas the effect of the signal extractor is constant for all channels. However, there seem to be extractor combinations whose inter-calibration constants correlate very well while others show a bigger spread, especially there seem to be two classes of signal extractors which produce good correlations with extractors within a same class and worse correlations with those belonging to the opposite class. Table 15 shows which extractor belongs to which class: All signal extractors which integrate the entire pulse belong to class A while those which perform a fit or integrate only parts of a pulse belong to class B.

In order to further test equation 96, the following relations are drawn in figure 130:

$$R^i_{E_y} = \frac{< R_{E_y} >}{< R_{E_x} >} \cdot R^i_{E_x} \approx \frac{f_{E_y}}{f_{E_x}} \cdot R^i_{E_x} \ , \tag{98}$$

where E_x denotes the signal extractor displayed on the x-axis and E_y the one on the y-axis. One can see that eq. 98 matches the data points well for all extractors of a same class, but not those obtained with extractors of a different class. The reason for this behaviour of the signal extractors is still not understood. One explanation could be limitations of the slew rate of the high-gain amplifiers and/or modifications of the pulse shape at high amplitudes. Although the slew rate of the amplifiers was tested directly in the lab, the response of the whole system – including AC-coupling the amplifiers – in combination with input pulse widths of the same order

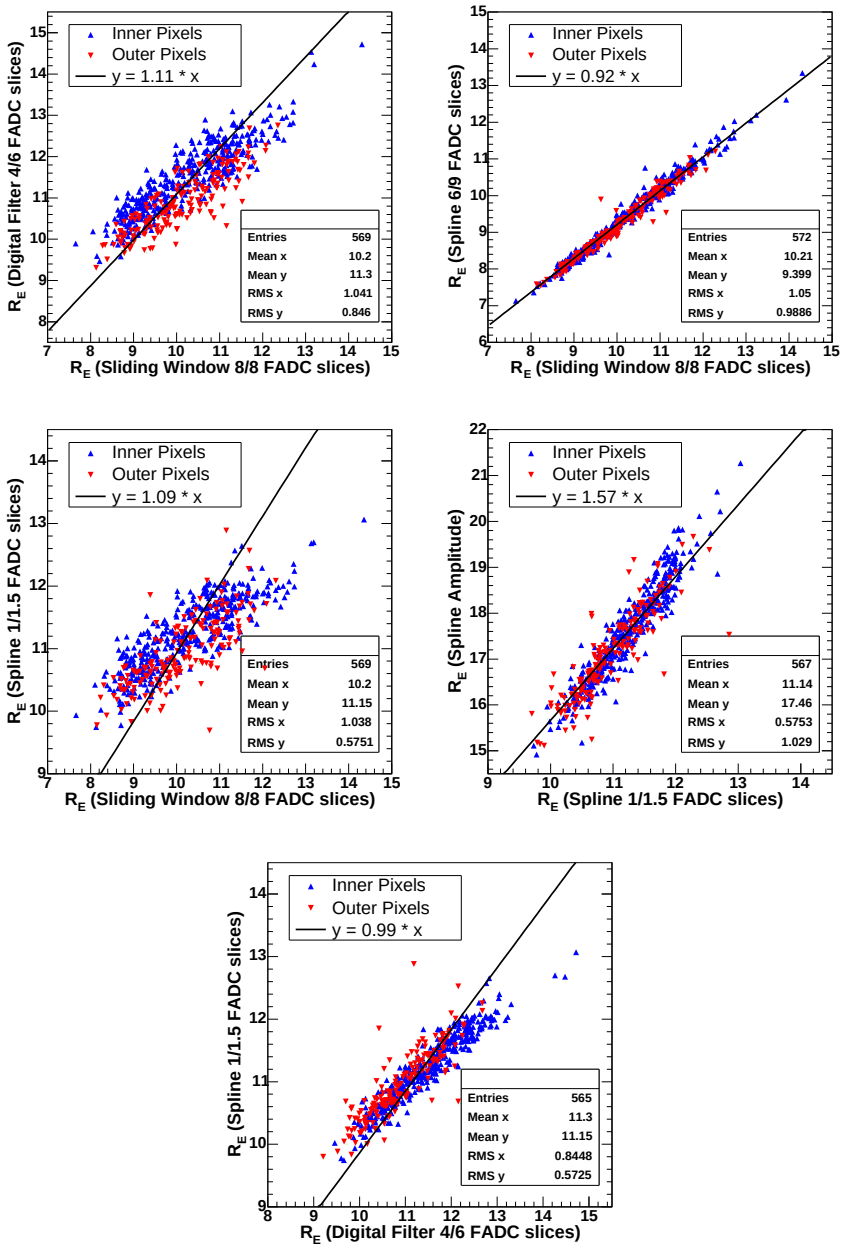

Figure 130: Distributions of the calibrated high-gain vs. low-gain signal ratios R_E, calculated with the digital filter fitting 4 high-gain and 6 low-gain FADC slices, the sliding window summing 8 FADC slices each and the spline integrating 6 high-gain and 9 low-gain FADC slices, 1 high-gain and 1.5 low-gain FADC slices and only the amplitude of spline. The values of R_E, obtained with the five different signal extractors, correlate well. Also equation 98 is displayed.

Classification of Signal Extractors		
Nr.	Name	Class
20	Sliding Window 6/6	A
21	Sliding Window 8/8	A
23	Spline Amplitude	B
24	Spline Integral 1/1.5	B
25	Spline Integral 2/3	B
27	Spline Integral 6/9	A
28	Digital Filter 6/6	B
29	Digital Filter 4/4	B
	Digital Filter 4/6	B

Table 15: The classification of signal extractors with respect to their correlation properties of the high-gain vs. low-gain inter-calibration constants R^i_E. Extractors of a same class produce values of R^i which correlate very well with each other and extractors of a different class do correlate, but show a much bigger spread.

of magnitude as the shaping time was not [246]. A different possibility could be wrong estimations of the low-gain pedestals which affect big extraction windows stronger than small ones. The second hypothesis assumes that the AC-coupling at the input of the FADCs would not be fast enough to level out possible differences in the low-gain voltage offset. Unfortunately, there is no way to measure directly these pedestal offsets since the low-gain extraction window coincides more or less with the GaAs-switching noise and the subsequent low-gain pulse.

Figure 131 shows the extracted high-gain vs. the low-gain charge, obtained with three standard signal extractors: A fully integrating sliding window, a digital filter combination and a spline integrating just the mininum of one FADC slice around the pulse maximum. While the full pulse integration yields a linear high-gain vs. low-gain signal dependency, the digital filter and to a much larger extent, the small window-sized spline show significant deviations from linearity. This result points to the first hypothesis of modifications of the pulse shape with increasing amplitude. The above results show, in accordance with the signal extractor evaluations of section 5.11 that not fully integrating signal extractors show robustness problems with respect to modifications of the pulse form and linearity.

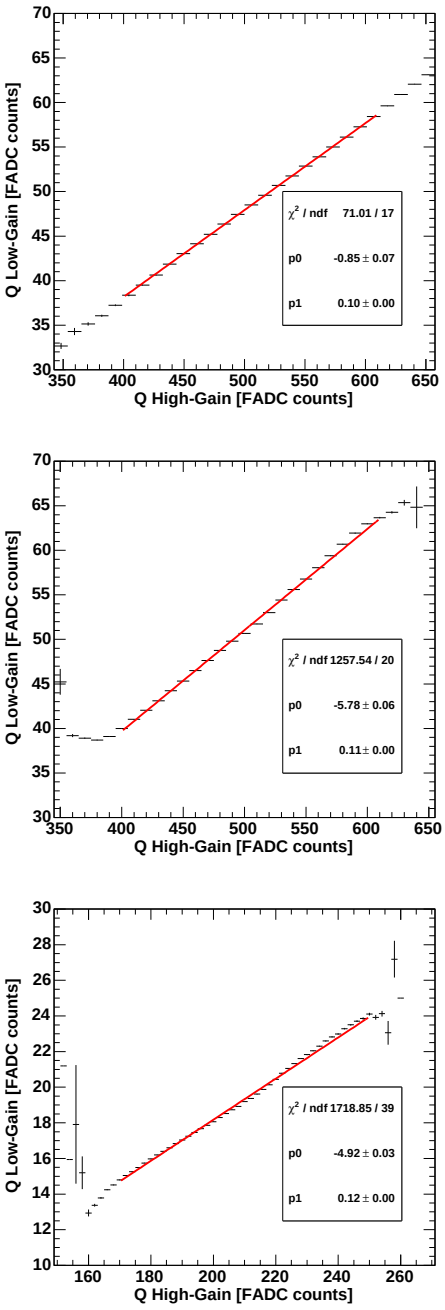

Figure 131: Distributions of the high-gain vs. low-gain signal, calculated with three standard signal extractors. Top: sliding window integrating the full pulse, center: digital filter fitting four and six FADC slices for high-gain and low-gain, respectively, bottom: spline integrating one FADC slice around the high-gain maximum and 1.5 FADC slices around the low-gain maximum

6.2 Linearity of the Amplification Chain

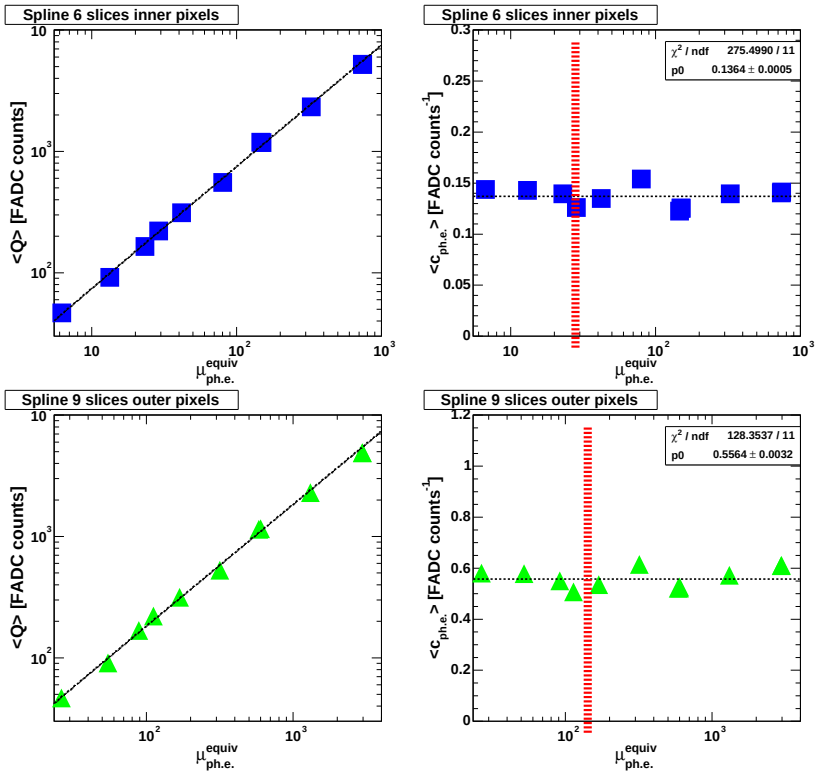

Figure 132: Distributions of the reconstructed charge vs. reconstructed number of photo-electrons (left) and the conversion factor c_{phe} vs. number of photo-electrons (right), separately for inner and outer pixels. The pulse was interpolated with a cubic spline and six high-gain FADC slices and nine low-gain FADC slices around the spline maximum were integrated. The red line indicates the intensity of the standard calibration pulse from 10 UV Leds.

In this section, the linearity of the signal amplification and extraction chain is tested. For this reason, conversion factors from FADC counts to photo-electrons area defined:

$$c_{\mathrm{phe}} := \mu^{equiv}_{\mathrm{phe}} / < \widehat{Q} > , \tag{99}$$

where $\mu^{equiv}_{\mathrm{phe}}$ is the mean number of photo-electrons, obtained with the F-Factor method (see chapter 4.6), obtained from and employed for the inner pixels. In the case of the outer pixels, this number gets multiplied with the ratio of photo-sensitive areas which is exactly a factor 4 in the case of the MAGIC camera [46].

[46] A more detailed description and justification of this concept of ***equivalent photo-electrons*** will be given in section 7.4.

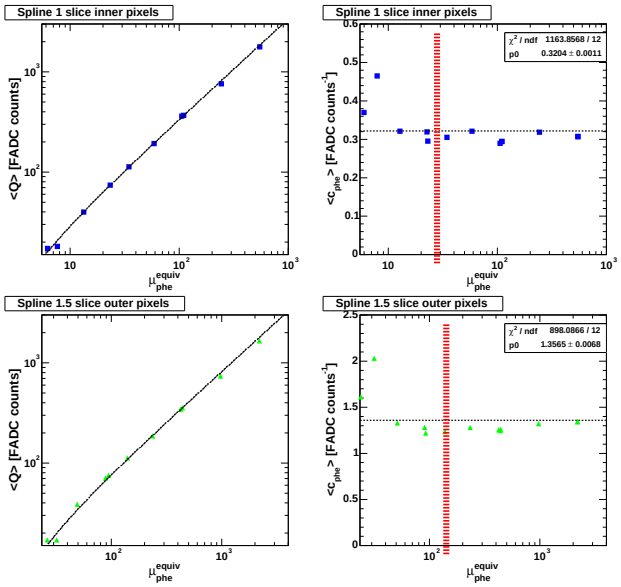

Figure 133: Distributions of the $< Q >$ vs. μ_{phe} (left) and $< c_{\mathrm{phe}} >$ vs. μ_{phe} (right). The pulses were interpolated with a cubic spline and one high-gain FADC slices and 1.5 low-gain FADC slices around the spline maximum were integrated. The red line indicates the intensity of the standard calibration pulse from 10 UV Leds.

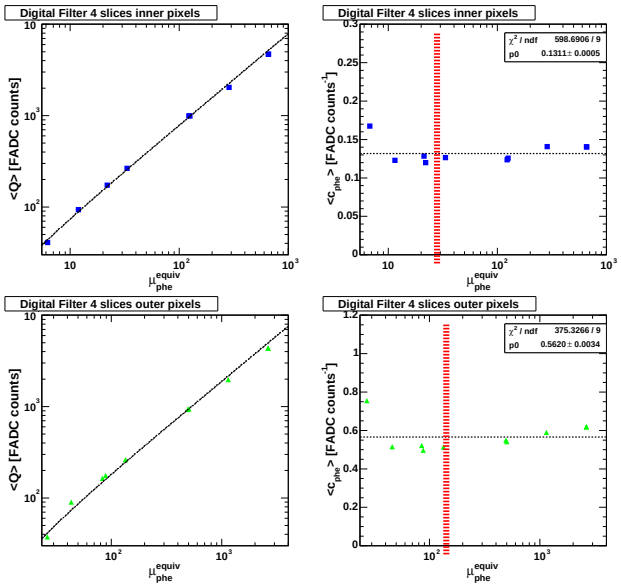

Figure 134: Distributions of the $< Q >$ vs. μ_{phe} (left) and $< c_{\mathrm{phe}} >$ vs. μ_{phe} (right). The pulses were fitted to a blue sample pulse using the digital filter method. The red line indicates the intensity of the standard calibration pulse from 10 UV Leds.

The mean reconstructed signal of a series of calibration pulses of same intensity, $< \widehat{Q} >$, depends on the signal extractor and has been corrected with the high-gain vs. low-gain intercalibration factors from the last chapter.

As the photo-multiplier and the subsequent optical transmission devices [200] are linear devices over a wide dynamic range, the number of equivalent photo-electrons per charge c_{phe} is expected to remain constant over the tested linearity region.

Figure 132 (left) shows the behavior of the cameera average of $< \widehat{Q} >$ vs. $\mu_{\mathrm{phe}}^{equiv}$ over more than two orders of magnitude, whereby the signal was extracted in the stablest possible way: A fully integrating spline which interpolates the 6 consecutive high-gain slices with the highest signal content and the 9 corresponding low-gain slices. One can see the overall linear behaviour, both for inner and outer pixels. A closer look (figure 132 (right)) reveals that the average conversion factors $< c_{\mathrm{phe}} >$ scatter much more than expected from simple statistics, with peak-to-peak amplitude of 20% at the transition between high-gain and low-gain extraction. It should be realized however that the extraction of the calibration parameters is affected by fluctuations above the saturation limit (in the case of the high-gain extraction) or below the "low-gain switch" limit (in the case of the low-gain extraction). Also a very low intensities, the extracted charges and number of photo-electrons are affected biased from the night sky background. Outside of these critical regions, $< c_{\mathrm{phe}} >$ scatters by about 10% peak-to-peak, which can be considered as the systematic precision of the linearity calibration. Note especially that no obvious sign for saturation at high intensities can be discerned.

Whenever other signal extractors are used, especially those which show dependencies on the pulse form (recall chapter 5.11), the linearity of the extracted signals is stronger affected by distorsions of the pulse form and possible saturation effects. Figures 133 and 134 show the average reconstructed signals and conversion factors per light pulse intensity, for signals extracted with two standard extractors, used especially for the low-energy analyses in MAGIC: A spline integrating only 1 and 1.5 FADC slices around the spline maximum for high-gain and low-gain pulses, respectively and the digital filter. It seems that in these cases, the outer pixels show already a hint for saturation effects, which cannot be disentangled from the systematic uncertainty of the procedure to determine these parameters, though. Excluding the biased low-intensity region, a peak-to-peak spread of maximally 20% is observed here, yielding an upper limit to possible (average) low-gain saturation effects up to signals of 1000 photo-electrons per photo-multiplier.

6.3 Cross-Talk in the Camera and Short-term Temporal Uniformity of Light Pulses

Taking advantage of the fact that the individual readout channels of the camera work in an autonomous way and no interference between neighbouring pixels is assumed, the correlation behaviour of the registered signals with those obtained from other channels can be used to determine whether the intensity of the emitted light pulses drifts with time on short time-scales.

For this reason, the extracted signals q_i of the individual channels i are getting averaged over a big number N_{pix} of channels on an event-by-event basis to yield an average charge Q:

$$Q := \frac{1}{N_{pix}} \sum_{i=1}^{N_{pix}} q_i \ . \tag{100}$$

After the end of one calibration sequence, the variance of the averaged signals Q is calculated:

$$\mathrm{Var}[Q] =< Q^2 > - < Q >^2 \ , \tag{101}$$

where the averages go over the events of one light pulser sequence. Inserting eq. 100 into eq 101, one obtains:

$$\begin{aligned} \mathrm{Var}[Q] &= \frac{1}{N_{pix}^2} \sum_{i=1}^{N_{pix}} \sum_{j=1}^{N_{pix}} \mathrm{Cov}(q_i, q_j) \qquad \text{with :} \\ \mathrm{Cov(q_i, q_i)} &= < q_i q_j > - < q_i >< q_j > \\ &= \rho_{ij} \cdot \sigma_i \cdot \sigma_j \ , \end{aligned} \tag{102}$$

where $\mathrm{Cov}(q_i, q_j)$ is the ***cross-correlation matrix*** and ρ_{ij} the ***correlation coefficients*** of the camera (σ_i and σ_j are the individual widths of the signal distributions q_i and q_j, respectively). In case of no correlation between different channels, the non-diagonal elements of ρ_{ij} are on average zero, with a statistical width of $1/\sqrt{N}$, where N is the number of events in one calibration sequence. In case two or more readout-channels yield correlated signals, e.g. due to cross-talk, outliers in the distribution of ρ_{ij} are expected, whereas in case of drifts or non-Poissonian variations of the intensity of the light pulses, the distribution of ρ_{ij} would be skewed and not centered at zero any more [247].

Figure 135 shows the distribution of the off-diagonal elements of ρ_{ij} for a standard calibration sequence of about 4000 UV light pulses and another calibration run which was taken with intense blue light. Like expected in both cases, the distribution is centered around zero with a width of approximately $\sigma = 1/\sqrt{N}$. At least for these cases, no sign for cross-correlation has been found, i.e. each pixel of the camera behaves un-correlated to those of the rest of the camera.

Assuming therefore that the sums of $\mathrm{Cov}(q_i, q_j)$ give zero for the off-diagonal elemets $i! = j$, the following relation can be expected:

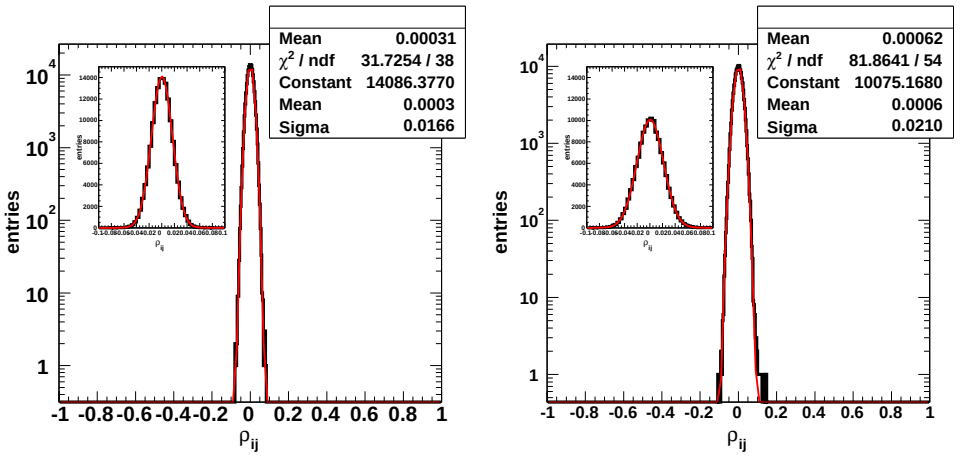

Figure 135: Distribution of correlation coefficients ρ_{ij}. Left: a typical calibration run with medium intense UV-colored LEDs, right: intense blue LEDs which saturated the low-gain channel. Mal-functionning pixels had been excluded before.

$$\begin{aligned} \mathrm{Var}[Q]^{uncorr} &\approx \frac{1}{N_{pix}^2}\sum_{i=1}^{N_{pix}}(< q_i^2 > - < q_i >^2) \\ &\approx \frac{1}{N_{pix}}\cdot\Big(\frac{1}{N_{pix}}\sum_{i=1}^{N_{pix}}(< q_i^2 > - < q_i >^2)\Big) \\ &\approx \frac{1}{N_{pix}}\cdot < \mathrm{Var}[q] > , \end{aligned} \tag{103}$$

where $< \mathrm{Var}[q] >$ is the average variance of the individual pixels' signal distributions q_i. In case of full correlation ($\rho_{ij} = 1$), all non-diagonal elements of $< q_{ij} >$ would be of the same size as the diagonal elements, and the variance of the averaged signal becomes:

$$\begin{aligned} \mathrm{Var}[Q]^{corr} &\approx \frac{1}{N_{pix}}\sum_{i=1}^{N_{pix}}(< q_i^2 > - < q_i >^2) \\ &\approx < \mathrm{Var}[q] > , \end{aligned} \tag{104}$$

thus approximating the average of the individual signal variances. One can then contruct a short-term correlation test parameter R:

$$R = 1 - \sqrt{\frac{< \mathrm{Var}[q] >}{N_{pix}\cdot \mathrm{Var}[Q]}} , \tag{105}$$

which is zero in the case of no correlation and one in the case of full correlation. The parameter R will be different from zero especially in the case of short-term variations of the light pulser output, getting reflected in non-Poissonian signal variances. Figure 136 shows the evolution of the R-parameter for typical calibration sequences taken at 50 Hz and evaluated every 500 events, for inner and outer pixels separately. One can see that the obtained values oscillate around zero, with slight overall positive offsets of about 2% (see the fit result). It is not clear whether this small, but statistically significant number reflects a residual overall correlation or simply the systematic limitation of this method. For this reason, the mean values of R have been calculated for a whole observation period, with results shown in figure 137 (note that the scale is different between both figures). Again, a small positive offset of about 2% is obtained for both inner and outer pixels. In conclusion, no obvious short-term variation of the light pulser intensity can be deduced from these figures and the calibration pulse sequences are sufficiently stable, certainly if compared to the systematic uncertainties which have been obtained for the absolute calibration level in the previous chapters and which can reach easily 5%.

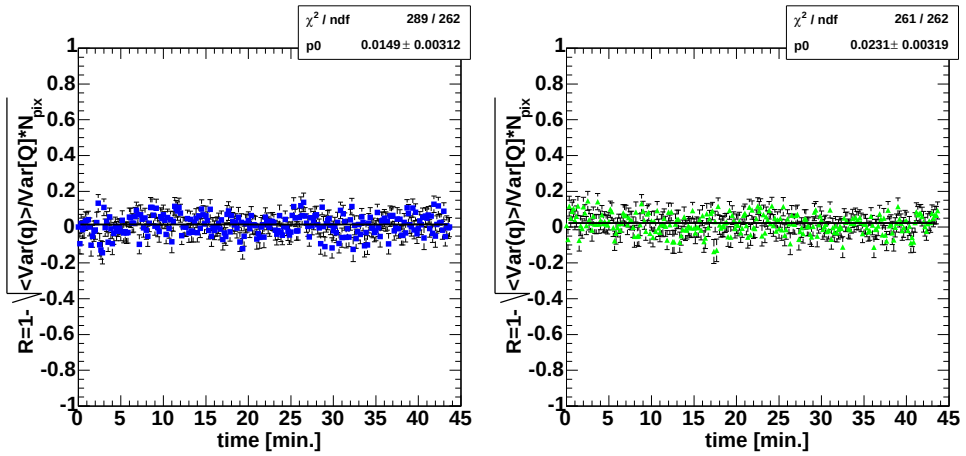

Figure 136: Short-term variations test parameter R, obtained from interlaced calibration pulses during 45 minutes of data taking. Left: inner pixels, right: outer pixels.

6.4 Medium-term Variations of Light Pulser Intensity and Camera Gains

In the following, variations of typical calibration parameters are investigated over two medium-size time scales: A typical data taking sequence of about 45 minutes and an observation period of one month. Using calibration pulses, interlaced with normal data taking, at a rate of 50 Hz, the calibration parameters are getting updated every 10 seconds. The here investigated parameters are:

The mean number of photo-electrons $\mu_{\text{p.e.}}$: Calculated with the F-Factor Method

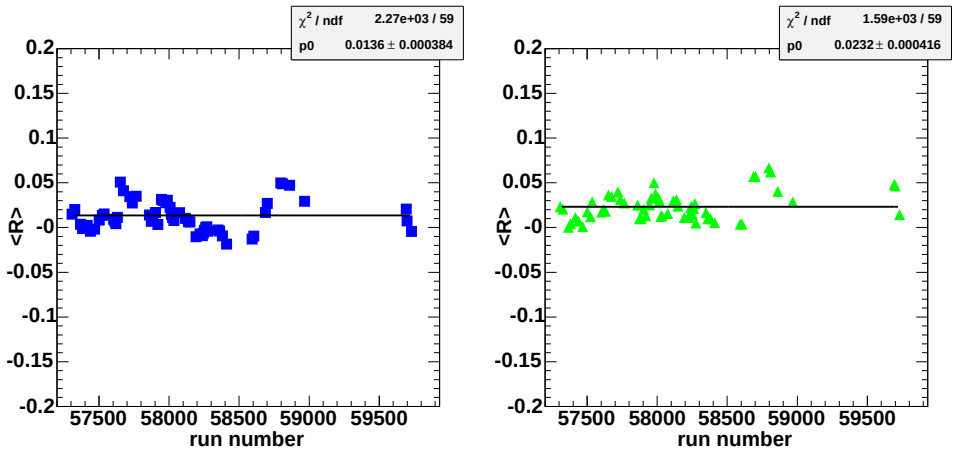

Figure 137: Short-term variations test parameter R, averaged over typical interlaced calibration pulse sequences during one month of data taking. Left: inner pixels, right: outer pixels.

(see section 4.6, eq. 58), $\mu_{p.e.}$ has been obtained by averageing the number of photo-electrons, obtained from each inner pixel, and reflects directly the light output of the calibration pulser. In case of the outer pixels, $\mu_{p.e.}$ gets multiplied with the ratio of covered light guide areas, which is exactly four in the case of the MAGIC camera (see also section 3.7).

The average conversion factors $< c_{\text{p.e.}} >$: Defined as the mean number of photo-electrons per accumulated mean charge at the output of the signal transmission chain, $c_{\text{p.e.}}$ reflects the gain of each signal detection and amplification channel. Its average $< c_{\text{p.e.}} >$ follows global gain drifts, e.g. due to temperature changes.

Figure 138 shows the development of mean number of photo-electrons $\mu_{\text{p.e.}}$ and the average conversion factors $< c_{\text{p.e.}} >$ for inner and outer pixels, respectively, for a typical data taking sequence of 45 minutes, taken in June, 2006. While $\mu_{\text{p.e.}}$ is affected only by statistical fluctuations, varying less than 1% (RMS), clear drifts can be discerned for the conversion factors. Closer investigations revealed that these drifts are closely correlated with temperature variations inside and outside the camera [190] and can vary by at most 20% in time-scales of hours to days. The gains are thereby positively correlated with temperature.

The following conclusions can be drawn from these studies: The determination of the mean number of photo-electrons $\mu_{\text{p.e.}}$ is stable on medium time-scales, with a relative precision better than 1%. This stability allows to average $\mu_{\text{p.e.}}$ (e.g. over 10 calibration sequences, as in the standard calibration procedure), to remove part of the remaining statistical fluctuations.

The gains of the camera drift on time-scales of minutes to hours, sometimes differently for inner and outer pixels (see e.g. figure 139). They have to be corrected therefore with the use of interlaced calibration light pulses (or optionally interlaced

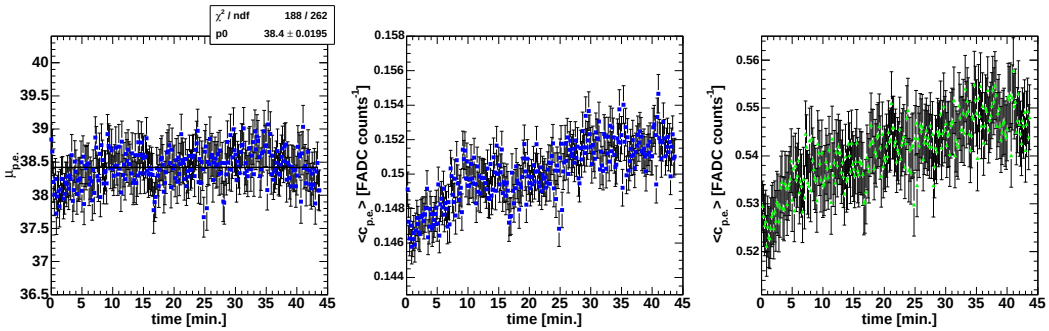

Figure 138: Variations of the mean number of photo-electrons $\mu_{\text{p.e.}}$ in the camera and the average conversion factors $< c_{\text{p.e.}} >$ for inner and outer pixels over one typical data taking sequence. All scales have been adjusted to cover 10% of the mean value.

calibration sequences), which are currently fired at a rate of 50 Hz, with conversion factor updates every 10 seconds.

The relative fluctuations of $< c_{\text{p.e.}} >$ with respect to the local average amount to about 0.6 %, yielding thus an upper limit to the statistical precision of the individual conversion factors $c_{\text{p.e.}}$ of about 10 %. These are upper limits instead of measurements since the gains of the optical transmitters can fluctuate up to 8 % and 12 % for inner and outer pixels, respectively, on time-scales of 5 minutes (see section 3.8).

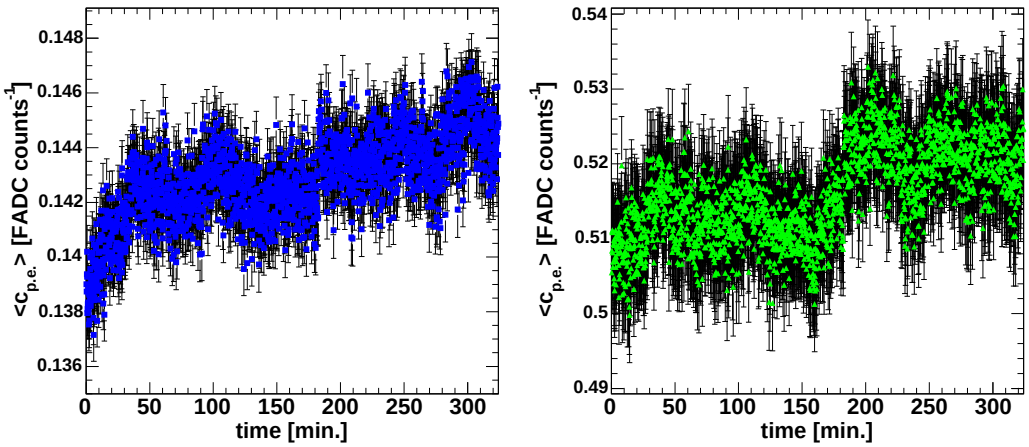

Figure 139: Variations of the average conversion factors $< c_{\text{p.e.}} >$ for inner and outer pixels over one night of data taking. All scales have been adjusted to cover 10% of the mean value.

6.5 Long-term Evolution of the Camera

In this section, the long-term evolution of typical calibration parameters is investigated for their behaviour during the last two years of data taking. Ordinary calibration runs were used for this study, taken at 500 Hz, about four to five times each night. All calibrations were performed with the standard calibration pulse, fired from ***10 UV LEDs***.

Figure 140 shows some of the investigated parameters: The mean number of photo-electrons (top) follows the temperature variations between Summer and Winter, with dependencies already outlined in the previous chapter. More typical for the evolution of the camera is the average conversion factor $< c_{phe} >$, defined as the inner pixels' average of the mean number of photo-electrons per accumulated charge. This parameter is inversely proportional to the gain of the photo-multiplier (and the subsequent signal transmission chain). One can see a steady rise of the conversion factor until February 2006 when it falls again. In order to understand this behaviour, it is important to know that the power supply of the MAGIC camera did not allow to raise the high voltages of the photomultipliers higher than 1300 V until a new version was installed in February 2006. A couple of pixels had already reached that upper limit during the first ***flat-fielding*** procedure, so the average voltage of the inner pixels could not be raised with respect to that first level for that reason. The fitted slope in figure 140 reflects therefore directly the gain drop of the photo-multipliers: about 10 % a year. As soon as the new power supply was installed, a flat-fielding was performed raising the average voltage such that the average gain of one year before was recovered.

The third plot of figure 140 shows the signal dispersion to calibration pulses over the year. Red lines mark the times when a flat-fielding was performed. It is rapidly checked that no flat-fielding procedure has failed: Every single flat-fielding reduced the spread with respect to the values before. The longest period without flat-fielding is found from August 2004 to August 2005 where the increase of dispersion with time can be measured (black fit): 3.2 ± 1.2 % per year. There is also a "learning-curve" visible: Flat-fieldings get better with time reaching a currently best value of slightly less than 10 % relative dispersion.

Finally, all calibration runs taken with different intensities, were analyzed according to the procedure described in chapter 4.6: From $\mathrm{Var}[\widehat{Q}]/ < \widehat{Q}^2 >$ vs. $1/ < \widehat{Q} >$ test plots, the combination of $\mu_1 \cdot F^2$ can be extracted, where μ_1 is the gain of the photo-multiplier for a single photo-electron, and F the ***excess-noise factor***. The bottom plot of figure 140 shows that the combination of $\mu_1 \cdot F^2$ has remained more or less stable, consistent with the expectation that the value of F^2 has increased the same amount, as the gain μ_1 has decreased. It would have been nice though to have a statistically significant measure of this hypothesis, by taking more calibration runs at different intensities. During the last two years, this was not possible because against the will of the responsible persons. I hope that these plots convince them of the necessity to take calibration runs at different intensities at least once per month.

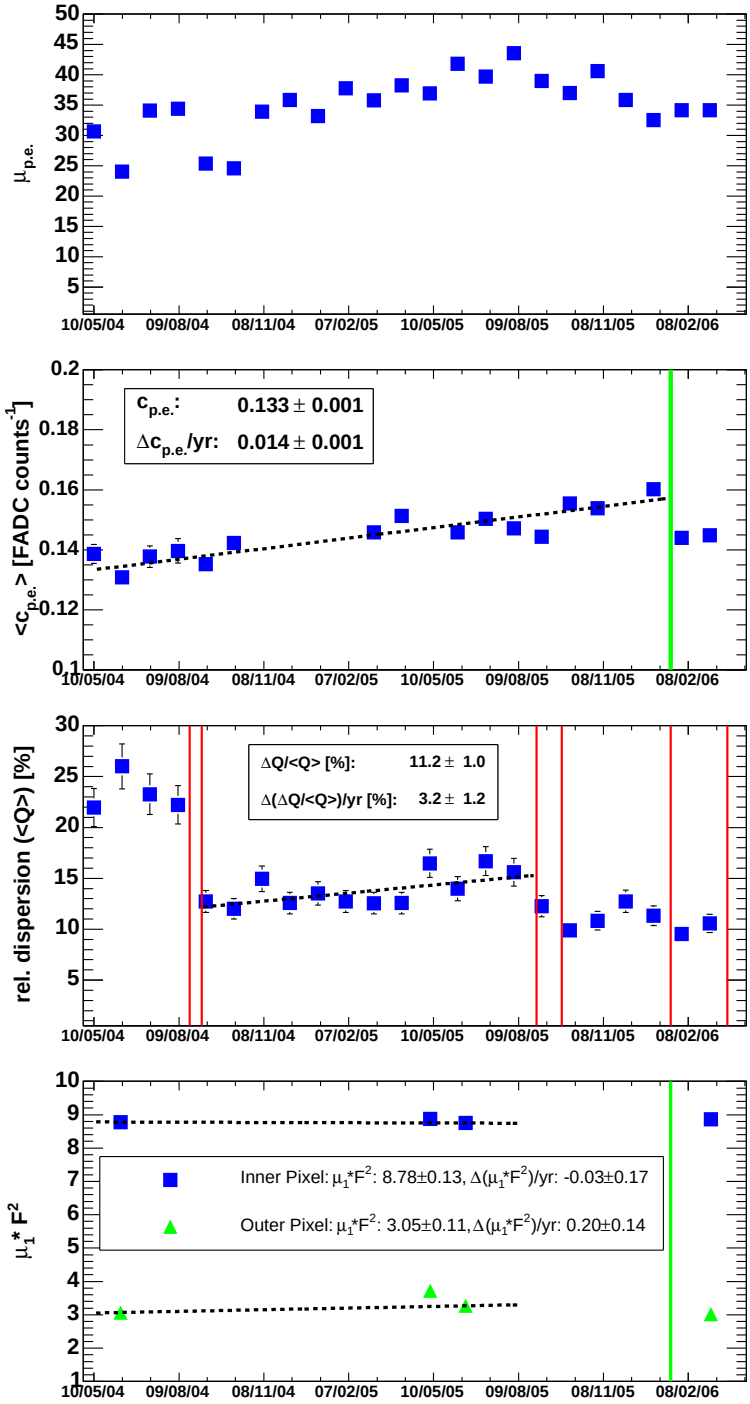

Figure 140: Evolution of calibration parameters during two years of data taking. Top: mean number of photo-electrons, second: average conversion factor. Left out points mark periods where a different signal extractor had to be used. The green line marks the installation of a new power supply. Third: Dispersion of extracted signals, the red lines mark the nights when the camera was flat-fielded. Bottom: Combination of gain and excess noise factor $\mu_1 \cdot F^2$, obtained from calibration runs with different intensities.

6.6 Absolute Light Calibration

Several absolute calibration runs have been taken over the last year, summarized in tables 16 and 17. One can see that only strong light intensities could be used in combination with the PIN diode, otherwise the intrinsic noise of diode and pre-amplifier introduces a bias into the measurements. All calibrations performed with the PIN diode lose precision with time since no maintainance access to the PIN diode box itself has been performed, and it is not clear whether the glass window in front of the PIN diode has been affected by the bad weather last Winter. For this reason, only results taken in May 2005 are 100 % trustful for the moment. These results show a 17±8 % higher light flux than the one obtained from the F-Factor method. This value is consistent with the expectation that the square of the excess noise factor has increased by about 10 % since the start of the data taking of the telescope in 2004. The absolute calibration level should be raised accordingly. Later in time, this difference increases, however coupled with big uncertainties. Certainly, only a dedicate maintainance access to the PIN diode with subsequent absolute light calibrations will determine whether the evolution of this discrepancy is correct.

In the case of the blinded pixels, any light intensity can be used as far as enough statistics is accumulated, at least in the case of the small intensities. Two of the blinded pixels have become functional in November, 2005 while the third one is still not usable due to a corrupt transmission line. One can see that all measurements made with the blinded pixels yield lower absolute light fluxes than those made with the PIN diode. Moreover, a difference is obtaiend between calibration pulses in UV, extracted from the high-gain readout channel and the intense blue pulses, extracted from the low-gain channel. A long-term evolution cannot be determined yet since more data is needed, taken in different months. Again here, a bigger sample of different intensities and colours would be desirable.

Absolute Calibration Results PIN Diode							
Date	Configuration	$< N_{\text{p.e.}}^{\text{PIN Diode}} >$	$N_{\text{ph}}^{\text{PIN Diode}}$ $(\cdot 10^6)$	$< N_{\text{p.e.}}^{\text{Camera}} >$	$N_{\text{ph}}^{\text{Camera}}$ $(\cdot 10^6)$	Ratio	Comments
May 2005	20 Leds BLUE	38550±300	$10.9^{+0.7}_{-0.6}$	608±6	9.3 ± 0.5	1.17±0.02(stat)±0.08(syst)	QVT-read-out
May 2005	10 Leds BLUE	18490±130	$5.25^{+0.4}_{-0.3}$	295±3	4.5 ± 0.3	1.17±0.02(stat)±0.08(syst)	(fig. 90)
May 2005	23 Leds BLUE	44950±400	$12.8^{+0.8}_{-0.6}$	724±6	11.1 ± 0.7	1.15±0.03(stat)±0.08(syst)	FADC read-out (fig. 92)
Nov 2005	23 Leds BLUE	44890±2000	$12.8^{+0.8}_{-0.7}$	698±6	10.7 ± 0.7	1.19±0.04(stat)±0.12(syst)	no
Nov 2005	23 Leds BLUE	45400±2000	$12.9^{+0.8}_{-0.7}$	703±6	10.8 ± 0.7	1.16±0.04(stat)±0.12(syst)	direct
Nov 2005	23 Leds BLUE	45400±2000	$12.9^{+0.8}_{-0.7}$	696±6	10.7 ± 0.7	1.20±0.04(stat)±0.12(syst)	self-calib.
Feb 2006	10 Leds BLUE	19190±200	$5.4^{+0.4}_{-0.3}$	276±3	4.2 ± 0.3	1.30±0.03(stat)±0.1(syst)	
Feb 2006	10 Leds BLUE	19110±200	$5.4^{+0.4}_{-0.3}$	277±3	4.2 ± 0.3	1.29±0.03(stat)±0.1(syst)	

Table 16: If not stated otherwise, all uncertainties include systematics, except for the mean excess noise factor of photomultipliers of the inner camera and possible degradations of the quality of the glass window in front of the PIN Diode (does not apply to measurements of May 2005). The systematic uncertainties between measurements at different times are strongly correlated.

Absolute Calibration Results Blind Pixel							
Date	Configuration	$< \mu_{\text{p.e.}}^{\text{Blind Pixel}} >$	$N_{\text{ph}}^{\text{Blind Pixel}}$ $(\cdot 10^6)$	$< N_{\text{p.e.}}^{\text{Camera}} >$	$N_{\text{ph}}^{\text{Camera}}$ $(\cdot 10^6)$	Ratio	Comments
Nov 2005	23 Leds BLUE	0.75±0.04	9.3 ± 0.6	696±6	10.7 ± 0.7	0.87±0.03(stat)±0.09(syst)	Blind Pixel #1
Nov 2005	23 Leds BLUE	0.078±0.002	9.7 ± 0.5	696±6	10.7 ± 0.07	0.91±0.03(stat)±0.09(syst)	Blind Pixel #3
Feb 2006	10 Leds UV	0.0083±0.0004	$0.6._{-0.04}^{+0.05}$	39.7±2.5	0.58 ± 0.04	1.03±0.04(stat)±0.1(syst)	Blind Pixel #3
Feb 2006	10 Leds BLUE	0.05±0.003	3.55 ± 0.2	276±3	4.2 ± 0.3	0.85±0.03(stat)±0.08(syst)	Blind Pixel #3
Feb 2006	10 Leds BLUE	0.044±0.003	4.0 ± 0.5	276±3	4.2 ± 0.3	0.95±0.15(stat)±0.09(syst)	Blind Pixel #1 low statistics

Table 17: If not stated otherwise, all uncertainties including systematics, except for the mean excess noise factor of photomultipliers of the inner camera. The systematic uncertainties between measurements at different times are correlated.

6.7 Arrival Time Offsets

The photo-multipliers introduce a time delay, the "transit time (TT)", in the amplified photo-electrons signal, depending on the applied high-voltage (HV). Together with smaller relative delays due to different lengths of the optical fibers, these delays have to be calibrated relatively to each other in order to obtain a correct timing information for the analysis.

Using the light pulser at different intensities, the time offsets δt_i of each pixel i of the readout and detection chain were measured. Event by event, the reconstructed arrival time difference of every channel with respect to a reference channel was measured and its mean and RMS calculated in a prescription, presented in section 5.9. The former yields the measured relative time offset while the latter is the convolution of the arrival time resolution of the measured and the reference channel:

$$t_i^{offset} \approx \mu(\delta t_i) \quad (106)$$

$$t_i^{res} \approx \sigma(\delta t_i)/\sqrt{2} \quad (107)$$

While the time resolutions were studied in detail already in chapter 5.9), here the absolute time offsets are investigated. Figure 141 shows the time offset versus the applied HV for each PMT. Like expected, one can see a clear anti-correlation. The smaller the applied HV, the longer the signal takes to travel from the first photo-cathode to the anode.

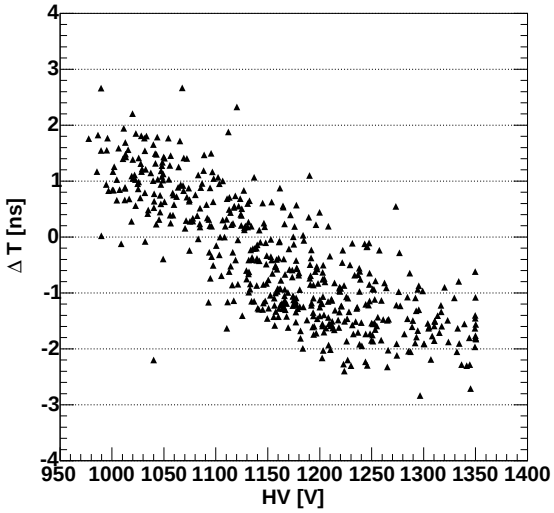

Figure 141: Calibrated arrival time offsets vs. high voltage applied to the corresponding photo-multiplier.

6.8 Summary

The light pulser of the calibration system is stable on short time scales and apt for being used as a calibration device. Deviations from Poissonian behavior, expressed in overall correlations of the captured light pulses between different channels of the photomultiplier camera are smaller than 3 %.

On time scales of minutes to hours, temperature dependencies exist in the amount of emitted light, however these dependencies do not affect typical calibration sequences which last 10 seconds. The camera in turn, does show gain drifts of up to 20% which can be corrected using calibration sequences interlaced during normal data taking.

The photon detection and amplification chain behaves linearly up to intensities of 700 photo-electrons per inner pixel and if the pulse integral is concerned. Signal extractors which integrate only parts of pulse around its maximum can suffer non-linearity affects of up to 20 % at an intensity of 700 photo-electrons. The overall systematic precision of the linearity calibration is better than 10 %. Further dependencies on the pulse form deformation with amplitude have been observed in the inter-calibration between high-gain and low-gain amplification channel.

The camera evolves also on time scales of months to years. From the evolution of the average conversion factors, a gain drop of:

$$\frac{d\mu_1}{dT} = -(10 \pm 1)\%/\text{year} \tag{108}$$

and an increase in relative gain dispersion of:

$$\frac{d(\Delta\mu_1)}{dT} = (2.3 \pm 1.2)\%/\text{year} \tag{109}$$

have been observed. Both are regularly getting corrected with the use of a ***flat-fielding*** procedure. At the same time, the combination of gain, multiplied with the excess noise factor square: $\mu_1 \cdot F^2$ seem to remain constant. Although data is missing to make this statement statistically significant, these findings suggest that the average excess noise factor F^2 increases by about (10±7)% per year.

These findings are supported by the results obtained with absolute calibrations using the PIN diode which shows a $1.17 \pm 0.02(\text{stat.}) \pm 0.08(\text{syst.})$ % higher light flux in May 2005 than the one obtained with the F-Factor method. If one considers that the telescope started data taking in October 2003, an increase of (11±5) % in square of the excess noise factor during one and a half year, as suggested above, the excess is consistent F^2 has to be assumed to match that observation. The PIN diode measurements themselves suggest an excess of the excess noise factor square of 12 % in 9 months and (14±6) % per year which is even higher than the above assumptions (see figure 142). Due to uncertainties in the current state of the PIN diode, this value has to be taken with care however, and measured again after a maintainance access to the PIN diode.

The blind pixels are operational only for a very short time and sparse data is available. First measurements yield a (10±10) % lower light flux than the one

obtained with the F-Factor method. Moreover, a dependency of that value on the light pulser colour seems to exist, yielding higher numbers around 1.0 when UV light is used.

These results can be compared to those obtained from an absolute calibration using muon rings [248, 249] where the efficiency of the whole telescope, including mirrors, was obtained. Numbers presented in these studies show a degradation of the overall photon to photo-electron conversion factor of about 7±2% per year (see figure 142). Assuming that the effect is entirely due to the degradation of the excess noise factor, the number is consistent with the findings above.

Table 18 summarizes all measurements of the degradation of the excess noise factor. A global value of:

$$\frac{d(F^2)}{dT} = (7 \pm 1.5)\%/\text{year} \tag{110}$$

It is important to realize that the uncertainty on this number can be reduced easily by monitoring the camera frequently over a longer time period using the absolute light calibrations and intensity calibrations. It is suggested to perform such measurements at least once per month, ideally once per week.

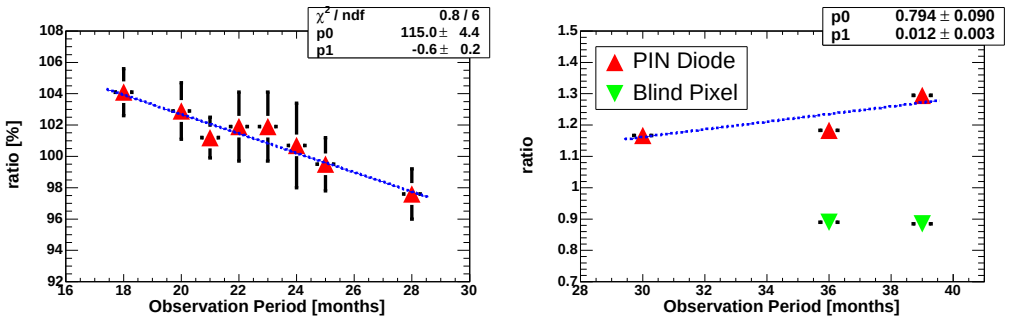

Figure 142: Left: Evolution of the conversion photons to photo-electrons, obtained from analysis of muon rings, in combination with the standard calibration without correction of the long-term evolution of the average excess noise factor (from data of [248]). Right: Evolution of the ratio of the absolute light flux measurements with PIN diode and blinded pixels per light flux measurement with the excess noise factor method. Every observation period corresponds to one month.

Long-term Evolution of Excess Noise		
Method	Result (ΔF^2/yr) [%]	Comments
Var$[\widehat{Q}]/ < \widehat{Q}^2 >$ vs. $1/ < \widehat{Q} >$ test plots	10±7	
PIN diode absolute	11±5	
PIN diode evolution	14±6	
Blind Pixels absolute	-6±6	
Blind Pixels evolution	-2±10	
Muons	7±2	includes mirrors
Total	6.9±1.5	
Total without muons	6.7±3.0	

Table 18: Measurements of the degradation of the excess noise factor with time.

.

7 Data Analysis

This chapter gives an overview of the main analysis concepts, before these will be applied to data in the next chapter. The standard data transfer procedure foresees to send data from La Palma to Europe, either via tape or, since recently, via a 2 MByte/s Ethernet link. These data consist of ON data, whenever the telescope was pointing at the presumed source, and OFF data, with the telescope pointing at a different part of the sky, at the same zenith angle, observational conditions and average star light intensity as the one obtained with the ON pointing [47]. Also simulated gamma-ray showers are available from the diverse institutes of the collaboration, for different telescope pointings and point-spread functions of the mirrors. Additionally, auxiliary data from the individual subsystems is gathered.

All three main ***data types*** can contain three different ***run types*** which are combined in an observation ***sequence***:

Pedestal Run: This run contains usually 1000 events, taken with random trigger and used to calculate the pedestal offsets for the calibration run.

Calibration Run: This run contains usually 4096 events, taken with the standard calibration light pulses from ***10 UV Leds*** (slots 12 and 13, see figure 61) and the calibration trigger. It is used to calculate the conversion factors and arrival time offsets.

Cosmics Runs: These consist of as many data runs as the source was observed. Each run contains usually 53521 (or less) events, taken with the level-1 majority trigger, which requires 4 neighboring channels to exceed a pre-set ***discriminator threshold (DT)*** The DT's depend on the amount of light of night sky and are usually adjusted such that a Galactic source is observed with a 25 % higher threshold condition than an extra-galactic source. This configuration yields an average event rate of typically 200 Hz. Additionally, ***interlaced calibration light pulses*** are fired at a rate of 50 Hz, getting triggered with the calibration trigger.

Subsequently, all three data types are passed through the same analysis chain:

Run selection procedure: Eliminates too short runs (having less than 10 events), or runs taken under obviously bad observation conditions, e.g. runs explicitely marked as test runs, very low event rates or strong mis-pointing of the telescope.

Signal extraction from FADC slices: Calculates the charges and arrival times from the FADC slices of each channel and each event.

[47] There is also data taken in "wobble"-mode, i.e. the telescope pointing 0.4° off the presumed source, alternating the offset at fixed time intervals. With steady, point-like sources, that observation mode yields higher sensitivities since no time is lost to take OFF data. Because of the dead-time introduced when changing between the Wobble-positions, we never use the "wobble"-mode for Gamma Ray Burst observations, though.

Calibration: Converts the extracted charges to equivalent numbers of photo-electrons, using the calibration light pulses, applies the timing offsets and excludes mal-functioning pixels.

Image cleaning: Recognizes and eliminates pixels which contain no signal from a Cherenkov light flash.

Pre-selection: Based upon very basic quality criteria, like the number of remaining channels or the total number of accumulated photo-electrons after cleaning, a first event selection is made, removing typically 3–5 % of the events.

Calculation of quality parameters: Mainly the Hillas-parameters [250] and a couple of further quality criteria are calculated. These are then getting combined to one single quality parameter, called "hadronness".

Application of quality cuts: Only those events are getting selected which have a low "hadronness"-parameter and sometimes fulfill further requirements, based on the total number of photo-electrons or further image parameters which were not included in the calculation of "hadronness".

Calculation of significances: Finally, the reconstructed angle between the incidence direction of the cascade and he telescope pointing direction, expressed in the so-called *ALPHA*-parameter, is used to determine whether an excess of cascades from the observed source position can be seen. If so, the significance of the number of excess events is calculated.

Calculation of upper limits: In case of too low significances (usually taken as $5\,\sigma$), an upper limit to the number of gamma rays is calculated for the observation period.

Most of the functionality is available as executable programs within the Magic Reconstruction and Analysis Software (MARS):

callisto [48]: performs the signal extraction and calibration steps. Most of its functionality was coded by the author.

star [49]: performs the image cleaning and calculation of quality parameters.

melibea [50]: performs the calculation of the "hadronness" and offers the possibility to apply first quality cuts.

flux: calculates spectra and effective areas.

The remaining tasks have not yet been standardized, and small analysis "macros" were written by the author.

In the following, the more elaborate parts of this chain are described, before they will be applied to analyze the data of GRB050713a.

[48] stands for: *CALibrate LIght Signals and Time Offsets*
[49] stands for: *STandard Analysis and image Reconstruction*
[50] stands for: *MErge and Link Image parameters Before Energy Analysis*

7.1 Signal Extraction from FADC Slices

The first step of the signal reconstruction consists of the determination of the mean ***pedestal offset*** and the ***clock noise amplitude***. This is done by taking advantage of the large tail of FADC slices behind a triggered event whenever the high-gain pulse is not too high and therefore the low-gain switch was not applied. In this case, the last 15 FADC slices contain only noise and are used to extract the pedestal parameters. According to a study performed by Nepomuk Otte [251], the 30 FADC slices of one channel have to fulfill the condition that the maximum FADC slice content minus the minimum FADC slice content of the entire FADC slices array does not exceed a threshold of 40 FADC counts. In this case the event is considered as usable for the pedestal calculation. After 500 usable events, an update of the mean pedestal and the clock-noise amplitude of the corresponding channel is made.

Using the results of the latest pedestal update, the signal extractor calculates the charges and arrival times from the 30 FADC slice contents per channel and event. According to the results obtained in chapter 5, the ***Digital Filtering Method*** is used as standard signal extraction algorithm, in an implementation which fits the high-gain pulse form of 4 FADC slices to the one expected for calibration or cosmics pulses, respectively, and the low-gain pulse form of 6 FADC slices.

The ***Blinded Pixels*** signals are extracted using the integrated charge of a ***Fixed Window*** of 14 FADC slices, and the ***PIN Diode*** signal with its large shaping time gets extracted using the maximum of an interpolating ***Spline***.

7.2 Calibration

In a first step, the calibration parameters (mean number of photo-electrons, conversion factors, time offsets) are calculated from a dedicated calibration file which itself uses pedestal offsets calculated from a previously taken pedestal file. This calibration procedure determines which pixels have to be excluded, calculates the conversion factors from extracted signal to equivalent photo-electrons and the arrival time offsets. These numbers are then used to calibrate the first 10 seconds of cosmics data. The conversion factors are subsequently getting updated with the results of every 500 interlaced calibration pulses, while the mean number of photo-electrons is updated every 5000 pulses.

The calibration of a Gamma Ray Burst data set is slightly different from this standard calibration because there is no time to take pedestal and calibration runs before the source is observed. Instead, the interlaced calibration events from the observation of the previous source are used which calibrate directly the first 10 seconds of the GRB data. All following data is then calibrated with the interlaced calibration events of the same GRB data set.

The *callisto* program incorporates a series of checks to sort out mal-functioning pixels. Especially the following exclusion criteria can apply:

1. Channels which are not equipped with photomultipliers, e.g. the central pixel of the camera and one channel providing the alimentation for the blinded pixels.

2. From the distribution of pedestal RMSs of inner or outer pixels separately, those channels are discarded which lie 4.5 RMS below or 25 RMS above the median pedestal RMS. This criterion discards dead photo-multipliers or channels showing higher fluctuations than a star can produce. About 5–10 pixels are typically excluded by this criterion.

3. Pixels where the low-gain channel goes into saturation in more than 0.5 % of the calibration events. This criterion discards pixels heavily affected by catastrophic events (e.g. sparks between photo-cathode and first dynode). About 0–1 pixels get typically excluded by this criterion.

4. Channels with the mean of the distribution of pulse maxima positions smaller or equal the first FADC slice or bigger or equal the last but one FADC slice of the signal extraction window. This criterion applies if the signal extractor window starts too early or too late and leaves out the late or early parts of the calibration pulse. Under normal conditions, no pixel gets excluded by this criterion.

5. Channels showing an RMS of the distribution of pulse maxima positions bigger than 1.7 FADC slices. This criterion discards all pixels whose signals are uncorrelated in arrival time with the calibration light pulses and are therefore considered as noise. Additionally to criterion 2, about 1–3 pixels get usually excluded by this criterion.

6. Pixels which saturate the high-gain channel more than 15 % of the calibration events, but have not applied the low-gain switch in more than 5 % of the events. This criterion discards pixels with high-gain signal distributions too distorted because of the missing upward fluctuating events, but also distorted low-gain distributions because the low-gain switch has not been applied for the downward fluctuating events. This condition applies to 1–2 channels, depending on the time passed since the last flat-fielding.

7. Channels showing a reconstructed mean signal $\widehat{Q}$ less than 2.5 times the extractor resolution $\sqrt{V}$ (eq. 67). This criterion removes typically 0–2 further mal-functioning pixels.

8. Channels showing a reconstructed signal lower than 0.5 times or higher 1.5 times the median signal of the entire camera. This criterion cuts out usually about 0–5 badly mis-flatfielded pixels.

9. Channels showing a reconstructed number of photo-electrons 4.5 RMS below or above the median number of photo-electrons, separately for inner or outer pixels of the camera. This criterion cuts out typically about 0–5 channels with apparently deviating (hardware) behaviour compared to the rest of the camera.

10. All pixels with reconstructed negative signals or numbers of photo-electrons smaller than one. Pixels with a negative (pedestal-subtracted) variance occur, especially when stars are focused onto that pixel during the pedestal run (resulting in a large pedestal RMS), which have moved to a neighboring pixel during the calibration run. In this case, the number of photo-electrons would result artificially negative. If these channels do not show any other deviating behaviour, their number of photo-electrons gets replaced by the mean number of photo-electrons in the camera, and the channel is further calibrated as normal.

Under normal conditions, about 1–2 % of the pixels are getting excluded directly after a recent flat-fielding, otherwise the percentage can go up to even 5 %. Every repair access to the camera brings down the number of discarded pixels, but it has not been observed so far that no channel at all would be excluded. The signals of an excluded pixel are later replaced by the mean signal of its direct neighbors.

From the remaining pixels, the number of photo-electrons $\widehat{N}_{\text{ph.e.}}$ is calculated, following eq. 58, without applying the very small corrections Q_{sh} and $\sigma_e ta$. The median number of photo-electrons from the pixels of the inner camera (eq. 61) defines then the reference value for the calibration, the so-called ***equivalent photo-electrons***. The equivalent number of photo-electrons for the outer pixels is thereby multiplied with factor four (the ratio of active photon-detection area between an outer and an inner pixel). From the mean reconstructed charges μ_{gauss} (eq. 57) and the number of equivalent photo-electrons, the conversion factors $c_{\text{ph.e.}}$ are constructed (eq. 99) for each not-excluded channel.

An analog procedure, described in section 6.7, yields to the arrival time offsets t^{offset} (eq. 107).

During the calibration loop over the data runs, extracted signals as well as pedestal offsets and RMSs are getting converted to ***equivalent photo-electrons*** with $c_{\text{ph.e.}}$ and extracted arrival times shifted to calibrated arrival times by t^{offset}. Using the interlaced calibration events, all conversion factors $c_{\text{ph.e.}}$ are getting updated every 10 seconds. The time offsets are calculated only once per data sequence.

7.3 Image Cleaning

The image cleaning removes pixels which apparently do not form part of the shower image. As the later shower reconstruction relies on second moments of the image [250], any disturbing pixels far from the rest of the shower, can severely mis-lead the image reconstruction. It is therefore mandatory not to add pixels to the image which contain only noise. On the other hand, any unnecessary tightening of the exclusion limits will lead to signal loss at low gamma-ray energies. For this reason, clever algorithms are needed which have to be adjusted such as to provide a low energy threshold and ensure that the vast majority of the images are un-affected by noise.

In the following, two algorithms are presented which have been used in the analysis part: The ***absolute cleaning*** algorithm, which is used in a standard way by the collaboration, and the ***time cleaning*** algorithm which was developed by the author [51].

The Absolute Cleaning

The absolute cleaning compares the number of reconstructed photo-electrons $\widehat{N}_{\mathrm{phe}}$ with the reference values N_1 and N_2. It loops over the whole camera three times and discards or adds pixels at every step:

1. STEP 1: pixels with $\widehat{N}_{\mathrm{phe}} < N_1$ are removed
2. STEP 2: pixels without direct neighbors having survived the previous step are removed
3. STEP 3: pixels with direct neighbors having survived the previous steps and which fulfill $\widehat{N}_{\mathrm{phe}} > N_2$ are included again.

This algorithm is simple and robust if initialized with high enough values for N_1 and N_2. It is not strongly affected by different levels of night-sky background whenever the levels N_1 and N_2 are much higher than typical values of the pedestal RMS. This is especially important at low energies where the systematic difference between the pedestal RMS of the MC simulated star-field is 30% lower than the one of the real Galactic star field. As the absolute cleaning does not use the arrival time information, it will certainly not reach the lowest possible energy threshold. Moreover, different levels of noise between individual pixels (e.g. due to stars in the field-of-view of the camera) are not taken into account, i.e. the reference values N_1 and N_2 have to be chosen so high that the algorithm is not affected by increased levels of noise in parts of the camera.

The Time Cleaning

This algorithm scales the signal threshold with the noise level of the corresponding channel and uses the differences in pulse arrival times between neighboring pixels δt and to the mean arrival time of the shower ΔT. At the beginning, the bias B_{ped} from the case of no signal (compare table 10) gets subtracted from every reconstructed number of photo-electrons: $\widehat{N}^{corr}_{\mathrm{phe}} = \widehat{N}_{\mathrm{phe}} - B_{ped}$. In a next step, the ratio of the bias-corrected signal to the noise fluctuations are calculated: $R = \widehat{N}^{corr}_{\mathrm{phe}} / \sqrt{\mathrm{Var}[\widehat{N}_{\mathrm{phe}}]\Big|_{N_{\mathrm{phe}}=0}}$ and compared to the reference values R_1 and R_2 (see also section 5.6 and eq. 87). Additionally, the difference in arrival time between

[51] There is also a time cleaning algorithm developed independently by Nepomuk Otte. That algorithm employs some of the concepts presented here, in a different implementation. It was extensively compared to this algorithm in [252].

ABSOLUTE CLEANING		
N_1 ($\widehat{N}_{\rm phe}$)	N_2 ($\widehat{N}_{\rm phe}$)	surviving noise events (%)
10.0	10.0	0.1
9.0	9.0	0.4
8.0	8.0	0.5
7.5	6.0	0.8
7.5	5.0	0.9
7.5	4.5	1.0
7.5	4.0	1.1
7.5	3.0	1.2
7.5	2.0	1.6
7.0	6.0	1.3
7.0	5.0	1.4
7.0	4.0	1.6
7.0	3.0	1.7
7.0	2.0	2.2
6.5	6.0	3.0
6.5	5.0	3.1
6.5	4.0	3.4
6.5	3.0	3.6
6.5	2.0	4.2
6.0	6.0	5.6
5.0	5.0	40.1
4.0	4.0	97.1

Table 19: Probabilities to get an additional island in a shower image, only due to noise for the absolute image cleaning algorithm with different thresholds N_1 and N_2. The numbers were calculated by Valeria Scapin.

neighboring pixels $\delta\mathbf{t_{ij}}$ is calculated. The maximally allowed time difference $\delta\mathbf{t}^{max}$ between neighboring pixels is fixed to 0.7 FADC slices (2.3 ns) which reflects the time resolution of the digital filter below 5 photo-electrons and an additional spread of 700 ps due to the staggering of the mirrors. The maximally allowed time offset of one channel to the mean shower time, $\mathbf{\Delta T}^{max}$ is fixed to 1.5 FADC slices ($\pm$5 ns). Pixels with values of R greater than twice the reference level R_1 are allowed to deviate by $2\Delta T^{max} = 10$ ns. According to a study made by Diego Tescaro [253], the physical time spread of cosmics showers ranges typically from $2-3$ ns. The chosen global time offset window of $\pm$5 ns includes possible time jitters and leaves a security margin of at least 5 ns for unusually stretched showers in time.

The time image cleaning algorithm loops three times over the whole camera and discards or adds pixels at every step:

TIME CLEANING		
R_1 (σ)	R_2 (σ)	surviving noise events (%)
5.0	5.0	0.0
4.0	4.0	0.2
3.5	2.5	0.2
3.5	1.5	0.2
3.5	1.0	0.3
3.5	0.5	0.3
3.0	2.5	0.3
3.0	1.5	0.3
3.0	0.75	0.4
3.0	0.5	0.4
2.5	2.0	0.9
2.5	1.0	1.3
2.5	0.75	1.5
2.5	0.5	1.7
2.5	0.25	2.0
2.0	2.0	5.2
1.0	1.0	84.5

Table 20: Probabilities to get an additional island in a shower image, only due to noise for the time image cleaning algorithm with different threshold values R_1 and R_2. Under typical observation conditions, the values R_1 and R_2 can be translated to thresholds for the numbers of photo-electrons with the relation $N \approx 1 + R$. The numbers were calculated by Valeria Scapin.

1. STEP 1: pixels with $R < R_1$ are removed
2. STEP 2: the mean arrival time is calculated from the remaining pixels
3. STEP 3: pixels with $\mathbf{\Delta T} > \mathbf{\Delta T}^{max}$ are removed
4. STEP 4: pixels without direct neighbors having survived the previous step are removed
5. STEP 5: pixels with direct neighbors having survived the previous step and which fulfill $R > R_2$ and $\delta\mathbf{t} < \delta\mathbf{t}^{max}$ are included again.

This algorithm allows to reduce the reference values R_1 and R_2 because the additional time criteria are applied. Different levels of noise (e.g. due to stars in the field-of-view of the camera) are taken into account by comparing the signal directly to the amount of noise fluctuations. The algorithm should be therefore mainly immune against increased levels of noise in parts of the camera [52].

[52] This is not entirely true at very low levels of noise where the fluctuations are affected by

In order to choose suitable parameters, the probability was calculated that an event contains a separate island only due to noise. To do so, a pedestal run was taken with the telescope pointing at a Galactic source. The run was then calibrated and the image cleaning algorithms applied with different initializations. For each of these, the percentage of events was counted which leave at least two surviving neighbouring pixels in the image. The resulting tables 19 (for the absolute cleaning) and 20 (for the time image cleaning) were calculated in collaboration with Valeria Scapin.

These numbers show that the inclusion of the pulse arrival times leads to lower effective signal levels, as expected. Table 21 summarizes the obtained signal thresholds for three different "robustness"-levels: rejecting more than 99 %, 98 % or 95 % of the noise islands. In the subsequent analysis presented in chapter 8, a probability of more than 98 % was required leading to the following threshold conditions:

Absolute Cleaning: the levels $N_1 = 7$ and $N_2 = 4$ photo-electrons

Time Cleaning: the levels $R_1 = 2.5$ and $R_2 = 0.5$ pedestal RMS

Surviving Events (%)	Absolute cleaning N_1 (N_{phe})	Absolute cleaning N_2 (N_{phe})	Time cleaning R_1 (σ)	Time cleaning R_2 (σ)
$\lesssim$1	7.5	4.5	2.5	1.5
$\lesssim$2	7.0	2.5	2.5	0.25
$\lesssim$5	6.5	2.0	2.0	2.0

Table 21: Suggested cleaning levels for a given maximal percentage of surviving islands due to noise.

Figure 143 shows an example of a typical low-energy gamma-ray shower, cleaned with the absolute and the time image cleaning. The improved efficiency of the time cleaning at low energies is clearly visible.

7.4 Quality Parameters

Those N pixels which survived the image cleaning are then used to calculate the classical Hillas parameters [250].

SIZE

The *SIZE* of the image is the sum of the pixel charges, expressed in ***equivalent photo-electrons***. It is proportional to the total integrated light content of

the Poissonian character of the incident background light flux. Positive deviations from the most probable value occur usually at higher probabilities than in the case of Gaussian fluctuations.

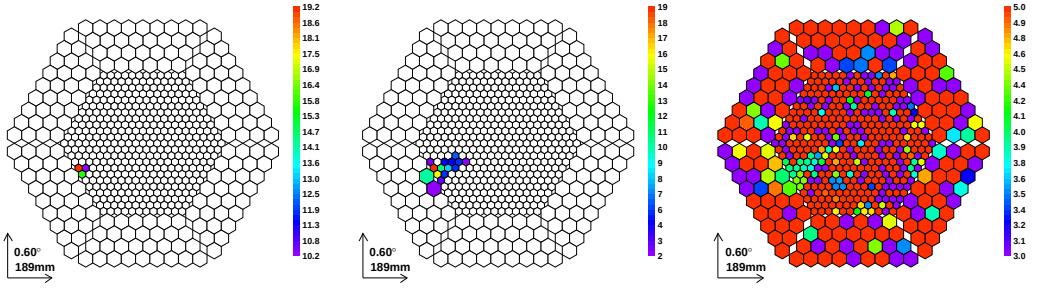

Figure 143: Example of a simulated gamma-ray shower of 90 GeV energy, cleaning with the absolute (left) and the time cleaning (center). The right plot shows the reconstructed arrival times.

the shower. In the case of the MAGIC camera, η_{comm} has been chosen as the average photo-detection efficiency of the inner pixels. There, the equivalent number of photo-electrons equals the number of actually registered photo-electrons on average. Outer pixels, in turn, have on average a factor $\eta_{inner}/\eta_{outer} \approx 1.5$ higher numbers of equivalent photo-electrons than actual numbers of photo-electrons. This construction has the advantage to avoid discontinuities of the reconstructed image parameters at the edge between areas of different pixel types. On the other hand, the simple assumption that the variance of *SIZE* equals the same *SIZE*, because of Poissonian fluctuations, is only true for images entirely comprised in the inner part of the camera.

As the number of created electrons in an electro-magnetic shower is proportional to the energy of the shower and the emitted number of Cherenkov photons per unit path length of an electron is almost constant (see also section 3.1), the sampled part of the emitted shower light reflects already well the shower energy and *SIZE* can be used therefore as a first measure of the shower energy.

WIDTH, *LENGTH*, *DIST* and *ALPHA*

Further (classical) Hillas parameters are sketched in figure 144 and contain the parameters [250, 254]:

***WIDTH*:** The RMS spread of light along the minor axis of the image, a measure of the lateral development of the cascade.

***LENGTH*:** The RMS spread of light along the major axis of the image, a measure of the vertical development of the cascade.

***DIST*:** The distance from the centroid of the image to the source position in the camera.

***ALPHA*:** The angle between the major axis of the image and the radius drawn from the center of the camera through the center of the image.

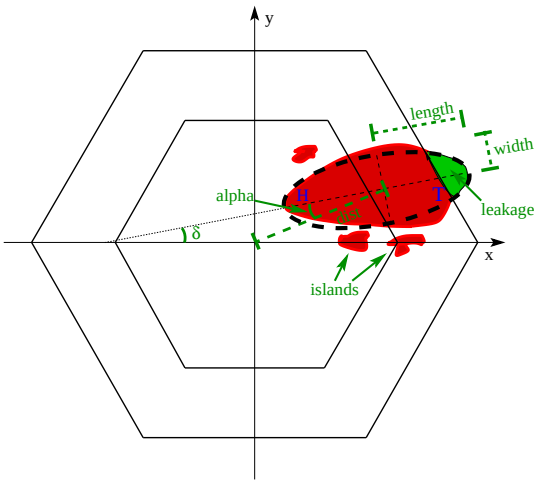

Figure 144: Sketch of image parameters: The red areas show those pixels having survived the image cleaning procedure. The black dotted line show the reconstructed ellipse, with the parameters LENGTH, WIDTH, DIST, ALPHA and LEAKAGE. Head (H) and tail (T) of the shower are displayed as well as three additional "islands".

In order to calculate these parameters, the first and second moments of the image are calculated from the positions x and y (measured in degrees) of each pixel in the camera which has survived the image cleaning procedure:

$$\begin{aligned} < x >= \frac{\sum_{i=0}^{N} x_i w_i}{\sum_{i=0}^{N} w_i} \quad , \quad < y >= \frac{\sum_{i=0}^{N} y_i w_i}{\sum_{i=0}^{N} w_i} \\ < x^2 >= \frac{\sum_{i=0}^{N} x_i^2 w_i}{\sum_{i=0}^{N} w_i} \quad , \quad < y^2 >= \frac{\sum_{i=0}^{N} y_i^2 w_i}{\sum_{i=0}^{N} w_i} \\ < xy >= \frac{\sum_{i=0}^{N} x_i y_i w_i}{\sum_{i=0}^{N} w_i} \end{aligned} \tag{111}$$

where the weights w_i are typically a power α of the pixel size in equivalent photoelectrons: $w_i = SIZE_i{}^{\alpha}$.

The first moments can be combined into a parameter describing the distance of the center of the ellipse from the center of the camera [53]:

$$DIST = \sqrt{< x >^2 + < y >^2} \tag{112}$$

In the following, we set $\widehat{\mathrm{var}}(x) :=< x^2 > - < x >^2$, $\widehat{\mathrm{var}}(y) :=< y^2 > - < y >^2$ and $\widehat{\mathrm{cov}}(x,y) :=< xy > - < x >< y >$, where the hats indicate that the expressions

[53] In case the source position is not the camera center (e.g. when observing in Wobble mode), the first moments have to be calculated with respect to the new source position.

yield true variances only in the case of $\alpha = 0$ (all weights are 1). The second moments get then combined in the "covariance" matrix M:

$$M = \begin{pmatrix} \widehat{\mathrm{var}}(x) & \widehat{\mathrm{cov}}(x,y) \\ \widehat{\mathrm{cov}}(x,y) & \widehat{\mathrm{var}}(y) \end{pmatrix} , \tag{113}$$

which is then rotated by an angle δ such that M^{rot} becomes diagonal in the new coordinate system:

$$M^{rot} = \begin{pmatrix} \cos\delta & \sin\delta \\ -\sin\delta & \cos\delta \end{pmatrix} \cdot M \cdot \begin{pmatrix} \cos\delta & -\sin\delta \\ \sin\delta & \cos\delta \end{pmatrix} = \begin{pmatrix} \lambda_1 & 0 \\ 0 & \lambda_2 \end{pmatrix} \tag{114}$$

The solution of eq. 114 and the requirement $\lambda_1 \geq \lambda_2$ yields the rotation angle and the diagonalized matrix:

$$\begin{aligned} \tan\delta &= \frac{\widehat{\mathrm{var}}(y) - \widehat{\mathrm{var}}(x) + \sqrt{\left(\widehat{\mathrm{var}}(y) - \widehat{\mathrm{var}}(x)\right)^2 + 4 \cdot \widehat{\mathrm{cov}}(x,y)^2}}{4 \cdot \widehat{\mathrm{cov}}(x,y)^2} \\ LENGTH^2 &:= \lambda_1 = \frac{\widehat{\mathrm{var}}(x) + 2 \cdot \tan\delta \cdot \widehat{\mathrm{cov}}(x,y) + \tan^2\delta \cdot \widehat{\mathrm{var}}(y)}{1 + \tan^2\delta} \\ WIDTH^2 &:= \lambda_1 = \frac{\widehat{\mathrm{var}}(x) - 2 \cdot \tan\delta \cdot \widehat{\mathrm{cov}}(x,y) + \tan^2\delta \cdot \widehat{\mathrm{var}}(y)}{1 + \tan^2\delta} , \end{aligned} \tag{115}$$

yielding the ellipse's major ($LENGTH$) and minor ($WIDTH$) half axes. With the above definitions, a unit vector along the main axis of the ellipse is obtained:

$$\vec{a} = \frac{1}{1 + \tan^2\delta} \begin{pmatrix} 1 \\ \tan\delta \end{pmatrix} \tag{116}$$

and such the angle $ALPHA$ can be calculated (see fig 144) [54]:

$$ALPHA = \arccos\left(\frac{< x > + \tan\delta \cdot < y >}{DIST \cdot \sqrt{1 + \tan^2\delta}}\right) , \tag{117}$$

with $ALPHA$ ranging from -90° to +90°, depending on whether the shower center is found in the left or right part of the camera [55].

The reason to define parameters based on the second moments of the image lies in the fact that electromagnetic showers tend to produce "cleaner" reconstructed

[54] Equation 117 does not include possible other reference points than the center of the camera, nor the inclusion of the "head-tail" information, i.e. knowledge about the direction in which the shower was moving. For more detailed information about these possibilities, see [255, 256].

[55] There is also a different definition of $ALPHA$ ranging from -180° to +180°, which makes sense only if the head-tail information is known, i.e. the time-flow direction of the shower. In this work, only the absolute value of $ALPHA$, obtained from the classical definition between -90° to +90°, is used. See also [255].

ellipses, i.e. showing on average a smaller ratio *WIDTH/LENGTH*, than images from hadronic showers which tend to look more fragmented and yield "rounder" reconstructed ellipses. On the contrary, the *ALPHA* parameter gives an estimate of the arrival direction of the shower. Especially showers traveling parallel to the telescope axis yield *ALPHA*-values concentrated around zero. While cosmics rays (hadronic showers) do not show any preferred arrival direction, gamma rays from astro-physical sources do so and show thus excesses at low *ALPHA*-values.

CONC, *CONC4*, *LEAKAGE*, *NUMBER ISLANDS*

Further (non-classical) image parameters are:

***CONC*:** Fraction of equivalent photo-electrons, contained in the two brightest pixels, per total image *SIZE*.

***CONC4*:** Fraction of equivalent photo-electrons, contained in the four brightest pixels, per total image *SIZE*.

***LEAKAGE*:** Fraction of equivalent photo-electrons, contained in the outmost ring of the camera, per total image *SIZE*.

***NUMBER ISLANDS*:** Number of separated areas with signal, after the image cleaning.

While the concentration parameter *CONC* is used mainly to identify and reject ***non-shower*** events, the leakage parameter *LEAKAGE* is an approximate measure of the part of a shower which lies outside of the sensitive area of the camera. Images with large values of *LEAKAGE* lack necessarily precision in the determination of the image parameters. Finally, the number of separated islands has turned out to be a useful quality parameter to distinguish hadronic (more than one island) from electromagnetic showers (only one island).

7.5 Multivariate Classification

A common problem in experimental physics is the separation of signal from background where quality parameter distributions overlap and the separability of both is low. In such a situation, probability density functions (***p.d.f.***) should be constructed, which in the ideal case incorporate the full description of the physical models of all processes at play and the entire information captured by the detector. A p.d.f. for electromagnetic showers and one for hadronic showers can be constructed, depending on the telescope parameters, which yield directly both signal and background probabilities. Unfortunately, especially the hadronic shower development is hard to model statistically, and many necessary parameters cannot be included in a straight-forward way, e.g. atmospheric conditions. Nevertheless, efforts are made in that direction, without being completed so far [257].

In this analysis only reduced information, based on the image parameters, is used to determine the ***p.d.f.*** for a given data set. In the case of one only parameter, signal and background acceptance can be readily visualized as a distribution along that variable. In the case of multiple variables – which are in general correlated – this is not possible any more and sophisticated ***multivariate classification methods*** have been invented to extract the acceptances from a set of parameters and construct a one-dimensional p.d.f. Many of these methods employ random techniques used to construct the probability density model on ***training data samples*** and to determine their efficiencies on ***test data samples***. For a detailed description and comparison of these methods, see [258].

Random Forest

The analysis presented in this thesis, is based on an implementation of the ***random forest***-technique, developed by Leo Breiman [259] and implemented in the MAGIC analysis software by Thomas Hengstebeck [260]. As other classification methods, it is based on the construction of ***decision trees***: If every image parameter (out of N) is thought of as a vector in an N-dimensional parameter space, all signal and background events (e.g. from the training sample) are contained in an N-dimensional hypercube. The tree starts at one corner of the hypercube, called the ***root node***. Subsequently one image parameter (dimension of the hyperspace) is selected randomly and a ***cut value*** on that parameter chosen such that the ***Gini index*** of the two samples gets minimized. The Gini-index can be expressed in terms of the number of events on the left or right side of the cut value:

$$Q_{Gini} = 2 \cdot \left(\frac{N_{signal}^{left} \cdot N_{bg}^{left}}{N_{tot}^{left}} + \frac{N_{signal}^{right} \cdot N_{bg}^{right}}{N_{tot}^{right}} \right) \tag{118}$$

The next step chooses another parameter randomly, starting from the obtained cut value (the *first node*). This partitioning of the hypercube in smaller sub-cubes is performed until the node is ***pure***, i.e. the Gini index is zero or the number of remaining events in the sub-hypercube is less than a certain threshold, usually 1–10 events. The corresponding node is then called a ***terminal node***.

In order to avoid ***overfitting***, various (usually 50 to 100) random trees are grown, starting from different points of the hypercube on a random subsample of the training sample. The combination of ***random forests*** constitutes an ensemble of uncorrelated trees, which are combined to form a more generalized predictor.

In order to classify an event, each of the trees is followed until its terminal node. Depending on whether the event lies inside or outside the corresponding terminal hyper-cube, a value of 0 (for gamma-like terminal nodes) or 1 (for hadron-like terminal nodes) is assigned to the event. As there is a whole forest, each random tree assigns a value l to the event and the parameter *HADRONNESS* can be calculated:

$$HADRONNESS = \frac{\sum_{i=0}^{N_{trees}} l_i}{N_{trees}} \tag{119}$$

Per definition, the *HADRONNESS* ranges from 0 to 1 and yields values distributed close to 1 for hadron-like and close to 0 for gamma-like event, if the two event types are separable within the chosen set of parameters. Otherwise, values distributed around 0.5 are expected for both types of events.

A separate feature of the ***random forest*** algorithm has been used frequently in the collaboration: By adding a scale parameter, like the number of equiv. photo-electrons, to the list of quality parameters, the classifier can be brought to optimize the separation of signal from background for every bin of the scale parameter. To function properly, this procedure requires that the two original distributions of the scale parameter are brought to match, either by removing events from the background training sample or from the signal training sample.

The parameter with the highest discrimination power, *ALPHA*, is not included in the list of parameters for the random forest training, since parts of the distribution of *ALPHA* are needed to estimate the background in the signal region from an unbiased estimate of the background from the pure background region of that distribution (see the analysis part of the next chapter). This capability is lost if *ALPHA* is included in the calculation of *HADRONNESS* and later cuts on *HADRONNESS* are applied.

Energy Estimation

Already the number of photo-electrons per shower image, expressed in the variable *SIZE*, is correlated with the shower energy and can serve thus for an energy estimate *ENERGY*. Especially at high energies, this approach works fine, although the conversion factor between *SIZE* and energy has to be retrieved for every telescope pointing zenith angle. Moreover, the total amount of light detected from a shower reflects not only an energy dependence but also a distance dependence.

A more precise approach uses a slightly modified version of the ***random forest*** algorithm: Instead of separating signal from background distributions, random forest is getting trained to separate the population of events with matching (simulated) energy from those having energy outside a corresponding energy bin. Then, a loop over all energy bins is performed to train the estimator. Subsequently, the combination of image parameters determines the probability of an event to belong to a given energy bin and the one with the highest probability is getting selected. This approach yields energy resolutions of the order of $\sim 25\%$ at higher energies and $\sim 30\%$ around the energy threshold.

7.6 Determination of Significances and Cuts on *HADRONNESS* and *ALPHA*

After the calculation of the *HADRONNESS* parameter, the analyzer remains with simulated MC gamma data sets, an ON and various OFF data sets. In the following, efficient cuts on *HADRONNESS* have to chosen, separately for every bin in *ENERGY*, and finally an ***ALPHA-plot*** is made showing the distribution of the absolute value of *ALPHA* ($|ALPHA|$) for ON data and for $\kappa \cdot$ OFF data, where κ is

a normalization constant obtained by demanding that the histogram integral from $|ALPHA| = 30°$ to $|ALPHA| = 80°$ be the same for ON and normalized OFF data. That range in the distribution of $|ALPHA|$ is assumed to be almost signal-free [254]. Figure 145 gives an example of an $ALPHA$-plot, if the observed source (in this case the Crab Nebula) is visible. Later, the number of excess events N_{ex} between ON and OFF data in the range from $|ALPHA| = 0$ to $|ALPHA| = ALPHA_{cut}$ is counted. The value $ALPHA_{cut}$ has to be determined beforehand, otherwise the calculated significance of the number of excess events would be biased [56]. Following a maximum likelihood calculation by Ti-Pei Li and Yu-Qian Ma [261], the significance can then be obtained from the above numbers [57]:

$$S = \sqrt{2} \cdot \Big[\quad N_{ON} \cdot \ln\left(\tfrac{1+\kappa}{\kappa} \cdot \tfrac{N_{ON}}{N_{ON}+N_{OFF}}\right) + N_{OFF} \cdot \ln\left((1+\kappa) \cdot \tfrac{N_{OFF}}{N_{ON}+N_{OFF}}\right) \Big]^{1/2} . \tag{121}$$

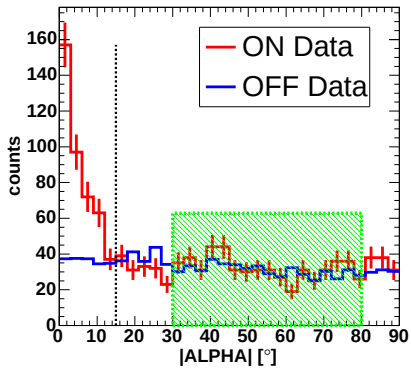

Figure 145: Example of an ALPHA-plot, obtained from 45 minutes of Crab-Nebula observation. The dashed line shows a possible value of $ALPHA_{cut}$, while the shaded green area shows the background normalization region.

In the following, an ***un-biased, efficient algorithm*** is presented to compute cut-values for *HADRONNESS* and $|ALPHA|$ which maximize the significance for a

[56] Unfortunately, this rather trivial finding has not yet been realized by parts of our collaboration.

[57] Since about half a year ago, parts of the collaboration have been using a modified formula:

$$S = \sqrt{2} \cdot \Big[\quad N_{ON} \cdot \ln\left(\tfrac{1+\gamma}{\gamma} \cdot \tfrac{N_{ON}}{N_{ON}+\kappa N_{OFF}/\gamma}\right) + N_{OFF} \cdot \ln\left((1+\gamma) \cdot \tfrac{1/(\Delta N_{BG})^2}{N_{ON}+\kappa N_{OFF}/\gamma}\right) \Big]^{1/2} , \tag{120}$$

with $\gamma = (\Delta N_{BG})^2/(\kappa N_{OFF})$ and $(\Delta N_{BG})^2 = (\kappa \cdot \Delta N_{OFF})^2 + (\Delta\kappa \cdot N_{OFF})^2$, claiming that the new formula corrects an error in Li and Ma's calculation, namely having neglected the uncertainty on the normalization constant κ. Frankly speaking, I cannot reproduce formula 120. Moreover, that approach has neither been documented nor published so far and especially not tested with MC simulations. As Li and Ma's simulations describe formula 121 apparently well for a wide range of values of κ, I decided thus to stick to original formula by Li and Ma.

possible signal in the ON data. The following steps are required:

1. Determine a best guess for the cut value on *ALPHA* by fitting the simulated gamma distribution with a Gaussian. Figure 146 gives examples of such fits. One can see that the width of the *ALPHA* distribution depends on the energy range. The cut value $ALPHA_{cut}$ is then chosen to 2.5 times the sigma of the Gaussian. This choice assures that almost the entire signal is contained between $ALPHA = 0$ and $ALPHA = ALPHA_{cut}$.
2. Calculate test significances S_{test} using formula 121, while scanning cut values on *HADRONNESS* from 0 to 1 in intervals of 0.05. The variables N_{ON}, N_{OFF} and κ are thereby approximated in the following way:

N_{OFF}: The number of OFF events after all cuts minus the cut on $|ALPHA|$, multiplied with $|ALPHA|_{cut}/90$. This number gives a correct estimate for N_{OFF} if the distribution of $|ALPHA|$ is flat for background which is approximately the case (see chapter 8). In this case, the estimate is also un-biased (which it would not be if the number of OFF events are counted after a cut in $|ALPHA|$.

N_{ON}: The number of estimate background in the signal region N_{OFF} plus the number of simulated gamma events after all cuts, scaled down by a constant factor F_{scale}. That factor is chosen such that the maximally achievable significance is about $5\,\sigma$.

κ: The number of ON events divided by the number of OFF events before any cuts.

Note that no ON data is used in this procedure, except for the calculation of background normalization factor κ.

3. Then, S_{test} is getting maximized as a function of the cut values $HADRONNESS_{cut}$. Last, the position of the maximum is taken as cut value on *HADRONNESS* for all data samples, including the ON data.

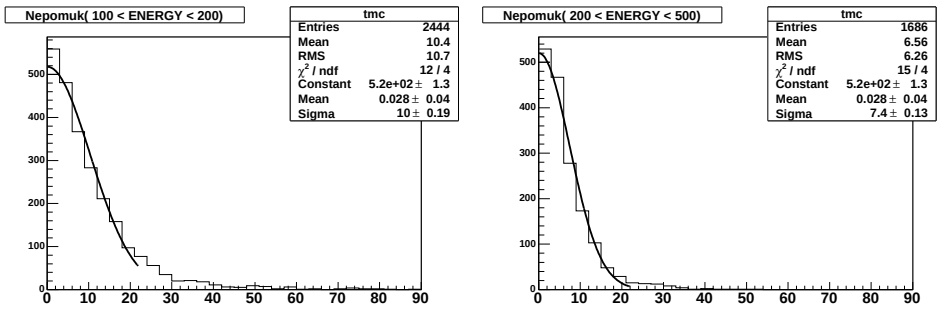

Figure 146: Distributions of ALPHA for simulated MC gamma events. Left: 100 to 200 GeV reconstructed ENERGY, right: 200 to 500 GeV.

It is important to note that this procedure is completely unbiased with respect to fluctuations of the ON data – an important characteristic for dealing with small or no signals at all [58].

7.7 Calculation of Effective Areas

By lack of an adequate calibrated high-energy gamma-ray source in the sky, the effective area A_{eff} of a Cherenkov telescope has to be derived by means of MC simulation. A_{eff} depends on the energy E of the incident gamma-ray, on the telescope pointing zenith angle θ (at low energies also on the azimuth angle) and the atmospheric conditions. It can be defined as:

$$A_{\mathit{eff}}(E,\theta) = \lim_{N_{sim}(E)\to\infty,\ A_{sim}\to\infty} A_{sim} \cdot \frac{N_{analysis}(E,\theta)}{N_{sim}(E)} \ , \tag{122}$$

where $N_{sim}(E,\theta)$ is the number of simulated gamma-rays with energy E, A_{sim} the simulated incidence area and $N_{analysis}(E,\theta)$ the number of remaining events after correct simulation of the telescope zenith angle, trigger and the application of all analysis cuts. In practice, the limit is replaced by a sufficiently large numbers A_{sim} and $N_{sim}(E)$.

In case one works with energy bins (e.g. in the calculation of upper limits), $N_{analysis}(E,\theta)$ will also contain cuts on the reconstructed energy. Figure 147 shows a typical distributions of $A(E)$: Without cuts on $ENERGY$ and cutting out an energy bin. One can see that the true (simulated) energy extends will beyond the limits of reconstructed energy, because of the limited energy resolution.

7.8 Calculation of Upper Limits

Knowing a gamma-ray flux $dN_\gamma/dEdAdt$, observed with a Cherenkov telescope of effective area $A(E)$, during a time interval $[T_{min}, T_{max}]$ with an effective on-time function $\epsilon(t)$, one could predict the number of events registered by the telescope as follows:

$$N_{obs} = \int_0^\infty \int_{T_{min}}^{T_{max}} \frac{dN_\gamma}{dE\,dA\,dt} \cdot A(E) \cdot \epsilon(t)\,dt\,dE \ , \tag{123}$$

or, dividing the observed number of excess events in bins of reconstructed energy E_r:

$$N_{obs}(E_r^{min}, E_r^{max}) = \int_0^\infty \int_{T_{min}}^{T_{max}} \frac{dN_\gamma}{dE\,dA\,dt} \cdot A(E, E_r^{min}, E_r^{max}) \cdot \epsilon(t)\,dt\,dE \ , \tag{124}$$

where E_r^{min} and E_r^{max} are the bin limits of reconstructed energy.

[58] Parts of the collaboration make scans through the parameter space spanned by *ALPHA* and *HADRONNESS* and search for maxima of the significance using the same ON and OFF data samples. Because of the introduced bias, that procedure will over-estimate the resulting significances.

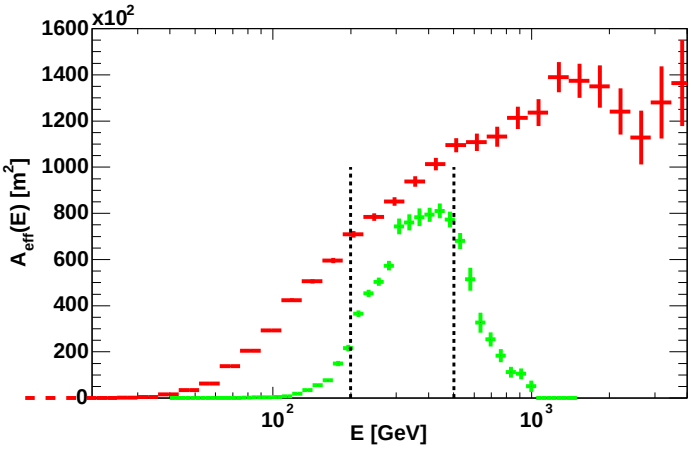

Figure 147: Distributions of effective areas for a telescope pointing zenith angle around 40° and typical analysis cuts. The red crosses show the effective area without cuts in reconstructed energy, while the green crosses have cuts in $200 < ENERGY < 500$ *GeV applied.*

In case of no signal, the telescope measures on average zero events $N_{obs} = 0$, but also different (positive and negative) numbers are possible since N_{obs} follows a statistical distribution. From the number of observed events, the analyzer derives first an upper limit on the number of observable events, typically giving a confidence level of 95%: $N_{>95\%}$. In a next step, eq. 124 is translated to an un-equality:

$$N_{>95\%}(E_r^{min}, E_r^{max}) > \int_0^{\infty} \int_{T_{min}}^{T_{max}} \frac{dN_\gamma}{dE\, dA\, dt} \cdot A(E, E_r^{min}, E_r^{max}) \cdot \epsilon(t)\, dt\, dE \ , \quad (125)$$

which has to be transformed into an upper for $dN_\gamma/dEdAdt$.

7.8.1 Upper Limits for Number of Observable Events

Typically, the method of the *ALPHA*-plot yields the following numbers:

N_{ON}^{obs}**:** The number of observed events from ON data within the signal region (e.g. from $0 < ALPHA < ALPHA_{\,cut}$.

N_{OFF}^{obs}**:** The number of observed events from OFF data within the signal region

ΔN_{OFF}**:** The statistical uncertainty on N_{OFF}

$\Delta\epsilon$**:** A global systematic uncertainty of the efficiency of the detector

Based on these number, the observed number of excess events is calculated:

$$N_{EX}^{obs} = N_{ON}^{obs} - N_{OFF}^{obs} \; . \tag{126}$$

An upper limit on N_{EX} is then constructed in two steps: Construction of a probability density function (***p.d.f.***) for N_{EX}, given a hypothesis on the mean physical number μ_{EX}, and inversion of the original p.d.f. to yield a p.d.f. for μ_{EX}, given all observed numbers.

Construction of p.d.f.

Given a hypothesis on the true mean number of excess events μ_{EX} and background events μ_{OFF} (usually not an integer numbers), the probability distribution for observing values of N_{ON} is constructed: $P(N_{ON} \,|\, \mu_{EX}; \mu_{OFF}; \Delta\mu_{OFF})$. E.g. for the (unrealistic) case of pure Poissonian fluctuations for N_{ON} and a perfectly known mean background μ_{OFF} without uncertainty ($\Delta\mu_{OFF} = 0$), one gets

$$P(N_{ON} \,\big|\, \mu_{EX}; \mu_{OFF}) = \frac{(\mu_{EX} + \mu_{OFF})^{N_{ON}} \cdot e^{-(\mu_{EX}+\mu_{OFF})}}{N_{ON}!} \; . \tag{127}$$

The ***confidence interval*** defines a range $[N_{ON}^{low}, N_{ON}^{up}]$ outside which would lie the results N_{ON} of only a percentage α of experiments (carried out under the same conditions):

$$P\left(N_{ON} \in [N_{ON}^{low}, N_{ON}^{up}] \,\big|\, \mu_{EX}; \mu_{OFF}; \Delta\mu_{OFF}\right) = 1 - \alpha \; . \tag{128}$$

In case of upper limits, the confidence interval counts the percentage of experiments yielding $N_{ON} > N_{ON}^{up}$.

Inversion of p.d.f.

Starting from probability distributions $P(N_{ON} \,|\, \mu_{EX}; \mu_{OFF})$, a second distribution $P(\mu_{EX} \,|\, N_{ON}^{obs}; N_{OFF}^{obs})$ has to be retrieved, predicting the probability for the true mean number of excess events, given the observations N_{ON}^{obs} and N_{OFF}^{obs}. To solve this (non-trivial) problem, two branches of statistics have been developed: a ***Bayesian*** and a ***frequentist*** approach. The first uses Bayes' theorem:

$$\begin{aligned} P(\mu_{EX} \,\big|\, N_{ON}^{obs}; \mu_{OFF}; \Delta\mu_{OFF}) \;\; &= \;\; P(N_{ON} \,\big|\, \mu_{EX}; \mu_{OFF}; \Delta\mu_{OFF}) \cdot \\ &\quad \cdot P(\mu_{EX} \,\big|\, \mu_{OFF}; \Delta\mu_{OFF}) \; , \end{aligned} \tag{129}$$

where $P(\mu_{EX} \,|\, \mu_{OFF}; \Delta\mu_{OFF})$ are called "prior probabilities" for μ_{EX}. The strength of this method lies in the fact that un-physical regions or other prior knowledge about μ_{EX} can be included in $P(\mu_{EX} \,|\, \mu_{OFF}; \Delta\mu_{OFF})$. One possible choice for the prior probability was made by O. Helene [262], namely $P(\mu_{EX} \,|\, \mu_{OFF}; \Delta\mu_{OFF}) = N$, where N is simply a normalization constant. That choice assumes thus a uniform

probability for the entire signal range from $[0, \infty]$. An upper limit is then obtained via the condition:

$$\int_{N_{>\,95\%}}^{\infty} P(\mu_{EX} \,|\, N_{ON}^{obs}; \mu_{OFF}; \Delta\mu_{OFF})\, d\mu_{EX} = \alpha \ . \tag{130}$$

The ***confidence level*** (***CL***) is then defined as:

$$CL = (1 - \alpha) \cdot 100\,[\%] \ . \tag{131}$$

By convenience, confidence levels are typically chosen to be 95 % [59].

The ***frequentist*** approach proceeds to construct a ***confidence belt*** according to the prescription of Neyman [264]: For each hypothesis μ_{EX}, a horizontal confidence interval satisfying eq. 128 is drawn (see figure 148 for the example p.d.f. of eq. 129, with background $\mu_{OFF} = 3$). Given a measured value N_{ON}^{obs}, one can then ***invert*** the confidence interval to obtain limits $[\mu_{EX}^{low}, \mu_{EX}^{up}]$ (depending on N_{ON}^{obs}) which satisfy a confidence interval for μ_{EX}:

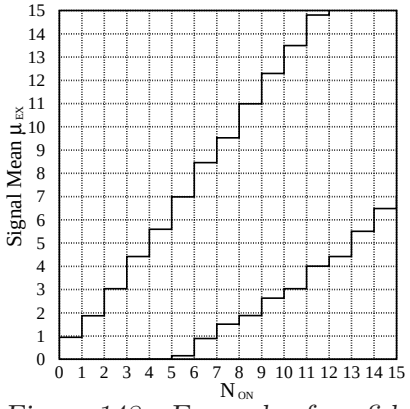

Figure 148: Example of confidence belt. From [263].

$$P\left(\mu_{EX} \in [\mu_{EX}^{low}, \mu_{EX}^{up}] \,\middle|\, N_{ON}; \mu_{OFF}; \Delta\mu_{OFF}\right) = \alpha \tag{132}$$

$$\text{or :} \quad P\left(\mu_{EX} < \mu_{EX}^{up}] \,\middle|\, N_{ON}; \mu_{OFF}; \Delta\mu_{OFF}\right) = \alpha \ , \tag{133}$$

whereby the first is said to yield a ***central confidence interval*** and the second an ***upper confidence limit*** [60]. As above, the choice of α is free, but usually 0.05 is taken ($\equiv$ 95% CL). The prescription to construct the limits μ_{EX}^{low} and μ_{EX}^{up} is then said to yield the correct ***coverage*** if in a series of experiments the true (unknown) value μ_{EX}^{true} is found in between the limits in $(1-\alpha)$ of the cases. The Bayesian construction eq. 129 does in general ***not*** yield the correct coverage. The prescription shown in figure 148 however does so by construction.

After the commonly used prescription by Gary Feldman and Robert Cousins [263], the construction of a confidence interval for the case of ***more than one measured parameter*** or ***more than one possibility for μ_{EX} to yield a same limit N_{ON}^{up} or N_{ON}^{low}***, those values of μ_{EX} are chosen which have the highest relative probability and are physically allowed.

The original prescription of [263] was enlarged by Wolfgang Rolke and Angel López [265] to a confidence belt construction which includes a probability model for the background

[59] Other choices sometimes seen are: 90 % or 99 %.

[60] There is a separate problem related to the choice of both methods, known as the "flip-flop" problem which is not further explained here.

$$[\mu_{EX}^{low}, \mu_{EX}^{up}] = [\mu_{EX}^{low};, \mu_{EX}^{up}](N_{ON}, N_{OFF}, \Delta N_{OFF}) \tag{134}$$

and later [266] including a probability model of the overall efficiency ϵ and its p.d.f.:

$$[\mu_{EX}^{low}, \mu_{EX}^{up}] = [\mu_{EX}^{low}, \mu_{EX}^{up}](N_{ON}, N_{OFF}, \Delta N_{OFF}, P(\epsilon)) \tag{135}$$

Although traditionally upper limits in Cherenkov telescopy have been published using the Bayesian approach of O. Helene [262], that method can result in considerable under-coverage and does not give any prescription of how to include systematic uncertainties on the efficiency. The (GRB working group of the) MAGIC collaboration has published so far upper limits using the enlarged method by Rolke et al. [266] (e.g. in [267]) to obtain upper limits $\mu_{EX}^{up} \equiv N_{>95\%}$. One of the authors of [266] has provided an implementation of their method [268] for seven typical experimental situations. One of these models (model #3) was found to match most of the situations found in typical analyses of MAGIC data: N_{ON} distributed Poissonian, the down-scaled number of OFF events $\kappa \cdot N_{OFF}$ in first approximation Gaussian with a width $\kappa \cdot \sqrt{N_{OFF}}$ [61] and the efficiency Gaussian, centered around 1. The rather complicated formulae used in [268] cannot be presented here, but are fully described in [266].

7.8.2 Particle Flux Upper Limits

Since in the case of no signal neither the energy spectrum of the source dN_γ/dE, nor the time evolution dN_γ/dt are unknown, some reasonable assumptions have to be made: Typically in these cases, power-law spectra can be assumed or combinations of power-law spectra and exponential cut-offs:

$$\begin{aligned} \frac{dN_\gamma}{dE\,dA\,dt} &= f_0 \cdot \big(\frac{E}{E_0}\big)^{-\alpha} \\ \frac{dN_\gamma}{dE\,dA\,dt} &= f_0 \cdot \big(\frac{E}{E_0}\big)^{-\alpha} \cdot \exp\big(-\frac{E-E_0}{E_b}\big)\,, \end{aligned} \tag{136}$$

where E_0 is the mean energy at which the limit is calculated [62] and α the hypothetical spectral index. E_b is the break energy of the exponential cut-off and A_0 a reference area. The light curve dN_γ/dt has to be assumed approximately constant, otherwise the observation time window $[T_{min}, T_{max}]$ would need to be split into smaller parts.

Making the above assumption, eq. 124 can be re-written to yield an expression for the flux limit:

[61] Note that for the case $\kappa > 1$ and $N_{OFF} < 10$, this assumption is not valid any more and model #2 should be used, instead.

[62] Only differential upper limits will be treated here. Since at poor energy resolutions, the integration boundaries are not well defined, integral limits do not make much sense and are skipped in the following further discussions.

$$f_0 < \frac{N_{>95\%}(E_r^{min}, E_r^{max})}{\int_0^\infty \left(\frac{E}{E_0}\right)^{-\alpha} \cdot A(E, E_r^{min}, E_r^{max})\, dE \cdot \int_{T_{min}}^{T_{max}} \frac{\epsilon(t)}{t}\, dt} \ , \tag{137}$$

with only measured values on the right side, except for the spectral index α. The integral $\int_{T_{min}}^{T_{max}} \frac{\epsilon(t)}{t}\, dt$ is also called the ***effective ON time*** T_{eff} and the integral over the effective area: $\int_0^\infty \left(\frac{E}{E_0}\right)^{-\alpha} \cdot A(E, E_r^{min}, E_r^{max})\, dE$ can be called the weighted effective area average $< A_{\mathit{eff}} >$. In its short form, equation 137 is then written:

$$f_0 < \frac{N_{>95\%}(E_r^{min}, E_r^{max})}{< A_{\mathit{eff}}(E_r^{min}, E_r^{max}, \alpha) > \cdot T_{\mathit{eff}}} \ . \tag{138}$$

f_0 has conveniently the units: [photons/cm^2/s/TeV].

7.8.3 Particle Fluence Upper Limits

In case a limit on the fluence from a hypothetical gamma-ray source is desired, the test spectra eq. 136 have to be converted to fluences:

$$\begin{aligned} \frac{dN_\gamma}{dE\, dA} &= F_0 \cdot \left(\frac{E}{E_0}\right)^{-\alpha} \\ \frac{dN_\gamma}{dE\, dA} &= F_0 \cdot \left(\frac{E}{E_0}\right)^{-\alpha} \cdot \exp\left(-\frac{E - E_0}{E_b}\right) , \end{aligned} \tag{139}$$

and limits on the fluence F_0 are derived:

$$F_0 < \frac{N_{>95\%}(E_r^{min}, E_r^{max})}{< A_{\mathit{eff}}(E_r^{min}, E_r^{max}, \alpha) >} \ . \tag{140}$$

Expression 140 makes only sense, if the information is provided that the source had been observed during an effective ON time T_{eff} in the time interval from T_{min} to T_{max}. Especially for highly variable sources like GRBs, limits on the fluence are preferred since they are independent from the light-curve of the hypothetical emission. F_0 has conveniently the units: [photons/cm^2/TeV].

7.8.4 Spectral Energy Density Upper Limits

Very often, the spectral energy density (***SED***) $E^2 \cdot dN_\gamma/dEdAdt$ at a given energy is a preferred parameter over the particle flux since many physical processes emit approximately the same power in different energy ranges. In order to place an upper limit on the SED, the test spectra eq. 136 are transformed in energy density spectra:

$$\begin{aligned} E^2 \frac{dN_\gamma}{dE\, dA\, dt} &= P_0 \cdot \left(\frac{E}{E_0}\right)^{-\alpha+2} \\ E^2 \frac{dN_\gamma}{dE\, dA\, dt} &= P_0 \cdot \left(\frac{E}{E_0}\right)^{-\alpha+2} \cdot \exp\left(-\frac{E - E_0}{E_b}\right) , \end{aligned} \tag{141}$$

It is straightforward to see that:

$$P_0 < \frac{N_{>95\%} < E(\alpha)^2 >}{< A_{\mathit{eff}}(E_r^{min}, E_r^{max}, \alpha + 2) > \cdot T_{\mathit{eff}}} \ , \tag{142}$$

where the mean square energy $< E(\alpha^2) >$ has to estimated from MC simulations of the corresponding test spectra and application of all cuts. P_0 is mostly given in units of [erg/cm^2].

7.9 Analysis of Muons

Two important telescope parameters can be retrieved with a dedicated analysis of the signal captured from muons, commonly emitted in hadronic showers: The total photon detection efficiency of the entire telescope including the mirrors and the spherical aberration, expressed in the point-spread-function (PSF). Moreover, the muon rate as such reflects the atmospheric conditions.

Muons passing close to the mirror are recognized by their characteristic circular images, captured from the Cherenkov light cone of a single particle. The images can be analyzed with the help of the ***RICH***-technique, commonly used in accelerator experiments. From the geometry of the system and the number of Cherenkov photons emitted per unit path length and unit wavelength interval (eq. 24) follows the number of photo-electrons N_{phe} collected per unit azimuth angle $d\phi$ in the focal plane [269]:

$$\begin{aligned} \frac{dN_{\mathrm{phe}}}{d\phi} &= \frac{\alpha\, I}{2} \cdot \sin(2\,\theta_c) \cdot D(\phi) \ , \qquad \text{with :} \\ I &= \int_{\lambda_1}^{\lambda^2} \frac{\epsilon(\lambda)}{\lambda^2}\, d\lambda \quad \text{and :} \\ D(\phi) &= R\left[\sqrt{1 - (\rho/R^2)\sin^2\phi} + (\rho/R)\cos\phi\right] \qquad (\rho/R \leq 1) \ , \end{aligned} \tag{143}$$

where α is the fine structure constant, θ_c the Cherenkov angle, $\epsilon(\lambda)$ the photon detection efficiency, ρ the impact parameter of the muon and R the radius of the mirror.

From the (fitted) muon ring radius, the impact parameter ρ can be reconstructed, while the integrated photon detection efficiency is estimated by comparion of the photo-electron intensity $dN_{\mathrm{phe}}/d\phi$ along the ring with MC simulated muons and detector. From the outcome of this comparison, an absolute calibration of the telescope as a whole can be performed (see also section 6.8).

The width of each muon ring in turn, reflects the mirror aberrations, the position of the focal plane of the camera and multiple scattering effects of the muon itself. Again by comparison with MC simulation, the PSF as the main contribution to the aberration can be estimated. The precision of such measurements lie around $\pm 10\,\%$ [249]. Under normal conditions, a (cleaned) muon rate of about 2 Hz is obtained.

8 Gamma Ray Bursts Observation

In the first observation cycle of MAGIC, 11 Gamma Ray Bursts could be observed during their early afterglow phase (see table 22). The observation of two bursts, namely GRB050713a and GRB050904, covered also parts of their prompt emission phase – a novelty for Cherenkov telescopes.

GRB	Satellite	ΔT_{alert} [s]	ΔT_{start} [s]	zenith angle [°]
GRB050421	SWIFT	58	83	52
GRB050502	INTEGRAL	18	990	30
GRB050505	SWIFT	540	637	49
GRB050509a	SWIFT	16	35	58
GRB050509b	SWIFT	15	36	70
GRB050528	SWIFT	43	77	50
GRB050713a	SWIFT	13	40	49
GRB050904	SWIFT	82	92	24
GRB060121	HETE	15	583	48
GRB060203	SWIFT	171	185	44
GRB060206	SWIFT	16	25	13

*Table 22: Observed gamma ray bursts in cycle-I observation phase: ΔT_{alert} gives the time difference between the onset of the burst and its reception by the **gspot**-connection to **GCN**, ΔT_{start} the time until burst could be observed. Compilation by Markus Garczarczyk.*

Whereas GRB050904 has earned vast publicity for being the furthest ever observed GRB (at a redshift of $z \approx 6.3$ [270, 271]), it is hard to believe that gamma rays succeed to travel such a long distance without being absorbed by the ***EBL*** (see chapter 2.12.1). On the other hand, the redshift of GRB050713a has not been measured – it is therefore possible that that GRB has happened close enough to be detectable by MAGIC.

With the participation of the author, a fast standard analysis was performed, yielding no signal, and upper limits were published [81, 267]. That analysis was not optimized at all for low energies and further not tested on a known source. These short-comings are overcome here, where a much refined analysis is presented, dedicated to yield the lowest possible energy threshold and achieve improved sensitivities. Results from [267] will serve thereby as benchmarks.

In order to cross-validate the results, a second test sample was analyzed, namely a flare of the AGN Mrk501, observed 12 days before GRB050713a, under similar observation conditions (except for the observation zenith angle). That flare yielded the highest gamma ray flux ever observed by MAGIC, data from that period is therefore expected to yield a strong signal.

8.1 The Data Samples

GRB050713a was detected on July, 13$^{\text{th}}$, 2005, at 04:29:02.39 UTC by the BAT detector on the SWIFT satellite. The alert was distributed via the GCN [272] within 13 seconds (SWIFT trigger 145675), with an uncertainty of 3 arcmin radius. The XRT and the UVOT detectors, also located on SWIFT, found a fading source at RA: 21h 22m 09.6s, Dec: +77d 04m 30.3s. The MAGIC telescope started to observe the position 40 seconds after the onset of the burst (T_0). While the brightest part of the keV emission occurred within $T_0 + 20s$, three smaller peaks followed at $T_0 + 50$s, $T_0 + 65$s and $T_0 + 105$s, thus after the start of the observation of MAGIC (see figure 149). The burst position was then observed for 2223 seconds in a zenith angle range between 49° to 50°, additionally 3000 seconds of OFF data were taken two nights later.

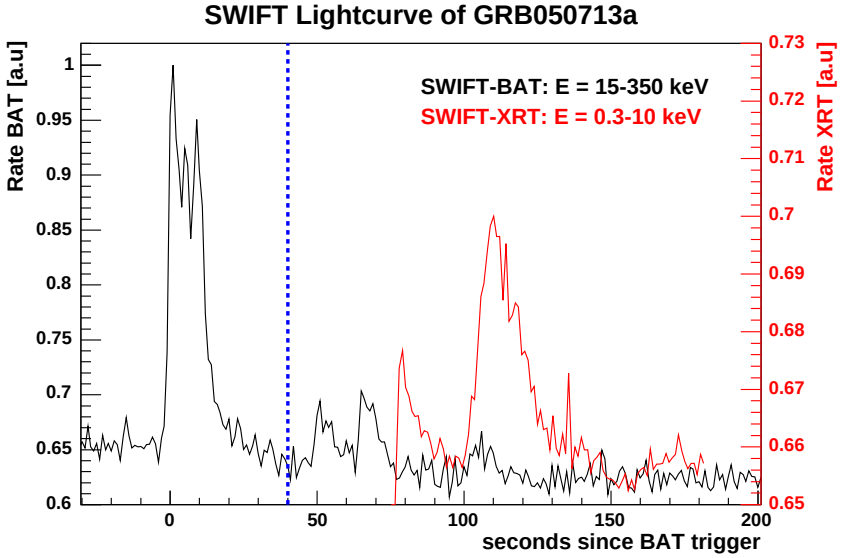

Figure 149: Light curve of GRB050713a, as observed by SWIFT: In black, the BAT light curve in (15–150 keV), in red XRT (0.3–10 keV). The blue line shows the start of the observation with MAGIC.

The following data samples were used for the analysis:

GRB050713a: 2184 seconds (effective on-time) of ON data, with 90 seconds taken during the prompt emission and 2900 seconds (effective on-time) of OFF data, taken during two nights later with the telescope pointing at the same position in the sky. Moreover, 60 kEvts of MC simulated gamma showers for pointing zenith angles from $48° - 50.5°$ and a point spread function of $0.05°\sigma$ were used. For systematic checks, another 60 kEvts of a slightly worse point spread function of $0.07°\sigma$ was also run through the analysis chain (see explanations later in section 8.3).

Start	End	Day	zenith angle [deg.]	DT	Trigger Rate [Hz]	Remarks
GRB050713a ON						
61345	61346	2005-07-13	49 - 50	40	120	no interlaced calib. events
61347	61351		50 - 50	40	120	
GRB050713A OFF						
61531	61544	2005-07-15	49 - 50	32	200	
Mrk501 ON						
59834	59839	2005-07-01	21 - 24	32	220	
59840	59851		14 - 21	40	170	
Mrk501 OFF						
59713	59718	2005-06-29	15 - 24	32	230	
59720	59723		12 - 15	32	270	
59940	59948	2005-07-02	16 - 20	32	220	
60399	60412	2005-07-06	16 - 23	32	300	excluded 60406-60409
60632	60637	2005-07-08	15 - 18	32	250	excluded 60636
Spark Events						
52631	52633	2005-04-11			1	

Table 23: Collection of the data samples used for this analysis. DT stands for "Discriminator Threshold".

Mrk501: 3930 seconds (effective on-time) of ON data and about 3600 seconds of OFF data, both with the telescope pointings from 15° to 25° zenith angle, taken during three different nights. Additionally, about 122 kEvts of MC simulated gamma showers with zenith angles ranging from 15° to 27° were used.

Closed Camera: For systematic studies, additional 30 minutes (1500 events) were analyzed, taken with closed camera and triggered by the usual level-1 majority trigger (so-called "spark runs").

Table 23 lists all the relevant run parameters for the analyzed data: One can see that unfortunately, the OFF data for GRB050713a was taken with different discriminator threshold (***DT***) settings compared to the ON data. This happened due to a misunderstanding by the shifters: The source observed directly before GRB050713a was a Galactic source, therefore the *DT*'s had been initialized to a higher value which were kept as such since after a GRB alert, there is usually no time to modify the

DT settings. Two days later, the shifters took the OFF GRB050713a data applying the discriminator thresholds of $DT = 32$ because they saw it was an extra-galactic source. From the different DT's follow also different raw trigger rates.

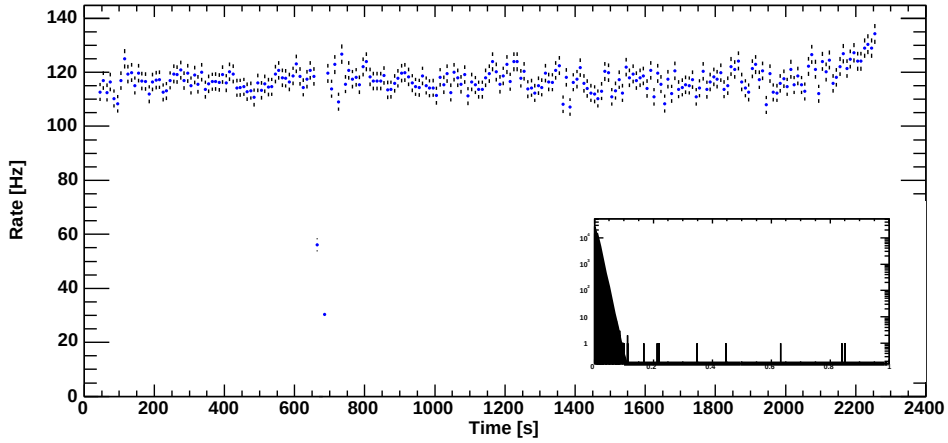

Figure 150: Raw event rates of GRB050713a after suppression of the interlaced calibration events. The inset shows the distribution of time differences between consecutive events.

Figure 150 shows the raw trigger rates (after elimination of the interlaced calibration events) during the observation of GRB050713a. While the first two runs were taken (erroneously) without interlaced calibration events, the shifters stopped data taking (from $T_0 + 665$ s to $T_0 + 687$ s) to retrieve the interlaced calibration events.

A similar problem occurred during the observation of Mrk501: The shifters realized that the rates had passed the 400 Hz trigger limit and thought it would be safer to raise the discriminator thresholds. For this reason, the Mr501 ON data set is also split in two parts: about 20 minutes taken with $DT = 32$ and another half an hour taken with $DT = 40$ (see figure 151). Apart from that problem, the Mrk501 data resulted to be of very good quality, except for the OFF data taken on July, 6^{th}, where half of the runs had to be excluded.

Figure 152 shows the distributions of the (calibrated) pedestal RMS for the GRB050713a data sets. One can see that ON and OFF data agree well while after two years of data taking, fluctuations in the outer pixels are still simulated too high. As the analysis presented here relies on images contained in the inner camera, this discrepancy is not of great importance, though.

8.2 Pointing Precision in GRB Observation Mode

Many concerns have been raised about MAGIC's capabilities to point to a GRB position with the necessary speed and required precision. The latter is investigated here with the help of the ***star-guider*** data: a sensitive CCD camera monitoring

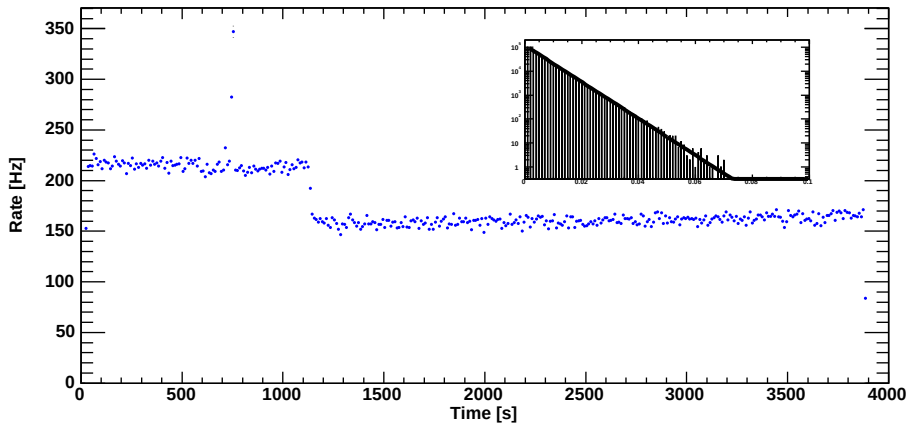

Figure 151: Raw event rates of the Mrk501 ON data, taken on July 1st, 2005. The decrease in rate happens when the shifters decided to increase the discriminator thresholds.

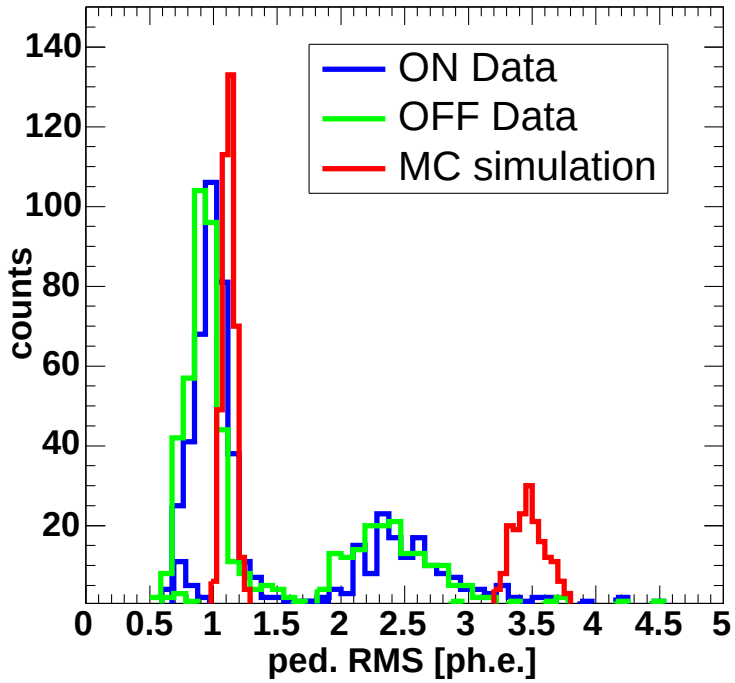

Figure 152: Distributions of the pedestal RMS for the GRB050713a data sets. The left histograms belong to the inner pixels and the right ones to the outer pixels.

constantly the viewed star-field and three out of the six reference LEDs on the camera (see section 3.5). A dedicated analysis program constantly searches for significant light excesses over the surrounding background level and match their positions with cataloged stars.

Unfortunately, the star-guider was not calibrated properly when the GRB050713a data were analyzed. This check yields therefore only estimates on the relative deviation from typical offsets in zenith and azimuth angle. An absolute pointing calibration on a point-like gamma ray source at zenith angles around 50° was performed elsewhere [273] stating an accuracy of 0.03°.

Figure 153 resumes all relevant information obtained from the star-guider data: On the top parts, the nominal zenithal and azimuthal pointing positions are displayed, with the GRB050713a observation at the end of the night. The bottom parts show the pure offsets, as measured with the positions of the cataloged stars and a temptative absolute calibration. One can learn the following from figure 153: First, the telescope shows a mis-pointing about 0.15°in zenith and up to 0.4°in azimuth during and shortly after culmination of an observed source. GRB050713a is not affected by this problem however, and the total average mis-pointing is smaller than 0.1°. The first measurement of the zenith offset after the acceptance of the alert yields an additional zenith offset of 0.05°.

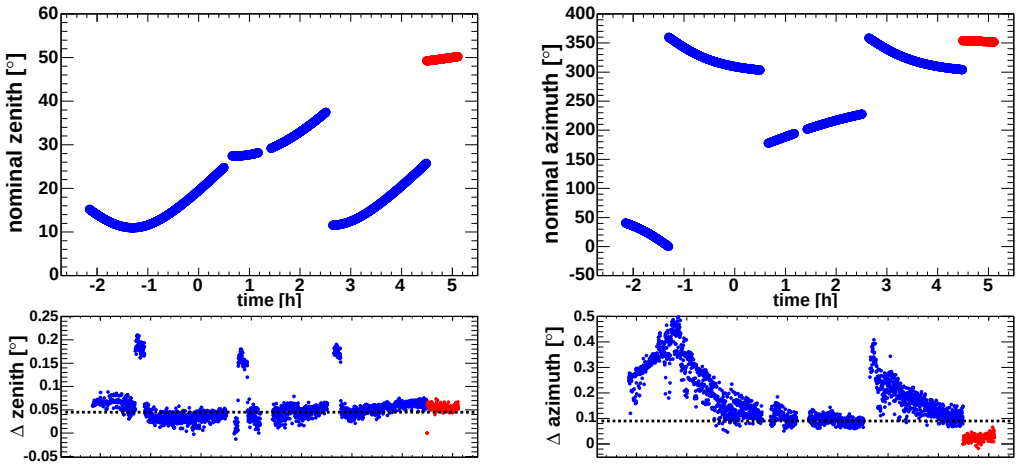

Figure 153: Relevant parameters from the star-guider data during the night when GRB050713a ocurred. Top: nominal zenith and azimuth angle, in red the GRB050713a pointing. Bottom: Deviations from the nominal pointing, using the positions of the recognized cataloged stars. The black dashed lines show a temptative calibration of the offsets.

In total, the telescope never points off source by more than 0.11°, which is about the size of one inner pixel and smaller than the precision of the *ALPHA*-plot.

8.3 Spherical Aberration of the Mirrors in GRB Mode

Under normal conditions, the mirrors of the MAGIC telescope are getting re-aligned with the use of the ***AMC*** before starting to track a new source. Because a full laser re-alignment takes more than three minutes, the telescope would lose too much time with this procedure when a GRB alert occurs. Instead, look-up tables (LUTs) were created from the telescope pointing positions and the results of each corresponding alignment. These LUTs were then used to focus the mirrors automatically while the telescope was moving toward to the position of GRB050713a.

As that procedure was implemented recently before GRB050713a occurred and later several small bugs were found in the scripts which define the automatic procedure, there is some uncertainty about the true PSF during the observation of GRB050713a. From posterior experience with the (bugfree) LUTs, a PSF of about $0.05^\circ\,\sigma$ would be expected, while the muon analysis (section 7.9) produced an estimated PSF of $0.045\pm0.005^\circ\,\sigma$. That value is obtained however only from the entire data sample and a dedicated measurement for the time of the prompt emission was not possible (remember a muon rate of 2 Hz). It is therefore not certain which value the PSF had exactly during the first minute of GRB050713a observation.

In order to monitor a possible degradation of the PSF just during the prompt emission phase of GRB050713a, a second sample of simulated gamma showers with PSF=$0.07^\circ\,\sigma$ was analyzed in parallel to the sample simualted with the estimated value of PSF=$0.05^\circ\,\sigma$. With the second simulation, the worsening of the upper limit was measured if indeed the AMC had not yet finished all the mirror adjustments.

8.4 Calibration and Excluded Pixels

The data was calibrated as described in section 7.2, using the MAGIC Analysis Software [63].

In total, 27 pixels had to be excluded plus two channels which were not equipped with photo-multipliers.

Figure 154 shows the mean calibrated signal, interpolated in case of the rejected pixels. The signals of the outer pixels were multiplied with 0.25 to obtain the camera response per pixel area unit and a smooth transition between inner and outer pixels (except for trigger area effects). One can see a flat camera response except for some pixels (red points) which are known to show spark events from time to time. For comparison, a similar figure is shown on the right side, taken with the closed camera. Some of the islands observed in figure 154, reappear on the right side, not all however. Furthermore, a small deficit of 5–10% at the lower right part of the inner camera is observed, covering a group of four to five pixels. Figure 155 shows the mean arrival times for pulses exceeding a threshold of 15 photo-electrons. The structure seen in figure 155 is due to a different time offset of the trigger cells in the upper right part of the camera, a hardware problem which was repaired only in October of that year. It

[63] MARS release version V0-10-8.

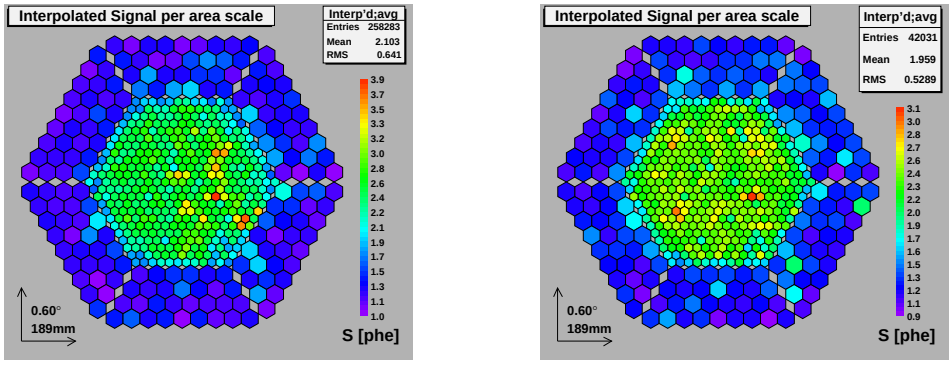

Figure 154: Mean calibrated signals in equivalent photo-electrons, left: GRB050713a, right: Spark runs.

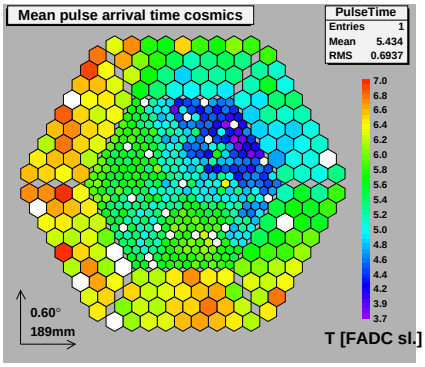

Figure 155: Mean reconstructed pulse position for the GRB050713a data. A lower signal threshold of 15 photo-electrons had been applied.

does not affect the signal reconstruction efficiency though, as can be seen comparing figure 154 with figure 155.

8.5 Image Cleaning

All calibrated data was cleaned using the absolute and the time image cleaning, respectively with the algorithms introduced in section 7.3. According to table 21, a probability of 2% was accepted that additional islands from fluctuations of the noise may appear. The resulting image cleaning levels were then:

absolute cleaning: $N_1 = 7$ and $N_2 = 4$ photo-electrons.

time cleaning: $R_1 = 2.5$ and $R_2 = 0.5$ pedestal RMS.

Additionally, the data sample using the time cleaning, weighted the first and second moments of the image with the calibrated charge, elevated to 1.5 ($\alpha = 1.5$ in eq. 111).

The further analysis was hence split in two parts according to the two cleaned data samples. Figure 156 shows the averaged signal after image cleaning for the two

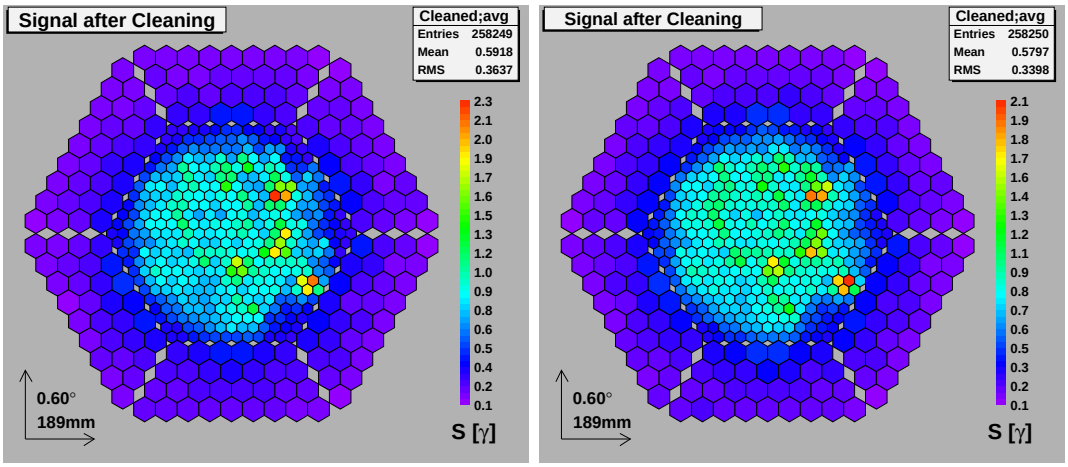

Figure 156: Averaged signal per pixel in photo-electrons after image cleaning: Left: absolute cleaning, right: time cleaning.

cleaning algorithms. One can see the same "hot spots" as already found in figure 154 which are probably due to the sparking pixels. It seems that the relative importance of the sparks to the signal is less pronounced if the time cleaning algorithm is used. At the lower right edge of the camera and the rightmost part, clear deficits are discerned for both cleaning algorithms. Checking thoroughly the calibration parameters for these parts of the camera, no deviating behavior was found there. Especially, the positions of the voids do not coincide with the positions of rejected pixels (which are seen as white spots in figure 155). As the same areas do not show any deviating behavior in calibration runs, the most plausible explanation would be that these voids coincide with less efficient trigger cells.

The averaged centers ($<x>, <y>$) of the reconstructed ellipses ("center of gravity") are shown in figures 157 (for the GRB050713a ON data) and 158 (for the simulated gamma showers). Again, one can observe that the camera seems to be illuminated more uniformly when the time cleaning with lower thresholds is used, however areas of less efficiency remain in the right side of the camera. which coincide with the voids observed previously. The exact reason for these inefficiencies is still unclear.

8.6 Pre-selection

Before the *HADRONNESS* is calculated and the energy reconstruction performed, an event pre-selection is applied to the data. The involved cuts are either required to exclude the "spark events" or they are simply loose cuts that practically cause no signal loss and exclude events which would otherwise only confuse the calculation of random forest matrices. This is the case for two cuts on *LEAKAGE* and the number of islands *ISLANDS*, defined in section 7.4. Being an explicit low-energy analysis,

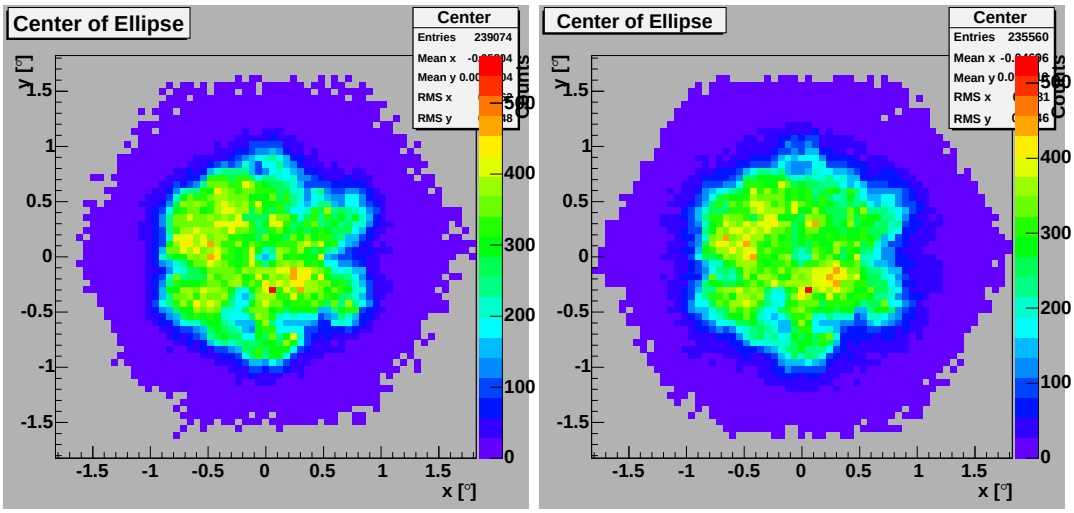

Figure 157: Average center-of-gravity of the reconstructed image ellipses for the GRB050713a data. Left: absolute cleaning, right: time cleaning.

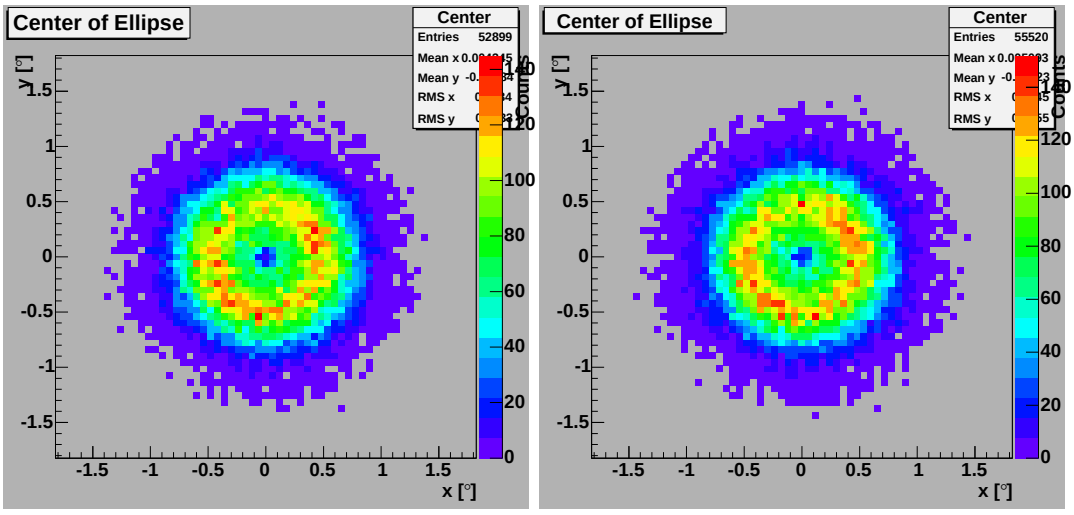

Figure 158: Average center-of-gravity of the reconstructed image ellipses for MC simulated gamma showers. Left: absolute cleaning, right: time cleaning. The preferred distance from the camera center for low-energy events lies in a ring between $DIST \approx 0.3°$ and $DIST \approx 0.8°$.

no signal is lost by cuts on these two high-energy parameters:

$$LEAKAGE < 0.01 \quad (144)$$

$$ISLANDS < 2 \quad (145)$$

Further cuts need a more detailed explanation and are presented in the following:

SIZE

As this analysis is dedicated to low-energy events, a strong cut on the parameter *SIZE* is applied:

$$60\,\text{phe} < SIZE < 400\,\text{phe} \quad (146)$$

The lower *SIZE* limit eliminates images which can hardly be reconstructed correctly, while the upper limit of 400 phe is unusual, but justified given the fact that a high-energy analysis has already been performed, and a dedicated training of cuts on low energy events is preferred here.

Figures 159 shows the distributions of $\log(SIZE)$ for the GRB050713a data samples. A shift between ON and OFF data is observed, mainly because of the different discriminator threshold settings. Shown in figure 159 are also the distributions from simulated gamma showers and the gamma showers test sample with worse PSF. As expected, a loss of events at low sizes can be observed if the PSF worsens.

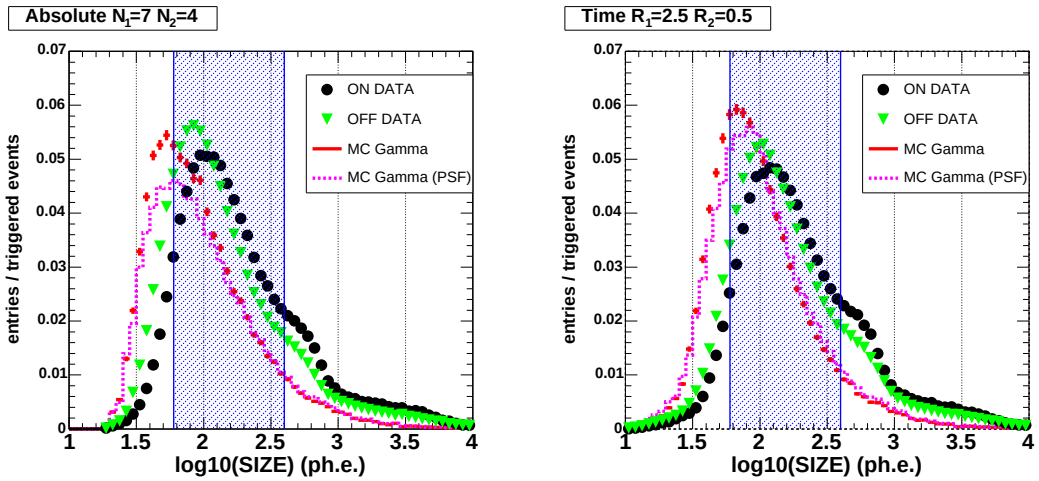

Figure 159: Normalized distributions of the parameter log(SIZE) for the GRB050713a data. The blue lines show the cuts applied previous to the further analysis: 60 phe $< SIZE <$ 400 phe. *Left: absolute cleaning, right: time cleaning.*

Similar behaviors are seen in the Mrk501 data (figure 160) where the ON data distributions agree well with the ones from the OFF data, whenever the data were

taken with the same discriminator thresholds. Otherwise a shift is obtained, similar to one of figure 159.

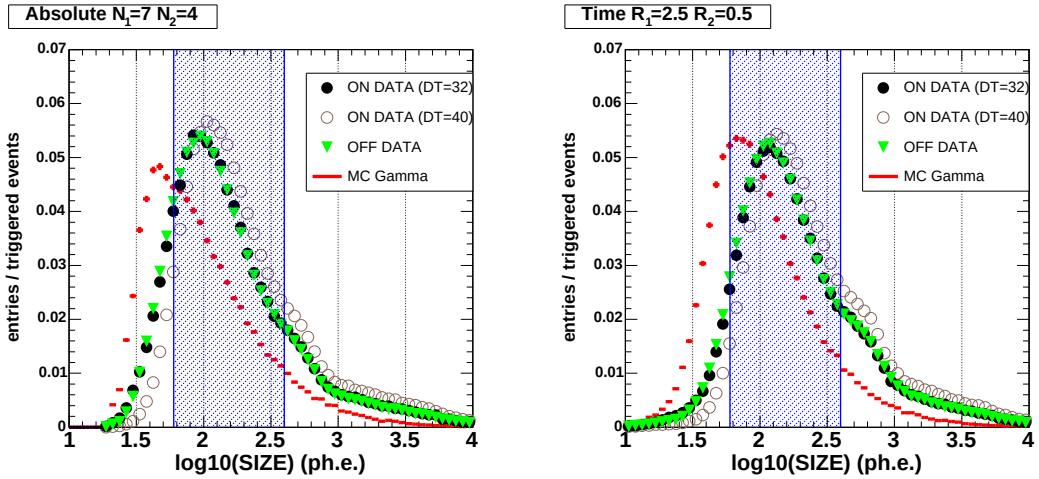

Figure 160: Normalized distribution of the parameter log(SIZE) for the Mrk501 data. The blue lines show the cuts applied previous to the further analysis: $60\,\text{phe} < SIZE < 400\,\text{phe}$. *Left: absolute cleaning, right: time cleaning.*

DIST

Low-energy events arrive mainly in a ring around the camera center at distances between 0.3° and 0.8° (recall figure 158). It is therefore useful to make a cut on the *DIST* parameter. While at low values of *DIST*, the *ALPHA* parameter cannot be determined any more, events with higher *DIST* die out at low energies. The following pre-selection cut was therefore applied:

$$0.33^\circ < DIST < 0.86^\circ \tag{147}$$

Figure 161 shows the distribution of the *DIST* parameter versus the logarithm of *SIZE* and the applied cuts for the GRB050713a data samples, cleaning with the time algorithm. One can see that only the lower cut on *SIZE* removes a sizeable amount of gamma ray signal. (A similar picture is obtained with data coming out of the absolute cleaning.)

Spark Events

Events triggered by sparks between the cathode and the mylar foil acting as light guides, show a large signal in and around the corresponding channel, but do not affect the rest of the camera. The reconstructed signals from such events are thus very

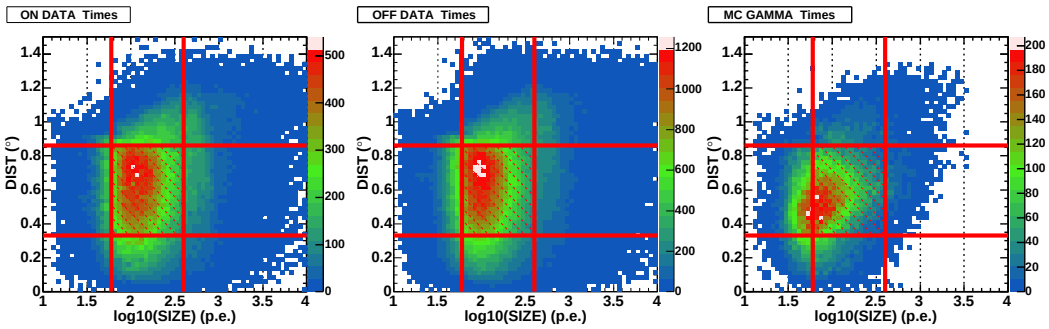

Figure 161: Distributions of the parameter DIST for the GRB050713a data, cleaning with the time algorithm. The red lines show the pre-selection cuts.

concentrated in the sparking channel. For this reason, a cut on the concentration parameter *CONC* can efficiently remove the spark events:

$$\log(CONC) < 0.65 - 0.45 \cdot \log(SIZE) \tag{148}$$

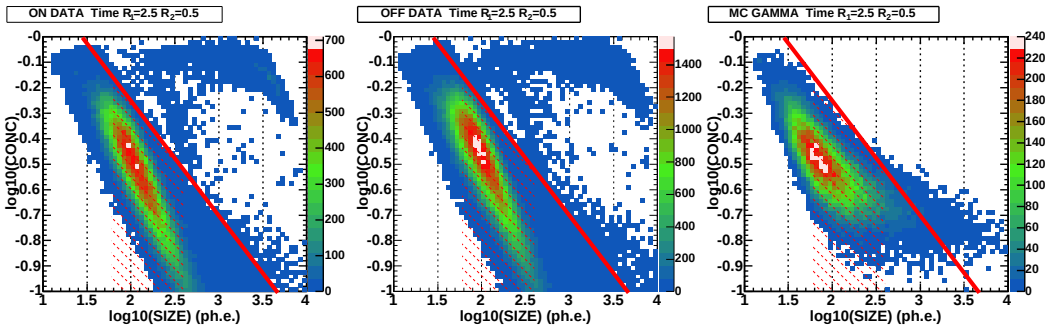

Figure 162: Distributions of the parameter log(CONC) vs. log(SIZE) for the GRB050713a data, cleaning with the time algorithm. The DIST cut from the previous paragraph has already been applied. Red lines show the pre-selection cut: $\log(CONC) < (0.65 - (0.45 * \log(SIZE))$.

Figure 162 shows the $\log(CONC)$ vs. $\log(SIZE)$ plane with the cut eq. 148. While ON and OFF data show a branch of events on upper right side of the plane which can be associated to the spark events and are removed by the pre-selection cut, the simulated gamma shower events are not affected. (A similar picture is obtained with data coming out of the absolute cleaning.) On the contrary, if the same cut is applied to the data taken with closed camera (figure 163), almost all events are removed, either by the cut on $\log(CONC)$ or the one on *SIZE*. Here it is interesting to see that the image cleaning algorithm does not affect the distribution of events from the closed camera run. Would these events contain low sized signals close to the noise level, a stronger difference would be expected between the two differently cleaned data sets.

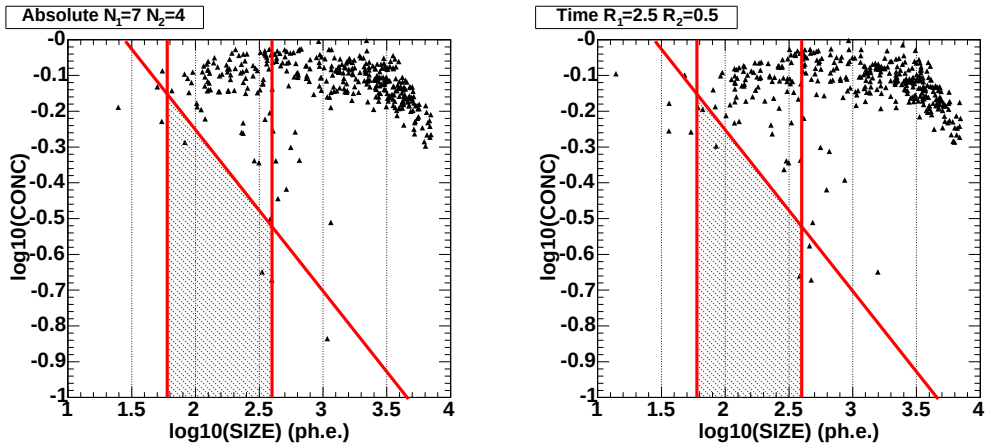

Figure 163: Distribution of the parameter log(CONC) for the data taken with closed camera ("spark runs"). The red lines indicate the applied cuts on SIZE and $\log(CONC) < (0.65 - (0.45 * \log(SIZE))$. *Left: absolute cleaning, right: time cleaning.*

8.6.1 *SIZE* after Pre-selection

After applying the pre-selection cuts, the distributions of the logarithm of *SIZE* is shown for the GRB050713a data (figure 164). The ON data distribution remains shifted with respect to the one from the OFF data, whereas the distributions of simulated gamma showers with the worse PSF (histogram "MC (PSF)") show an event loss at low sizes compared to the one with smaller PSF (histogram "MC"), but no general shift towards higher sizes. This is an expected effect point spread function: Loss of signal concentration and thus event loss at low energies. Based on these findings, it seems even more unlikely that the difference in PSF were a reason for the disagreement between ON and OFF data sample. Instead, it is reasonable to assume that the observed discrepancy is entirely due to the different discriminator threshold settings. Figure 164 indicates also that the efficiency for gamma showers is higher if the time image cleaning algorithm is used.

8.6.2 Camera Homogeneity after pre-selection

We now investigate if the pre-selection has improved the camera homogeneity: Figures 165 show the center-of-gravity (COG) from the GRB050713a data samples for the two differently cleaned data sets. The voids have not disappeared, instead an excess of events at the left center has appeared. and an additional void at the lower left part of the camera (at "7 o' clock") shows up. While the latter void might be attributed to three close excluded pixels, the excess is not understood. Further inspection revealed that these inhomogeneities appear above all at low energies, which explains partly the increased sensitivity of the time image cleanings towards them.

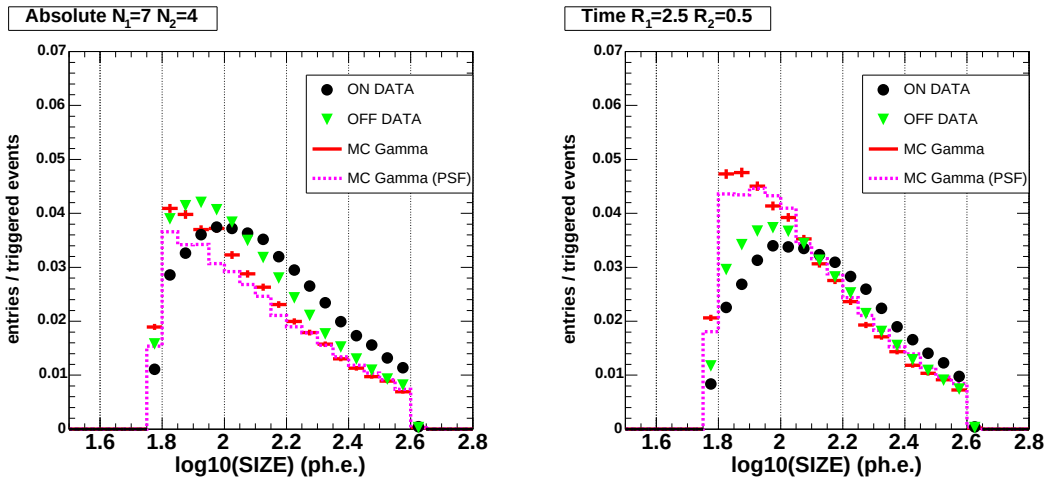

Figure 164: Normalized distributions of the parameter log(SIZE) for the GRB050713a data after pre-selection. Left: absolute cleaning, right: time cleaning.

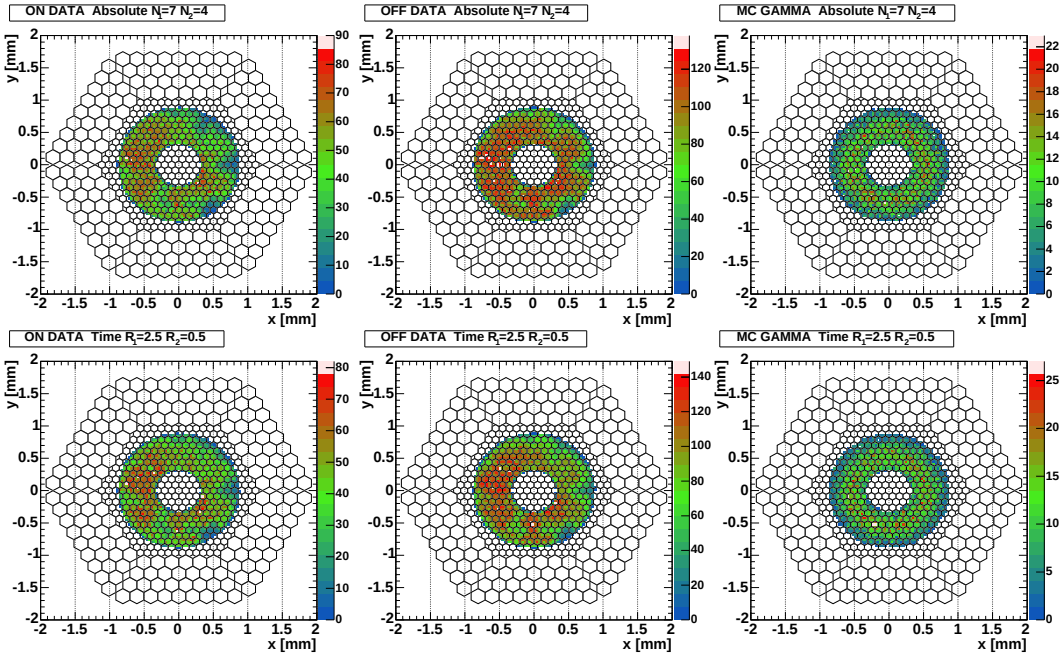

Figure 165: The center-of-gravity, obtained from the GRB050713a data after pre-selection. Left: ON data, center OFF data, right: simulated gamma showers. Top: absolute cleaning, bottom: time cleaning.

8.6.3 Cut Efficiencies

Tables 24 and 25 list the selection efficiencies for all cleaning steps applied until now. In general, the time image cleaning algorithm yields better efficiencies for the simulated gamma ray shower samples than the absolute cleaning algorithm. More than half the triggered gamma events do not enter the further analysis, mainly because of the cuts in *SIZE*.

The hadron samples (OFF and ON) yield slightly higher efficiencies, also due to the cuts in *SIZE*. Important is the matching of efficiencies between ON and OFF data, which is the case for both image cleaning algorithms. Curiously, the matching is better for the GRB05013a data than for the Mrk501 data.

In the last row of table 24, the cut efficiency for the spark runs is shown: The last cut on the log(*CONC*) effectively removes all sparking events.

	Selection Efficiencies GRB050713a				
Image Cleaning Algorithm	MC gammas PSF=0.05°	MC gammas PSF=0.07°	OFF Data	ON Data	Sparks Data
Total events	61042	53571	571414	258250	564
	part of events surviving Image Cleaning				
Absolute	0.87	0.79	0.93	0.93	0.98
Time	0.91	0.90	0.91	0.91	0.99
	part of events surviving after *SIZE* cut				
Absolute	0.49	0.46	0.63	0.64	0.13
Time	0.58	0.58	0.63	0.63	0.15
	part of events surviving after pre-selection				
Absolute	0.47	0.44	0.57	0.58	0.002
Time	0.54	0.55	0.52	0.53	0.004
	part of events surviving final cuts				
Absolute	0.19	0.19	0.06	0.07	0.0
Time	0.18	0.22	0.05	0.05	0.0
	part of events surviving final cuts and alpha<15				
Absolute	0.18	0.16	0.011	0.012	0.0
Time	0.17	0.19	0.008	0.009	0.0

Table 24: Selection efficiencies for the GRB050713a data samples.

8.7 Calculation of *HADRONNESS*

After applying the above cuts, the image parameters were combined to one single parameter, the *HADRONNESS*, using the prescriptions outlined in chapter 7.5.

	Selection Efficiencies Mrk501					
Image Cleaning Algorithm	MC gammas	OFF Data 29/06	OFF Data 02/07	OFF Data 08/07	ON Data DT=32	ON Data DT=40
Total events	122850	272040	344819	218245	263812	451979
	part of events surviving image cleaning					
Absolute	0.81	0.90	0.97	0.96	0.95	0.98
Time	0.90	0.89	0.96	0.96	0.93	0.97
	part of events surviving size-cut					
Absolute	0.44	0.61	0.67	0.65	0.65	0.70
Time	0.56	0.62	0.67	0.67	0.65	0.67
	part of events surviving pre-cuts					
Absolute	0.34	0.42	0.45	0.44	0.44	0.49
Time	0.42	0.38	0.41	0.40	0.40	0.42
	part of events surviving final cuts					
Absolute	0.26	0.18	0.19	0.19	0.19	0.21
Time	0.27	0.13	0.14	0.14	0.13	0.14
	part of events surviving final cuts and alpha<15					
Absolute	0.19	0.03	0.03	0.03	0.03	0.04
Time	0.20	0.02	0.02	0.02	0.02	0.03

Table 25: Selection efficiencies for the Mrk501 data samples.

After a re-sizing procedure which removed OFF data events until the distributions of *SIZE* agreed between the simulated gamma showers and the OFF data training samples, the following variables were introduced in the ***random forest*** algorithm:

- *SIZE*, *DIST*, *WIDTH*, *LENGTH*, *CONC*, *CONC4*
  and sign(cos(*DELTA* · *ALPHA*))**M3LONG*.

Figures 166 to 171 show the distributions of these parameters for the GRB050713a data. In general, there are quite remarkable differences between the two data sets which have been obtained from the two image cleaning algorithms, nevertheless the distributions agree well between the ON and OFF data samples, except for some details:

Shift in concentration parameters: A small shift is observed in the two concentration parameters between ON and OFF data. Inspection of the same distributions for the Mrk501 data (not shown here) revealed that the data sets taken with same discriminator thresholds show well matching distributions of

the parameters *CONC* and *CONC4* while similar shifts appear in the data sets taken with different DTs.

PSF dependency: Three parameters show a sizeable dependency on the point spread function: *WIDTH*, *CONC* and *CONC4*.

Because of the first observation, the Random Forest training was not performed using the last four runs of the ON data as hadrons training sample, instead of the OFF data. It has been shown [260] that hadron samples with gamma event contaminations of up to 1% yield the same efficiency as in the case of no contamination. This decision should therefore introduce less bias to the result than using a deviating OFF data sample. The approach was justified afterwards when it became clear that no signal was found in the last four runs of GRB050713a data and the assumption of less than 1% contamination was justified.

Figure 172 shows the mean decrease of the ***Gini index***, obtained from the training of the random forest algorithm for GRB050713a data emerging from the two different image cleanings. That variable is a measure of the background rejection efficiency of a given cut parameter in the presence of the parameters (see section 7.5). For the absolute cleaned data, the parameter *LENGTH* results to be the strongest cut parameter while the parameter *CONC4* is most efficient in case of the time cleaning. The second row of figure 172 shows the effect of a worsening of the PSF for the relative importance of each parameter. As already expected from the findings above, those parameters which show a dependency on the PSF, suffer a change in their relative importance. Especially a dramatic change in the importance of the *WIDTH* parameter is observed in the case of the time cleaned data. Comparing the efficiency of the *WIDTH* against the *LENGTH* parameter, one can see that the order gets inverted: If the worse PSF is used, the relative importance of the *WIDTH* parameter increases. The absolute cleaning seems to be more stable against modifications of the PSF, although changes are also observed there, e.g. in the importance of the *DIST* parameter.

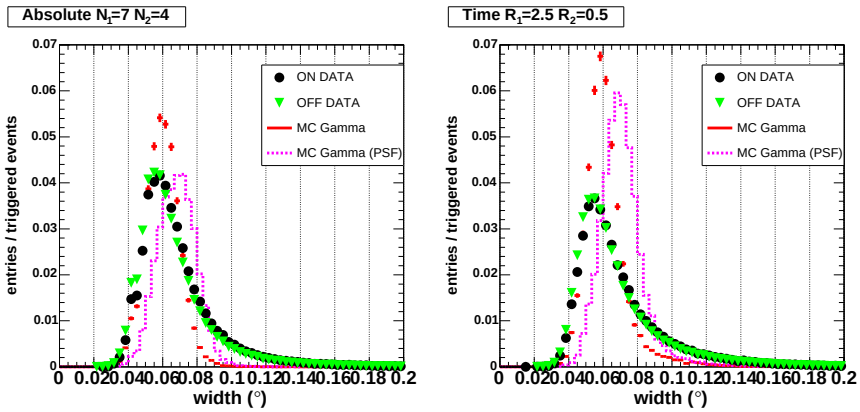

Figure 166: Normalized distributions of WIDTH for the GRB050713a data. Left: absolute cleaning, right: time cleaning.

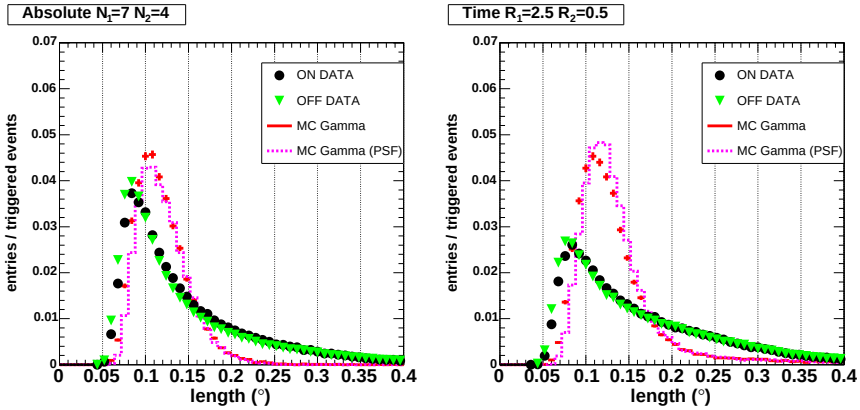

Figure 167: Normalized distributions of LENGTH for the GRB050713a data. Left: absolute cleaning, right: time cleaning.

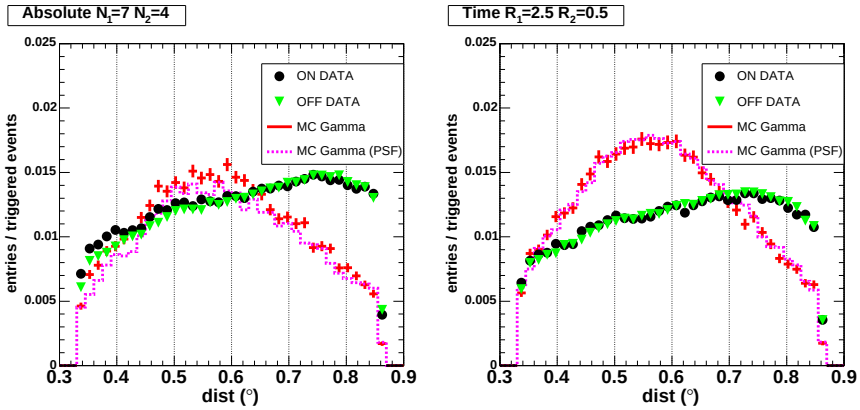

Figure 168: Normalized distributions of DIST for the GRB050713a data. Left: absolute cleaning, right: time cleaning.

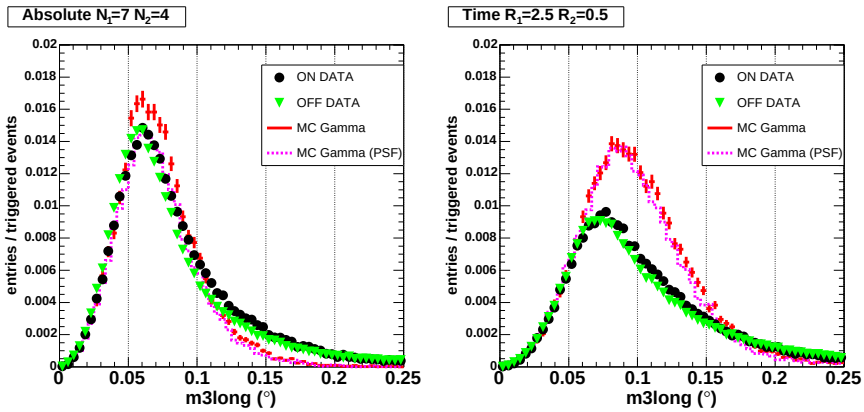

Figure 169: Normalized distributions of M3LONG for the GRB050713a data. Left: absolute cleaning, right: time cleaning.

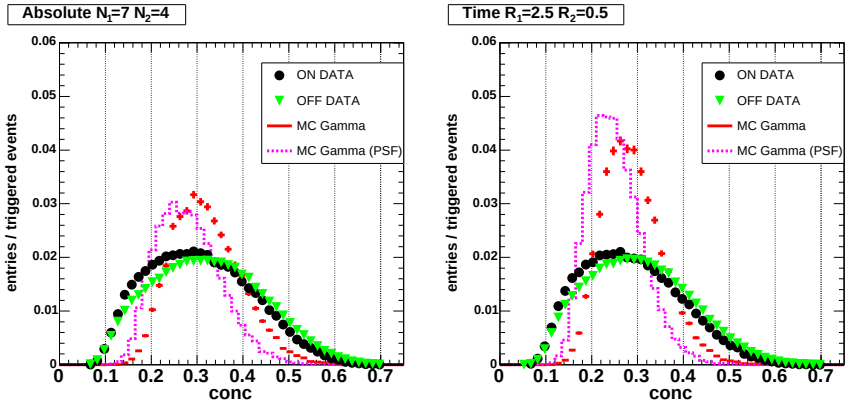

Figure 170: Normalized distributions of CONC for the GRB050713a data. Left: absolute cleaning, right: time cleaning.

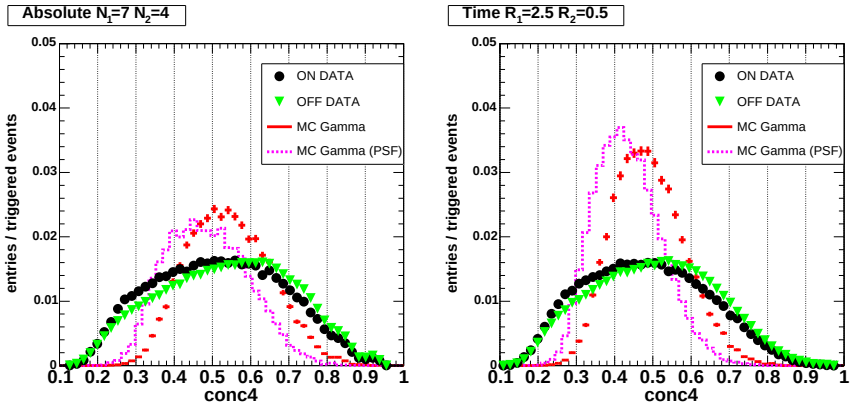

Figure 171: Normalized distributions of CONC4 for the GRB050713a data. Left: absolute cleaning, right: time cleaning.

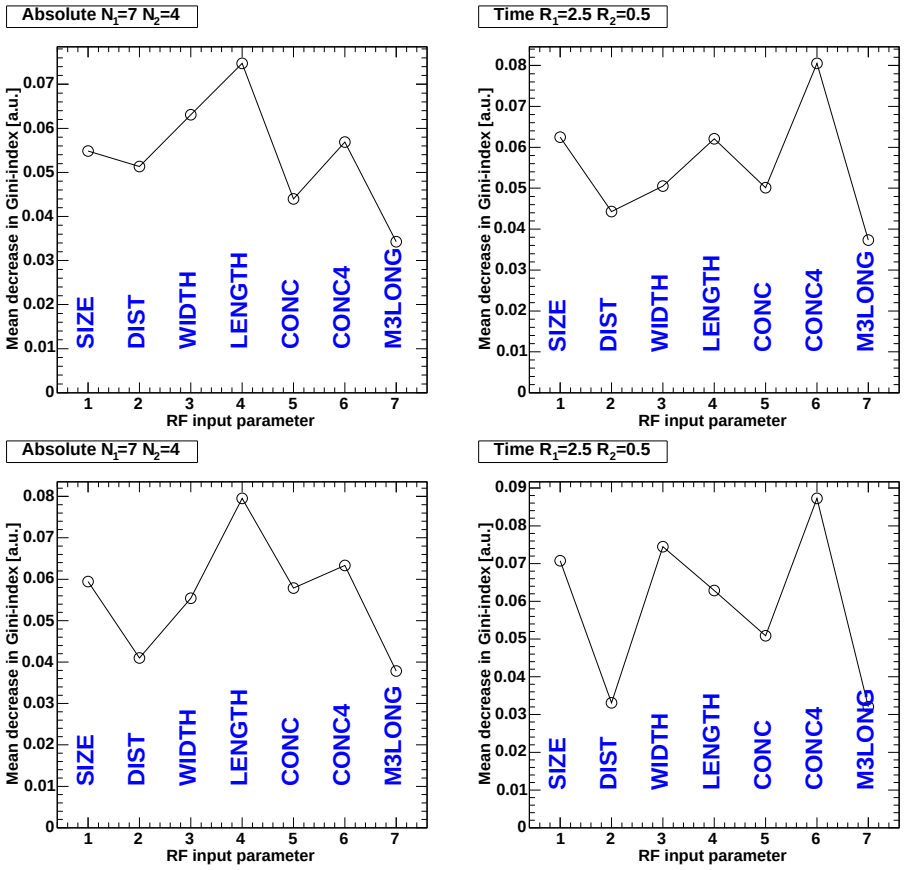

Figure 172: Mean decrease in Gini index for every parameter used in the Random Forest training of the GRB050713a data. The values are proportional to the relative importance of the parameter in the rejection of the background. Top: Training with standard simulated gamma showers, bottom: training with simulated gamma showers and a worse PSF. Left: absolute cleaning, right: time cleaning.

8.8 Test of Cut Parameters

One often raised, major objection to the random forest method, concerns the question of reliability regarding systematic differences between simulation and real data: How can one be sure that the algorithm separates gamma showers from hadronic ones instead of shortcomings of the experimental data from the simulated detector under ideal conditions? One possible test of the above objection consists in comparing the distributions of real-data gamma showers with the simulated ones. In order to do so, a well-separated gamma sample was created from the Mrk501 data using the following test cuts:

$$
\begin{aligned}
ISLANDS &< 2 \\
LEAKAGE &< 0.005 \\
0.45^\circ &< DIST < 0.78^\circ \\
SIZE &> 90 \text{ phe} \\
120 \text{ GeV} &< ENERGY < 200 \text{ GeV} \\
HADRONNESS &< 0.08 \quad \text{for absolute cleanings} \\
HADRONNESS &< 0.2 \quad \text{for time cleaning} \\
|ALPHA| &< 10^\circ \quad \text{for absolute cleanings} \\
|ALPHA| &< 15^\circ \quad \text{for time cleaning}
\end{aligned}
$$

These choices provide us with gamma samples at rather low energy, contaminated by less than 15% hadrons. After applying these cuts, the distributions of those variables which were used in the random forest training, were plotted for MC simulated gamma showers, ON data and OFF data and a ***Kolmogorov-Smirnov*** (***KS***) test was applied between the simulated gamma distribution and the ON data distribution, subtracted by the OFF data distribution.

Figures 173 to 178 show the results of all parameters. Within the limited statistics which provide this sample, all distributions agree well, i.e. the KS probability is larger than 10%, except for the variables *CONC* and *CONC4*. in combination with the absolute image cleaning (Prob KS $< 0.1\%$ and $< 1.8\%$ for *CONC* and *CONC4*, respectively). The time cleaning shows also low, but still acceptable probabilities for these parameters (Prob KS = 3% for *CONC* and <1.7% for *CONC4*). Table 26 lists all obtained KS probabilities.

Based on these results, some caution should be used dealing with the results of absolute cleaning, whereas the time algorithm gives still statistically acceptable results.

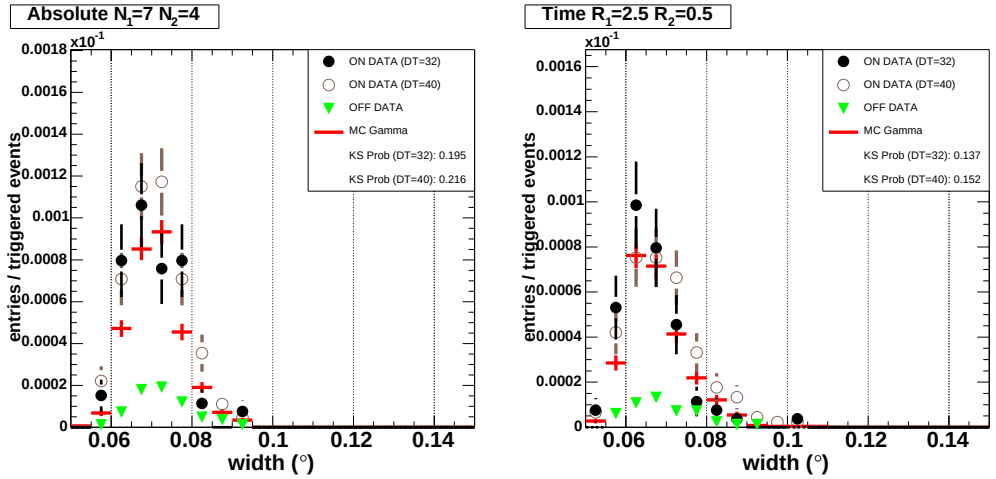

Figure 173: Normalized distributions of WIDTH for the gamma-enriched Mrk501 data sample. Left: absolute cleaning, right: time cleaning.

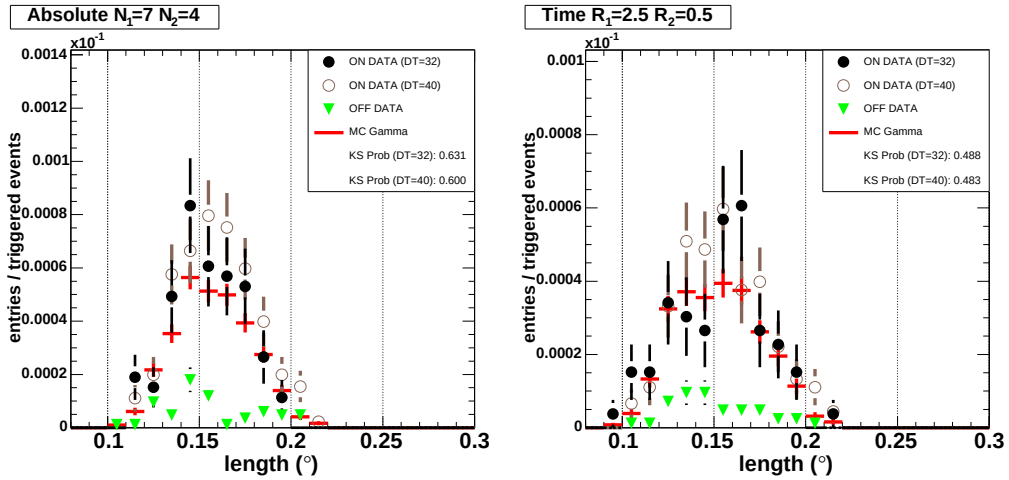

Figure 174: Normalized distributions LENGTH for the gamma-enriched Mrk501 data sample. Left: absolute cleaning, right: time cleaning.

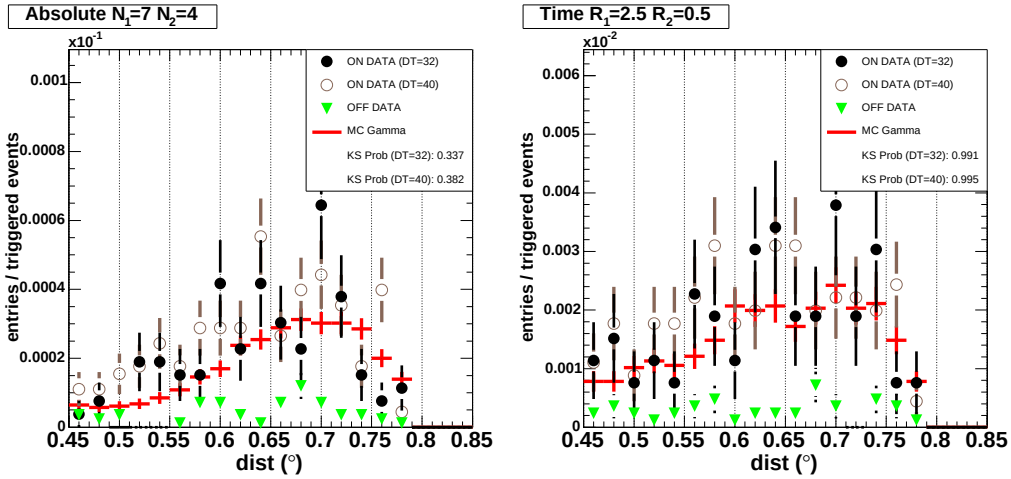

Figure 175: Normalized distributions of DIST for the gamma-enriched Mrk501 data sample. Left: absolute cleaning, right: time cleaning.

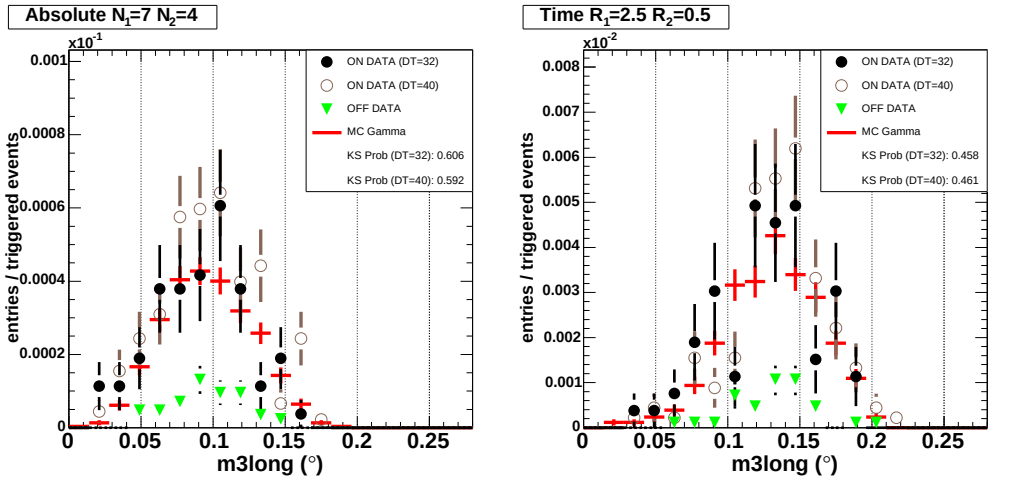

Figure 176: Normalized distributions of M3LONG for the gamma-enriched Mrk501 data sample. Left: absolute cleaning, right: time cleaning.

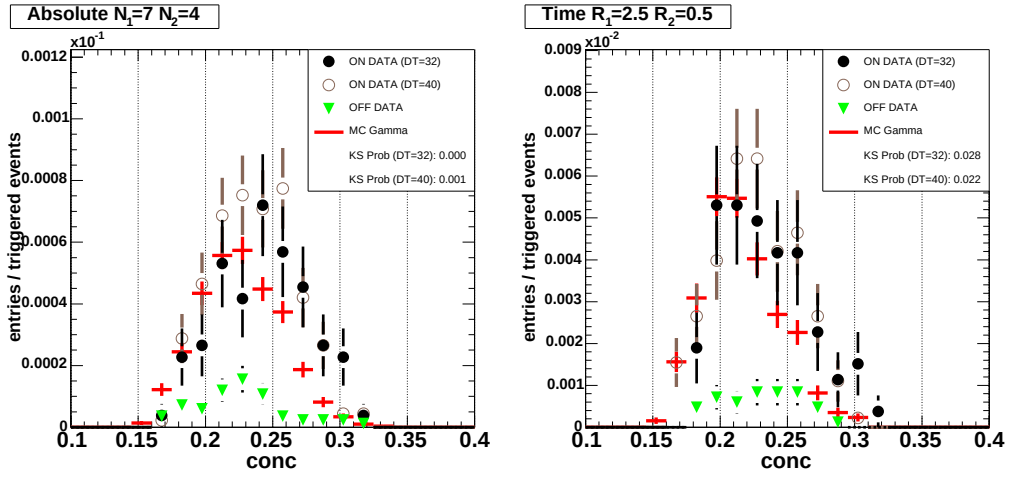

Figure 177: Normalized distributions of CONC for the gamma-enriched Mrk501 data sample. Left: absolute cleaning, right: time cleaning.

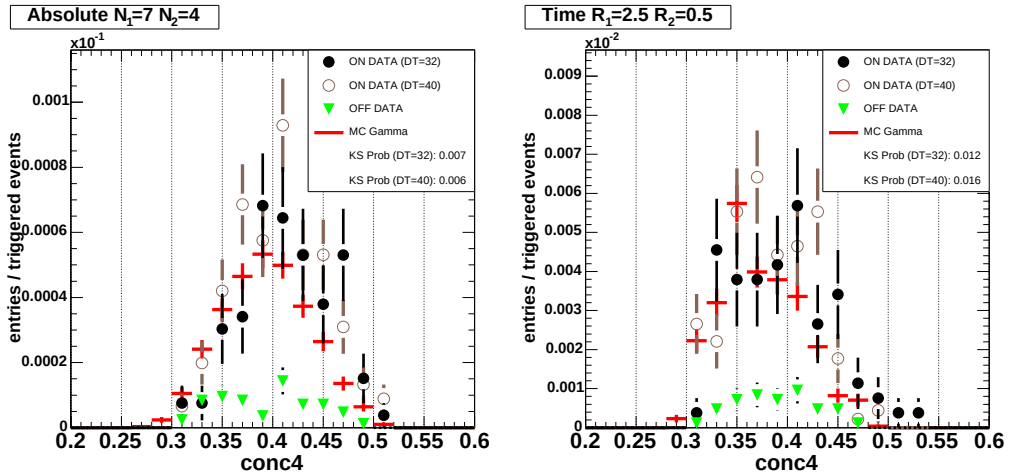

Figure 178: Normalized distributions of CONC4 for the gamma-enriched Mrk501 data sample. Left: absolute cleaning, right: time cleaning.

KS Test Probabilities				
parameter	absolute cleaning		time cleaning	
	DT=32	DT=40	DT=32	DT=40
WIDTH	0.20	0.22	0.14	0.15
LENGTH	0.63	0.60	0.49	0.48
DIST	0.34	0.38	0.99	1.00
M3LONG	0.61	0.59	0.49	0.46
CONC	0.000	0.001	0.03	0.02
CONC4	0.01	0.01	0.01	0.02

Table 26: Kolmogorov-Smirnov test probabilities for the parameters used to train the HADRONNESS calculation.

8.9 Rates with Increasing Cut Strength

With the calculated *HADRONNESS* values, a first look at the GRB050713a ON data event rates can be held, applying increasingly strong cuts on *HADRONNESS* and a fixed cut on the absolute value of *ALPHA*:

$$\begin{aligned} HADRONNESS &< \{0.9\,,\,0.5\,,\,0.2\,,\,0.15\,,\,0.1\} \\ |ALPHA| &< 30^\circ \end{aligned}$$

If there were gamma ray emission peaks within the observed time windows, structures in the event rate should show put gradually with increasing purity of the sample. Figure 179 shows these rates for the absolute and the time cleaning. One can observe a gradual decrease in event rate for both image cleanings, but further no persistent features can be discerned – except for the 22 seconds of data taking stop at 10.5 minutes (see section 8.1). Another interesting observation can be made in figure 179: While at low values of *HADRONNESS*, the event rates are higher for the absolute cleaned data, from values of $HADRONNESS = 0.15$ on, the trend is inverted and higher event rates for the time cleaned data appear. This points already to a higher gamma and lower hadron efficiency of the time cleaning and is consistent with the global cut efficiencies found in table 24.

8.10 Energy Reconstruction

The shower energy was reconstructed using the prescription of section 7.5. A dedicated ***random forest*** matrix was trained to recognize the energy of an event, based on the same parameters as those used for the *HADRONNESS* calculation (section 8.7), plus the zenith angle information.

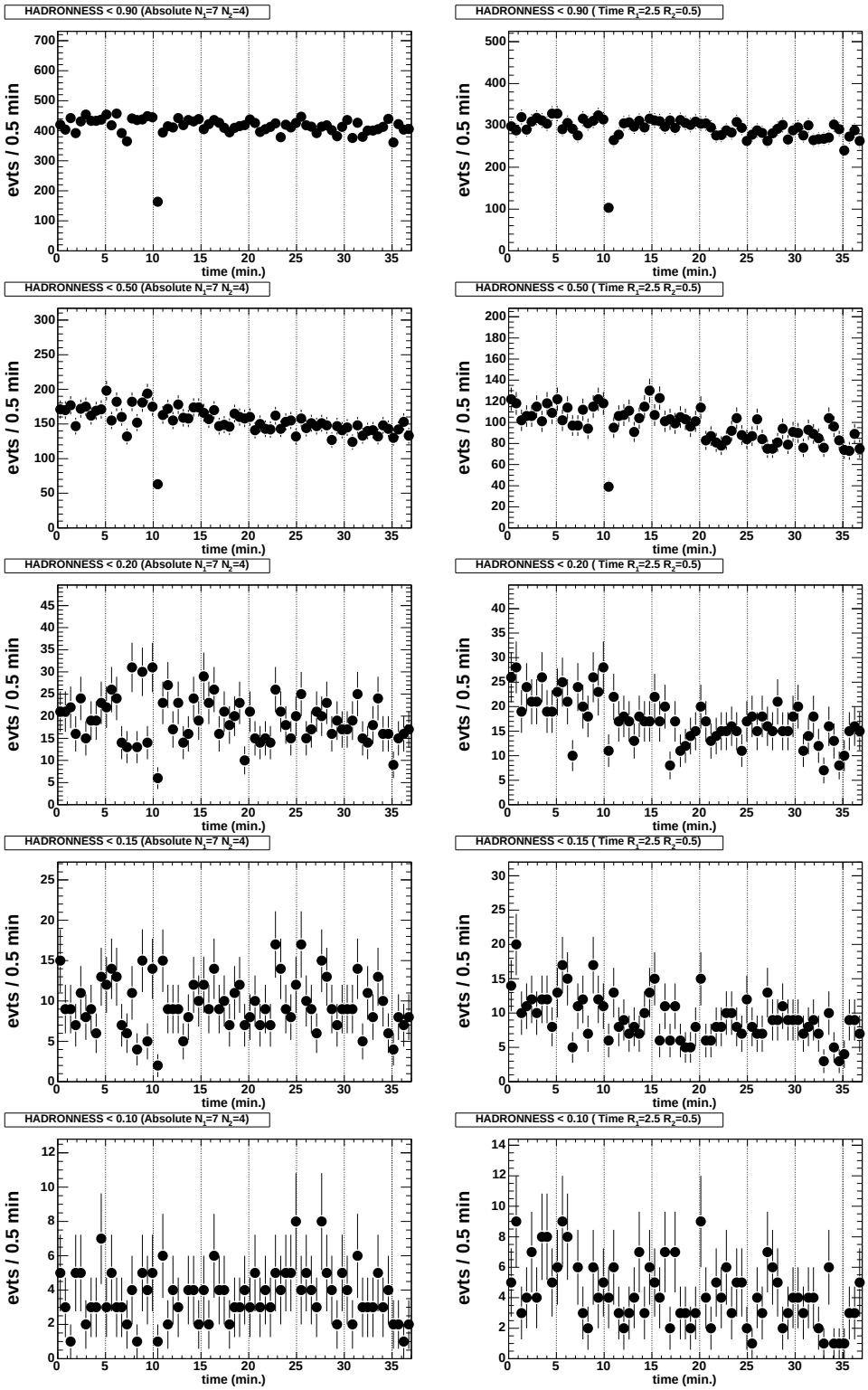

Figure 179: Event rates with increasing cut strength in HADRONNESS, shown in bins of 30 seconds. Left: absolute cleaning, right: time cleaning.

Precision and bias of the reconstructed energy can be estimated from figure 180 where the reconstructed vs. true simulated energy is plotted, for both simulations using different PSFs. In the obtained energy ranges after cuts, no bias of the energy reconstruction is seen, at least not for simulated showers. A closer look into two bins of reconstructed energy (figure 181) reveals that a degradation of the energy resolution due to the use of the worse PSF is present, but almost negligible. Energy resolutions of about 30% from 100 GeV to 200 GeV and about 25% from 200 GeV to 500 GeV are obtained if the time image cleaning is used.

8.11 Cut Optimization

Various attempts were made at this point to find combinations of cuts which allow to lower the energy threshold to a minimum. The experience showed however that results could vary quite considerably for image sizes below 90 photo-electrons where the analysis lost stability. In this case, any choice for combinations of cuts become very subjective and necessarily introduces a ***bias***. Moreover, inspection of events with sizes between 60 and 90 photo-electrons revealed a widening of the *ALPHA*-distributions such that typical *ALPHA*-plots lost plausibility, even if the significances might have risen somewhat.

As the aim of this study was to obtain an ***un-biased*** reduction of the energy threshold, a further *SIZE*-cut seemed appropriate:

$$SIZE > 90 \text{ phe} , \tag{149}$$

followed by the automatic (un-biased) cut determination algorithm outlined in chapter 7.6.

One more cut had to be set on the *DIST* parameter. Figure 182 shows the distribution of *DIST*, plotted against the parameter $|ALPHA|$, for the two data sets obtained from the two image cleaning algorithms. One can see that unfortunately, a structured *ALPHA*-distribution is obtained for real data above $DIST \approx 0.8$. This is most probably a geometrical effect, since the transition region from active trigger region to the outer passive parts of the camera is found there. What is worse: the structures appear slightly different between the ON and OFF data samples. In order to obtain data samples un-affected by this effect, a stricter cut on *DIST* was therefore applied:

$$\begin{aligned} 0.45^\circ &< DIST < 0.78^\circ \quad \text{(Mrk501 data)} \\ 0.42^\circ &< DIST < 0.75^\circ \quad \text{(GRB050713a data)} \end{aligned}$$

The difference in both limits are due to the zenith angles at which both sources were observed which cause the distributions of *DIST* to shift slightly.

Figure 183 shows distributions of the *HADRONNESS* parameter for the GRB050713a data and the four analysis branches obtained so far. One can observe an acceptable overall agreement between ON and OFF data and a better separability between

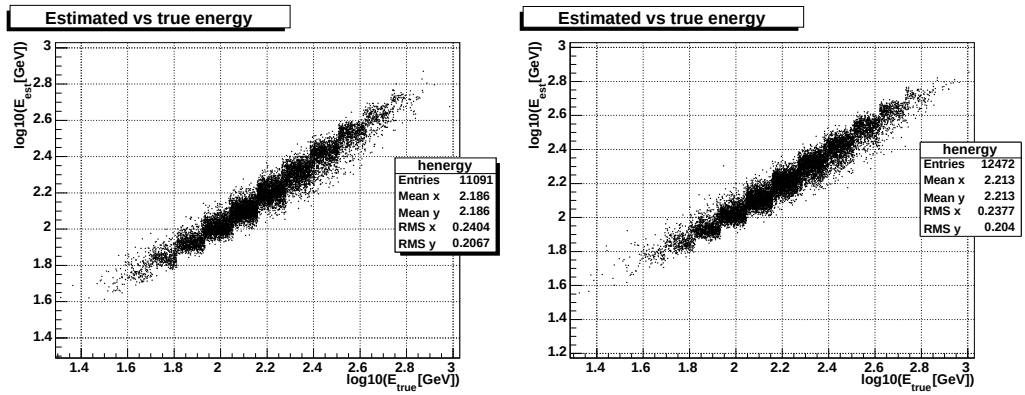

Figure 180: Reconstructed vs. true simulated energy. Left: Simulated PSF of $0.05^\circ\sigma$*, right: PSF=* $0.07^\circ\sigma$*.*

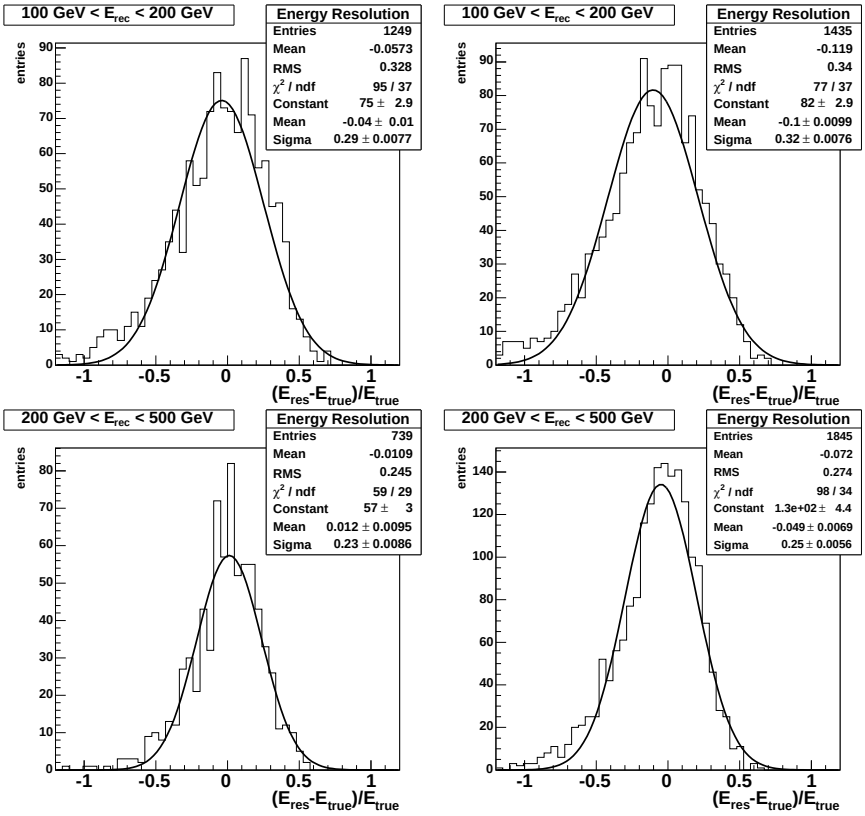

Figure 181: Distributions of the relative energy reconstruction error $(E_{rec} - E_{true})/E_{true}$ *for simulated gamma showers, cleaned with the time cleaning and final cuts applied. Left: Simulated PSF of* $0.05^\circ\sigma$*, right: PSF=* $0.07^\circ\sigma$*. Top: energy bin* $100\,\mathrm{GeV} < E_{rec} < 200\,\mathrm{GeV}$*, bottom:* $200\,\mathrm{GeV} < E_{rec} < 500\,\mathrm{GeV}$*.*

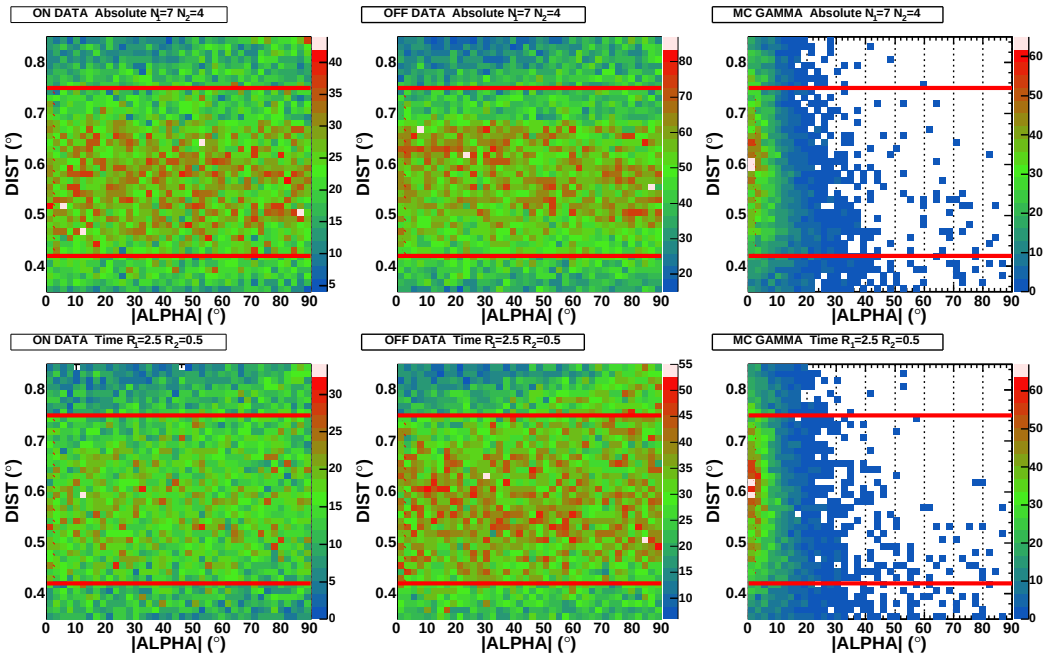

Figure 182: Distributions of the parameters DIST vs. the absolute value of ALPHA for the GRB050713a data and further final cuts applied. Top: absolute cleaning, bottom: time cleaning. The red lines indicate the final cuts on DIST.

the gamma- and hadron- samples if the time image cleaning was used. Strangely, the same hold for the gamma showers simulated with the ***worse*** PSF. Although in agreement with the findings of table 24, this behaviour is counter-intuitive and not yet understood. It might be that at low energies, a dilution of the showers leads to better reconstructability because of the discreteness of the grid formed by the pixel camera. This hypothesis can only be investigated with MC simulations of cameras with different photomultiplier sizes, though. Certainly, in the design phase of the MAGIC camera, no time information was ever used in the optimization procedure for the camera parameters. As we will see later, the effect of the simulated PSF on the upper limits is small though, and the small curiosity found here was further not followed up.

From here on, the analysis was split in bins of reconstructed energy ($ENERGY$). For the Mrk501 data, the following bins were chosen:

1. 45 GeV $<$ $ENERGY$ $<$ 75 GeV
2. 60 GeV $<$ $ENERGY$ $<$ 100 GeV
3. 100 GeV $<$ $ENERGY$ $<$ 150 GeV
4. 150 GeV $<$ $ENERGY$ $<$ 300 GeV

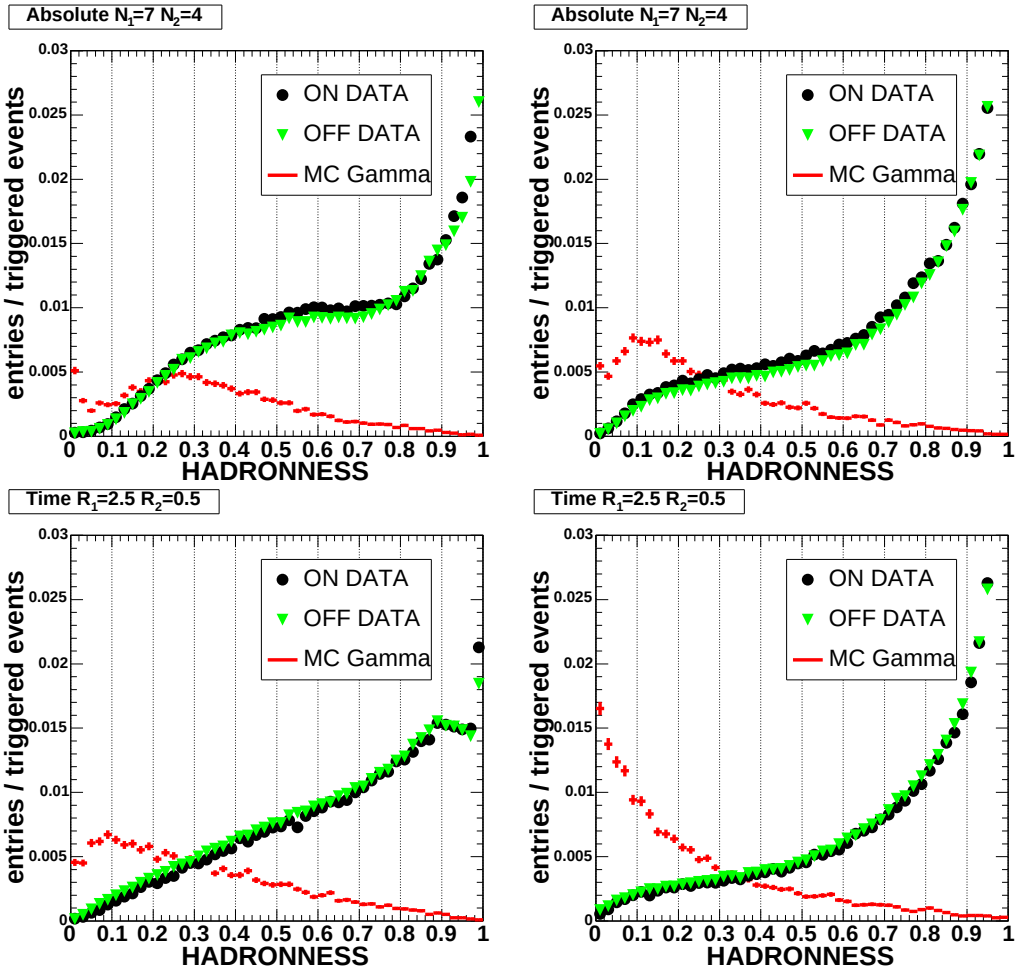

Figure 183: Distributions of HADRONNESS for the GRB050713a data. Top: absolute cleaning, bottom: time cleaning. Left: using simulated gamma showers with PSF = 0.05°σ, right: PSF = 0.07°σ. All other final cuts (except for ALPHA) had been applied to the data before.

Energy bins nr. 2–4 correspond to consecutive bins containing more or less the same number of events while bin nr. 1 is an attempt to push the energy limit to the minimum.

The GRB050713a data was analyzed in two bins:

1. 100 GeV $<$ *ENERGY* $<$ 200 GeV
2. 200 GeV $<$ *ENERGY* $<$ 500 GeV

Below 100 GeV and above 500 GeV, no event survived the *SIZE* cut of the previous data reduction steps, the two bins cover thus the entire data sample.

In the following, the cut on *HADRONNESS* was chosen according to the procedure outlined in section 7.4. Figure 184 gives an example of the obtained test significances, depending on cut value of the *HADRONNESS* parameter. With this procedure, individual cut values on *HADRONNESS* and *ALPHA* were obtained for every bin in *ENERGY*, and each data set obtained from the two image cleaning algorithms. Moreover by construction, the procedure yields cut values depending on the effective ON time of the ON data sample.

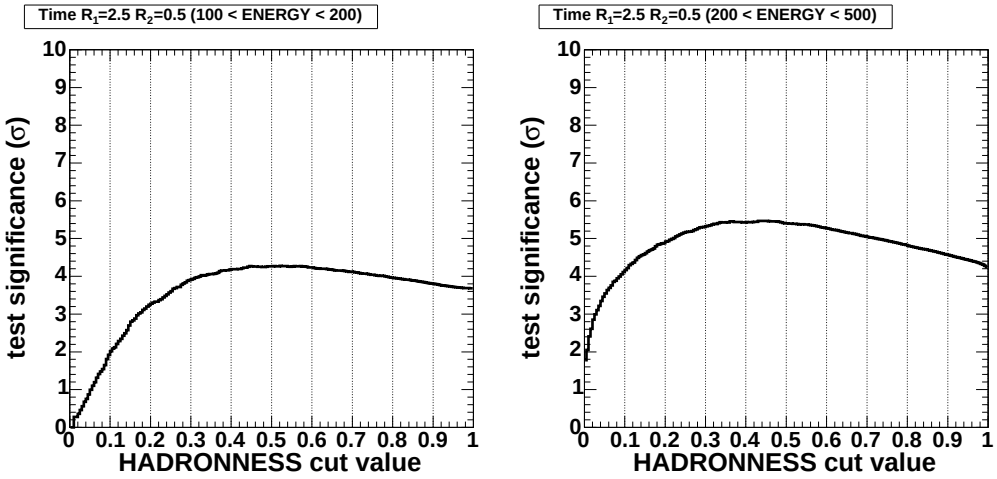

Figure 184: Test significances for a simulated gamma-ray signal and GRB050713a OFF data, for different cuts in HADRONNESS. Left: 100 to 200 GeV reconstructed energy, right: 200 to 500 GeV.

8.12 Results Mrk501 Test Data

Figures 185 and 186 show the *ALPHA*-plots of the different reconstructed energy bins with the calculated significances from ON and OFF data. Table 27 lists all cut values and results obtained from the automatic procedure. In general, the time image cleaning yields tighter cuts both on *ALPHA* as on *HADRONNESS*, except for the highest energy bin. At energies above 100 GeV, the two image cleaning algorithms

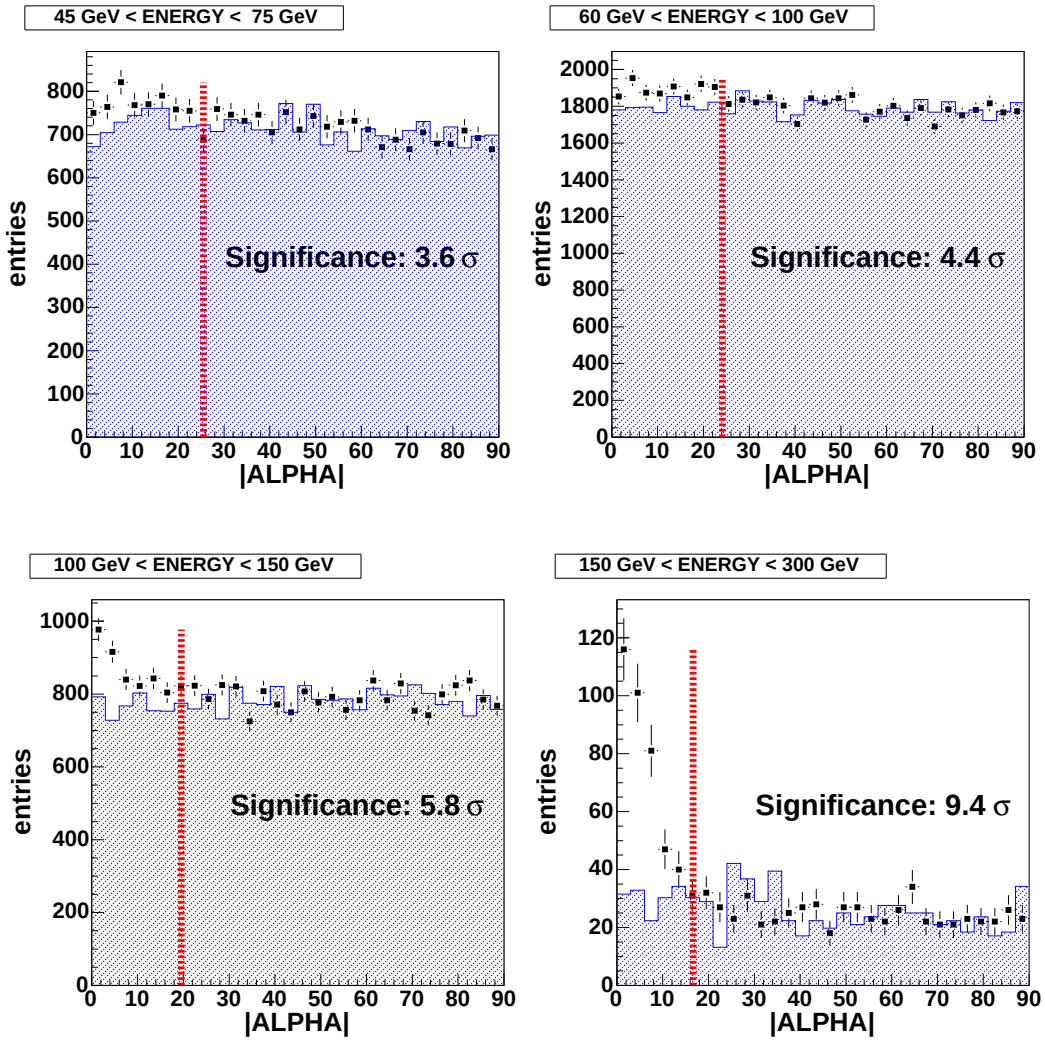

*Figure 185: Distributions of the absolute value of ALPHA for the Mrk501 data, obtained with the **absolute cleaning**. The four plots correspond to bins of reconstructed energy: 45 to 75 GeV, 60 to 100 GeV, 100 to 150 GeV and 150 to 300 GeV. The red line limits the region within which the significance was calculated and was determined beforehand by MC simulations of gamma showers.*

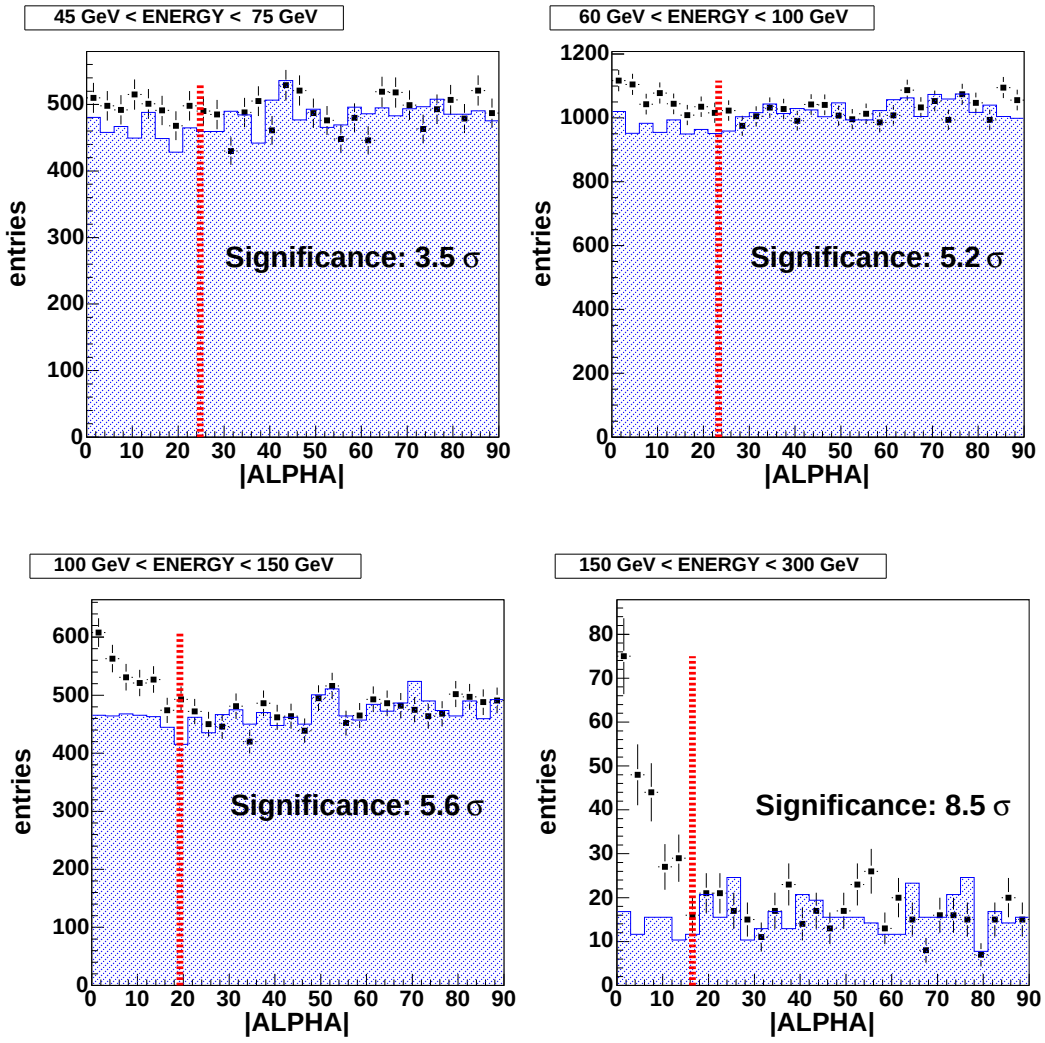

*Figure 186: Distributions of the absolute value of ALPHA for the Mrk501 data, obtained with the **time cleaning**. The four plots correspond to bins of reconstructed energy: 45 to 75 GeV, 60 to 100 GeV, 100 to 150 GeV and 150 to 300 GeV. The red line limits the region within which the significance was calculated and was determined beforehand by MC simulations of gamma showers.*

yield equivalent results, with slightly better efficiency obtained with the absolute cleaning, whereas below 100 GeV, the time cleaning algorithms yields slightly better significances. This is expected since the time cleaning works with lower signal thresholds and accepts thus more low-energetic showers. On the other side, the edges of the well-defined energetic showers are washed out and produce then less well-defined ellipses. This result has been confirmed by other groups working with data taken at low zenith angles.

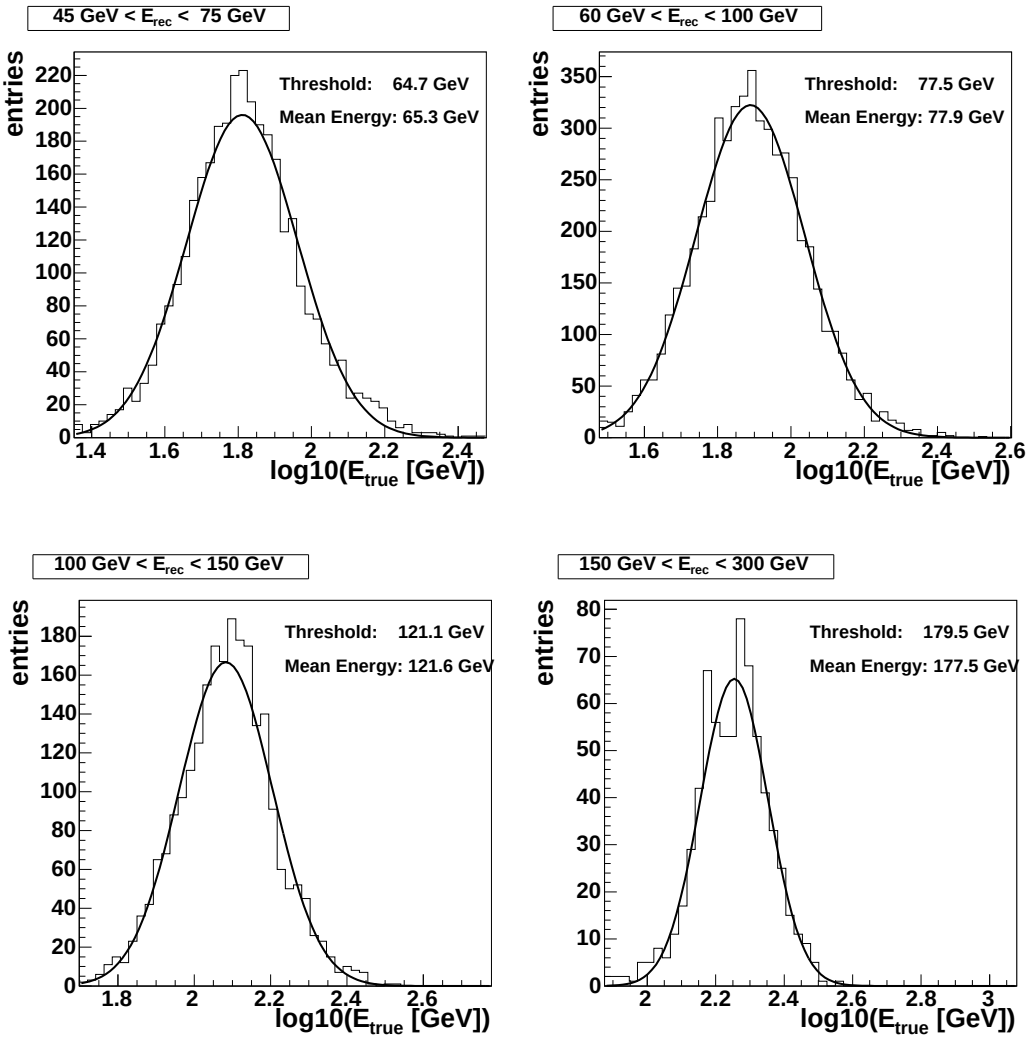

Figure 187: Distributions of simulated MC energy for the Mrk501 data, obtained with the time image cleaning and all cuts applied. The four plots correspond to bins of reconstructed energy: 45 to 75 GeV, 60 to 100 GeV, 100 to 150 GeV and 150 to 300 GeV.

Figure 187 shows the distribution of the simulated gamma shower energies for the four bins in reconstructed energy, exemplary for the time image cleaning. One can

Image Cleaning Method	Reconst. Energy Range (GeV)	cut *HADR.-NESS*	cut *ALPHA* (°)	Number Excess Events	Sign. Li Ma	mean energy MC (GeV)
Absolute	45 - 75	0.69	26	375 ± 104	3.6	68
	60 - 100	0.70	24	744 ± 170	4.4	80
	100 - 150	0.61	20	603 ± 103	5.8	120
	150 - 300	0.30	17	234 ± 24	9.4	178
Time	45 - 75	0.55	25	287 ± 82	3.5	65
	60 - 100	0.58	23	614 ± 117	5.2	78
	100 - 150	0.56	19	453 ± 80	5.6	122
	150 - 300	0.34	16	153 ± 18	8.5	177

Table 27: Results from the Mrk501 data.

see that a mean energy of 65 GeV is obtained in the lowest energy bin, marginally detected with $3.5\,\sigma$. However, the signal in the subsequent bin is detected significantly well above $5\,\sigma$ at a mean energy of 78 GeV. It is important to realize that all numbers on Mrk501 can be improved easily if the OFF data statistics is increased, data is abundantly available since the telescope conditions did not change during the entire June and the beginning of July, 2005. This test analysis serves uniquely to demonstrate that if there is a strong enough gamma-ray signal, the analysis presented here is able to detect it.

The significant detection of Mrk501 below 100 GeV allows to extend its spectrum to energies below 60 GeV, as shown in figure 188. As the reason for this test analysis is to demonstrate the power of this analysis instead of producing physics results on Mrk501, no further interpretation of that spectrum will be given here. As no unfolding has been performed, it has to be taken with some care anyhow.

Concluding this section, it has been shown that this analysis is able to extract a significant signal well below 100 GeV from one hour of Mrk501 flare data, with an energy threshold of less than 80 GeV. A possible spectrum can even be extended down to 50 GeV. According to relation 8 connecting energy threshold with observational zenith angle, a threshold of less than 200 GeV is thus expected for the GRB050713a data, taken at 49° zenith angle.

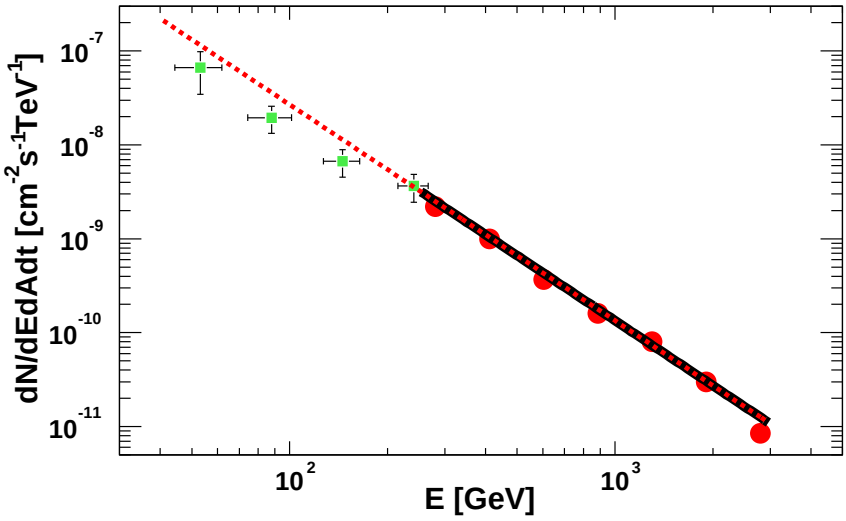

Figure 188: Extended spectrum of Mrk501 in flaring state. The red points show the result of the standard analysis, with spectral fit (black line), while the green markers show the extended spectrum below 60 GeV. No unfolding has been performed, apart from a spill-over correction.

8.13 Results GRB050713a Data

The GRB050713a data was analyzed in four ways:

1. Taking the first 90 s of observation which correspond to the prompt emission phases of the BAT instrument on SWIFT, and the remaining six runs (starting at about 7.7 min after start) as OFF data.
2. Taking the first three runs (about 1000 seconds) as ON data and the rest as OFF data.
3. Taking the entire ON data sample and the OFF data from two days later.
4. Searching in time bins of 100 s ON data, using the data outside the corresponding time bin as OFF data.

After applying all the previously explained analysis steps, none of these four searches showed a significant excess over background. For this reason, upper limits were placed starting from the observed number of excess events and the number of background events in the signal region of the *ALPHA* distribution. In order to determine the 95% CL upper limit on the number of events in each energy bin, the prescriptions of Feldman and Cousins [263] and Rolke et al. [265] were used (see section 7.8.1). Thereby, an overall efficiency of 90% was assumed and a systematic uncertainty of 27% (see explanations in a later section 8.16).

In order to convert the limits on the number of excess events to fluxes and fluences

(see section 7.8.2), the following representative test spectra were tried:

$$\begin{aligned} \frac{dN_\gamma}{dE\,dA\,dt} &= f_0 \cdot \big(\frac{E}{E_0}\big)^{-\alpha} \\ \frac{dN_\gamma}{dE\,dA\,dt} &= f_0 \cdot \big(\frac{E}{E_0}\big)^{-2.5} \cdot \exp\big(-\frac{E-E_0}{E_b}\big)\ , \end{aligned} \tag{150}$$

where E_0 is the mean energy at which the limit is calculated and α one of the test spectral indices:

$$\alpha = \{1.0\,,\ 2.0\,,\ 2.25\,,\ 2.5\,,\ 3.0\}\ . \tag{151}$$

The second function simulates an exponential cut-off with a break energy at $E_b = 200\,\mathrm{GeV}$.

8.13.1 Prompt Emission Phase

After determining the cuts on *HADRONNESS* and *ALPHA*, energy thresholds around 160 GeV (for the lower bin in reconstructed energy) and 280 GeV (for the upper bin) were obtained (see figure 189).

Figure 190 shows the resulting *ALPHA* plots in the two bins of reconstructed energy and the retrieved significances. No signal is observed in neither of the two energy bins.

The results of the analysis on the prompt emission phase are summarized in table 28. The obtained significances vary around zero, reaching once $-2.8\,\sigma$. Like in the case of the Mrk501 data, the time image cleaning yields the lowest threshold.

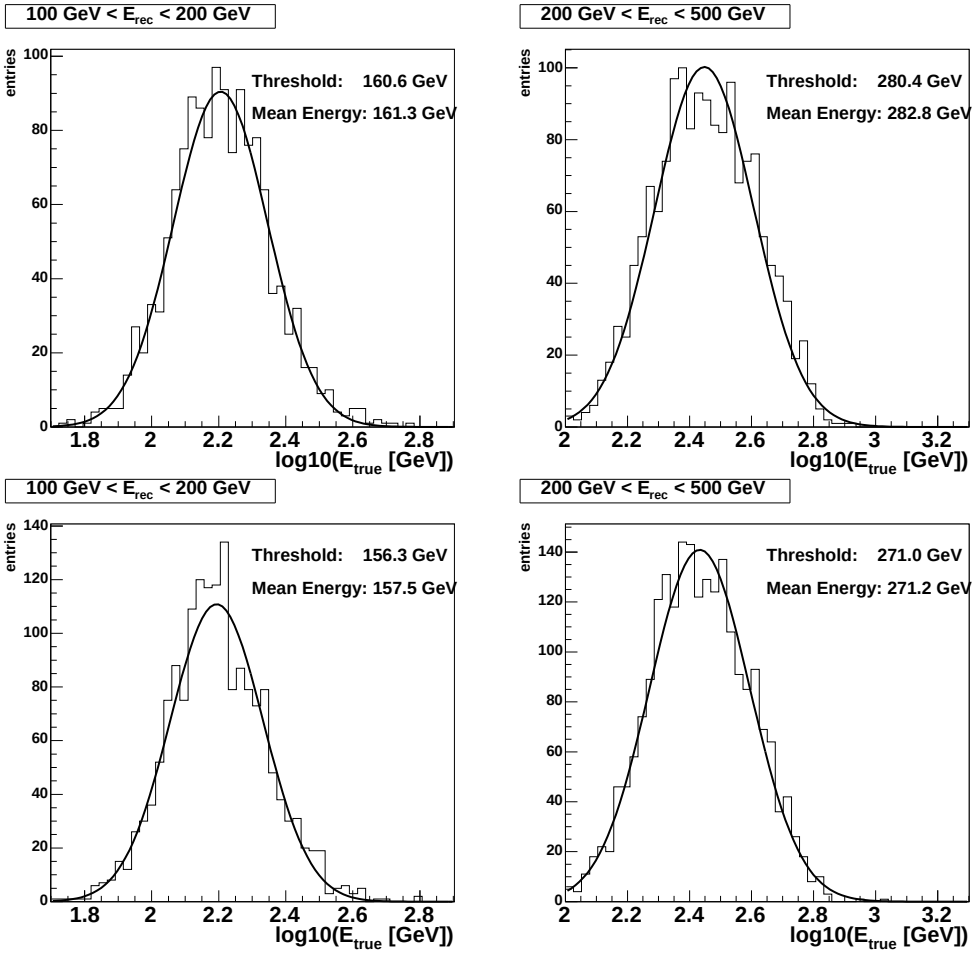

Figure 189: Distributions of simulated MC energy for the GRB050713a data, obtained with the time image cleaning and all cuts applied. Left: 100 to 200 GeV, right: 200 to 500 GeV reconstructed energy; Top: $PSF = 0.05^{\circ}\sigma$, bottom: $PSF = 0.07^{\circ}\sigma$.

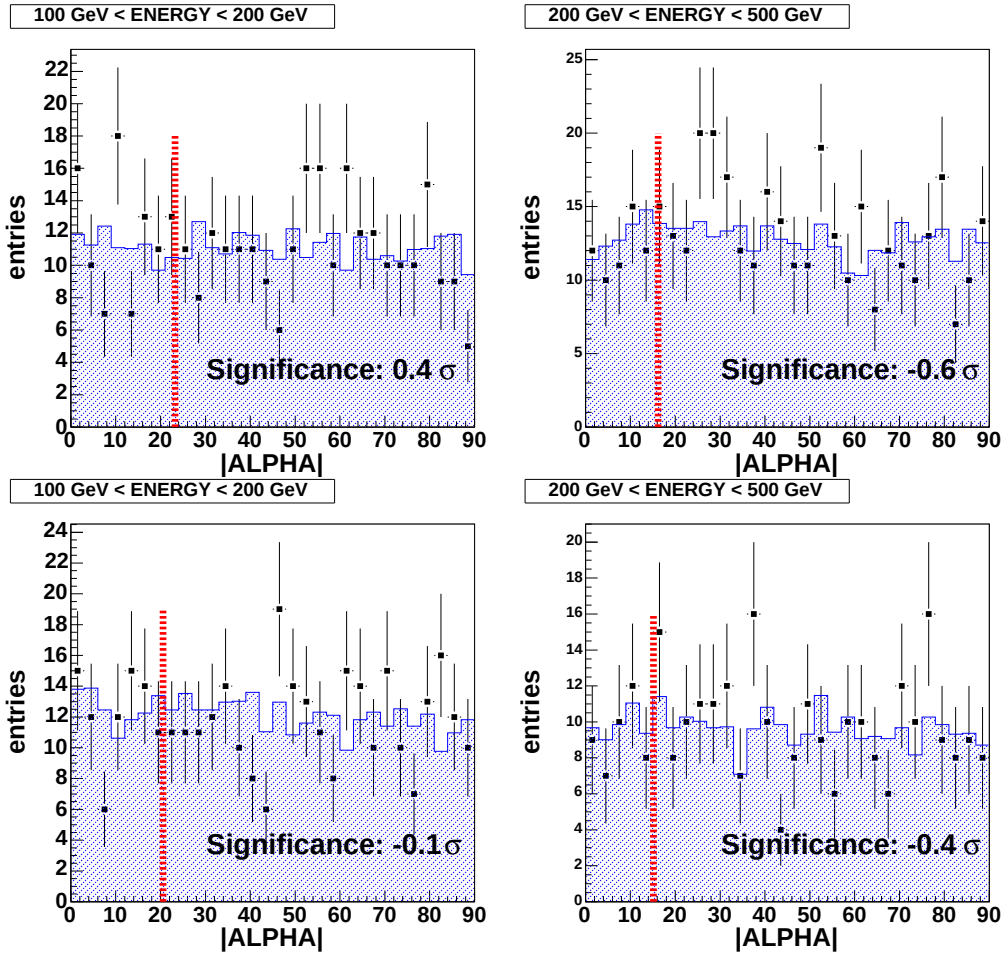

Figure 190: Distributions of ALPHA for the 90 seconds of the prompt emission. Left: 100 to 200 GeV and right: 200 to 500 GeV reconstructed energy; Top: absolute cleaning, bottom: time cleaning. The red line limits the region within which the significance was calculated and was determined beforehand by MC simulations of gamma showers.

Image Cleaning Method	Energy Range (GeV) (1)	cut *HADR.-NESS* (2)	cut *ALPHA* (°) (3)	Evts ON (4)	Evts OFF (5)	Ex-cess (6)	Sign. Li Ma (7)	U.L. F.C. (95% CL) (8)	U.L. Rolke (95% CL) (9)	Mean E_γ (GeV) (10)
Absolute	100 - 200	0.59	23	82	78.8	3	0.4	22.6	69.3	173
(PSF= 0.05°σ)	200 - 500	0.47	16	60	65.0	-5	-0.6	12.3	23.6	288
Absolute	100 - 200	0.49	30	38	34.7	3	0.5	17.1		170
(PSF= 0.07°σ)	200 - 500	0.44	19	58	82.4	-24	-2.8	4.1		274
Time	100 - 200	0.60	21	74	74.8	-1	-0.1	17.5	40.6	161
(PSF= 0.05°σ)	200 - 500	0.49	15	46	49.0	-3	-0.4	12.1	24.2	283
Time	100 - 200	0.42	26	33	42.5	-9	-1.4	5.8		158
(PSF= 0.07°σ)	200 - 500	0.40	18	52	49.0	3	0.4	18.8		271

*Table 28: Results of ALPHA-analysis for GRB050713a Prompt Emission Data: 1) Reconstructed energy 2) Obtained with the procedure outlined in section 7.6 3) Obtained from a Gaussian fit to the distribution of ALPHA from MC simulated gamma events. The cut is chosen at 2.5σ of the Gaussian (see section 7.6). 4) Remaining ON data events after cuts in range $0 < ALPHA < ALPHA_{cut}$. 5) Remaining OFF data events after cuts in range $0 < ALPHA < ALPHA_{cut}$, normalized to number of events ON data in range $30 < ALPHA < 90$. 6) Rounded number of excess events: $N_{ON} - \kappa \cdot N_{OFF}$. For the upper limits, the non-rounded numbers have been used. 7) Significance, calculated with Li and Ma [261], formula 17 8) Upper limit on excess events, calculated after the prescription of Feldman and Cousins [263] 9) Upper limit on excess events, calculated after the prescription of Rolke et al. [265], assuming a mean efficiency of 95% and an uncertainty on the efficiency of 57%. 10) Mean simulated γ-energy, all cuts applied *) Upper limit calculated with the prescription of Helene [262], instead of Feldman-Cousins [263].*

8.13.2 First 1000 Seconds

Figure 191 shows the *ALPHA*-plots, obtained from the serach in the first 1000 seconds of GRB050713a observation. Again, no signal can be seen in neither of the two energy bins.

Table 29 summarizes all results of the analysis on the first 1000 seconds observation data. As before, the obtained significances vary around zero, not exceeding $\pm 1\sigma$.

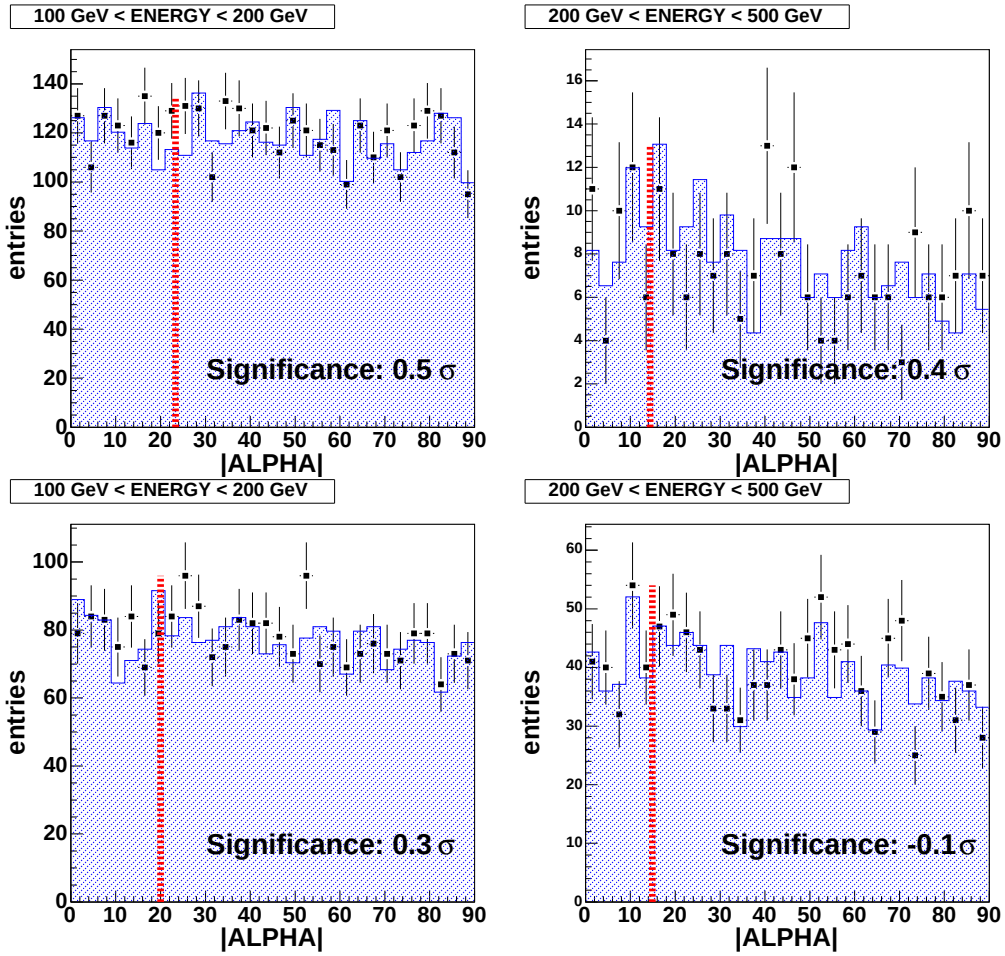

Figure 191: Distributions of the parameter ALPHA for first 1000 s of GRB050713a observation. Left: 100 to 200 GeV and right: 200 to 500 GeV reconstructed energy. Top: absolute cleaning, bottom: time cleaning. The red line limits the region within which the significance was calculated and was determined beforehand by MC simulations of gamma showers.

Image Cleaning Method	Energy Range (GeV) (1)	cut *HADR.-NESS* (2)	cut *ALPHA* (°) (3)	Evts ON (4)	Evts OFF (5)	Ex-cess (6)	Sign. Li Ma (7)	U.L. F.C. (95% CL) (8)	U.L. Rolke (95% CL) (9)	Mean E_γ (GeV) (10)
Absolute	100 - 200	0.56	23	854	836.3	18	0.5	84.7*	120.2	174
(PSF= 0.05°σ)	200 - 500	0.11	14	37	34.3	3	0.4	16.1	23.7	352
Time	100 - 200	0.46	20	474	465.9	8	0.3	60.4*	82.9	162
(PSF= 0.05°σ)	200 - 500	0.29	15	167	167.8	-1	-0.1	31.1*	39.7	293

*Table 29: Results ALPHA-analysis for GRB050713a Data, First Three Runs: 1) Reconstructed energy 2) Obtained with the procedure outline in section 7.6 3) Obtained from a Gaussian fit to the distribution of ALPHA from MC simulated gamma events. The cut is chosen at 2.5σ of the Gaussian (see section 7.6). 4) Remaining ON data events after cuts in range $0 < ALPHA < ALPHA_{cut}$. 5) Remaining OFF data events after cuts in range $0 < ALPHA < ALPHA_{cut}$, normalized to number of events ON data in range $30 < ALPHA < 90$. 6) Rounded number of excess events: $N_{ON} - \kappa \cdot N_{OFF}$. For the upper limits, the non-rounded numbers have been used. 7) Significance, calculated with Li and Ma [261], formula 17 8) Upper limit on excess events, calculated after the prescription of Feldman and Cousins [263] 9) Upper limit on excess events, calculated after the prescription of Rolke et al. [265], assuming a mean efficiency of 95% and an uncertainty on the efficiency of 27%. 10) Mean simulated γ-energy, all cuts applied *) Upper limit calculated with the prescription of Helene [262], instead of Feldman-Cousins [263].*

8.13.3 Entire Data Sample

The resulting *ALPHA*-plots of the search in the entire data sample are shown in figure 192 and results summarized in table 30. The obtained significances seem to be slightly shifted towards positive values, although not with sufficient significance. In one case, on excess of $1.7\,\sigma$ significance was found, which can be considered a statistical fluctuation. These plots and the following tables have to be considered as possibly problematic due to the observed disagreements between ON and OFF data.

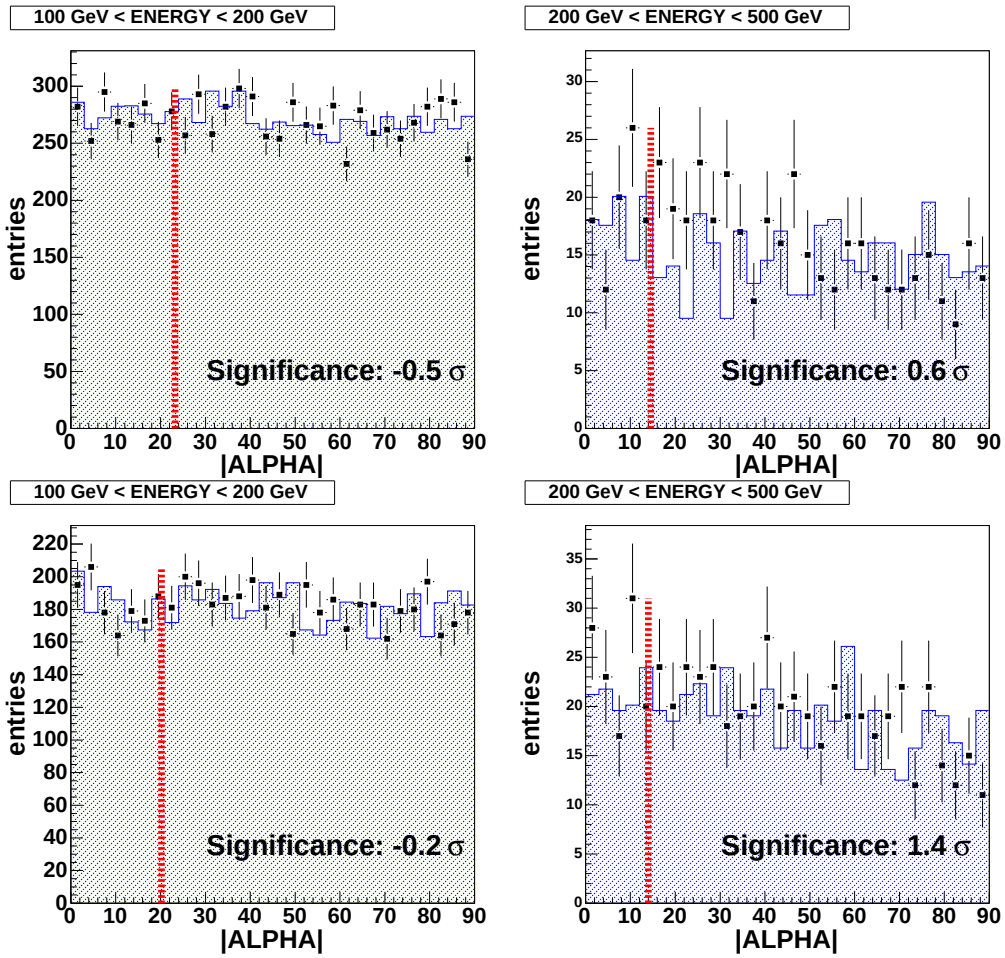

Figure 192: Distributions of ALPHA for the entire GRB050713a data set. Left: 100 to 200 GeV and right: 200 to 500 GeV reconstructed energy. Top: absolute cleaning, bottom: time cleaning.

Image Cleaning Method	Energy Range (GeV) (1)	cut *HADR.-NESS* (2)	cut *ALPHA* (°) (3)	Evts ON (4)	Evts OFF (5)	Ex-cess (6)	Sign. Li Ma (7)	U.L. F.C. (95% CL) (8)	U.L. Rolke (95% CL) (9)	Mean E_γ (GeV) (10)
Absolute	100 - 200	0.58	23	1902	1929.4	-27	-0.5	87.1*	97.9	173
(PSF= 0.05°σ)	200 - 500	0.11	15	76	70.2	6]	0.6	24.6	36.3	354
Time	100 - 200	0.51	20	1095	1101.4	-6	-0.2	74.1*	91.0	162
(PSF= 0.05°σ)	200 - 500	0.15	14	99	82.7	16	1.4	37.6	58.4	331

*Table 30: Results of ALPHA-analysis for Whole GRB050713a Data: 1) Reconstructed energy 2) Obtained with the procedure outline in section 7.6 3) Obtained from a Gaussian fit to the distribution of ALPHA from MC simulated gamma events. The cut is chosen at 2.5 σ of the Gaussian (see section 7.6). 4) Remaining ON data events after cuts in range $0 < ALPHA < ALPHA_{cut}$. 5) Remaining OFF data events after cuts in range $0 < ALPHA < ALPHA_{cut}$, normalized to number of events ON data in range $30 < ALPHA < 90$. 6) Rounded number of excess events: $N_{ON} - \kappa \cdot N_{OFF}$. For the upper limits, the non-rounded numbers have been used. 7) Significance, calculated with Li and Ma [261], formula 17 8) Upper limit on excess events, calculated after the prescription of Feldman and Cousins [263] 9) Upper limit on excess events, calculated after the prescription of Rolke et al. [265], assuming a mean efficiency of 95% and an uncertainty on the efficiency of 27%. 10) Mean simulated γ-energy, all cuts applied *) Upper limit calculated with the prescription of Helene [262], instead of Feldman-Cousins [263].*

8.14 Results Upper Limits

From the results of the previous sections, differential upper limits on f_0 were calculated for the test spectral indices:

$$\alpha = \{\, 1.0\,,\ 2.0\,,\ 2.25\,,\ 2.5\,,\ 3.0\,\}\ , \tag{152}$$

and a power-law spectrum with index $\alpha = 2.5$ with exponential cut-off. The simulated break energy was $E_b = 200\,\mathrm{GeV}$. This situation was thought to be the most probable scenario: A mean high-energy spectral index of $\alpha = 2.25$ (see figure 14) and a spectral softening of $\Delta\alpha = 0.25$ during the GRB emission (see figure 12) which was observed with some delay by MAGIC. The upper limits on the number of events, $N_{>95\%}$, were calculated using the Feldman-Cousins prescription, for the moment, with the intention to include systematic uncertainties in the next section.

Tables 31, 32 and 33 list all differential flux upper limits, obtained from the first 90 seconds of prompt emission overlap, the first 1000 seconds and the whole data sample, respectively, for all six test spectra, the two simulated point spread functions and the two image cleaning algorithms. One observes that the spectral index changes the limits somewhat, but not considerably. Taking the worst case scenario of each sequence, one can be sure that the limit applies correctly at least to one case and there is no under-coverage for the other cases. For the case of $PSF = 0.05^\circ\,\sigma$, the following preliminary differential flux upper limits are then obtained:

$$f_0\,\big|_{160\,\mathrm{GeV}} < 5.7\cdot 10^{-9}\ \mathrm{ph\,cm^{-2}\,s^{-1}\,TeV^{-1}} \quad \text{(first 90 s)} \tag{153}$$
$$f_0\,\big|_{160\,\mathrm{GeV}} < 2.4\cdot 10^{-9}\ \mathrm{ph\,cm^{-2}\,s^{-1}\,TeV^{-1}} \quad \text{(first 1000 s)} \tag{154}$$
$$f_0\,\big|_{160\,\mathrm{GeV}} < 1.1\cdot 10^{-9}\ \mathrm{ph\,cm^{-2}\,s^{-1}\,TeV^{-1}} \quad \text{(entire 2200 s)} \tag{155}$$

$$f_0\,\big|_{280\,\mathrm{GeV}} < 1.5\cdot 10^{-9}\ \mathrm{ph\,cm^{-2}\,s^{-1}\,TeV^{-1}} \quad \text{(first 90 s)} \tag{156}$$
$$f_0\,\big|_{290\,\mathrm{GeV}} < 2.3\cdot 10^{-10}\ \mathrm{ph\,cm^{-2}\,s^{-1}\,TeV^{-1}} \quad \text{(first 1000 s)} \tag{157}$$
$$f_0\,\big|_{330\,\mathrm{GeV}} < 1.7\cdot 10^{-10}\ \mathrm{ph\,cm^{-2}\,s^{-1}\,TeV^{-1}} \quad \text{(entire 2200 s)} \tag{158}$$

As the observation times scale like 1:10:25, the derived differential flux limits should scale more or less like the one over the square root of these numbers which is the case.

The limits in the higher energy bin compare well with the MAGIC sensitivity at 50° zenith angle [274] while the upper energy bin cannot be compared directly because no analysis has reached yet so low in energy at that observation zenith angle.

8.15 Search in Time Slices of 100 Seconds

Finally, an additional search for peak emission in steps of 100 seconds was performed. To do so, the entire GRB050713a data sample was divided in 22 slices of equal time duration (exactly 101 seconds). Table 34 lists the used parameters for the peak

Image Cleaning Method	Differential Flux Upper Limits - PROMPT EMISSION						
	Mean Energy E_0 (GeV)	dN_γ/dE (10^{-9}cm^{-2}s^{-1}TeV^{-1}) (95% C.L.)					
		$\alpha = 1$	$\alpha = 2$	$\alpha = 2.25$	$\alpha = 2.5$	$\alpha = 3$	$E_b = 200$
Absolute	173	6.3	7.4	7.5	7.6	7.6	7.8
(PSF= 0.05°σ)	288	0.57	0.68	0.70	0.70	0.69	0.68
Absolute	170	6.7	8.1	8.3	8.4	8.5	8.9
(PSF= 0.07°σ)	274	0.19	0.24	0.25	0.26	0.26	0.27
Time	161	4.6	5.4	5.5	5.6	5.6	5.7
(PSF= 0.05°σ)	283	0.70	0.84	0.85	0.85	0.84	0.82
Time	158	2.2	2.6	2.7	2.7	2.8	2.9
(PSF= 0.07°σ)	271	1.4	1.5	1.5	1.5	1.5	1.5

Table 31: Upper limits for GRB050713a prompt emission data: α denotes the spectral index of the test spectrum. The last column shows an upper limit from a spectrum with exponential cutoff and break energy (see text).

Image Cleaning Method	Differential Flux Upper Limits - First 1000 Seconds						
	Mean Energy E_0 (GeV)	dN_γ/dE (10^{-9}cm^{-2}s^{-1}TeV^{-1}) (95% C.L.)					
		$\alpha = 1$	$\alpha = 2$	$\alpha = 2.25$	$\alpha = 2.5$	$\alpha = 3$	$E_b = 200$
Absolute	174	2.9	3.4	3.4	3.5	3.5	3.6
(PSF= 0.05°σ)	352	0.12	0.13	0.13	0.14	0.13	0.13
Absolute	169	2.7	3.3	3.3	3.4	3.5	3.6
(PSF= 0.07°σ)	280	0.26	0.33	0.35	0.36	0.36	0.38
Time	162	2.0	2.3	2.3	2.4	2.4	2.4
(PSF= 0.05°σ)	293	0.19	0.22	0.23	0.23	0.23	0.22
Time	157	2.9	3.0	3.0	3.0	3.0	3.2
(PSF= 0.07°σ)	275	0.39	0.40	0.42	0.42	0.42	0.44

Table 32: Upper limits for first 1000 s of GRB050713a data: α denotes the spectral index of the test spectrum. The last column shows an upper limit from a spectrum with exponential cutoff and break energy (see text).

Image Cleaning Method	Mean Energy E_0 (GeV)	Differential Flux Upper Limits - Total Sample dN_γ/dE (10^{-9}cm^{-2}s^{-1}TeV^{-1}) (95% C.L.)					
		$\alpha = 1$	$\alpha = 2$	$\alpha = 2.25$	$\alpha = 2.5$	$\alpha = 3$	$E_b = 200$
Absolute	173	1.4	1.4	1.4	1.5	1.5	1.5
(PSF= 0.05°σ)	354	0.10	0.11	0.12	0.12	0.12	0.12
Absolute	169	0.90	1.1	1.1	1.1	1.1	1.2
(PSF= 0.07°σ)	283	0.22	0.28	0.29	0.30	0.32	0.34
Time	162	0.91	1.1	1.1	1.1	1.1	1.1
(PSF= 0.05°σ)	331	0.14	0.16	0.16	0.16	0.17	0.17
Time	157	1.4	1.6	1.7	1.7	1.7	1.8
(PSF= 0.07°σ)	276	0.16	0.20	0.21	0.22	0.23	0.25

Table 33: Upper limits for total 2200 s of GRB050713a data: α denotes the spectral index of the test spectrum. The last column shows an upper limit from a spectrum with exponential cutoff and break energy (see text).

emission search. Only the time image cleaning was used, every of the 22 time slices was taken as ON data while the remaining data set was used as OFF data. A second search was performed shifting the phase of the time slice by 50 seconds.

The number of excess events are distributed randomly over time, as can be seen in figure 193 and the significances show the expected Gaussian distribution with a width of $\sigma \approx 1$ (figure 194).

From the absence of a signal in the peak emission search, a global upper limit can be derived from the time slice yielding the biggest number of excess events:

$$f_0\big|_{160\,\mathrm{GeV}} < 1.3 \cdot 10^{-8}\ \mathrm{ph\,cm^{-2}\,s^{-1}\,TeV^{-1}} \quad \text{any } 100\,\mathrm{s} \text{ interval} \tag{159}$$

$$f_0\big|_{280\,\mathrm{GeV}} < 2.1 \cdot 10^{-9}\ \mathrm{ph\,cm^{-2}\,s^{-1}\,TeV^{-1}} \quad \text{any } 100\,\mathrm{s} \text{ inverval} \tag{160}$$

Image Cleaning Method	Reconst. Energy Range (GeV)	cut *HADR.-NESS*	cut *ALPHA* (°)	U.L.$_{max}$ Excess (95% CL)	Mean E_γ MC (GeV)
Time (PSF= 0.05°σ)	100 - 200	0.61	20	41.1	161
	200 - 500	0.49	15	37.1	283

Table 34: Results of the automatic analysis for the GRB050713a time slices search, using all ON data outside the corresponding time slice as OFF-data.

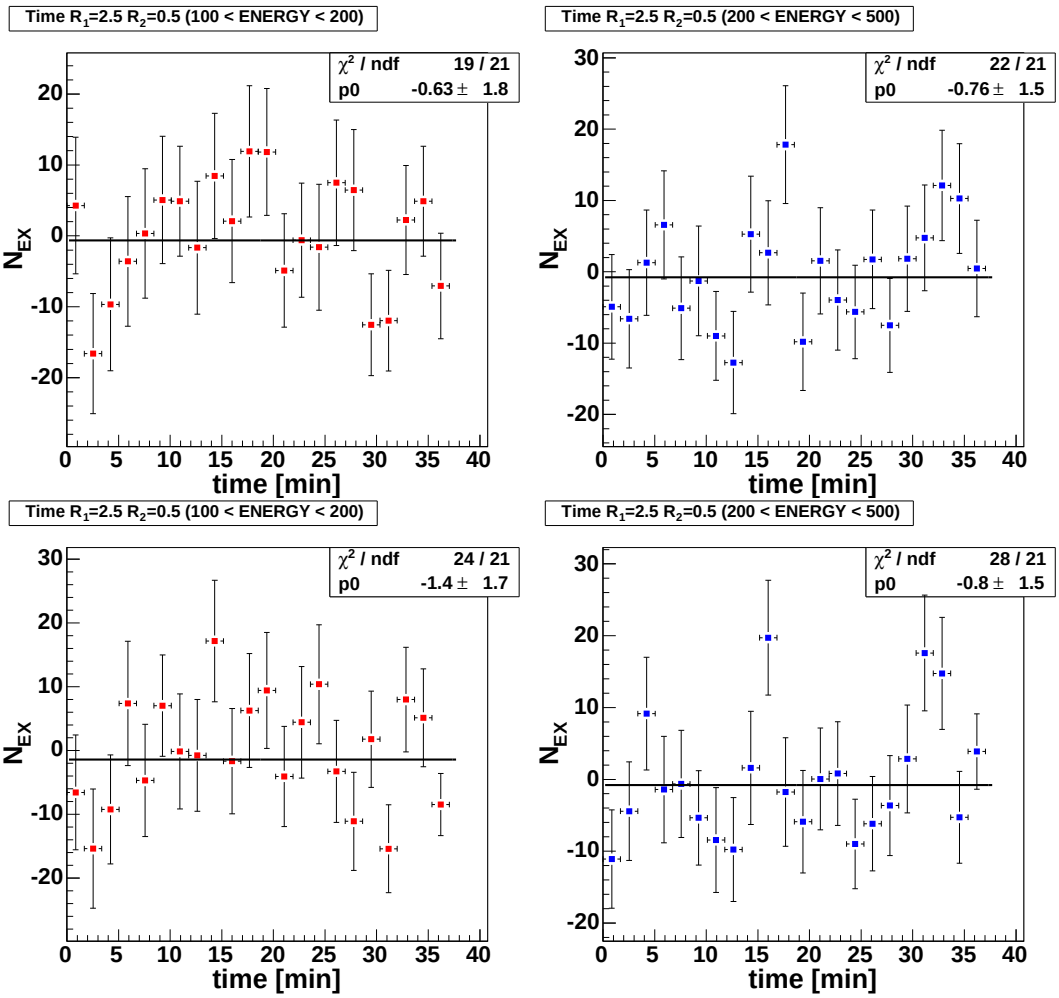

Figure 193: Number of excess events vs. time for the peak search. Left: 100 to 200 GeV, right: 200 to 500 GeV reconstructed energy. On the bottom, the phase has been shifted by 50 seconds.

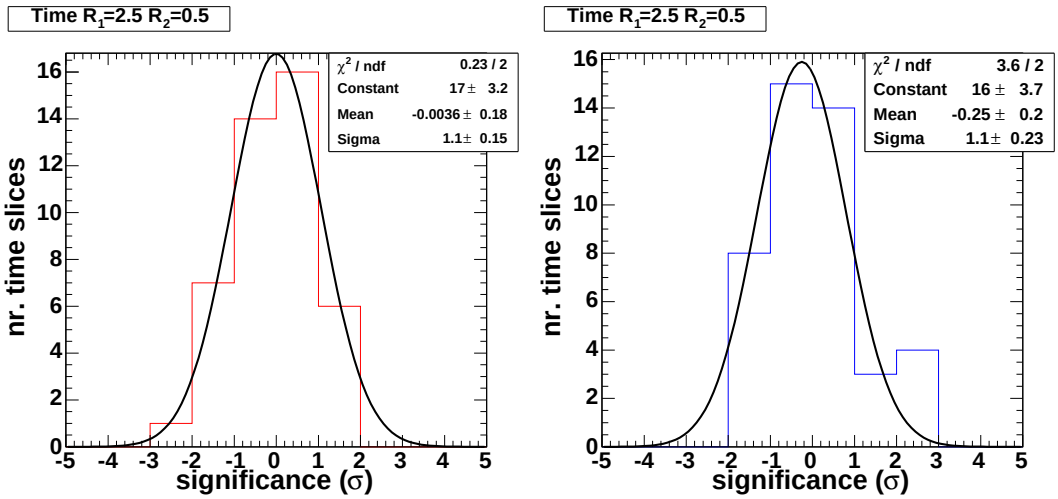

Figure 194: Distributions of the signal significances from the peak search. Left: 100 to 200 GeV, right: 200 to 500 GeV reconstructed energy.

8.16 Effect of Systematic Uncertainties on the Limits

Three systematic uncertainties have been investigated in more detail since they do not appear as such in other analyses or have a different magnitude: a possible worsening of the PSF during the prompt emission phase, trigger inefficiencies in the camera and the effect of a shift in the determination of the absolute energy scale.

Point-spread Function

The effect of a worsening of the PSF from $0.05^\circ\,\sigma$ to $0.07^\circ\,\sigma$ can be seen in tables 31 through 33: although not visible in the case of the prompt emission limits, due to a statistical fluctuation, the limits worsening of on average 35 % if the PSF degrades. Although we know that the PSF lies around $0.05^\circ\,\sigma$ what concerns the overall data sample, we can now use the amount of worsening to determine the systematic uncertainty due to a possible worsening of the PSF during the prompt emission. To be clear and repeat what has been said already in section 8.3: the uncertainty applies only to the analysis of this particular burst, for the reasons given in section 8.3.

Trigger Inefficiencies

Figure 195 shows the center of gravity with all cuts applied for the entire data taken on GRB050713a. In case of a homogeneous camera, the distribution should be flat, while the inefficiencies observed in section 8.6.2 are still present and reduce the camera acceptance. The lower energy bin exhibits voids at the right side of the camera and the lower left part which coincide with those already observed with a

much bigger statistics (figure 165), although somewhat reduced due to the cut in *DIST*.

In order to quantify the effect, the azimuthal projection of the center of gravity was inspected and the relative deficit of the two bins corresponding to the two voids calculated. Figure 196 shows such projections. On average, the deficit has been reduced to about 5%.

In the end, a global 5% inefficiency was assumed and a further systematic uncertainty of 5% due to the limited statistics available to determine the global deficit.

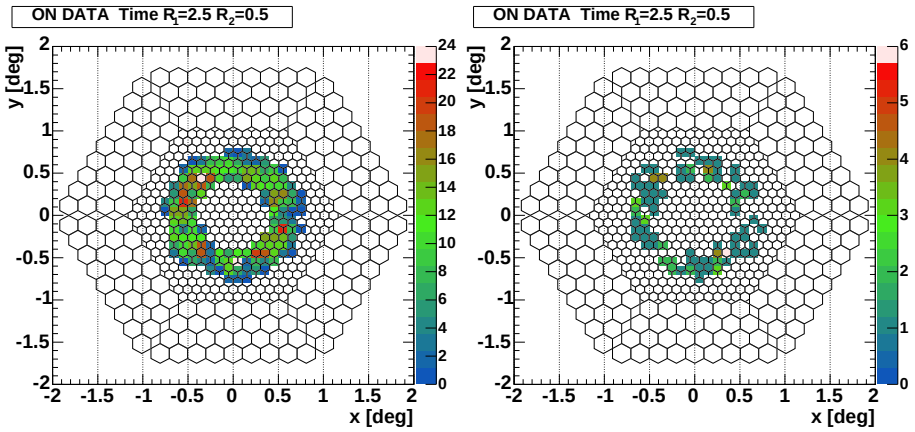

Figure 195: Distributions of the center-of-gravity, obtained with cuts derived for the entire sample of GRB050713a. Left: 100 to 200 GeV, right: 200 to 500 GeV reconstructed energy.

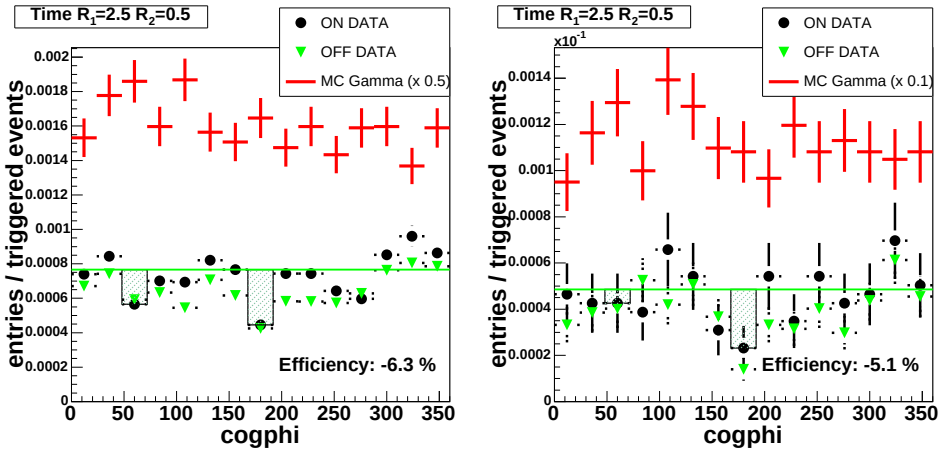

Figure 196: Azimuthal projections of the center-of-gravity, for the entire sample of GRB050713a, all cuts applied. Left: 100 to 200 GeV, right: 200 to 500 GeV reconstructed energy. The green lines show a fit to the ON data with those bins excluded which are suspected to contain inefficiencies.

Absolute Energy Scale

Following the results of the first part of this thesis (section 6.8), a global absolute calibration uncertainty of about 13 % has to be assumed, due to the not yet implemented correction of the degradation of the excess noise factor of the photomultipliers (10 %) and the systematic uncertainty due to the different pulse forms of cosmics and calibration light pulses in combination with the digital filter (8 %). An uncertainty in the abolute light calibration reflects itself directly in the determination of the absolute energy scale. If the spectrum of the limited flux was known, this error could be easily propagated to the systematic uncertainty of the flux limit. Because of the unknown spectral index however, the propagation is ambiguous. For this reason, a different approach was followed here: the absolute calibration uncertainty will be counted on the uncertainty of the mean energy at which the limit applies.

Further Systematic Uncertainties

Further systematic uncertainties can only be quantified by their average deviation from simulations. The following parts were included in the estimate:

atmosphere model (US standard vs. La Palma)	15%
atmosphere summer-winter variation	15%
changing atmospheric conditions:	
Mie scattering, varying atmospheric extinction	10%
trigger inefficiency	10%
data-MC agreement	5-10%

Summing up these values quadratically, a global uncertainty of about 27% is obtained for the longer data taking periods and 44% for the prompt emission phase which includes the uncertainty on the point-spread-function. In total, a mean efficiency of real data with respect to MC simulations of 0.95±0.27 and 0.95±0.57 is then assumed for both cases, respectively.

These uncertainties have been incorporated in the limits following the approach by Rolke, López and Conrad [265]. Tables 28 through 30 had already included a calculation of theses limits, together with the Feldman-Cousins results.

On the side of the absolute energy scale, another 15–20 % due to atmospheric conditions plus the 13 % systematic uncertainty on the absolute calibration is assumed. These values sum up quadratically to about 22 %. In order to propagate these uncertainties onto the flux limits, different analyzes would need to be performed now, with simulated energy scales spread accordingly. This procedure is not yet foreseen in the MAGIC analysis chain and, as the precision of the limits turns out not to be crucial, this analysis restricts itself to stating an uncertainty on the absolute energy scale. Since the evolution of the effective areas of the MAGIC telescope is quite smooth, it is expected that a specific theoretical spectrum to be tested by this limit, could

simply propagate that uncertainty according to the spectral index of that theory and the error in doing so is negligible.

After including all systematic uncertainties, the following inclusive differential particle flux upper limits are obtained:

$$f_0\big|_{160\,\mathrm{GeV}} < 1.3\cdot10^{-8}\ \mathrm{ph\,cm^{-2}\,s^{-1}\,TeV^{-1}} \quad \text{(first 90 s)} \tag{161}$$
$$f_0\big|_{160\,\mathrm{GeV}} < 3.3\cdot10^{-9}\ \mathrm{ph\,cm^{-2}\,s^{-1}\,TeV^{-1}} \quad \text{(first 1000 s)} \tag{162}$$
$$f_0\big|_{160\,\mathrm{GeV}} < 1.4\cdot10^{-9}\ \mathrm{ph\,cm^{-2}\,s^{-1}\,TeV^{-1}} \quad \text{(entire 2200 s)} \tag{163}$$
$$f_0\big|_{160\,\mathrm{GeV}} < 1.6\cdot10^{-8}\ \mathrm{ph\,cm^{-2}\,s^{-1}\,TeV^{-1}} \quad \text{(any 100 s interval)} \tag{164}$$

$$f_0\big|_{280\,\mathrm{GeV}} < 3.0\cdot10^{-9}\ \mathrm{ph\,cm^{-2}\,s^{-1}\,TeV^{-1}} \quad \text{(first 90 s)} \tag{165}$$
$$f_0\big|_{290\,\mathrm{GeV}} < 2.9\cdot10^{-10}\ \mathrm{ph\,cm^{-2}\,s^{-1}\,TeV^{-1}} \quad \text{(first 1000 s)} \tag{166}$$
$$f_0\big|_{330\,\mathrm{GeV}} < 2.6\cdot10^{-10}\ \mathrm{ph\,cm^{-2}\,s^{-1}\,TeV^{-1}} \quad \text{(entire 2200 s)} \tag{167}$$
$$f_0\big|_{280\,\mathrm{GeV}} < 2.8\cdot10^{-9}\ \mathrm{ph\,cm^{-2}\,s^{-1}\,TeV^{-1}} \quad \text{(any 100 s inverval)} \tag{168}$$

with 22 % uncertainty on the determination of the absolute energy scale.

8.17 Fluence and Spectral Energy Density Limits

According to the prescriptions eq. 140, limits on the fluence have been calculated, following the same procedure as in the previous chapters:

$$f_0\big|_{160\,\mathrm{GeV}} < 1.2\cdot10^{-6}\ \mathrm{ph\,cm^{-2}\,TeV^{-1}} \quad \text{(first 90 s)} \tag{169}$$
$$f_0\big|_{160\,\mathrm{GeV}} < 3.3\cdot10^{-6}\ \mathrm{ph\,cm^{-2}\,TeV^{-1}} \quad \text{(first 1000 s)} \tag{170}$$
$$f_0\big|_{160\,\mathrm{GeV}} < 3.1\cdot10^{-6}\ \mathrm{ph\,cm^{-2}\,TeV^{-1}} \quad \text{(entire 2200 s)} \tag{171}$$
$$f_0\big|_{160\,\mathrm{GeV}} < 1.6\cdot10^{-6}\ \mathrm{ph\,cm^{-2}\,TeV^{-1}} \quad \text{(any 100 s interval)} \tag{172}$$

$$f_0\big|_{280\,\mathrm{GeV}} < 2.7\cdot10^{-7}\ \mathrm{ph\,cm^{-2}\,TeV^{-1}} \quad \text{(first 90 s)} \tag{173}$$
$$f_0\big|_{290\,\mathrm{GeV}} < 2.9\cdot10^{-7}\ \mathrm{ph\,cm^{-2}\,TeV^{-1}} \quad \text{(first 1000 s)} \tag{174}$$
$$f_0\big|_{330\,\mathrm{GeV}} < 5.7\cdot10^{-7}\ \mathrm{ph\,cm^{-2}\,TeV^{-1}} \quad \text{(entire 2200 s)} \tag{175}$$
$$f_0\big|_{280\,\mathrm{GeV}} < 2.8\cdot10^{-7}\ \mathrm{ph\,cm^{-2}\,TeV^{-1}} \quad \text{(any 100 s inverval)} \tag{176}$$

While the calculation of the fluence limits is straightforward, the calculation of the limits on the spectral energy density (eq. 142) magnifies the effect of the spectral index, mainly because of the average energy square term. Table 35 gives an example for the prompt emission data. One can see that very hard spectra produce significantly higher limits. As it cannot be excluded that the spectral index is that hard at least locally (it may be an Inverse Compton peak), the worst case scenario was taken,

which raises the limits quite considerably [64]. Moreover, the uncertainty on the mean energy has to be propagated here yielding about 40% systematic uncertainty on the SED limit. The obtained limits on the spectral energy density read as follows:

$$f_0\big|_{160\,\mathrm{GeV}} < 1.5\cdot 10^{-9}\ \mathrm{erg\,cm^{-2}\,s^{-1}} \quad \text{(first 90 s)} \tag{177}$$
$$f_0\big|_{160\,\mathrm{GeV}} < 3.5\cdot 10^{-10}\ \mathrm{erg\,cm^{-2}\,s^{-1}} \quad \text{(first 1000 s)} \tag{178}$$
$$f_0\big|_{160\,\mathrm{GeV}} < 1.5\cdot 10^{-10}\ \mathrm{erg\,cm^{-2}\,s^{-1}} \quad \text{(entire 2200 s)} \tag{179}$$
$$f_0\big|_{160\,\mathrm{GeV}} < 1.4\cdot 10^{-9}\ \mathrm{erg\,cm^{-2}\,s^{-1}} \quad \text{(any 100 s interval)} \tag{180}$$

$$f_0\big|_{280\,\mathrm{GeV}} < 3.8\cdot 10^{-10}\ \mathrm{erg\,cm^{-2}\,s^{-1}} \quad \text{(first 90 s)} \tag{181}$$
$$f_0\big|_{290\,\mathrm{GeV}} < 7.3\cdot 10^{-11}\ \mathrm{erg\,cm^{-2}\,s^{-1}} \quad \text{(first 1000 s)} \tag{182}$$
$$f_0\big|_{330\,\mathrm{GeV}} < 7.0\cdot 10^{-11}\ \mathrm{erg\,cm^{-2}\,s^{-1}} \quad \text{(entire 2200 s)} \tag{183}$$
$$f_0\big|_{280\,\mathrm{GeV}} < 5.2\cdot 10^{-10}\ \mathrm{erg\,cm^{-2}\,s^{-1}} \quad \text{(any 100 s inverval)} \tag{184}$$

Image Cleaning Method	Flux Density Upper Limits - PROMPT EMISSION						
	Mean Energy E_0 (GeV)	$E^2\cdot dN_\gamma/dE$ (10^{-10}erg$\cdot$cm^{-2}s^{-1}) (95% C.L.)					
		$\alpha=1$	$\alpha=2$	$\alpha=2.25$	$\alpha=2.5$	$\alpha=3$	$E_b=200$
Time	161	13.1	7.5	7.2	6.9	6.2	5.9
(PSF= $0.05^\circ\sigma$)	283	3.2	2.0	1.9	1.9	1.8	1.7

Table 35: Flux density upper limits for GRB050713a prompt emission data: α denotes the spectral index of the test spectrum. The last column shows an upper limit from a spectrum with exponential cutoff and break energy.

8.18 Physical Interpretation

Unfortunately, the redshift of GRB050713a could not be measured up to date, making it difficult to draw conclusions about whether any GRB model has been excluded by these limits or not, simply because it is possible that GRB050713a lies so far away that all gamma-rays have been absorbed by the Meta-Galactic Radiation Field.

Three telescopes have claimed to see counterparts in the optical and near infrared (see table 36), although without a possible measurement of the redshift.

One temptative measurement of the redshift could be made in X-rays, namely by XMM-Newton [278]. The obtained spectrum was fitted best if a redshifted neutral

[64] This approach is different from [267] where the limits had been multiplied simply by $< E >^2$.

Claims of Optical Counterparts					
telescope	location	wavelength band	magnitude	time after burst	reference
Raptor	Los Alamos	R-band	18.4	22.4 s	[275]
Liverpool	La Palma	R-band	19.2	3 min	[276]
NOT	La Palma	R-band	n.a.	47 min	[277]
TNG	La Palma	I-band	n.a.	47 min	[277]

Table 36: Claims for optical counterparts of GRB050713a by other ground-based telescopes. None of these observations could determine a redshift.

hydrogen absorber component was included in the fit. The redshift of that component came out as $z_{absorb} = 0.55$ with 90 % CL ranges of $z = (0.4 - 2.6)$, thus very badly determined.

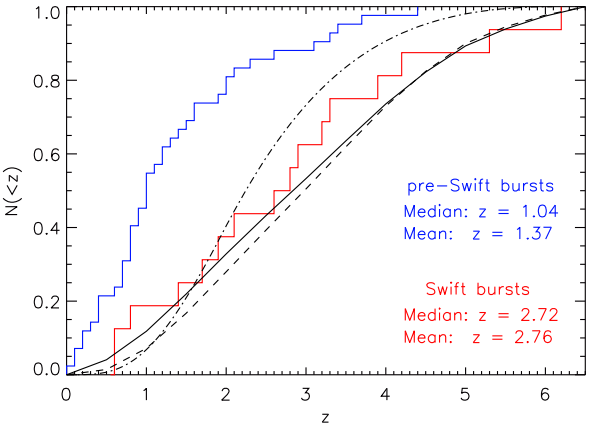

Figure 197: Cumulative distribution of redshifts of GRBs triggered by the SWIFT satellite (from [67]). About one third of the bursts do not have any redshift information.

From the distribution of redshifts of bursts that triggered SWIFT (figure 197), a mean redshift of $z \approx 2.7 - 2.8$ would be expected. If GRB050713a were that far away, MAGIC would not have had any chance to observe it, at least not at a zenith angle of 50°.

Only if situated at $z \lesssim 0.5$, one can conclude that GRB050713a did not emit more than about 10% of its radiated energy in the hundreds of GeV energy domain from $[T_0 + 40\,\mathrm{s}, T_0 + 130\,\mathrm{s}]$, i.e. during the last 90 s of its prompt emission. This is in agreement with the pure synchrotron emission models with a spectral index greater than $\alpha \approx 2.05$. Remember however that GRBs show usually power law spectra with $\alpha = (1.5 - 3.5)$ at high energies, with tendency to softer spectra at late times of the prompt emission. Only an unusually steep spectral index around $dN_\gamma/dE \propto E^{-2.0}$ could be excluded in this scenario. The same applies to Pe'er Asaf's

model [148] which would be excluded if two conditions apply: a close redshift and the observation of a second spectral component at MeV-energies. Both conditions do not hold, however will be given in the near future with the launch of the GLAST detector [279].

From the BAT observation and a flux measurement by KONUS-Wind [280], one can derive the spectrum up to the break energy, however there is no information about the spectral slope available at higher energies. Figure 198 combines the known spectra at several stages of the prompt emission, together with the most probable extensions at the higher energy side. The green line, showing the spectrum during the main emission peak, does not coincide with the MAGIC observation window and should only give an idea about the capabilities of this analysis, would the main peak have fallen into the MAGIC observation window.

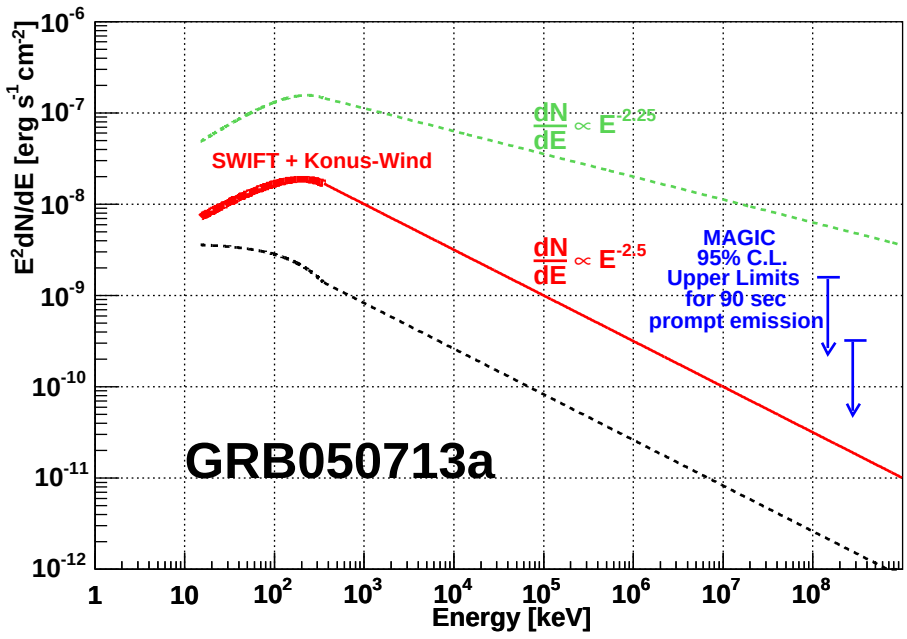

Figure 198: SWIFT BAT spectra in the energy range between 15 and 350 keV for different time intervals. Red line: $T_0 - 70\,s$ to $T_0 + 121\,s$, as reported in [281]. Green dashed line: spectrum of main peak from T_0 to $T_0 + 20\,s$. Black dashed line: average spectrum of MAGIC observation window from $T_0 + 40\,s$ to $T_0 + 130\,s$ (all spectra derived by M. Garczarczyk and S. Mizobuchi). Blue arrows: upper limits from this analysis, for the 90 seconds of the MAGIC observation overlap with the prompt emission.

Apart from the missing redshift information, GRB050713a has been a particularly well investigated burst. Figure 199 resumes the light curves, as obtained from various experiments and upper limits, including the ones of this work. One can see two

prominent X-ray flares, a major discovery by its own from this burst [81]. These flares are not understood at all up to now and point to a re-activation of the central engine after the main burst. The lack of a GeV counterpart to these flares would probably marginally exclude some of the predictions of Wang et al. [150], would the burst be close enough.

Possible future measurements of the redshift of GRB050713a or on the still varying assumptions about density and evolution of the MRF might shed new light on these limits. This is however out the scope of this work and the Air Imaging Cherenkov Telescopy as a whole. More important is the fact that the MAGIC Telescope has established itself as a functioning gamma-ray burst observatory capable to do fast enough follow-up observations at energies above 50 GeV.

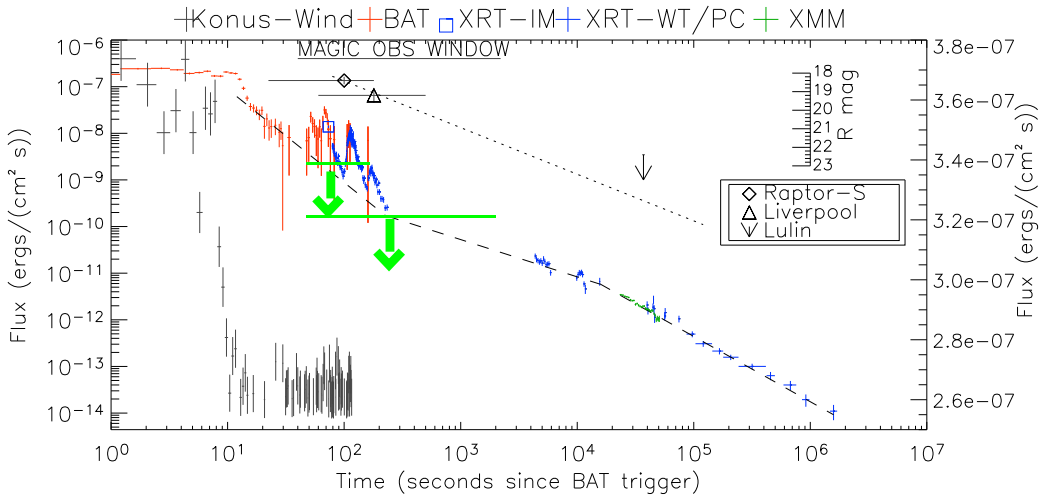

Figure 199: Light curve of GRB050713a, with observations of all experiments included. The left axis applies to all shown light curves except for the Konus-Wind points where the right axis applies. The inset axis shows additionally the magnitudes of the optical telescope observations, scaled to the outer left axis. The green limits are those obtained in this analysis, at 160±30 GeV. The first limit applies to the time window $[T_0 + 40\ \mathrm{s}, T_0 + 130\ \mathrm{s}]$ *of observation overlap with the prompt emission. The second limit was obtained from the entire observation* $[T_0 + 40\ \mathrm{s}, T_0 + 2260\ \mathrm{s}]$.

8.19 Summary

The data taken during the prompt emission of GRB050713a and 37 minutes afterwards was analyzed in a dedicated low-energy analysis. For this reason, two different image cleaning algorithms were applied to the data, among which a new algorithm employing the time information of each reconstructed photomultiplier signal. Additionally, a new unbiased way to optimize the cuts on *HADRONNESS* and $|ALPHA|$

was developed. The analysis was first tried on a test source, namely flare data of the AGN Mrk501, taken at the beginning of July, 2005. The test analysis lead to a $5\,\sigma$ detection of gamma-ray signals between 60 and 100 GeV for only one hour of ON data and can easily be extended to higher significances by adding more OFF data to this analysis. It could be shown that at least three more bins can be added to the spectrum of Mrk501 toward lower energies, if compared with the standard analysis.

The new analysis was then applied to the GRB050713a data. The following results were obtained:

- No signal was detected, neither during the 90 seconds overlap with the prompt emission, nor during the subsequent 37 minutes of GRB050713a data, nor in any of the 100 seconds time slices during the 37 minutes of data.
- The pointing precision of the telescope is not affected by the fast operation mode, used to point to a gamma-ray burst with the maximally allowed speed.
- The point spread function of the reflector is not deteriorated what concerns the whole 37 minutes of GRB050713a data. For the 90 seconds prompt emission overlap, no clear statement can be made so far, however the effect of a maximally worsened PSF has been investigated and included in the upper limit for the prompt emission.
- The camera suffers from inhomogeneities at the level of 5 %, after application of all cuts, the sensitivity of this analysis is reduced directly by this amount.
- Systematic uncertainties on the sensitivity sum up to 44 % in the case of the prompt emission overlap and 27 % for the rest of the data.

The following differential particle flux upper limits (95% CL) could be derived:

$$f_0\big|_{160\,\mathrm{GeV}} < 4.2\ \mathrm{C.U.} \quad \text{first } 90\,\mathrm{s} \tag{185}$$
$$f_0\big|_{160\,\mathrm{GeV}} < 1.1\ \mathrm{C.U.} \quad \text{first } 1000\,\mathrm{s} \tag{186}$$
$$f_0\big|_{160\,\mathrm{GeV}} < 0.45\,\mathrm{C.U.} \quad \text{entire } 2220\,\mathrm{s} \tag{187}$$
$$f_0\big|_{160\,\mathrm{GeV}} < 5.2\ \mathrm{C.U.} \quad \text{any } 100\,\mathrm{s} \text{ interval} \tag{188}$$

$$f_0\big|_{280\,\mathrm{GeV}} < 4.1\ \mathrm{C.U.} \quad \text{first } 90\,\mathrm{s} \tag{189}$$
$$f_0\big|_{290\,\mathrm{GeV}} < 0.40\,\mathrm{C.U.} \quad \text{first } 1000\,\mathrm{s} \tag{190}$$
$$f_0\big|_{330\,\mathrm{GeV}} < 0.36\,\mathrm{C.U.} \quad \text{entire } 2220\,\mathrm{s} \tag{191}$$
$$f_0\big|_{280\,\mathrm{GeV}} < 3.8\ \mathrm{C.U.} \quad \text{any } 100\,\mathrm{s} \text{ inverval}\ , \tag{192}$$

assuming an additional systematic uncertainty of 22 % in the determination of the absolute energy scale. The Crab unit (C.U.) was thereby assumed to be:

$$1\,\mathrm{C.U.} := 1.5 \cdot 10^{-3} \big(\frac{E}{\mathrm{GeV}}\big)^{-2.58} \mathrm{ph\,cm^{-2}\,s^{-1}\,TeV^{-1}}\ , \tag{193}$$

measured by MAGIC in the range from 300 GeV to 5 TeV [65].

Even including these systematics, the limit in the upper energy bin results to be 15 % lower than the one published from a previous standard analysis, in cooperation with the author [267], while the limit in the lower energy bin cannot be compared directly with the published result since the standard analysis does reach so far down in energy.

[65] Taking interpolated values from the direct measurements at these energies, the Crab unit diminishes by about 10% at 160 GeV and by less than 5% at 280 GeV.

9 Conclusions

Because of their huge effective collection areas, Imaging Atmospheric Cherenkov Telescopes (IACTs) are excellent instruments to observe the gamma-ray sky at energies ranging from 50 GeV to larger than 20 TeV. Among the current IACTs, the MAGIC telescope has the largest mirror area and thus the lowest treshold in energy. In addition, MAGIC is the fastest IACT in the world: Able to reach any position in the sky within less than 50 seconds allows to observe the prompt emission of Gamma-ray Bursts, for the first time by an IACT.

For the construction of the MAGIC Telescope, the Institut de Física d'Altes Energies (***IFAE***) took the responsability to construct the photo-multiplier camera and the calibration system. The latter was installed at the telescope by the author and analyzed in this thesis. The three main parts of the system – the LEDs based light pulser, three blinded pixels and the calibrated PIN diode – have been described, as well as the way to treat data obtained from theses devices. The author has written an amount of tools to analyze the data captured by the calibration devices and effectively use them to reconstruct and calibrate all signals from the photo-multiplier camera.

While the overall functionality of all parts of the system has been investigated, its stability over the last two years of data taking was proven. It is therefore possible to ***reliably calibrate*** the MAGIC camera, which includes: the relative response of each photo-multiplier to incident photons, the absolute overall response of the camera, including its evolution in time and all necessary corrections needed to obtain stable analysis results during years of data taking. With these results and the provided accompanying software, the camera of the MAGIC telescope can be understood and operated such as foreseen in its design.

An important part of the analysis constitutes the signal extraction, where different algorithms have been characterized by their statistical properties. Advanced signal reconstruction algorithms open a new window to lower analysis energy thresholds and permit to use the time information for shower analyses. Following the results of these investigations, robust and stable signal extractors are provided as well as those which reach the lowest possible analysis thresholds: 1.7 photo-electrons root-mean-square-error per channel for typical observation conditions of extra-galactic sources. These algorithms provide also an excellent time resolution: 1 ns for signals equivalent to 10 photo-electrons and better at higher intensities.

The MAGIC camera has proven to work stably during the last two years, showing an overall gain drop of 10% per year and an increase of gain dispersion of 3% per year. Both are getting corrected for by raising the high-voltages of the camera and adjusting them to yield approximately equal gains for all pixels in the camera (the flat-fielding procedure). This work has shown that additionally the quality of the photo-multiplier, described by the excess noise factor, decreases with time, by about a same amount as the gain drops.

Using the above findings, a complete analysis chain dedicated to low-energy events was developed and used to analyze the first data taken ever during the prompt

emission of a Gamma-ray Burst, following an alert from the SWIFT satellite. The data was searched for signals from gamma-ray showers, without success whereupon upper limits have been calculated. These upper limits would pose important limitations to existing models predicting high-energy gamma emission, if the redshift of the source was known – which is unfortunately not the case for this burst (and about one third of all GRBs detected by SWIFT).

All steps of that analysis were cross-checked on data taken during an exceptionally bright flare of the Active Galactic Nuclei Markarian 501, demonstrating that an energy threshold around 65 GeV can be reached.

Other issues of concern about MAGIC observations in GRB mode could be investigated and rebutted: The pointing precision of the telescope just after the fast movement toward the source and the functionning of the automatic mirror adjustment during the fast movement.

MAGIC is now constantly receiving GRB alerts, at a rate of about 1–2 per month. Up to now, one more burst was followed-up during its prompt emission phase. Although that burst has become famous because of being the farthest ever seen gamma-ray burst, observations at energies around 100 GeV are doomed to seeing nothing because of the absorption of these photons by the extra-galactic background light. It is however only a question of time when the first close enough burst is followed up by MAGIC and new chapters in gamma-ray burst physics might be opened.

References

[1] V. Hess, *Über Beobachtungen der durchdringenden Strahlung bei sieben Freiballonfahrten*, Physik. Zeitschr. **13** (1912) 1084, available on `http://www.mpi-hd.mpg.de/hfm/HESS/public/HessArticle.pdf`.

[2] M. Longair, *High energy astrophysics*, Volume 1, Cambridge Univerity Press, second edition, 1992.

[3] T. Gaisser and T. Stanev, *Cosmic Rays*, chapter 24, p. 1, Volume 592 of [178], 2004, available on `http://pdg.lbl.gov/`.

[4] K. Kampert, The kascade air shower experiment: Composition analyzes and energy spectrum, in *26^{th} International Cosmics Rays Conference, Salt Lake City, Utha*, 1999.

[5] N. Hayashida et al., *The anisotropy of cosmic rays arrival directions around 10^{18} eV*, Astroparticle Physics **10** (1999) 303.

[6] M. Longair, *High energy astrophysics*, Volume 2, Cambridge Univerity Press, second edition, 1994.

[7] A. Swordy, *The Energy Spectra and Anisotropies of Cosmic Rays*, Space Sci. Rev. **99** (2001) 85.

[8] List of macro pictures and results, `http://www.df.unibo.it/macro/macro_pict.htm`, 1998.

[9] R. Klebesadel, I. Strong, and R. Olson, *Observations of Gamma-Ray Bursts of Cosmic Origin*, Astrophys. Journal **182** (1973) L85.

[10] S. Kulkarni et al., *Identification of a host galaxy at redshift z = 3.42 for the γ-ray burst of 14 December 1997*, Nature **393** (1999) 35.

[11] E. Costa et al., *Discovery of an X-ray afterglow associated with the γ-ray burst of 28 February 1997*, Nature **387** (1997) 783.

[12] E. Waxman, *Cosmological Gamma-Ray Bursts and the Highest Energy Cosmics Rays*, Physical Review Letters **75** (1995) 386, astro-ph/9505082.

[13] M. Vietri, *On the acceleration of Ultra High Energy Cosmic Rays in Gamma Ray Bursts*, Astrophys. Journal **453** (1995) 883.

[14] R. Hartman et al. (EGRET Collab.), *The Third EGRET Catalog of High-Energy Gamma-Ray Sources*, Astrophys. Journal Suppl. **123** (1999) 79.

[15] T. Weekes, M. Cawley, and D. Fegan, *Observation of TeV Gamma-Rays from the Crab Nebula Using the Atmospheric Cerenkov Imaging Technique*, The Astrophysical Journal **342** (1989) 379.

[16] M. Gaug, *Detection of Atmospheric Muon Neutrinos with the AMANDA Neutrino Telescope*, Diploma thesis, Humboldt-Universität zu Berlin, 2002, available on `http://atlas.ifae.es/~markus/diplom.ps.gz`.

[17] E. Fermi, *On the Origin of Cosmic Radiation*, Physical Review **75** (1949) 1169.

[18] E. Derishev et al., *Particle acceleration through multiple conversions from a charged into a neutral state and back*, Physical Review **D68** (2003) 43003.

[19] G. Rybicki and A. Lightman, *Radiative Processes in Astrophysics*, John Wiley & Sons, 1979.

[20] V. Schönfelder, editor, *The Universe in Gamma Rays*, Springer, 2001.

[21] R. Diehl, *Gamma-Ray Production and Absorption Processes*, chapter 2, In Schönfelder et al. [20], 2001.

[22] F. Jones, *Calculated Spectrum of Inverse Compton Scattered Photons*, Physical Review **167** (1968) 1159.

[23] J. Wang, L. Qinghuan, and G. Xie, *Spectral Relation between X-rays and Gamma Rays for Blazar High-Energy Emission*, The Astrophysical Journal **457** (1996) L65.

[24] M. Boettcher and C. Dermer, *High-energy Gamma-Rays from Ultra-high-energy Protons in Gamma-Ray Bursts*, Astrophys. Journal **499** (1998) L131, astro-ph/9801027.

[25] F. Aharonian et al. (H.E.S.S. Collab.), *High-energy particle acceleration in the shell of a supernova remnant*, Nature **432** (2004) 75.

[26] F. Aharonian, *Very High Energy Cosmic Gamma Radiation*, World Scientific, 2004.

[27] T. Gold, *Rotating Neutron Stars as the Origin of the Pulsating Radio Source*, Nature **218** (1968) 731.

[28] D. Thompson et al., *Supplement to the Second EGRET Catalog of High-Energy Gamma-Ray Sources*, Astrophys. Journal Suppl. **107** (1996) 277.

[29] P. Goldreich and W. Julian, *Pulsar Electrodynamics*, Astrophys. J. **157** (1969) 869.

[30] P. Sturrock, *A Model of Pulsars*, Astrophys. J. **164** (1971) 529.

[31] M. Ruderman and P. Sutherland, *Theory of Pulsars: Polar Caps, Sparks, and Coherent Microwave Radiation*, Astrophys. J. **196** (1975) 51.

[32] K. Cheng, C. Ho, and M. Ruderman, *Energetic Radiation from Rapidly Spinning Pulsars. II. Vela and Crab*, Astrophys. J. **300** (1986) 522.

[33] J. Chiang and R. Romani, *Gamma Radiation from Pulsar Magnetospheric Gaps*, Astrophys. J. **400** (1992) 629.

[34] F. Aharonian et al. (HEGRA Collab.), *The unidentified TeV source (TeV J2032+4130) and surrounding field: Final HEGRA IACT-System results*, Astronomy and Astrophys. (2005), astro-ph/0501667.

[35] M. Lang et al. (Whipple Collab.), *Evidence for TeV gamma emission from TeV J2032+4130 in Whipple archival data*, Astronomy and Astrophys. **423** (2004) 415.

[36] Y. Butt et al., *Chandra/Very Large Array Follow-Up of TeV J2032+4131, the Only Unidentified TeV Gamma-Ray Source*, Astrophys. Journal **597** (2003) 494.

[37] D. Torres, E. Domingo-Santamaria, and G. Romero, *High-Energy Gamma Rays from Stellar Associations*, Astrohpys. Journal **601** (2004) L75, astro-ph/0312128.

[38] P. Parkinson, Recent results from the milagro tev gamma-ray observatory, in *40th Rencontres de Moriond on Very High Energy Phenomena in the Universe*, 2005.

[39] K. Ragan, From stacee to veritas, Presentation given at the CAP Congress, UBC, 2005.

[40] C. Urry and P. Padovani, *Unified Schemes for Radio-Loud Active Galactic Nuclei*, Publ. Astron. Soc. Pac. **107** (1995) 803, astro-ph/9506063.

[41] M. Rees, *Black Hole Models For Active Galactic Nuclei*, Ann. Rev. Astr. Astrophys. **22** (1984) 471.

[42] T. Schweizer, *Analysis of the Large Gamma Ray Flares of Mkn 421 as Observed with HEGRA CT1 on the Island La Palma in 2001*, PhD thesis, Universitat Autònoma de Barcelona, 2002, available on `http://wwwmagic.mppmu.mpg.de/publications/theses/ThomasS\_thesis.ps.gz`.

[43] J. Quinn et al., *Detection of Gamma Rays with E>300 GeV form Markarian 501*, Astrophys. Journal **456** (1996) 83.

[44] M. Punch et al., *Detection of TeV photons from the active galaxy Markarian 421*, Nature **358** (1992) 477.

[45] D. Kranich et al., Evidence for qpo structure in the tev and X-ray light curve during the 1997 high state gamma emission of mkn 501, in *26th International Cosmics Rays Conference, Salt Lake City, Utha*, 1999.

[46] F. Aharonian et al. (HEGRA Collab.), *Is the giant radio galaxy M87 a TeV gamma-ray emitter?*, Astronomy and Astroph. **403** (2003) L1.

[47] K. Mannheim, *The Proton Blazar*, Astron. Astrophys. **269** (1993) 67, astro-ph/9302006.

[48] K. Mannheim, *Possible Production of High-Energy Gamma Rays from Proton Acceleration in the Extragalactic Radio Source Markarian 501*, Science **279** (1998) 684, astro-ph/9803241.

[49] I. Mirabel et al., *A double-sided radio jet from the compact Galactic Center annihilator 1E1740.7-2942*, Nature **358** (1992) 215.

[50] R. Fender and T. Macarone, *Cosmic Gamma-Ray Sources*, Kluwer Academic Publishers, Dordrecht, 2004.

[51] I. Mirabel and L. Rodrigues, *A superluminal source in the Galaxy*, Nature **371** (1994) 46.

[52] I. Mirabel and L. Rodriguez, *Source of Relativistic Jets in the Galaxy*, Ann. Rev. Astron. Astrophys. **37** (1999) 409.

[53] J. Paredes et al., *Discovery of a High-Energy Gamma-Ray-Emitting Persistent Microquasar*, Science **288** (2000) 2340.

[54] F. Aharonian et al. (H.E.S.S. Collab.), *Discovery of Very High Energy Gamma Rays Associated with an X-ray Binary*, Science **309** (2005) 746.

[55] J. Albert et al. (MAGIC Collab.), *Variable very high energy gamma-ray emission from the microquasar LS I +61 303*, Science (2006), accepted for publication.

[56] D. Torres et al., *Luminous Infrared Galaxies as Plausible Gamma-Ray Sources for the Gamma-Ray Large Area Space Telescope and the Imaging Atmospheric Cherenkov Telescopes*, Astrohpys. Journal **607** (2004) L99.

[57] E. Domingo-Santamaria and D. Torres, *High energy gamma-ray emission from the starburst nucleus of NGC 253*, Astronomy and Astroph. **444** (2005) 403, astro-ph/0506240.

[58] C. Itoh et al., *Detection of a diffuse TeV gamma-ray emission from the nearby starburst galaxy NGC 253*, Astronomy and Astroph. **396** (2002) L1.

[59] F. Aharonian et al. (H.E.S.S. Collab.), *A Search for very high energy gamma-ray emission from the starburst galaxy NGC 253 with H.E.S.S.*, astro-ph/ **0507370** (2005).

[60] F. Aharonian et al. (H.E.S.S. Collab.), *Serendipitous discovery of the unidentified extended TeV gamma-ray source HESS J1303-631*, Astronomy and Astroph. **439** (2005) 1013, astro-ph/0505219.

[61] F. Aharonian et al., *A New Population of Very High Energy Gamma-Ray Sources in the Milky Way*, Science **307** (2005) 1938.

[62] C. Brogan et al., *Radio SNR Coincident with HESS J1813-178*, Astrophys. Journal **629** (2005) L105, astro-ph/0505145.

[63] P. Ubertini et al. (Integral Collab.), *Integral IGR J18135-1751 = HESS 1813-178*, Astrophys. Journal **629** (2005) L109, astroph/0505191.

[64] C. Meegan et al., *Spatial distribution of γ-ray bursts observed with BATSE*, Nature **355** (1992) 143.

[65] G. Fishman and C. Meegan, *Gamma-Ray Bursts*, Ann. Rev. Astronomy and Astrophys. **33** (1995) 415.

[66] S. Djorgovski et al., The cosmic gamma-ray bursts, in V. Gurzadyan, R. Jantzen, and R. Ruffini, editors, *IX Marcel Grossman Meeting*, World Scientific, Singapore, 2001.

[67] P. Jacobsson et al., *A mean redshift of 2.8 for Swift gamma-ray bursts*, Astronomy and Astrophys. **445** (2005), accepted for publication, astro-ph/0509888.

[68] K. Mannheim, R. Protheroe, and J. Rachen, *On the Cosmic Ray Bound for Models of Extragalactic Neutrino Production*, Physical Review **D63** (2001) 023003, astro-ph/9812398.

[69] M. Takeda et al., *Extension of the Cosmic Rays Energy Spectrum beyond the Predicted Greisen-Zatsepin-Kuzmin Cutoff*, Physical Review Letters **81** (1998) 1163, astro-ph/9807193.

[70] G. Fishman, *Observed Properties of Gamma-Ray Bursts*, Astron. and Astrophys. Suppl. Ser. **138** (1999) 395.

[71] R. Preece et al., *BATSE Observations of Gamma-Ray Bursts Spectra. IV. Time-resolved High-energy Spectroscopy*, Astrophys. Journal **496** (1998) 849.

[72] B. Paczynski, *Gamma-ray bursters at cosmological distances*, Astrophys. Journal **308** (1986) L43.

[73] J. Goodman, *Are Gamma-Ray Bursts Optically Thick?*, Astrophys. Journal **308** (1986) L47.

[74] R. Preece and D. Band, *The BATSE Gamma-Ray Burst spectral catalog. High time resolution spectroscopy of bright bursts using high energy resolution data*, Astrophys. Journal Suppl. **126** (2000) 19, astro-ph/9908119.

[75] C. Kouveliotou et al., *Identification of Two Classes of Gamma-ray Bursts*, Astrophys. Journal **413** (1993) L101.

[76] K. Hurley et al., *Detection of a gamma-ray burst of very long duration and very high energy*, Nature **372** (1994) 652.

[77] D. Band et al., *Batse Observations of Gamma-Ray Burst Spectra. I. Spectral Density*, Astrophys. Journal **413** (1993) 281.

[78] A. Falcone, *The Giant X-ray Flare of GRB050502B: Evidence for Late-time Integral Engine Activity*, Astrophysical Journal **641** (2006) 1010, astro-ph/0512615.

[79] T. Galama et al., *Optical Follow-Up of GRB 970508*, Astrophys. Journal **497** (1998) L13.

[80] E. Derishev, V. Kocharovsky, and V. Kocharovsky, *Phyical parameters and emission mechanisms in gamma-ray bursts*, Astronomy and Astrophys. **372** (2001) 1071.

[81] D. C. Morris, J. Reeves, V. Pal'shin, M. Garczarczyk, A. D. Falcone, D. N. Burrows, H. Krimm, N. Galante, M. Gaug, S. Mizobuchi, C. Pagani, A. Stamerra, M. Teshima, A. P. Beardmore, O. Godet, N. Gehrels, *GRB 050713A: High Energy Observation of the GRB Prompt and Afterglow Emission*, Astrophys. Journal (2006), submitted, astro-ph/0602490.

[82] G. Ghirlanda, G. Ghisellini, and D. Lazzati, *The collimation-corrected GRB energies correlate with the peak energy of their νF_ν spectrum*, Astrophys. Journal **616** (2004) 331, astro-ph/0405602.

[83] G. Ghisellini, `http://www.merate.mi.astro.it/~ghirla/deep/blink.htm`.

[84] R. Sari, T. Piran, and J. Halpern, *Jets in Gamma-Ray Bursts*, Astrophys. Journal **519** (1999) L17.

[85] R. Wijers et al., *Detection of Polarization in the Afterglow of GRB 9990510 with the ESO Very Large Telescope*, Astrophys. Journal **523** (1999) L33.

[86] S. Covino et al., *GRB 990510: linearly polarized radiation from a fireball*, Astronomy and Astrophys. **348** (1999) L1.

[87] S. Woosley, *Gamma-Ray Bursts from Stellar Mass Accretion Disks Around Black Holes*, Astrophys. Journal **405** (1993) 273.

[88] A. MacFadyen and S. Woosley, *Collapsars: Gamma-Ray Bursts and Explosions in Failed Supernovae*, Astrophys. Journal **524** (1999) 262.

[89] S. Woosley and A. MacFadyen, *Central Engines for Gamma-Ray Bursts*, Astron. Astrophys. Suppl. **138** (1999) 499.

[90] B. Paczyński, Gamma-Ray Bursts, in C. W. Akerlof and M. A. Srednicki, editors, *Texas/PASCOS '92: Relativistic Astrophysics and Particle Cosmology*, p. 321, 1993.

[91] B. Paczyński, *Are Gamma-Ray Bursts in Star Forming Regions?*, Astrophys. Journal **494** (1997) L45.

[92] M. Vietri and L. Stella, *A Gamma-Ray Burst Model with Small Baryon Contamination*, Astrophys. Journal **507** (1998) L45.

[93] T. Galama et al., *An unusual supernova in the error box of the γ-ray burst of 25 April 1998*, Nature **395** (1998) 670.

[94] J. Hjorth et al., *A very energetic supernova associated with the γ-ray burst of 29 March 2003*, Nature **423** (2003) 847.

[95] P. Mészáros, *The Supernova Connection*, Nature **423** (2003) 809.

[96] J. Hjorth et al., *The optical afterglow of the short γ-ray burst GRB 050709*, Nature **437** (2005) 859.

[97] J. Reeves et al., *The signature of supernova ejecta in the X-ray afterglow of the γ-ray burst 011211*, Nature **416** (2002) 512.

[98] R. Narayan, B. Paczyński, and T. Piran, *Gamma-Ray Bursts as the Death Throes of Massive Binary Stars*, Astrophys. Journal **395** (1992) L83, astro-ph/9204001.

[99] M. Rees, *Some Comments on Triggers, Energetics and Beaming*, Astronomy and Astrophys. Suppl. **138** (1999) 491.

[100] R. Voss and T. Tauris, *Galactic distribution of merging neutron stars and black hole - prospects for short gamma-ray bursts progenitors and LIGO/VIRGO*, Nature **437** (2005) 855.

[101] J. Villasenor et al., *Discovery of the short γ-ray burst GRB 050709*, Nature **437** (2005) 855.

[102] M. Rees and P. Mészáros, *Relativistic Fireballs - Energy Conversion and Timescales*, MNRAS **258** (1992) 41.

[103] M. Rees and P. Mészáros, *Unsteady Outflow Models for Cosmological Gamma-ray Bursts*, Astrophys. Journal **430** (1994) L93.

[104] P. Mészáros, *Theories of Gamma-Ray Bursts*, Ann. Rev. Astron. Astrophys. **40** (2002), astro-ph/0111170.

[105] M. Baring and A. Harding, *Photon opacity constraints for relativistically expanding gamma-ray burst sources*, Advances in Spase Research **15** (1995) 153.

[106] F. Daigne and R. Mochkovitch, *Gamma-ray bursts from internal shocks in a relativistic wind: temporal and spectral properties*, MNRAS **296** (1998) 275.

[107] A. Beloborodov, B. Stern, and R. Svensson, *Self-Similar Temporal Behavior of Gamma-Ray Bursts*, Astrophys. Journal **508** (1998) L25.

[108] R. Sari and T. Piran, *Variability in Gamma-Ray Bursts: A Clue*, Astrophys. Journal **485** (1998) 270.

[109] N. Lloyd-Ronning and V. Petrosian, *Synchrotron Radiation as the Source of Gamma-Ray Burst Spectra*, Astrophyiscal Journal **543** (2000) 722.

[110] C. Dermer and M. Boettcher, *Flash Heating of Circumstellar Clouds by Gamma-Ray Bursts*, Astrophys. Journal **534** (2000) L155.

[111] B. Panaitescu and P. Mészáros, *Simulations of Gamma-Ray Bursts from External Shocks: Time Variability and Spectral Correlations*, Astrophys. Journal **492** (1998) 683.

[112] P. Mészáros and M. Rees, *Gamma-Ray Bursts: Multiwaveband Spectral Predictions for Blast Wave Models*, Astrophys. Journal **418** (1993) L59.

[113] R. Sari and T. Piran, *The Early Afterglow*, Astron. Astrophys. Suppl. **138** (1999) 537.

[114] C. Akerlof et al., *Observation of contemporaneous optical radiation from a γ-ray burst*, Nature **398** (1999) 400.

[115] R. Wijers and T. Galama, *Physical Parameters of GRB 970508 and GRB 971214 from Their Afterglow Synchrotron Emission*, Astrophys. Journal **523** (1999) 177.

[116] T. Galama et al., *Physical Parameters of GRB970508 from Its Afterglow Synchrotron Emission*, Astron. and Astrophys. Suppl. Ser. **138** (1999) 451.

[117] F. Ryde, *The Cooling Behavior of Thermal Pulses in Gamma-Ray Bursts*, Astrophysical Journal **614** (2004) 827.

[118] A. Dar and A. DeRùjula, *A cannonball model of gamma-ray bursts: superluminal signatures*, (2000), astro-ph/00084874.

[119] A. DeRùula, Grbs in the cannonball model: An overview, in F. . R. Durouchoux, editor, *4^{th} Microquasar Workshop*, Center for Space Physics, Kolkata, 2002, astro-ph/020703.

[120] S. Dado, A. Dar, and A. DeRújula, *On the optical and X-ray afterglows of gamma ray bursts*, Astron. and Astrophysics **388** (2002) 1079.

[121] S. Dado, A. Dar, and A. DeRújula, *On the radio afterglow of gamma ray bursts*, Astron. and Astrophysics **401** (2003) 243.

[122] G. Ghisellini et al., *Compton dragged gamma-ray bursts: the spectrum*, MNRAS **316** (2000) L45.

[123] B. Stern and J. Poutanen, *Jets in Gamma-Ray Bursts*, MNRAS **352** (2004) L35, astro-ph/0405488.

[124] J. Frederiksen, P. Melcher, and E. Veje, *Electrical Band-gap energy of porous silicon at the porous silicon/crystalline silicon junction measured versus sample temperature*, Physical Review **B58** (1998) 12.

[125] V. Usov, *On the Nature of Nonthermal Radiation from Cosmological Gamma-Ray Bursters*, MNRAS **267** (1994) 1035.

[126] M. Lyutikov and R. Blandford, *Gamma Ray Bursts as Electromagnetic Outflows*, (2003), astro-ph/0312347.

[127] M. Lyutikov and V. Usov, *Precursors of Gamma-Ray Bursts: A Clue to the Burster's Nature*, Astrophyiscal Journal **543** (2000) L129.

[128] M. Sommer et al., *High-energy gamma rays from the intense 1993 January 31 gamma-ray burst*, Astrophysical Journal **422** (1994) L63.

[129] B. Dingus, J. Catelli, and E. Schneid, Bursts detected and not detected by egret imaging spark chambers, in *Gamma-Ray Bursts: 4^{th} Huntsville Symposium*, volume 428, p. 349, AIP Conf. Proc., 1998.

[130] M. González et al., *A GRB with high-energy Spectral Component Inconsistent with the Synchrotron Shock Model*, Nature **424** (2003) 749.

[131] M. Amenomori et al., *Search for 10 TeV burst-like events coincident with the BATSE bursts using the TIBET Air Shower Array*, Astronomy and Astrophys **311** (1996) 919.

[132] V. Connaughton et al., *A Search for TeV Counterparts to BATSE GRBs*, Astrophys. Journal **479** (1997) 859.

[133] V. Connaughton et al., *A Search for TeV GRBs on a 1-Second Time-scale*, Astroparticle Phys. **8** (1998) 179.

[134] L. Padilla et al., *Search for Gamma-Ray Bursts above 20 TeV with the HEGRA AIROBICC Cherenkov Array*, Astron. and Astrophys. **337** (1998) 43.

[135] R. Atkins et al., *The high-energy gamma-ray fluence and energy spectrum of GRB 970417A from observations with Milagrito*, Astroparticle Journal **583** (2003) 824, astro-ph/0207149.

[136] J. Poirier et al., *Sub-TeV Gammas in Coincidence with BATSE Gamma Ray Bursts*, Physical Review D **67** (2003) 042001.

[137] R. Atkins et al., *Constraints on Very High Energy Gamma-Ray Emission From Gamma-Ray Bursts*, Astroparticle Journal **630** (2005) 996, astro-ph/0207149.

[138] A. Jarvis et al., Grb observations around 100 gev with stacee, In *Proceedings of the 29th International Cosmics Rays Conference, Pune, India* [189].

[139] C. Dermer and J. Chiang, *Beaming, Baryon loading, and the Synchrotron Self-Compton Component in Gamma-Ray Bursts*, Astrophys. Journal **537** (2000) 785.

[140] R. Pilla and A. Loeb, *Emission Spectra from Internal Shocks in Gamma-Ray Burst Sources*, Astrophys. Journal **494** (1998) L167.

[141] B. Zhang and P. Meszaros, *High-Energy Spectral Components in Gamma-Ray Burst Afterglows*, Astrophys. Journal **559** (2001) 110.

[142] S. Razzaque, P. Mészáros, and B. Zhang, *GeV and Higher Energy Photon Interactions in GRB Fireballs and Surroundings*, Astrophys. Journal **613** (2004) 1072.

[143] T. Totani, *Very strong TeV emission as Gamma-Ray Bursts Afterglows*, Astrophys. Journal **536** (2000) L23, and ref. to prev. papers herein.

[144] F. De Paolis, G. Ingrosso, and D. Orlando, *High-energy gamma -ray emission from gamma-ray bursts*, Astronomy and Astrophys. **359** (2000) 514.

[145] C. Dermer and A. Atoyan, *Neutral beam model for the anomalous γ-ray emission component in GRB 941017*, Astronomy and Astrophysics **418** (2004) L5, astro-ph/0401115.

[146] A. Beloborodov, *Optical and GeV-TeV Flashes from GRBs*, Astrophys. Journal **618** (2005) L13.

[147] J. Granot and D. Guetta, *Explaining the High-Energy Spectral Component in GRB 941017*, Astrophys. Journal **598** (2003) L11.

[148] A. Pe'er and E. Waxman, *The high-energy tail of GRB941017: Comptonization of synchrotron self-absorbed photons*, Astrophys. Journal **603** (2004) L1.

[149] N. Galante, *Il Telescopio MAGIC per l'osservazione dei Gamma Ray Bursts*, Diploma thesis, Università degli studi di Padova, 2002, available on `http://www.pd.infn.it/magic/publi.html`.

[150] X. Wang, Z. Li, and P. Mészáros, *GeV-TeV and X-ray Flares from Gamma-Ray Bursts*, Astrophys. Journal **641** (2006) L89.

[151] A. Dar and A. DeRùjula, *The Cannonball Model of Gamma Ray Bursts: high-eneryg neutrinos and γ-rays*, (2001), astro-ph/0105094.

[152] J. Primack et al., *Probing galaxy formation with TeV gamma ray absorption*, Astroparticle Physics **11** (1999) 93.

[153] Y. Huang, Z. Dai, and T. Lu, *Failed Gamma-ray Bursts and Orphan Afterglows*, MNRAS **332** (2002) 735.

[154] C. Barraud et al., *Spectral analysis of 35 GRBs/XRFs observed with HETE-2/FREGATE*, Astron. and Astrophys **400** (2003) 1021.

[155] S. Dado, A. Dar, and A. DeRújula, *On the origin of X-ray flashes*, Astron. and Astrophysics **422** (2004) 381.

[156] R. Duncan and C. Thompson, *Formation of Very Strongly Magnetized Neutron Stars - Implications for Gamma-Ray Bursts*, Astrophys. Journal **392** (1992) L9.

[157] M. Varendorff, *Gamma-Ray Bursts*, chapter 15, In Schönfelder et al. [20], 2001.

[158] K. Hurley et al., *An exceptionally bright flare from SGR 1806-20 and the origin of short-duration γ-ray bursts*, Nature **434** (2005) 1098.

[159] R. Gould and G. Schréder, *Opacity of the Universe to High Energy Photons*, Physical Review Letters **16** (1966) 252.

[160] G. Fazio and F. Stecker, *Predicted High Energy Break in the Isotropic Gamma Ray Spectrum: a Test of Cosmological Origin*, Nature **226** (1970) 135.

[161] T. Kneiske et al., *Implications of cosmological gamma-ray absorption - II. Modification of gamma-ray spectra*, Astronomy and Astrophysics **413** (2004) 807, astro-ph/0309141.

[162] O. Blanch, *Study of the Gamma Ray Horizon with MAGIC as a new method to perform cosmological measurements*, PhD thesis, Universitat Autònoma de Barcelona, 2004, available on `http://wwwmagic.mppmu.mpg.de/publications/theses/Oscar\_thesis.ps.gz`.

[163] J. Albert et al., *Physics with a ground-based gamma-ray telescope of low energy threshold*, Astroparticle Physics **23** (2005) 493.

[164] C. Dermer, R. Schlickeiser, and A. Mastichiadis, *High-energy gamma radiation from extragalactic radio sources*, Astronomy and Astrophys. **256** (1992) L27.

[165] D. Spergel et al., *First Year Wilkinson Microwave Anisotropy Probe (WMAP) Observations: Determination of Cosmological Parameters*, Astrophys. Journal Supp. Series **148** (2003) 175.

[166] F. Prada et al., *Astrophysical inputs on the SUSY dark matter annihilation detectability*, Physical Review Letters **L93** (2004) 241301, astro-ph/0401512.

[167] S. Coleman and S. Glashow, *High-Energy Tests of Lorentz Invariance*, Physical Review Letters **D59** (1999) 116008, hep-ph/9812418.

[168] O. Blanch, J. Lopez, and M. Martiínez, *Testing the effective scale of Quantum Gravity with the next generation of Gamma Ray Telescope*, (2001), astro-ph/0107334.

[169] G. Amelino-Camelia et al., *Tests of quantum gravity from observations of γ-ray bursts*, Nature **393** (1998) 763, astro-ph/9712103.

[170] S. Biller et al., *Limits to Quantum Gravity Effects from Observations of TeV Flares in Active Galaxies*, Physical Review Letters **88** (1999) 2108, gr-qc/9810044.

[171] C. Baixeras et al. (MAGIC Collab.), *Commissioning and first tests of the MAGIC telescope*, Nuclear Instruments and Methods **A518** (2004) 188.

[172] H. Bichsel, D. Groom, and S. Klein, *Passage of Particles Through Matter*, chapter 27, p. 1, Volume 592 of [178], 2004, available on `http://pdg.lbl.gov/`.

[173] B. Rossi, *High Energy Particles*, Prentice-Hall, Inc., Englewood Cliffs, NJ, 1952.

[174] K. Greisen, Prog. Cosmic Rays Physics **3** (1956) 1.

[175] J. Nishimura and K. Kamata, *On the Theory of Cascade Showers, I*, Progress in Theoretical Physics **7** (1952) 185.

[176] K. Greisen, *Cosmic Ray Showers*, Annual Rev. of Nucl. Part. Science **10** (1960) 63.

[177] G. Grindhammer and S. Peter, The parameterized simulation of electromagnetic showers in homogeneous and smapling calorimeters, in R. Donaldson and M. Gilchriese, editors, *Proceedings of the Workshop on Calorimetry for the Supercollider, Tuscaloosa, AL*, Teaneck, NJ, 1989, World Scientific.

[178] Particle Data Group et al., *Review of Particle Physics*, volume 592, Physics Letters B, 2004, available on `http://pdg.lbl.gov/`.

[179] T. Gaisser, *Cosmic Rays and Particle Physics*, Cambridge University Press, 1990.

[180] M. Thomas and I. Richard, *Astronomical Refraction*, volume 17, John Hopkins APL Technical Digest, 1996.

[181] J. Barrio et al. (MAGIC Collab.), *The MAGIC Telescope – Design Study for the Construction of a 17 m Cherenkov Telescope for Gamma Astronomy above 10 GeV*, (1998), MPI-PhE/98-05.

[182] S. Oser et al., *High-Energy Gamma-Ray Observations of the Crab Nebula and Pulsar with the Solar Tower Atmospheric Cerenkov Effect Experiment*, Astrophys. Journal **547** (2001) 949.

[183] C. Benn and S. Ellison, *La Palma Night-Sky Brightness*, New Astron. Rev. **42** (1998) 503.

[184] K. Bernlöhr, Air shower cherenkov light simulations, available on `http://www.mpi-hd.mpg.de/hfm/CosmicRays/ChLight/ChLat.html`.

[185] A. Hillas, *The Origin of Ultra-High-Energy Cosmic Rays*, Annual Review of Astronomy and Astrophysics **22** (1984) 425.

[186] V. Chitnis and P. Bhat, *Simulation Studies on Arrival Time Distributions of Cherenkov Photons in Extensity Air Showers*, Astroparticle Physics **12** (1999) 45.

[187] V. Chitnis and P. Bhat, *Possible Discrimination between Gamma Rays and Hadrons Using Cherenkov Photon Timing Measurements*, Astroparticle Physics **15** (2001) 29.

[188] D. Sobczyńsky and E. Lorenz, *Simulation of the trigger performance of air Cherenkov telescopes for γ-astronomy*, Nuclear Instruments and Methods **A490** (2002) 124.

[189] *Proceedings of the 29^{th} International Cosmics Rays Conference, Pune, India*, 2005.

[190] J. Cortina et al., Technical Performance of the MAGIC Telescope, In *Proceedings of the 29^{th} International Cosmics Rays Conference, Pune, India* [189], available on `http://wwwmagic.mppmu.mpg.de/publications/conferences/icrc05/cortina_preform.pdf`.

[191] D. Petry (MAGIC Collab.), *The MAGIC Telescope - Prospects for GRB research*, Astron. Astrophys. Suppl. Ser. **138** (1999) 601.

[192] B. Riegel et al., A tracking monitor for the MAGIC telescope, In *Proceedings of the 29^{th} International Cosmics Rays Conference, Pune, India* [189], available on `http://wwwmagic.mppmu.mpg.de/publications/conferences/icrc05/riegel_starg.pdf`.

[193] J. Davies and E. Cotton, J. Solar Energy Science and Engineering **1** (1957) 16.

[194] D. Bastieri et al., The Mirrors for the MAGIC Telescopes, In *Proceedings of the 29^{th} International Cosmics Rays Conference, Pune, India* [189], available on `http://wwwmagic.mppmu.mpg.de/publications/conferences/icrc05/bastieri_mirror.pdf`.

[195] C. Bigongiari et al., *The MAGIC telescope reflecting surface*, Nuclear Instruments and Methods **A518** (2004) 193.

[196] M. Garczarczyk et al., The active mirror control of the MAGIC telescope, in *28th Internation Cosmics Rays Conference, Tsukuba, Japan*, p. 2935, 2003, available on `http://publications.mppmu.mpg.de/2003/MPP-2003-99/FullText.pdf`.

[197] A. Ostankov et al., *A study of the new hemispherical 6-dynodes PMT from electron tubes*, Nuclear Instruments and Methods **A442** (2000) 117.

[198] G. Blanchot et al., *Performance of a fast low noise front-end preamplifier for the MAGIC Imaging Cherenkov Telescope*, IEEE Transactions on Nuclear Science **46** (1999) 800.

[199] D. Paneque et al., *A Method to Enhance the Sensitivity of Photomultipliers for Air Cherenkov Telescopes*, Nuclear Instruments and Methods **A504** (2003) 109.

[200] D. Paneque, *The MAGIC Telescope: Development of new technologies and first observations*, PhD thesis, Technische Universität München, 2004, available on `http://wwwmagic.mppmu.mpg.de/publications/theses/David_thesis.ps.gz`.

[201] D. Paneque, *An optical properties studies of the new hemispherical PMTs from Electron Tubes*, Diploma thesis, Universitat Autònoma de Barcelona, 2001, available on `http://wwwmagic.mppmu.mpg.de/publications/theses/David_diplom.ps.gz`.

[202] E. Lorenz, private communication.

[203] M. Doro, *The Commissionning and Characterization of the Calibration System of the MAGIC Telescope*, Diploma thesis, Universitá di Padova, 2004, available on `http://wwwmagic.mppmu.mpg.de/publications/theses/LaureaMDoro.ps.gz`.

[204] A. Laille, PhD thesis, 2005, in preparation.

[205] R. Winston and W. Welford, *High Collection for Nonimaging Optics*, Academic Press, 1989.

[206] A. Karle, *Analog optical transmission of fast photomultiplier pulses over distances of 2 km*, Nuclear Instruments and Methods **A387** (1997) 274.

[207] E. Lorenz et al., *A fast, large dynamic range analog signal transfer system based on optical fibers*, Nuclear Instruments and Methods **A461** (2001) 517.

[208] M. Meucci et al., *The trigger system of the MAGIC telescope: on-line selection strategies for Cherenkov telescopes*, Nuclear Instruments and Methods **A518** (2004) 554.

[209] J. Cortina et al., The data acquisition of the MAGIC telescope, in *The Universe Viewed in Gamma Rays, Kashiwa, Chiba, Japan*, 2002.

[210] R. Stieher, *Konzeption, Entwicklung und Aufbau einer FADC-basierten Ausleseelektronik für das MAGIC Teleskop*, PhD thesis, Universität Siegen, 2001.

[211] T. Schweizer, private communication.

[212] N. Galante et al., The MAGIC Telescope and the Observation of Gamma Ray Bursts, 2003, available on `http://publications.mppmu.mpg.de/2003/MPP-2003-87/FullText.pdf`.

[213] The GCN homepage `http://gcn.gsfc.nasa.gov/`.

[214] J. Cortina et al., The control system of the MAGIC telescope, in *The Universe viewed in Gamma Rays, Kashiwa, Japan*, 2002, available on `http://publications.mppmu.mpg.de/2002/MPP-2002-147/FullText.pdf`.

[215] J. Capdevielle et al., *The Karlsruhe extensive air shower simulation code CORSIKA*, KFK Report **4998** (1992).

[216] D. Heck et al., *CORSIKA: A Monte Carlo Coode to Simulate Extensive Air Showers*, FZKA **6019** (1998), available on `http://www-ik.fzk.de/corsika/physics_description/corsika_phys.html`.

[217] D. Heck and J. Knapp, *Extensive Air Shower Simulation with CORSIKA: A User's Guide*, 2002, available on `http://www-ik.fzk.de/corsika/usersguide/usersguide.ps.gz`.

[218] K. Werner, *Strings, pomerons and the VENUS model of hadronic interactions at ultrarelativistic energies*, Phys. Reports **232** (1993) 87.

[219] P. Majumdar et al., Monte carlo simulation for the MAGIC telescope, In *Proceedings of the 29th International Cosmics Rays Conference, Pune, India* [189], available on `http://wwwmagic.mppmu.mpg.de/publications/conferences/icrc05/majumdar_mc.pdf`.

[220] T. Bretz and R. Wagner, The MAGIC Analysis and Reconstruction Software, in *28th Internation Cosmics Rays Conference, Tsukuba, Japan*, p. 2947, 2003, available on `http://publications.mppmu.mpg.de/2003/MPP-2003-97/FullText.pdf`.

[221] F. Rademaker and R. Brun, *ROOT: An Object-Oriented Data Analysis Framework*, Linux Journal **51** (1998), `http://root.cern.ch/`.

[222] T. Schweizer et al., *The Optical Calibration of the MAGIC Telescope Camera*, IEEE Transactions on Nuclear Science **49** (2002) 2497.

[223] M. Gaug, *MAGIC-TDAS 04-06: The Calibration System Hardware Manual*, 2004, available on `http://atlas.ifae.es/~markus/calibration_doc.ps.gz`.

[224] S. Nakamura et al., *Superbright Green InGaN Single-Quantum-Well-Structure Light-Emitting-Diodes*, Japanese Journal of Appl. Phys. **34** (1995) L1332.

[225] L. Mitchell, *Avalanche transistors give fast pulses*, Electronic design **6** (1969) 202.

[226] J. Koo and M. Pocha, *Physical modeling of avalanche-transistor switching*, NASA STI/Recon Techn. Rep. N **83** (1982) 16649.

[227] M. Errando, *Quantum efficiency measurements of the MAGIC PMTs*, Diploma thesis, Universitat Autònoma de Barcelona, 2006, in preparation.

[228] E. Bellamy et al., *Absolute calibration and monitoring of a spectrometric channel using a photomultiplier*, Nuclear Instruments and Methods **A339** (1994) 469.

[229] Leica, Disto special5, `http://www.leica-geosystems.com/cpd/en/ndef/lgs_8773.htm`.

[230] G. Knoll, *Radiation Detection and Measurement*, J. Wiley & Sons, third edition, 1999.

[231] L. Holl, E. Lorenz, and G. Mageras, *A measurement of the light yield of common inorganic scintillators*, IEEE Transactions on Nuclear Science **35 (1)** (1988) 105.

[232] E. Zalewski and J. Geist, *Silicon Photodiode Absolute spectral Response Self-Calibration*, Appl. Opt. **19** (1980) 1214.

[233] J. Geist, E. Zalewski, and A. Schaefer, *Spectral Response Self-Calibration and Interpolation of Silicon Photodiodes*, Appl. Opt. **19** (1980) 3795.

[234] P. Bandyopadhyay, Periodic table with X-ray properties, in *based on data compiled by W. H.McMaster et. al. Compilation of X-ray Cross-Sections*, National Bureau of Standards, 2000, available on `http://www.csrri.iit.edu/periodic-table.html`.

[235] H. Spieler, *Silicon semiconductor detectors*, chapter 28.10, pp. 29–31, Volume 592 of [178], 2004, updated Sept. 2005.

[236] H. Spieler, *Low-noise electronics*, chapter 28.11, pp. 32–36, Volume 592 of [178], 2004, revised Aug. 2003.

[237] R. Health, *Scintillation Spectrometry - Gamma-Ray Spectrum Catalogue*, γ-ray Spectrometry Center, Idaho National Engeneering and Environmental Laboratory, second edition, 1997, available on `http://www.radiochemistry.org/periodictable/gamma_spectra/`.

[238] B. Richard, *Table of Isotopes*, John Wiley & Sons, Univ. of California, eighth edition, 1996.

[239] R. Mirzoyan, *MAGIC-TDAS 00-15 Conversion factor calibration for MAGIC based on the use of measured F-factors of PMTs*, 2000.

[240] R. Mirzoyan and E. Lorenz, in *Proceedings of the 25th International Cosmics Rays Conference, Durban, South Africa*, volume 7, p. 265, 1997.

[241] F. James, R. Cousins, and G. Cowan, *Statistics*, chapter 32, p. 1, Volume 592 of [178], 2004, last revised August 2005.

[242] W. Press et al., *Numerical Recipes in C^{++}*, Cambridge University Press, second edition, 2002.

[243] W. Cleland and E. Stern, *Signal processing considerations for liquid ionization calorimeters in a high rate environment*, Nuclear Instruments and Methods **A338** (1994) 467.

[244] A. Papoulis, *Signal analysis*, McGraw-Hill, 1977.

[245] H. Bartko, M. Gaug, A. Moralejo and N. Sidro (MAGIC Collab.), *FADC Pulse Reconstruction Using a Digital Filter for the MAGIC Telescope*, (2005), astro-ph/0506459.

[246] M. Martínez, private communication.

[247] R. Barlow, *Statistics, A Guide to the Use of Statistical Methods in the Physical Sciences*, John Wiley & Sons, 1989.

[248] M. Meyer, *MAGIC-TDAS 05-10 Calibration of the MAGIC telescope using muon rings*, (2005).

[249] F. Goebel et al., Absolute energy scale calibration of the MAGIC telescope using muon images, In *Proceedings of the 29th International Cosmics Rays Conference, Pune, India* [189], available on `http://wwwmagic.mppmu.mpg.de/publications/conferences/icrc05/goebel_muons.pdf`.

[250] A. Hillas, Cherenkov light images of eas produced by primary gamma showers, in F. Jones, editor, *Proc. of the* 19$^{\text{th}}$ *International Cosmic Ray Conference, La Jolla*, pp. 445–448, 1985.

[251] N. Otte and F. Goebel, Calculation of pedestals from low-gain, in *MAGIC Analysis and software meeting, Udine*, 2004.

[252] M. Garczarczyk and M. Gaug, *MAGIC-TDAS 05-11 Analysis of the GRB050713a data using the Mkn501 flare*, (2005).

[253] D. Tescaro, *Informazioni temporali nelle immagini Cherenkov osservate dal telescopio MAGIC*, Diploma thesis, Universitá di Padova, 2005, available on `http://photon05.pd.infn.it:5210/Documents/tesi/tesiTescaro.ps.gz`.

[254] D. Fegan, *Topical Review: γ/hadron separation at TeV energies*, Journal of Physics G Nuclear Physics **23** (1997) 1013.

[255] W. Wittek, *MAGIC-TDAS 02-03 Image Parameters*, (2003).

[256] V. Scalzotto, *Development of new Technologies for the Selection of Rare Events for Gamma-Hadron Separation in Gamma-Ray Astronomy*, PhD thesis, Università degli Studi di Padova, 2006, in preparation.

[257] D. Mazin, PhD thesis, Universität München, 2006, in preparation.

[258] R. K. Bock, A. Chilingarian, M. Gaug, F. Hakl, Th. Hengstebeck, M. Jirina, J. Klaschka, E. Kotrc, P. Savicky, S. Towers, A. Vaciulis, W. Wittek, *Methods for multidimensional event classification: a case study using images from a Cherenkov gamma-ray telescope*, Nuclear Instruments and Methods **A516** (2004) 511.

[259] L. Breiman, *Random Forests*, Machine Learning **45** (2001) 5.

[260] T. Hengstebeck, Userguide for the mars random forest implementation. a method of g/h-separation for the magic telescope, 2004, `http://magic.physik.hu-berlin.de/protected/ranforest/`.

[261] T. Li and Y. Ma, *Analysis Methods For Results in Gamma-Ray Astronomy*, Astrophys. Journal **272** (1983) 317.

[262] O. Helene, *Upper Limit of Peak Area*, Nuclear Instruments and Methods **212** (1983) 319.

[263] G. Feldman and R. Cousins, *A Unified Approach to the Classical Statistical Analysis of Small Signals*, Physical Review D **57** (1997) 3873, physics/9711021.

[264] J. Neyman, Phil. Trans. Royal Society London **236** (1937) 330.

[265] W. Rolke and A. Lopez, *Confidence intervals and upper bounds for small signals in the presence of background noise*, Nuclear Instruments and Methods **A458** (2001) 745, he-ph/0005187.

[266] W. Rolke, A. Lopez, and J. Conrad, *Limits and Confidence Intervals in the Presence of Nuisance Parameters*, Nuclear Instruments and Methods **A551** (2005) 493, physics/0403059.

[267] J. Albert et al., *Flux upper limit of gamma-ray emission by GRB050713a from MAGIC Telescope observations*, Astroparticle Physics **641** (2006) L9, astro-ph/0602490.

[268] J. Conrad, Trolke, ROOT class, 2004, `http://root.cern.ch/root/html510/TRolke.html`.

[269] G. Vacanti et al., *Muon ring images with an atmospheric Cerenkov telescope*, Astroparticle Physics **2** (1994) 1.

[270] J. Haislip et al., *A photometric redshift of z = 6.39±0.12 for GRB 050904*, Nature **440** (2006) 181.

[271] N. Kawai et al., *An optical spectrum of the afterglow of a -ray burst at a redshift of z = 6.295*, Nature **440** (2006) 184.

[272] A. Falcone, *GRB050713a: Swift detection of Bright Burst*, GCN circular **3581** (2005), `http://lheawww.gsfc.nasa.gov/docs/gamcosray/legr/bacodine/gcn3_archive.html`.

[273] J. Albert et al., *MAGIC Observations of very high energy gamma-rays from HESS J1813-178*, Astrophys. Journal Letters **637** (2006) L41.

[274] R. Firpo, *Study of MAGIC Telescope sensitivity for Large Zenith Angle observations*, Diploma thesis, Universitat Auònoma de Barcelona, 2005, available on `http://magic.mppmu.mpg.de/publications/theses/RogerFirpo_tesina.pdf`.

[275] 2005, GCN GRB OBSERVATION REPORT, 3604.

[276] 2005, GCN GRB OBSERVATION REPORT, 3588.

[277] 2005, GCN GRB OBSERVATION REPORT, 3584.

[278] 2005, GCN GRB OBSERVATION REPORT, 3695.

[279] `http://glast.gsfc.nasa.gov/`.

[280] 2005, GCN GRB OBSERVATION REPORT, 3619.

[281] 2005, GCN GRB OBSERVATION REPORT, 3597.

Acknoledgements

When I was working in my previous experiment, I once read a PhD-thesis which started with a long thanks-giving sermon to God to have provided the student with all those people who helped him to write that thesis which, of course, was subsequently dedicated entirely to Him. As I personally don't believe in God, I have now and here the opportunity to express thanks to existing people who helped me or made this work possible at all. I really hope that they will read these pages and find here a part of the deep gratitude I feel towards them.

First of all, I want to thank my thesis-director, Manel Martínez Rodríguez, who stands at the beginning of this work, already four years ago. He offered me the opportunity to carry out this investigation and accompanied and supported my work during all this long time. I found him always a person, who is fascinated and enthusiastic about the possibilities of the MAGIC telescope, and further about fundamental physics research. It was also his optimism which made me decide to continue some time longer in this experiement.

The second person, who laid the fundaments of this investigation and whom I want to thank here, is Thomas Schweizer. He designed the calibration system and taught me, not only its functionning, but electronics and experimental physics at a much broader level.

I want thank very much Eckart Lorenz who dedicated a lot of time to the calibration system, and was helping non-stop to install the PIN Diode during one especially crucial week at La Palma. Among so many other things, he taught me handling of and knowledge about radio-active materials. In this context, I also want to thank Nepomuk Otte for having brought the corresponding material and a QVT to La Palma. In that respect, I am also grateful to Carmen Baixeras and Lluis Font who provided radio-active sources for tests at IFAE and helped to understand the resulting spectra.

People with whom I collaborated in the construction of the calibration system were further Javi Lopez, Pepe Flix, Emma de Oña Wilhelmi, Manel Martínez, Isaac Martínez, Manel Errando, Nuria Sidro, David Paneque and Sascha Ostankov. All of them have contributed in a decisive manner to its functionning, and it was a pleasure to put the pieces together at the telescope site with those working at IFAE.

I am extremely grateful to Michele Doro who wrote his diploma thesis on the calibration system and clarified some important points on the calibration . With him, I developped a sincere friendship whereupon he introduced me to his life in Italy and my present stay and work at the INFN at Padova. Similar thanks to Mose Mariotti for having me offered a post-doc position in his group and permitted me to finish this work there.

A big part of the signal extractor work has been done in collaboration with Hendrik Bartko whom I'm very thankful for having me shown so many small and useful details about signal analysis and LaTeX.

I am very grateful to Markus Garczarczyk for a wonderful cooperation in the analysis of GRB050713a and Abelardo Moralejo for his thorough look at the obtained

results. I also want to thank Nicola Galante, Antonio Stamerra and Riccardo Paoletti for having me shown how far the spirit of Galileo Galilei has penetrated the scientific community of Pisa.

Finally I want to thank here especially Donatella Pascoli who read the hardware parts with very careful attention and who did not stop asking questions until every detail was completely understood. For always useful and interesting discussions, I'm grateful to Javi Rico and Juan Cortina.

Last but not least, I want to take the opportunity here to thank my parents, Albin and Valerie Gaug who supported me during the time of my studies, had to suffer long years of absence from home and never doubted about the sense and necessity of what I was learning thereby.

The work was supported by the Spanish Ministery for Education and Science by a grant of three years in the framework of the FPU program.

Glossary

Abbreviations

ADC Analog to Digital Converter, see page 47.

AGN Active Galactic Nuclei, see page 10.

AIROBICC AIR shower Observation By angle Integrating Cherenkov Counter, see page 24.

AMC Active Mirror Control, see page 45.

BATSE Burst and Transit Source Explorer, see page 14.

BeppoSAX Satellite for Astronomy X (Beppo in honor of Giuseppe Ochialini), see page 14.

CAN-bus Controller Area Network, shared serial bus standard, developped for noisy environments. Achieves up to 250 kbit/s for network distances at 250 m. See page 71.

CANGAROO Collaboration of Australian and Nippon for a GAmma Ray Observatory in the Outback, operating since 1992, see page 13.

CCD Charged Coupling Device, sensor for recording images, see page 45.

CGRO Compton Gamma Ray Observatory, launched in 1991, see page 2.

CL Confidence Level, see page 189.

CORSIKA COsmic Ray SImulation for Kascade, see page 59.

CT1 Cherenkov Telescope 1, part of the HEGRA array. See page 73.

DAC Digital to Analog Converter, see page 55.

DAQ Data AcQuisition, see page 57.

DT Discriminator Threshold, see page 195.

EBL Extragalactic Background Light, see page 29.

EGRET Energetic Gamma Rays Experiment Telescope, onboard CGRO, see page 10.

f focal length: Distance from mirror in which parallel light rays get focussed into one point, see page 44.

FADC Flash ADC, see page 57.

FGPA Field-Programmable Gate Array, see page 57.

FiFo First in First outp, see page 57.

FOV Field Of View, see page 46.

FSR Fazio-Stecker Relation, see page 29.

FWHM Full Width at Half Maximum, corresponds to about $2.35\,\sigma$ in case of a Gaussian, see page 46.

GaAs Gallium Arsenide, semiconductor, see page 55.

GCN GRB Coordinates Network, see page 58.

GRAND Gamma Ray Astrophysics at Notre Dame, see page 24.

GRB Gamma ray Bursts: Short violent outbursts of gamma rays, see page 2.

GRH Gamma Ray Horizon, see page 29.

GSFC Goddard Space Flight Center, see page 58.

gspot Gamma Sources POinting Trigger, see page 58.

H.E.S.S. High Energy Stereoscopic System, inaugurated in 2004, see page 7.

HEGRA High Energy Gamma Ray Astronomy, running from 1987 to 2002, see page 9.

HETE-2 High Energy Transient Explorer, launched in 2000 in a second try after the exploded first version, see page 20.

HST Hubble Space Telescope, see page ix.

IAC Instituto de Astrofísica de Canarias, see page 43.

IACT Imaging Atmospheric Cherenkov Technique, see page 41.

IFAE Institut de Física d'Altes Energies, see page 253.

Integral INTErnation Gamma Ray Astrophysics Laboratory, launched in 2003, see page 58.

IPR Individual Pixel Rate Control, see page 56.

ISM Interstellar Medium: Matter distributed between the stars, with typical densities of $1\,\mathrm{cm}^{-3}$, see page 6.

KS Kolmogorov-Smirnov, see page 214.

L1T Level-1 Trigger, see page 56.

L2T Level-2 Trigger, see page 56.

LED Light Emitting Diode, see page 63.

LMC Large Magellanic Cloud, visible in southern hemisphere, see page 29.

LSP Lightest Super-symmetric Particle, see page 31.

MAGIC Major Atmospheric Gamma Imaging Cherenkov Telescope, see page 2.

MARS Magic Analysis and Reconstruction Software, see page 59.

MC Monte Carlo, see page iv.

Milagrito Prototype of Milagro, running from 1997 to 1998, see page 24.

Milagro Multiple Institution Los Alamos Gamma Ray Observatory, completed in 2004, see page 10.

MSSM Minimal Super-symmetric extension of the Standard Model, see page 31.

NSB Night Sky Background, see page 59.

p.d.f. probability density function, see page 181.

PC Personal Computer, see page 55.

PCI Peripheral Component Interconnect bus, see page 57.

PMT Photo Multiplier Tube, see page 46.

PSF Point Spread Function, measure of the spherical aberration, see page 46.

PTP 1.4 p-Terphenyl, wavelength shifter, see page 47.

RICH Ring Image CHerenkov, see page 192.

ROSAT Röntgen Satellite, launched in 1990, see page 7.

ROTSE Robotic Optical Transient Search Experiment, see page 21.

RS-485 Recommended Standard 485, serial data exchange standard, see page 45.

SED Spectral Energy Density $E^2 \cdot dN/dE$, see page 191.

SGR Soft Gamma Repeater, see page 28.

SMA SubMiniature version A, rigid connectors for coaxial cables.

SNR Supernova Remnant: The ejected material from a supernova expaning into the ISM, see page 7.

SSC Synchrotron Self Compton Model: The same synchrotron emitting population of electrons up-scatters the synchrotron radiation field, see page 6.

STACEE Solar Tower Atmospheric Cherenkov Effect Experiment, completed in 2003, see page 24.

SWIFT Multiwavelength satellite, repointing *swiftly* and automatically to the direction of a GRB, launched in 2004, see page 14.

TASC Total Absorbtion Shower Counter, part of EGRET, see page 23.

TCP/IP Transmission Control Protocol / Internet Protocol, see page 58.

TTL Transistor-Transistor Logic: low: 0–0.8 V, high:2–5 V.

US United States, see page 59.

UTC Universal Time Coordinated, atomic frequency standard of Greenwich Mean Time, see page 58.

VCSEL Vertical Cavity Surface Emitting Laser, see page 52.

XMM-Newton X-ray Multi Mirror Satellite, launched in 1999, see page 19.

XRF X-Ray Flash, see page 28.

XRT X-Ray Telescope on ***SWIFT***, sensitive from 0.3 to 10 keV,, see page 18.

Astrophysics

aberration Flaw in imaging properties of a mirror. For Cherenkov telescopes important are: **spherical aberration**, measured by the point spread function, **field curvature** causing the focus to change from the center to the egde of the FOV ($\propto \phi^2$), **distortion** causing variation of magnification across the FOV and **coma** causing parallel light rays striking the mirror away from the optical axis to produce comet-like tails spreading radially out from the optical axis. See page 44.

accretion disk A rotating disk of gas and dust matter around a variety of stars and other massive objects. Black holes are usually surrounded by accretion disks. Matter falling into a black hole radiate energy of up to 40 % of their rest mass.

afterglow Lingering radiation in shorter wavelengths remaining after a GRB, see page 2.

ankle Energy at which the cosmic rays energy spectrum bends over from a differential spectral index of -3 to a steeper spectrum. Situated around 3 EeV. The spectral index after the ankle is still under debate. See page 1.

Band-spectrum Function with which most of the GRB spectra can be fitted, see page 16.

black hole A region where matter collapses to infinite density and, as a result, the curvature of spacetime is extreme. The intense graviational field prevents any electromagnetic radiation from escaping from inside a region of the so-called Schwartzschild radius. Black holes can rotate (the *Kerr*-black hole) and can lose a part of their rotational momentum via the *Blanford-Znajek* (B-Z) mechanism, see page 7.

blazar A class of AGNs, seen with their jets pointed directly to us, see page 10.

bremsstrahlung Emission of charges, accelerated in a Coulomb field, especially those of nuclei, see page 6.

cannonball Optically thick, ultra-relativistic plasma ball, see page 22.

circumburst medium The medium being found around the progenitor of a GRB. Depending on the progenitor assumptions, it can be as thin as the interstellar medium ($1\,\mathrm{cm}^{-3}$) in the neutron-star merger model or rising up to more than $100\,\mathrm{cm}^{-3}$ in collapsar models. See page 21.

collapsar Supernova in which a (Wolf-Rayet) star's core collapses directly to a black hole, also known as ***hypernova***, see page 19.

cooling break Break in power law distribution of accelerated electrons, due to synchrotron radiation, see page 5.

cosmic rays Ionizing radiation impining on Earth's atmosphere. Consisting mainly of protons and He-nuclei. Energy spectrum follows power-laws. See page 1.

Crab Nebula SNR from a supernova, exploded in 1054. First and strongest steady TeV gamma ray source, ever observed. See page 8.

crab unit Based on the Whipple measurement of the energy spectrum from the Crab Nebula at 1 TeV (Hillas, et al., ApJ 503 (744) 1998), the high-energy gamma ray fluxes are commonly given in *Crab Units*:

$$1\,\mathrm{Crab} \equiv \frac{dn_\gamma}{dE}\,(1\ \mathrm{TeV}) = (3.2{\pm}0.17_{\mathrm{stat}}{\pm}0.6_{\mathrm{syst}}) \cdot 10^{-11}\mathrm{ph\ cm^{-2}\ s^{-1}\ TeV^{-1}}\ ,$$

or:

$$1\,\mathrm{Crab} \equiv \nu F_\nu\,(1\ \mathrm{TeV}) = (5.12 \pm 0.27_{\mathrm{stat}} \pm 0.96_{\mathrm{syst}}) \cdot 10^{-11}\mathrm{erg\ cm^{-2}\ s^{-1}}\ .$$

.

dark matter Matter that cannot be detected directly but whose existence can be inferred from dynamical studies, see page 30.

electrons and positrons Consituents of the cosmic rays. At energies below 100 GeV consitute about 1 % of the cosmic rays. As they produce electromagnetic showers in the atmosphere, they form an irreducible background for Cherenkov telescopes. See page 1.

extended sources Object seen by telescope which cannot be fit by a single point-spread function. See page 8.

external shock Relativistic shock occurring when an ultra-relativistic plasma shell runs into the circumburst medium, see page 21.

extra-galactic accelerators Objects outside our Galaxy which are thought to accelerate cosmic rays beyond the knee, e.g. active galactic nuclei, starburst galaxies and gamma ray bursts, see page 1.

Fermi acceleration Particle acceleration mechanism yielding power laws: Assume, a particle receives an increase of energy proportional to its energy every time when it crosses the shock wave: $\Delta E = \xi E$. After n crossings and an injection energy E_0, E_n becomes $E_0(1+\xi)^n$. The number of crossings needed to reach energy E_n can then be calculated: $n = \ln(\frac{E}{E_0})/\ln(1+\xi)$. If we add a probability of escape, P_{esc}, per shock wave crossing, the probability of remaining in the acceleration region multiplies to $(1-P_{esc})^n$. Now the proportion of particles accelerated to energies greater than E can be calculated:

$$\begin{aligned} N(\geq E) &\propto \sum_{m=n}^{\infty}(1-P_{esc})^m = \frac{(1-P_{esc})^n}{P_{esc}} \\ N(\geq E) &\propto \frac{1}{P_{esc}}(\frac{E}{E_0})^{-\gamma} \end{aligned}$$

with $\gamma = \ln(\frac{1}{1-P_{esc}})/\ln(1+\xi)$. See page 5.

fireball Optically thick, ultra-relativistic plasma, see page 20.

Galactic accelerators Objects in our Galaxy which are thought to produce cosmic rays beyond 1 GeV up to the knee, e.g. SNRs, pulsars, microquasars, OB-associations and dark matter clusters, see page 1.

gamma rays Consituents of the cosmic rays. As they are undeflected by the galactic and extragalactic magnetic fields, they point back to their source of emission and can be used for gamma ray astronomy. See page 1.

Ghirlanda relation Tight correlation, found by G. Ghirlanda, G. Ghisellini and D. Lazzati, between a GRB peak energy in the GRB rest frame and the collimation-corrected total energy of the burst E_γ: $E_{peak}^{obs}(1+z) \propto E_\gamma^{0.7}$. See page 18.

helium nuclei Second constituents of the cosmic rays up to the knee (after the protons). See page 1.

hypernova Supernova in which the star's core collapses directly to a black hole, also known as ***collapsar***, see page 19.

internal shocks Relativistic shocks between plasma shells of different velocity, see page 20.

inverse Compton scattering Relativistic scattering of electrons and photons where the photon gains energy from the electron, see page 6.

jet Bright, highly-directional outflow of matter and radiation. They typically come in pairs aiming at opposite directions and commonly occur where accretion disks are present.

Klein-Nishina regime Combined energy regime in which the Klein-Nishina cross section is valid for scattering of electrons and photons:

$$\sigma_{IC} = \frac{3}{8}\sigma_T \cdot \big(\frac{m_e c^2}{\gamma\,\epsilon}\big) \cdot \big(\ln(\frac{2\gamma\,\epsilon}{m_e c^2}) + \frac{1}{2}\big)\ , \tag{194}$$

where $\sigma_T = \frac{8}{3}\pi r_e^2$ is the *Thomson cross-section*, *gamma* is the electron Lorentz-factor and ϵ the intial photon energy (both in the lab. frame). Eq. 194 is valid if $\gamma\epsilon \gg m_e c^2$, see page 6.

knee Energy at which the cosmic rays energy spectrum bends over from a differential spectral index of -2.7 to -3. Situated around 4-5 PeV. See page 1.

long bursts GRBs lasting longer than 2 seconds, probably originating from collapsars, see page 16.

magnetar Very fast spinning neutron star with magnetic fields greater than 10^{14} G, see page 28.

magnetosphere Magnetic environment, created by an astrophysical object, see page 8.

messenger particles Particles which point back directly to their source of emission and carry information about its production, see page 5.

microquasar Object of stellar mass which displays in miniature some of the properties of quasars. See page 13.

Mie scattering Scattering of light by particles that are large in relation to the wavelength of the light, see page 38.

neutral pion decay Decay of the π^0 particle into two photons, see page 7.

neutrinos Weakly interacting particles, also produced in energetic astrophysical environments, see page 5.

neutron star Small, super-dense star composed mostly of tightly-packed neutrons. See page 8.

non-thermal State of objects (usually shocked plasma clouds) with densities so low that thermalization has not been possible. See page 1.

OB-association A loose grouping O stars and B stars, having emerged from the same interstellar cloud, scattered across a region of several hundred light years. See page 9.

OB-stars Young, hot stars having their maximum luminosity in the O (UV, 30 000-60 000 K) and B (blue, 10 000-30 000 K) band, see page 9.

outer gap model Pulsar emission model, see page 9.

plerion Supernova remnant with emission also inside the shell, probably from a pulsar wind ejected by a pulsar in its center, see page 8.

polar cap model Pulsar emission model, see page 8.

polar caps Region on the surface of a neutron star from which depart the magnetic field lines which cannot be closed due to the rotating light cylinder, see page 8.

power laws Differential energy spectra distributed as: $dN/dE \propto E^{-\alpha}$, with spectral index α. See page 5.

protons Primary constituents of the cosmic rays. Therefore the main background for Cherenkov telescopes. See page 1.

pulsar Fastly spinning neutron star, see page 8.

pulsar wind Characteristic ring flowing away from the pulsar's equatorial region and escaping jets, see page 9.

Rayleigh scattering Scattering of light by particles that are small in relation to the wavelength of the light, see page 38.

relativistic beaming A relativistic effect in which the radiation emitted from a particle travelling with a high Lorentz factor γ is emitted in a narrow beam of opening angle $1/\gamma$ in the direction of motion β. Observed from an angle θ w.r.t. β, it can be parameterized by the relativistic Doppler factor:

$$\delta = \frac{1}{\gamma(1 - \beta\cos(\theta))} \approx \frac{2\gamma}{1 + \theta^2\gamma^2} \ , \tag{195}$$

where the last approximation is valid for small angles θ and large γ. Observed energies appear then blue-shifted ($E_{obs} = \delta E_{em}$) and fluxes magnified ($F(\nu) = \delta^3 F'(\nu')$). See page 18.

reverse shock Shock front travelling backward in the rest frame of the outflow, see page 21.

shell type Supernova remnant with emission only from the shell, see page 8.

short bursts GRBs lasting shorter than 2 seconds, probably originating from neutron star mergers, see page 16.

standard candles Objects of known intrinsic brightness that can be used to set up distance scales. See page 18.

star formation rate The rate at which stars are forming in a galaxy. Of special interest is the evolution of the mean SFR with redshift which is one of the key parameters in cosmological models. See page 14.

starburst galaxies A galaxy in which star formation is taking place at an unusually large and rapid scale. The closest starburst galaxy is M82. See page 13.

superbubble A large cavity in the instellar medium, created by the explosion of several supernovae, typically created in OB-associations, see page 9.

supranova Supernova which creates a supramassive neutron star which collapses later to a black hole, see page 19.

synchrotron radiation Beamed photon emission of relativistic charges, accelerated by a magnetic field, see page 5.

thermal State of objects (usually stars) with densities high enough to be in thermal equilibrium, see page 1.

Thomson regime Combined energy regime in which the Thomson cross section is valid for scattering of electrons and photons:

$$\sigma_{IC} = \sigma_T \cdot \left(1 - \frac{2\gamma\epsilon}{m_e c^2}\right) , \tag{196}$$

where $\sigma_T = \frac{8}{3}\pi r_e^2$ is the *Thomson cross-section*, *gamma* is the electron Lorentz-factor and ϵ the intial photon energy (both in the lab. frame). Eq. 196 is valid if $\gamma\epsilon \ll m_e c^2$, see page 6.

Hardware

AC-coupling The PMT signals are AC-coupled at various places in the signal transmission and amplification chain. Adding up a constant number of FADC slices, the contribution of PMT pulses due to the light of night sky is then on average zero, only its RMS depends on the intensity of the background light, see page 111.

clock noise The MAGIC 300 MHz FADCs have an intrinsic clock noise occurring at a frequency of 150 MHz. The clock noise results in a superimposed AB-pattern on every signal. See page 111.

coating Milky lacquer containing a PTP wavelength shifter, applied to MAGIC PMTs, see page 48.

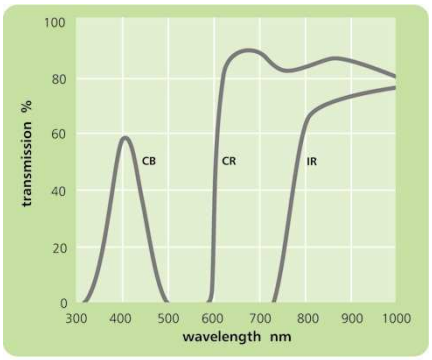

Filter characteristics give a measure of the blue, red and infrared response of photocathodes.

corning blue (CB) Photocathode luminous sensitivity to light from a tungsten-filament lamp with a colour temperature of 2856 K and transmitted through a Corning C.S. No. 5-58 blue filter, measured in: [A/lm], see page 49.

corning red (CR) Photocathode luminous sensitivity to light from a tungsten-filament lamp with a colour temperature of 2856 K and transmitted through a Corning C.S. No. 2-62 red filter, measured in: [A/lm], see page 49.

DAQ jumps Randomly occurring glitch of typically two FADC slices in the signal readout. Occurring in data recorded before mid 2005, see page 111.

discriminator threshold (DT) Nominal trigger threshold for the L1-trigger. Gets adjusted dynamically if the ***IPR*** of a channel becomes too high. Typical values are DT=32 for extra-galactic and DT=40 for galactic sources, see page 169.

excess-noise factor The additional variance to a signal, added by a photomultiplier:

$$F = \sqrt{1 + \frac{\sigma_1^2}{Q_1^2}} \ , \tag{197}$$

where Q_1 is the mean gain per incident photo-electron and σ_1 the width of the signal distributions per photo-electron. Illuminating the photomultiplier with a mean number of photo-electrons $< N_{phe} >$ and variances of $\mathrm{Var}[N_{phe}]$, the amplified signals Q will follow the relation:

$$\frac{\mathrm{Var}[Q]}{< Q >^2} = F^2 \cdot \frac{\mathrm{Var}[N_{phe}]}{< N_{phe} >} \ . \tag{198}$$

The excess-noise factor is always bigger than 1, see page 102.

flat-fielding A procedure to adjust the high-voltages of each photo-multiplier in the camera of a Cherenkov telescope such that the gains of all channels result to be the same. MAGIC reaches a typical ***flat-fielding precision*** of 10 %, see page 47.

high and low gain channel The MAGIC readout signal is split into two branches from which the high-gain branch gets amplified a factor 10 higher than the low-gain branch. The last gets delayed by about 55 ns and multiplexed into the high-gain branch by a $GaAs$-switch if the high-gain signal exceeds a threshold of about 50 photo-electrons, see page 55.

inner and outer pixels The MAGIC camera has two types of pixels, where the outer pixels have a factor four bigger area than the inner pixels. Taking into account additionally the different sizes of the light guides, their (quantum-effiicency convoluted) effective area is about a factor 2.6 higher. See chapter 3.7, see page 110.

pulse shaping The optical receiver boards shape the pulse with shaping times much larger than the typical intrinsic pulse widhts. Therefore, signal pulses have in first order always the same pulse shape, see page 111.

trigger jitter Jitter of one FADC slice in absolute arrival time introduced by the non-synchronization of the FADC clock with the MAGIC level-2 trigger, see page 111.

Statistics

Bayesian Named after the British mathematician Thomas Bayes, interpretations of probability are called Bayesian if they use Bayes' theorem:

$$P(A|B) = \frac{P(B|A) \cdot P(A)}{P(B)} \ , \tag{199}$$

where $P(A|B)$ denotes the posterior probability that A is true, given a measurement B, $P(B|A)$ is the probability to obtain a measurement B if the true value is A and $P(A)$ the prior probability that A occurs. $P(B)$ denotes the posterior probability that the measurement is made (which is usually 1), see page 188.

bias Difference between the expectation value of a signal estimator and the true value. See [241], see page 109.

confidence belt The ***confidence interval*** for each tried hypothesis is plotted versus the range of tested hypotheses μ. The area inclosed by the limits of the confidence interval are then called the confidence belt, see page 189.

confidence interval Interval in which a measurement of a parameter X_{obs} occurs with a given probability, assuming a true value of the parameter X and a probability distribution $P(X)$, see page 188.

confidence level Number of experiments which would yield an outcome inside the ***confidence interval***, only by statistical fluctuations. Measured in [%], see page 189.

consistency Characteristic of a signal estimator if the estimated value converges to the true value as the amount of data increases. See [241], see page 109.

coverage Taking a ***confidence interval*** $[X_1, X_2]$ and a fixed unkown value of the true parameter X_t. If a series of experiments measuring X and following a a prescription to contruct the intervals $[X_1, X_2]$ with $(1-\alpha)$ ***CL*** and these intervals contain the true value X_t in $(1-\alpha)$ of the cases, the prescription is said to yield the correct coverage. In case that X_t is part of the interval in less than $(1-\alpha)$ of the cases, the prescription undercovers the interval, in the contrary case, it overcovers the interval, see page 189.

decision trees A decision tree (or classification tree) is a predictive model: An ensemble of quality parameters is mapped about an item's target value. Starting from a root, each interior node corresponds to a possible (cut) value in one variable, followed by one or more child nodes in another variable. Finally, a leaf (or terminal node) represents the predicted target value if the variables have been followed the path from the root. See page 182.

efficiency Inverse of the ratio of the variance of the expectation value $\widehat{S}$ of a signal estimator and true value S to its minimum possible value $\mathrm{Var}_{min}[\widehat{S}]$. The last can be given by the Rao-Cramér-Frechet bound [241],

$$\mathrm{Var}_{min}(S) = \big(1 + \frac{\partial B}{\partial S}\big)^2 / I(S) \ , \tag{200}$$

where

$$I(S) = E\big[\big(\frac{\partial}{\partial S}\sum_i \ln f(x_i;S)\big)^2\big] \tag{201}$$

is the Fisher information. The sum is over all data, assumed independent and distributed according ot the p.d.f. $f(x;S)$ and B is the bias. See page 109.

fixed window algorithm Signal extractor being applied always to a same time window without permission to move inside the window, see page 110.

frequentist Classical interpretations of statistics are called frequentist, claiming that a posterior probability $P(A|B)$ for a true value of A, given a measurement B, has to be constructed by means of a ***confidence belt*** such that if A was a true random variable, the outcome of $P(A|B)$ will produce the correct ***coverage***, see page 188.

Gini index Developped by the Italian mathematician Corrado Gini, the Gini index is a measure of the degree of concentration (inequality) of a distribution along one parameter. It compares the **cumulative** normalized probability distribution P_{emp} of a ranked empirical distribution with the cumulative uniform probability distribution and can be defined as:

$$Q_{Gini}(N) = \frac{N + 1 + 2\sum_{i=1}^{N} P_{emp}(i)}{N} \tag{202}$$

is defined as the ratio of the difference of two arbitrary specimens to the mean value of all specimens and thus a number between 0 (perfect equality) and 1 (perfect inequality), see page 182.

Kolmogorov-Smirnov test Statistical test to determine whether two probability distributions f_1 and f_2 differ from each other. In the case of two histograms with the same binning, the cumulative distributions are calculated:

$$F^j = \frac{1}{N}\sum_{i=1}^{j} f_i \tag{203}$$

The maximum difference between both cumulative distributions defines the test statistic:

$$D = \max(F_1^j - F_2^j) \tag{204}$$

To retrieve significances from $D(N)$, tables or computer programs have to be used (e.g. the ROOT class TMath::KolmogorovTest(), see page 214.

mean-squared error Sum of bias B and variance of the expectation value $\widehat{S}$ of a signal estimator,

$$MSE = E\big[(\widehat{S} - S)^2\big] = \mathrm{Var}[\widehat{S}] + B^2 \ . \tag{205}$$

, see page 109.

multivariate classification methods Collection of procedures which associate every measurement $\vec{x}$ to to one of two possible groups such that misclassifications are minimized. The measurement $\vec{x}$ is thereby a multidimensional vector of quality parameter values $x = (x_1, x_2, ..., x_n)$, see page 182.

random forest An ensemble of ***decision trees***, obtained with random elements in the creation of each tree. See page 182.

robustness Characteristic of a signal estimator if the estimated value is insensitive to departures from assumptions in the p.d.f. owing to factors such as noise. See [241], see page 110.

sliding window algorithm Signal extractor which searches itself for the best suited signal within a global time window, see page 110.

test data samples Sub-set of data used for the determination of efficiency and error of a ***multivariate classification methods***. The test data sample has to different from the ***training data samples*** in order to eliminate biases, see page 182.

training data samples Sub-set of data used for the learning procedure of a ***multivariate classification methods***, whereby the answer to each putative classification is known beforehand, see page 182.

Analysis

equivalent photo-electrons the number of incident photons, divided by an average photo-detection efficiency. In the case of different pixel sizes, one common (artificial) photo-detection efficiency is constructed, making the number of equivalent photo-electrons proportional to the photon fluence per detection device at any place in the camera, rather than reflect the actual amount of photo-electrons seen by the photomultiplier. The concept of equivalent photo-electrons is needed to reconstruct shower images without discontinuities at the border between areas of different pixel size, see page 173.